UNIVERSIDADE DE BRASÍLIA

INSTITUTO DE GEOCIÊNCIAS

A PROVÍNCIA SCHEELITÍFERA SERIDÓ, PROVÍNCIA BORBOREMA, NORDESTE DO BRASIL: METALOGENIA E IMPLICAÇÕES GEOTECTÔNICAS

ROBERTO DE SIQUEIRA CORRÊA

TESE DE DOUTORADO N° 156

Brasília, 2019

UNIVERSIDADE DE BRASÍLIA

INSTITUTO DE GEOCIÊNCIAS

TESE DE DOUTORADO N° 156

A PROVÍNCIA SCHEELITÍFERA SERIDÓ, PROVÍNCIA BORBOREMA, NORDESTE DO BRASIL: METALOGENIA E IMPLICAÇÕES GEOTECTÔNICAS

Área de Concentração: Geologia Econômica e Prospecção

Aluno: Roberto de Siqueira Corrêa

Banca Examinadora:
Claudinei Gouveia de Oliveira (UnB - Orientador)
Paola Ferreira Barbosa (UnB)
Lena Virgínia Soares Monteiro (USP)
Francisco Valdir Silveira (CPRM)

Brasília, 2019

"I consider the positions of kings and rulers as that of dust motes.

I observe treasures of gold and gems as so many bricks and pebbles.

I look upon the finest silken robes as tattered rags.

I see myriad worlds of the universe as small seeds of fruit, and the greatest lake in India as a drop of oil on my foot.

I perceive the teachings of the world to be the illusion of magicians.

I discern the highest conception of emancipation as a golden brocade in a dream, and view the holy path of the illuminated ones as flowers appearing in one's eyes.

I see meditation as a pillar of a mountain, Nirvana as a nightmare of daytime.

I look upon the judgment of right and wrong as the serpentine dance of a dragon, and the rise and fall of beliefs as but traces left by the four seasons."

- *Buddha*

AGRADECIMENTOS

Reitero meus agradecimentos às pessoas que abençoaram-me com aprendizados:
Sejam elas da família
Ou de amizades de longa data.

Sinto gratidão àqueles e àquelas que prestigiaram-me com a convivência:
Sejam companheiros e companheiras do dia-a-dia
Ou pessoas que apenas acompanham-me em meu coração.

Jamais me esquecerei das situações que contribuíram para o meu crescimento,
Independente de terem sido prazerosas ou desagradáveis:
Venero a inevitabilidade.

Ao que está em cima e ao que está embaixo,
Ao que veio, ao que está, ao que virá,
Eu agradeço.

- Roberto de Siqueira Corrêa

RESUMO

Na literatura, o modelo clássico de *skarns* de scheelita postula que os depósitos originam-se a partir da interação entre fluidos magmático-hidrotermais e rochas carbonáticas. Há, entretanto, uma grande quantidade de exceções a essa regra. Dentre elas, destacam-se depósitos e ocorrências da Faixa de Dobramentos Seridó, que possui mais de 700 ocorrências documentadas de rochas portadoras de scheelita que nem sempre apresentam associações com plutonismo ou encaixantes carbonáticas. Alguns depósitos da área, tais como Bonfim, Brejuí, Bodó e Barra Verde, desenvolvem alterações que seguem o modelo clássico, formando diopsídio- e/ou granada-exoskarns no contato com os mármores da Formação Jucurutu. Outras ocorrências, por sua vez, produzem rochas com paragêneses dominadas por anfibólio e/ou biotita, interpretadas, respectivamente, como halos de alteração hidrotermal de natureza Ca-Ba e K.

Os representantes de depósitos com o halo Ca-Ba discutidos neste estudo incluem os das localidades de Bonfim, Morro do Careca, Salgadinho, Alívio, Recanto, Espinheiro e Pedro Tomás. Este domínio litológico apresenta uma vasta assembleia mineralógica composta por diopsídio, magnesiohornblenda-pargasita, andesina-labradorita, K-feldspato e hialofana, com menores quantidades de titanita, epidoto-allanita, barita, magnetita, carbonato, quartzo, molibdenita e scheelita. Análises de geoquímica de rocha total e de química mineral apontam metassomatismo em Ca, Mg, Fe, Ba, Na e ETRs.

Com relação ao halo K, este domínio foi encontrado nas localidades de Caçador, Salgadinho, Morro do Careca, Isidoro e Riachão. As rochas associadas a este halo são constituídas principalmente por bandas lepidoblásticas de biotita, com menores quantidades de magnesiohornblenda, albita-oligoclásio, K-feldspato, quartzo, muscovita/sericita, clorita, molibdenita, pirita e scheelita. É marcante o metassomatismo em Na, K, Si, Mo e W, além da sua associação com segregações quartzosas e diques pegmatíticos subconcordantes.

Ambos os halos desenvolvem feições de alteração similares, independentemente da rocha encaixante, observação suportada por datações U-Pb em zircão. No depósito de Bonfim, grãos reliquiares de idade Paleoarqueana contrastam com os cristais Neoarqueanos de Pedro Tomás e Paleoproterozoicos de Salgadinho e Caçador. Bordas neoformadas de alguns cristais de zircão, bem como análises $^{40}Ar/^{39}Ar$ em grãos de biotita e anfibólio, forneceram idades concordantes que remetem à transição do Neoproterozoico para o Ediacariano. Tais resultados geocronológicos, juntamente com observações meso- e microscópicas, refletem a importância do Ciclo Brasiliano para a formação da Província Scheelitífera do Seridó. Esta orogênese produziu e/ou reativou zonas de cisalhamento subverticais de *trend* N20°E, que limitam boa parte dos depósitos de tungstênio da área.

Desconsiderando os diques pegmatíticos, os halos Ca-Ba e K não apresentam relações espaciais/temporais com rochas carbonáticas e/ou intrusões. Neste sentido, a precipitação de scheelita é mais dependente do controle estrutural do que das rochas encaixantes. Assim, as rochas abordadas neste estudo são interpretadas como pertencentes às zonas de raiz dos *W-skarns* da região, em que cada halo é formado sob diferentes condições de pressão, temperatura, composição, pH, REDOX e razão fluido/rocha. Por fim, estas zonas podem ser correlacionadas às de outros sistemas magmático-hidrotermais, como halos sódico-cálcicos de depósitos Pórfiro e *IOCG*, podendo auxiliar na descoberta e na caracterização de novos depósitos.

ABSTRACT

In the literature, skarn deposits have their genesis commonly explained by the interaction between a magmatic-hydrothermal fluid and carbonatic rocks. There is, however, a large number of exceptions to this rule. One of the best examples of this fact may be the Seridó Mineral Province, where more than 700 scheelite occurrences have been documented. Important deposits, such as Bonfim, Brejuí, Bodó and Barra Verde, develop classic skarn alteration in the contact with marbles, forming diopside- and/or garnet-dominant parageneses. Other types of occurrences, though, account for amphibole- and/or biotite-dominant assemblages, interpreted as Ca-Ba and K haloes, respectively.

In this study, deposits and occurrences which are representative of the Ca-Ba hydrothermal alteration halo include Bonfim, Morro do Careca, Salgadinho, Alívio, Recanto, Espinheiro and Pedro Tomás. These neoformed rocks are constituted by a vast mineralogical assemblage, comprising diopside, magnesiohornblende-pargasite, andesine-labradorite, K-feldspar and hyalophane, with minor contents of titanite, epidote-allanite, barite, magnetite, carbonate, quartz, molybdenite, and scheelite. Both whole rock geochemistry and mineral chemistry analyses point to an enrichment in Ca, Mg, Fe, Ba, Na and REE.

Concerning the K halo, the occurrences of Caçador, Salgadinho, Morro do Careca, Isidoro and Riachão were studied. These rocks are constituted primarily by lepidoblastic biotite-rich bands, with minor amounts of magnesiohornblende, albite-oligoclase, K-feldspar, quartz, muscovite/sericite, chlorite, molybdenite, pyrite and scheelite. Rocks from this domain are characterized by an enrichment in Na, K, Si, Mo and W and occur associated with quartz segregations and subconcordant pegmatitic dykes.

Both haloes develop similar alteration patterns regardless of the wallrock. In the Bonfim, Pedro Tomás, Salgadinho and Caçador, relict zircon grains were dated by U-Pb, yielding a Paleoarchean age for Bonfim, a Neoarchean age for Pedro Tomás and Paleoproterozoic ages for Salgadinho and Caçador. The borders of some zircon crystals along with $^{40}Ar/^{39}Ar$ analyses in biotite and amphibole grains provided concordant ages set in the Neoproterozoic-Ediacaran transition. Both geochronological data and field and petrographic observations reflect the importance of the Brasiliano Cycle for W-Mo mineralization processes in the Seridó Mineral Province.

This orogenetic event deeply affected the Seridó Fold Belt, producing and/or reactivating subvertical N20°E-trending shear zones that control most tungsten deposits of the area. Apart from pegmatitic dykes, the Ca-Ba and K haloes do not show any clear association with carbonatic rocks and/or plutonic bodies. In this sense, scheelite deposition is much more structurally controlled than lithologically dependent. Hence, the rocks studied in this work are interpreted as the root zones of the W-skarns of the area, in which each halo is formed under different pressure, temperature, chemical, pH and REDOX conditions, as well as distinct fluid/rock ratios and hydrothermal solution compositions.

Finally, these haloes may be correlated with similar alteration patterns in other magmatic-hydrothermal systems, such as Porphyry, IOCG and RIRGS, which may help to discover new deposits by identifying and delimiting their root zones.

SUMÁRIO

CAPÍTULO I

1. INTRODUÇÃO

A Província Estrutural Borborema, localizada na Região Nordeste do Brasil, é conhecida mundialmente por ser uma área-chave para o entendimento da evolução geológica do planeta. Ela tem fornecido informações em diversos campos das geociências sobre eventos de formação de crosta, tectônica de placas e reconstruções paleogeográficas (Brito Neves et al., 2000). Embora exista vasta documentação tratando da diversidade de terrenos geológicos de diferentes idades que foram submetidos a eventos multifásicos de orogênese e/ou tafrogênese, ainda há uma série de questionamentos sobre sua formação (Cordani et al., 2013).

Com um histórico de publicações de mais de 30 anos, esta área ainda necessita de trabalhos regionais sobre geologia econômica. Embora várias teses, dissertações e artigos científicos tenham sido apresentados ao longo dos anos, tratando de depósitos singulares ou de pequenos conjuntos, ainda faltam dados que permitam realizar interpretações em escalas maiores. Estas conclusões, oriundas de técnicas analíticas de isótopos estáveis, como enxofre; de isótopos radiogênicos, como U-Pb e Ar/Ar; e de química mineral, possibilitariam obter informações sobre eventos de magmatismo, como fonte, idade, ambiente tectônico e fertilidade, além de processos metalogenéticos, como enriquecimento, acumulação e concentração de minérios. Tais trabalhos também carecem de maiores esclarecimentos sobre correlações entre processos de mineralização no Brasil e na África.

Deste modo, este trabalho de doutoramento pretendeu preencher algumas das lacunas abordadas acima, correlacionando, de maneira inédita na região, aspectos de geologia regional, incluindo idade e fonte de magmas, e sua influência na formação de depósitos minerais. O foco do trabalho se deu na Faixa Seridó, pertencente ao Domínio Rio Grande do Norte (Souza Neto et al., 2008). Esta região é conhecida por conter mais de 700 ocorrências de *skarns* de W, incluindo, ainda que de maneira subordinada e mais restrita, Au, Mo, Bi e Cu. Tais mineralizações estão correlacionadas por feições e processos de grande escala, envolvendo a influência de estruturas, desenvolvimento de halos de alteração hidrotermal, mecanismos de mineralização e eventos de magmatismo. A pesquisa visou correlacionar ocorrências e depósitos que possuam gênese e características metalogenéticas semelhantes e entender o seu significado no contexto da colagem brasiliana, com foco nas zonas de raiz do sistema de *skarn*, caracterizadas pelo desenvolvimento de halos de natureza cálcica/sódico-cálcica e potássica.

O desenvolvimento deste trabalho contribui para o avanço do conhecimento da área de estudo por apresentar novos dados de química mineral, isotópicos e geocronológicos que, a partir de interpretações, levarão à elaboração de modelos metalogenéticos e de evolução tectônica.

A estruturação do texto está segmentada em quatro capítulos: O primeiro consiste na contextualização geral do tema de estudo, incluindo o embasamento teórico utilizado, a metodologia empregada e objetivos alcançados, redigido em língua portuguesa; O Capítulo 2 consiste na conclusão da primeira fase do doutorado, com o artigo submetido para periódico internacional e, portanto, elaborado originalmente em língua inglesa; O terceiro abrange a fase final do doutorado, compreendendo um segundo artigo submetido para periódico internacional, também redigido em língua inglesa. Ambos os artigos referentes aos capítulos 2 e 3 foram submetidos para a revista *Ore Geology Reviews*. O quarto, por fim, consiste nas conclusões do trabalho em caráter mais abrangente, escrito em português. Há, ainda, um anexo eletrônico contendo os resultados de todas as análises de química mineral por microssonda eletrônica.

1.1. Hipótese de Trabalho

A pesquisa teve foco em um grupo de rochas já conhecido na literatura, atribuído a associações máficas/metamáficas (Moeri & Kloechner, 1979a,b), *skarns* a hornblenda e/ou biotita (Salim, 1993) e gnaisses calcissilicáticos (Cavalcante et al., 2016). A maior contribuição desta tese é justamente promover a reinterpretação acerca da origem destas rochas, levando à formulação da seguinte hipótese:

"As rochas abordadas neste estudo correspondem às zonas de raiz
da Província Scheelitífera do Seridó"

Desta afirmação, surgem dois grupos de questionamentos. O primeiro diz respeito ao seu embasamento teórico/conceitual: "O que são zonas de raiz?", "Qual a relação destas rochas com os *skarns* portadores de scheelita da região?", "Como ocorrências aparentemente tão distintas estão conectadas?", "Como ocorrem a migração do fluido hidrotermal e a deposição do minério neste sistema?", entre outros. O segundo, por sua vez, envolve os mecanismos para confirmar ou refutar a hipótese: "Quais técnicas analíticas devem ser utilizadas?", "Como situar estas ocorrências no espaço-tempo em meio à Colagem Brasiliana?", "Há discrepâncias entre as assinaturas químicas e isotópicas destas rochas com os *W-skarns*?", etc.

Com este ponto de partida, foram formulados os objetivos a serem alcançados e a metodologia a ser aplicada, descritos detalhadamente nos próximos tópicos.

1.2. Justificativa e Objetivos

Com a definição da hipótese, estabeleceram-se as diretrizes do trabalho, com alguns objetivos principais. O primeiro corresponde ao mapeamento, identificação, descrição e caracterização das rochas atribuídas às zonas de raiz dos *skarns* de tungstênio encontrados na região, utilizando, para tanto, uma metodologia clássica neste tipo de trabalho (Meinert et al., 2005), que é a de química mineral por Microssonda Eletrônica aliada ao imageamento por Microscópio Eletrônico de Varredura (MEV). Estas técnicas analíticas permitem identificar alterações crípticas, bastante comuns em depósitos hidrotermais e frequentemente invisíveis ao microscópio petrográfico. Além disso, permitem a correlação entre as diferentes texturas observadas com a mineralogia, a definição de assembleias minerais associadas a espectros distintos de condições físico-químicas, e a identificação de teores anômalos de alguns elementos, com destaque para metais base.

O segundo objetivo consiste num aprofundamento do estudo das zonas de raiz com o fim de compreender o seu posicionamento espaço-temporal em meio ao contexto geológico regional, envolvendo, para tanto, análises de geoquímica de rocha total e isótopos estáveis e radiogênicos, com o propósito de identificar possíveis fontes da mineralização, bem como datar os *skarns* e suas rochas encaixantes. De maneira mais ampla, a pesquisa empreendeu técnicas analíticas visando determinar os processos que envolvem a formação de magmas e soluções magmático-hidrotermais, com respeito à identificação de rochas-fonte e à natureza, acumulação, migração e deposição do fluido. Com estas análises, buscou-se uma melhor compreensão do papel do magmatismo brasiliano na formação dos depósitos da área de estudo e de determinar as idades dos protólitos em que os halos de alteração hidrotermal se desenvolveram.

Um terceiro objetivo consiste ainda em correlacionar as zonas de raiz identificadas na área de estudo com as de outros depósitos magmático-hidrotermais, como *Iron Oxide Copper Gold* (IOCG), Pórfiro e *Reduced Intrusion-Related Gold Systems* (RIRGS). Em profundidade, onde localizam-se as zonas de raiz, estas classes costumam apresentar uma série de semelhanças, respeitando condições específicas de ambiente tectônico, natureza dos magmas formadores, entre outros (Seedorff et al., 2008; Richards & Mumin, 2013).

Definições específicas dos questionamentos pertinentes ao estudo e metodologias utilizadas neste trabalho serão dadas nas próximas seções do Capítulo 1.

2. FUNDAMENTAÇÃO TEÓRICA

2.1. *Breve Revisão Sobre Skarns de Scheelita*

Sistemas pórfiros, de IOCG, *intrusion-related* e *skarns* são formados a partir da deposição de metais por fluidos hidrotermais. Estas soluções metassomáticas possuem origem magmática, podendo sofrer interação em maior ou menor grau com fluidos de outra natureza. Quando são produzidas

(exsolvidas), geralmente em estágios tardios da evolução de uma série magmática, ficam enriquecidas em elementos incompatíveis (e.g. Au, Cu, W) e complexantes (e.g. S, Cl, F, OH), que se ligam a metais e promovem o carreamento destes elementos até sítios propícios de deposição. Os halos de alteração hidrotermal são formados em diferentes estágios do processo de percolação de fluidos ao longo das rochas encaixantes, produzindo paragêneses que revelam condições distintas de formação, tais como profundidade, tempo, temperatura, pH, eH e composição química (Robb, 2005).

Estudos sobre o sistema magmático-hidrotermal têm sido feitos ao longo de décadas e identificados em sistemas pórfiros, IOCG, *intrusion-related* e *skarns* (Hart, 2007; Seedorff et al., 2008). Compreender os mecanismos de formação de halos de alteração hidrotermal, bem como o desenvolvimento de associações polimetálicas em diferentes modalidades de depósitos é a chave para realizar trabalhos prospectivos de sucesso (Candela & Piccoli, 2005; Williams et al., 2005). Embora os quatro tipos de depósitos citados possuam características muito contrastantes, seus processos de formação guardam muitas semelhanças. Um destes aspectos é o desenvolvimento de halos de alteração de natureza cálcica e/ou sódico-cálcica, que ocorrem em profundidade nestes sistemas, denominados de zonas de raiz (Carten, 1986; Richards & Mumin, 2013).

Trazendo o foco para depósitos do tipo *skarn* propriamente dito, comumente definidos como rochas calcissilicáticas formadas a partir da interação de material magmático/hidrotermal com rochas carbonáticas, podem apresentar diferentes gêneses, sem necessariamente necessitarem da presença de um pluton associado ou mesmo de encaixantes carbonáticas (Meinert et al., 2005). Com a ausência de magmatismo, *skarns* podem ser desenvolvidos a partir da percolação de fluidos hidrotermais ao longo de estruturas, bem como em sistemas geotermais e no assoalho oceânico. As rochas carbonáticas, por sua vez, podem ser substituídas virtualmente por qualquer litologia que seja submetida a metamorfismo regional e/ou de contato e que sofra interação com soluções metassomáticas, sejam elas de origem ígnea, metamórfica, meteórica ou marinha. *Skarns* são denominados *endoskarn* quando a alteração metassomática ocorre dentro da intrusão, e *exoskarn* quando as reações hidrotermais se dão na encaixante, e a alocação da zona de minério possui importantes implicações para o desenvolvimento do depósito (Chang & Meinert, 2004).

Os depósitos do tipo *skarn* são classificados com base nas suas *commodities*, podendo ser de Fe, Au, Cu, Zn, W, Mo e Sn (Figura 1). Cada um destes tipos tem características específicas e diferentes condições de formação, seguindo um *trend* do magmatismo mais primitivo para depósitos de Fe, até o plutonismo mais evoluído, formando Sn-*skarns* (Meinert, 1992). Fe-*skarns* apresentam enriquecimento geoquímico em Mg, Ni, V, Sc, empobrecimento em álcalis e Si, razão Rb/Sr<1, tem a magnetita como mineral-minério, e contam com uma maior proporção de *endoskarn* do que *exoskarn*. *Skarns* de ouro apresentam características intermediárias entre os de Fe e Cu, sendo enriquecidos em Mg, Bi, Te, As e Co, pobres em K, Si, associados a magmas reduzidos, metaluminosos e máficos ou intermediários e pertencem à variedade *gold-only* (Au^+ como íon predominante). Cu-*skarns* já tem maior afinidade com magmas calci-alcalinos, oxidados (série magnetita) e tipo-I, alojados em profundidades mais rasas e comumente apresentam textura porfirítica (Robb, 2005). Comparativamente com os Fe-skarn, são enriquecidos em Si, K, Ba, Sr e La e empobrecidos em Mg, Sc, Ni, Cr e V. Zn-*skarns* estão associados a magmas oxidados e costumam apresentar minerais de Fe e Mn. Mo-*skarns* ocorrem associados a magmas oxidados com intensa assimilação crustal. *Skarns* de Sn, por fim, ocorrem associados a plutons evoluídos, tipo-S, reduzidos, com alto conteúdo de SiO_2 e com intensa assimilação crustal, comumente relacionados a *greisens* (Meinert et al., 2005). Os *skarns* de W serão abordados mais à frente, por fazerem parte mais especificamente do tema desta pesquisa.

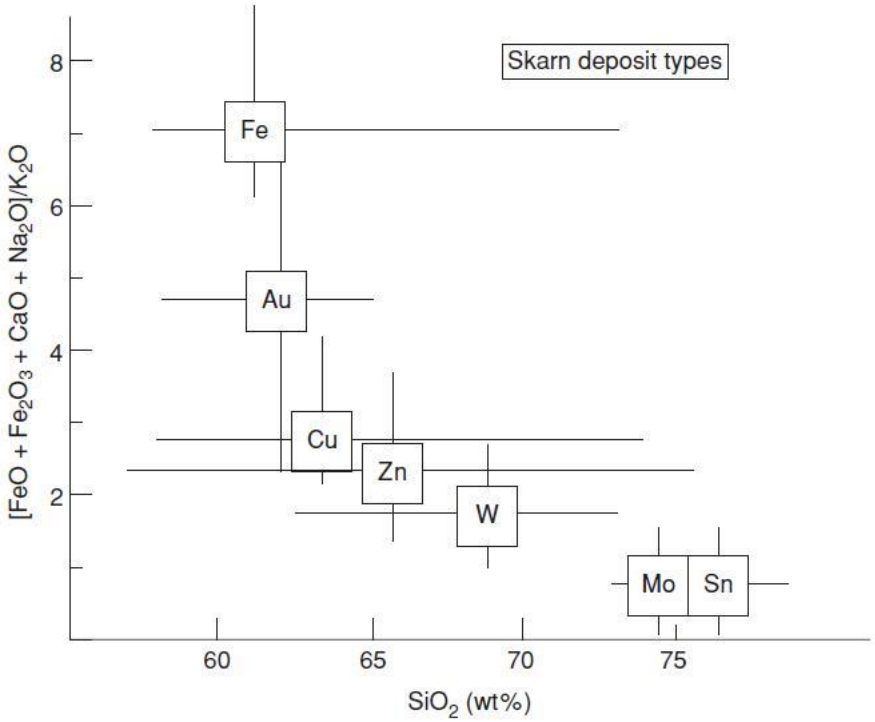

Figura 1. Gráfico de Tipos de Depósitos de *Skarn*, mostrando a relação entre a afinidade metalogenética e a natureza do magmatismo. Figura extraída de Meinert (1992).

O processo de formação de depósitos de *skarn* é complexo e multifásico (Figuras 2 e 3). Quando a intrusão atinge o pacote de rochas carbonáticas, ocorre metamorfismo de contato, desenvolvendo texturas típicas de *hornfels* e alterando a mineralogia, mas ainda num processo isoquímico (Pirajno, 1992). O início do processo metassomático se dá num segundo estágio, quando o fluido magmático-hidrotermal interage com as rochas encaixantes (Brown et al., 1985). Nesta fase, a solução hidrotermal costuma possuir temperaturas superiores a 500°C, salinidade superior a 50% em peso de NaCl, acrescentando Si, K, Na, Al, Fe e Mg no sistema. A alta reatividade das rochas encaixantes com o fluido faz com que a sua porosidade aumente, facilitando a circulação da solução ao longo da zona alterada (Meinert et al., 2005). Esta fase hidrotermal progressiva é caracterizada por formar uma paragênese de alta temperatura, que posteriormente é parcial ou totalmente reequilibrada para uma assembleia de baixa temperatura, definindo o terceiro estágio de alteração. Esta fase é retrogressiva, causada pela influência de um fluido magmático-hidrotermal tardio ou da mistura da solução inicial com águas meteóricas, conatas ou até mesmo marinhas (Robb, 2005). O fluido pertencente a este estágio é caracterizado por ser de natureza aquosa, possuir temperaturas inferiores a 400°C e apresentar salinidades inferiores a 20% em peso de NaCl. Este estágio é geralmente o principal responsável pela mineralização, pois provoca desestabilizações físico-químicas, alterando a temperatura, salinidade e condições REDOX, levando à precipitação de fases sulfetadas e/ou do minério (Pirajno, 2009).

Estudos envolvendo isótopos estáveis e radiogênicos se mostram úteis para entender os mecanismos de formação desta modalidade de depósito (Robb, 2005; Tombros et al., 2015). Para o caso em que as intrusões relacionadas à mineralização estão identificadas, é possível datar sua formação através de técnicas de isótopos U-Pb, Lu-Hf, além de termocronologia U-Th/He em zircão (Lu et al., 2013). Diretamente no *skarn*, é possível fazer termocronologia Ar-Ar em grãos de biotita e anfibólio, e Sm-Nd e Sr-Sr para determinar fontes e assinatura das rochas do depósito (Zheng et al., 2015). Para *skarns* que contém molibdenita, também é possível fazer análises Re-Os para datar a mineralização (Xia et al., 2015). Isótopos de C, O, H e S também se mostram eficazes para rastrear fontes e identificar processos (Meinert et al., 2005). Geralmente, sulfetos em *skarns* mostram variações de $\delta^{34}S$ saindo de valores tipicamente magmáticos, próximos a 0‰, nos arredores da intrusão até adquirir assinatura

transicional com as encaixantes e fluidos meteóricos/conatos, ficando superior a 10‰ (Pirajno, 2009; Barati & Gholipoor, 2014). Seguindo o mesmo padrão, valores de $\delta^{18}O$ em silicatos associados a *skarns* (e.g. piroxênio, granada e quartzo) mostram um contínuo entre assinaturas magmáticas e meteóricas, no intervalo de 4‰ a 9‰ (Brown et al., 1985). A evidência de mistura de fontes é mantida para valores de $\delta^{13}C$, situados em posições intermediárias entre o campo magmático e o de rochas encaixantes carbonáticas (Boomeri et al., 2010). Por fim, isótopos de H (δD) em silicatos hidratados (e.g. biotita e anfibólio) em *skarns* também possuem assinaturas na transição entre os campos ígneo e sedimentar/meteórico (Layne et al., 1991).

Uma importante ferramenta em estudos de *skarns* é a caracterização mineralógica de detalhe dos depósitos. Identificar relações texturais, temporais, bem como determinar a química mineral em análises de microssonda auxilia na definição de paragêneses e delimitação dos corpos mineralizados (Souza Neto et al., 2012). De maneira geral, os depósitos de *skarn* apresentam a relação espacial mineralógica de piroxênio distal e granada proximal, além de apresentarem alterações crípticas e mudanças de cor (Meinert et al., 2005). Temporalmente, são identificadas paragêneses pertencentes aos estágios de metamorfismo de contato e hidrotermal progressivo e retrogressivo (Robb, 2005; Figura 3). No metamorfismo, é desenvolvida uma assembleia calcissilicática bastante dependente da composição da encaixante. Nesta fase, para protólitos carbonáticos, é comum o desenvolvimento de diopsídio + plagioclásio cálcico ± granada cálcica ± epidoto (Smirnov, 1976). Com a entrada do fluido magmático-hidrotermal, salino, aquoso e de alta temperatura, o sistema é enriquecido com elementos e metais provindos do magma (Ismail et al., 2014). A segunda paragênese tende a reequilibrar ou alterar os minerais do primeiro estágio, sendo definida por diopsídio-hedenbergita + granada ferrosa ± actinolita-hornblenda ± plagioclásio cálcico ± feldspato potássico ± epidoto-allanita ± titanita ± apatita (Pirajno, 2009). No estágio metassomático retrogressivo, ocorre a percolação da solução hidrotermal de baixa temperatura e salinidade, gerando paragêneses com minerais hidratados, comumente incluindo actinolita-hornblenda + albita + calcita-dolomita + epidoto ± quartzo ± biotita ± magnetita ± sulfetos, além do minério (Brown et al., 1985). Além da caracterização mineralógica, análises por microssonda eletrônica também possibilitam realizar estudos de geotermobarometria, auxiliando a definir condições de formação desses depósitos (Salim, 1993).

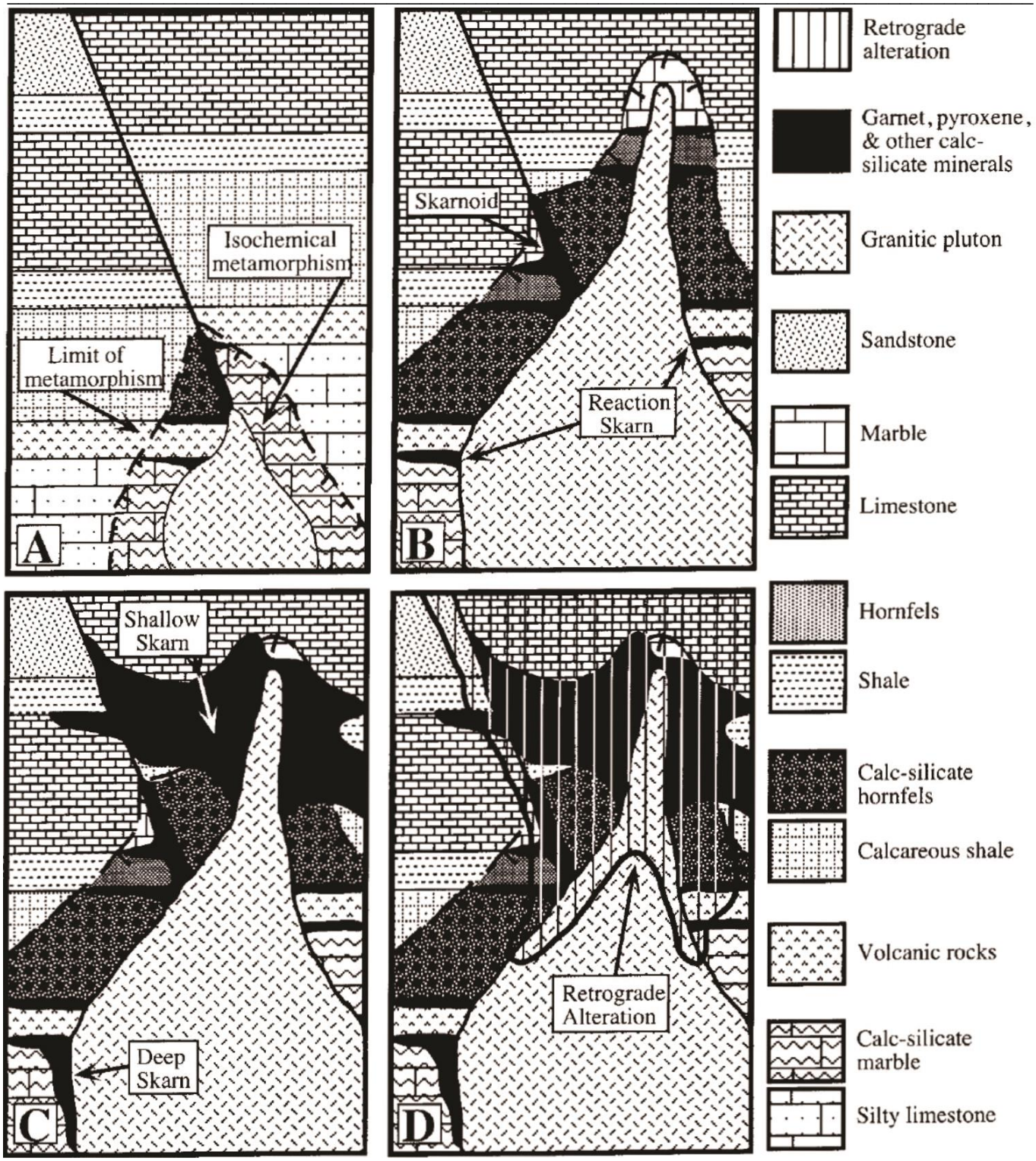

Figura 2. Quadro esquemático da formação de um depósito de *skarn*, extraído de Meinert et al. (2005). A: Intrusão do pluton e metamorfismo de contato. B: Aporte de fluidos magmático-hidrotermais causam recristalização e mudanças na mineralogia pré-existente, promovendo a circulação da solução hidrotermal ao longo das encaixantes, originando rochas calcissilicáticas. C: As características dos depósitos de *skarn* mudam conforme a profundidade, podendo ter importantes mudanças na assembleia mineralógica, regime de deformação, grau de metamorfismo, entre outros. Quanto mais próximo da superfície, maiores serão as diferenças físico-químicas entre o fluido hidrotermal e a rocha, e quanto mais profundo, as discrepâncias tenderão a se amenizar. D: Alteração retrogressiva, que frequentemente é a que está relacionada à mineralização. Esta fase pode representar um fluido de origem magmática tardio e de baixa temperatura ou mistura da solução mineralizante com águas meteóricas ou conatas.

Skarns mineralizados em tungstênio, com destaque para aqueles em que o minério principal é a scheelita, têm sido estudados ao logo de décadas, mostrando condições muito específicas para a sua formação (Smirnov, 1976; Souza Neto et al., 2008). De modo geral, W-*skarns* costumam apresentar muitas afinidades genéticas com Cu-*skarns*, apresentando o mesmo tipo de fonte para o magma. Depósitos de tungstênio desta natureza, entretanto, têm a tendência de estarem associados a séries

magmáticas mais diferenciadas, alojando-se em maiores profundidades e produzindo fluidos hidrotermais mais salinos que os *skarns* de cobre (Newberry & Swanson, 1986).

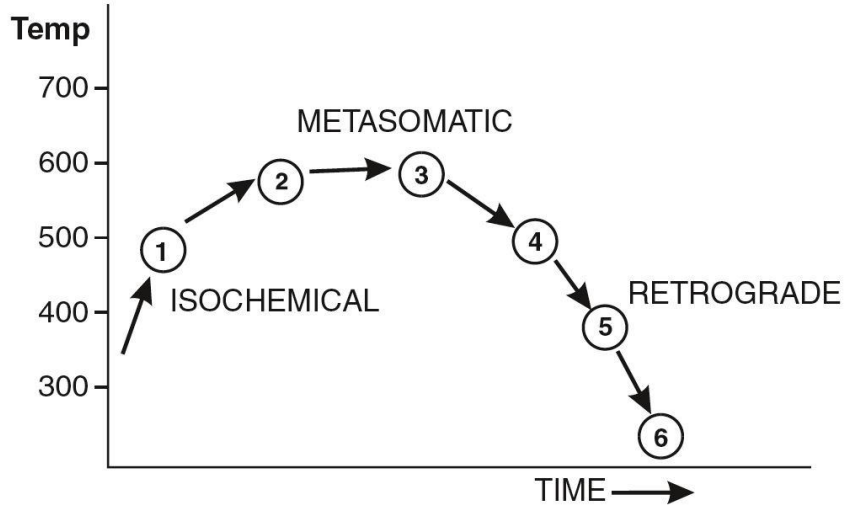

Figura 3. Diagrama relacionando os estágios de formação dos depósitos de *skarn*, extraído de Brown et al., 1985. 1: Metamorfismo de contato. 2-3: Estágio hidrotermal progressivo. 4-6: Fase hidrotermal retrogressiva. É importante destacar que há um intervalo de temperatura superior a 300°C, alterando as assembleias mineralógicas precursoras.

Tipicamente, os plutons relacionados aos *skarns* de tungstênio se apresentam na forma de corpos batolíticos alojados em ambientes de crosta continental espessada. Os magmas formadores dos depósitos de W-*skarn* são, em sua maioria, tipo-I, calci-alcalinos, reduzidos, metaluminosos a fracamente peraluminosos, e mostram evidências de contaminação crustal, com razões Sr-Sr em torno de 0,710 (Newberry, 1982; Figura 4). Os corpos ígneos relacionados a este tipo de depósito costumam ser os membros mais evoluídos de uma suíte, gerando uma associação cogenética de rochas graníticas, aplitos e pegmatitos (Rasmussen et al., 2011). O magma não precisa necessariamente ser enriquecido em W para gerar depósitos porque o comportamento fortemente incompatível deste elemento preserva-o no magma, e processos simples de cristalização fracionada conseguem aumentar a sua concentração de maneira eficiente. Magmas oxidados que precipitam magnetita como mineral acessório tendem a ter menores concentrações de W, pois este mineral incorpora tungstênio na sua estrutura, reduzindo sua concentração no sistema (Newberry & Swanson; 1986). Estudos experimentais (Manning & Henderson, 1984) ressaltam a importância do cloreto para a concentração de W no fluido. Magmas ricos em flúor não tem potencial para acumular tungstênio, pois o composto NaF faz com que o W tenha um comportamento compatível, enquanto altas concentrações de NaCl podem aumentar a incompatibilidade deste elemento em até uma ordem de grandeza.

À medida que a intrusão se diferencia, voláteis são produzidos e se mantém dissolvidos no magma até estágios tardios da cristalização, quando ocorre a exsolução do fluido. A solução magmática-hidrotermal é tipicamente aquosa e possui alto conteúdo de cloro e tungstênio, sendo a principal – quando não a única – fonte desse metal (Rasmussen & Mortensen, 2013).

Embora não sejam fonte de tungstênio, as rochas hospedeiras possuem papel importante no processo de mineralização. Quando são pobres em minerais carbonáticos e/ou ricas em hematita, oxidam o sistema, tendo pirita como sulfeto predominante e minerais calcissilicáticos de Fe^{3+} e de maior conteúdo de cálcio. Por outro lado, quando têm muito conteúdo de minerais carbonáticos, atuam como agentes redutores do sistema, tendo pirrotita como sulfeto dominante e maior concentração de minerais de Fe^{2+}, que substituem o íon Ca^{2+}. Neste contexto, rochas hospedeiras "redutoras" ajudam a produzir *skarns* com maior concentração de W, porque os minerais mais pobres em Ca possibilitam que mais tungstênio seja extraído do fluido hidrotermal (Newberry, 1982).

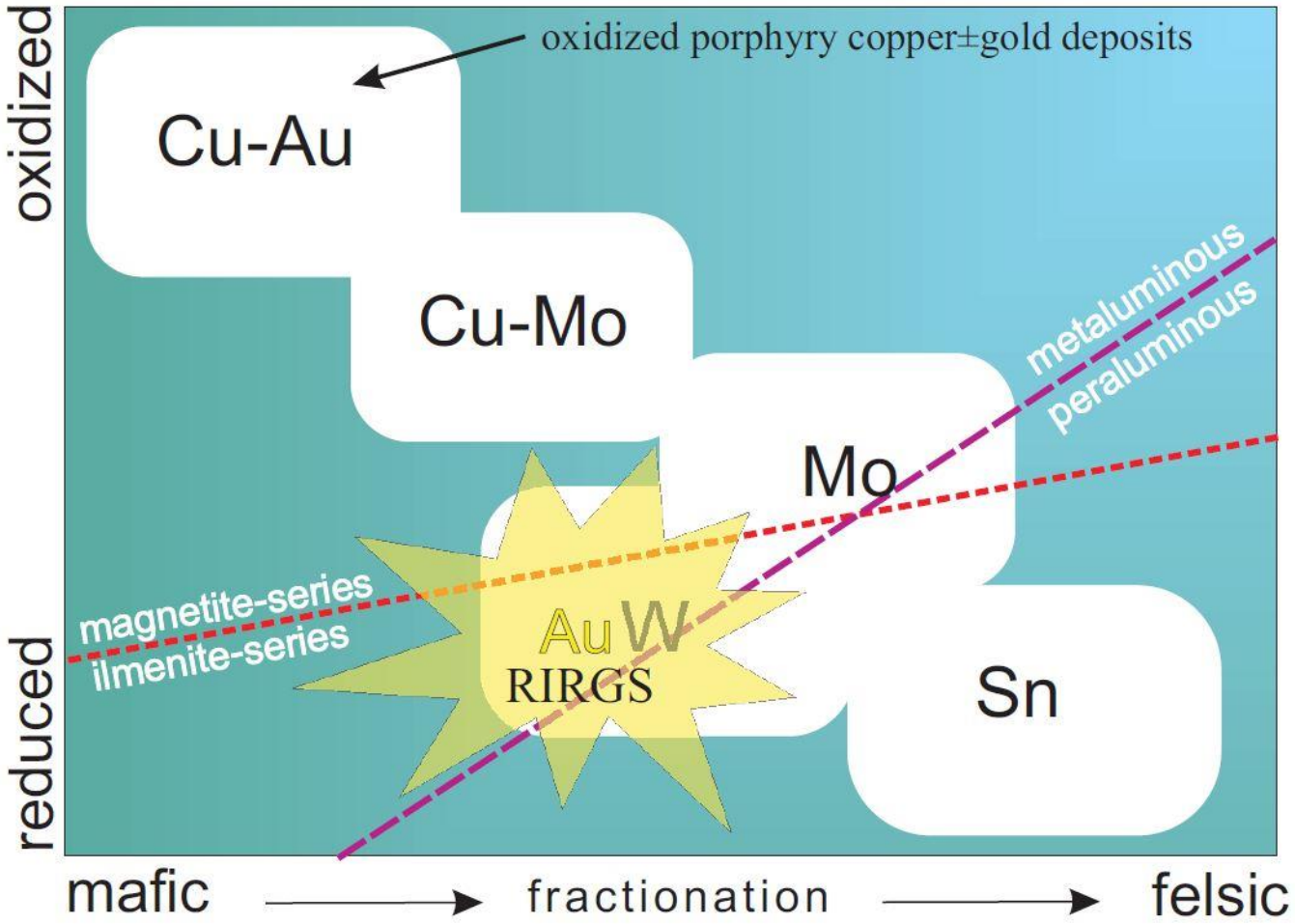

Figura 4. Relação entre o tipo de magmatismo e a afinidade metalogenética. Para o caso da associação Au-W, estes depósitos se formam sob condições reduzidas, tem magmas metaluminosos a fracamente peraluminosos e tem teores intermediários de SiO_2. Diagrama extraído de Hart (2007).

2.2. Contexto Geológico Regional

Ressalta-se que há seções de "Geologia Regional" nos capítulos 2 e 3. Por terem sido apresentados em formato de artigo, entretanto, alguns mapas relevantes para a compreensão geral da área de estudo não puderam ser contemplados nos dados segmentos e, consequentemente, serão expostos neste.

Ao longo dos anos, a Província Borborema tem sido sistematicamente estudada e revisada, sendo compartimentada em seis Domínios Tectônicos, definidos como Médio Coreaú, Ceará Central, Rio Grande do Norte, Zona Transversal, Pernambuco-Alagoas e Sul (Almeida et al., 1981; Brito Neves et al., 2000). Estas classificações passam constantemente por modificações, porém ainda mantém sua essência original (Van Schmus et al., 2008). Os domínios são limitados por estruturas do tipo *strike-slip* que uniram blocos com histórias de evolução distintas (Amaral et al., 2012). Estes terrenos passaram por diversos eventos metamórficos e deformacionais em diferentes ambientes tectônicos, levando a um sistema complexo de associações litológicas e depósitos minerais de origens variadas (Neves, 2003; Van Schmus et al., 2011). Outro fator de relevância na Província Borborema é a sua conexão com o continente africano, evidenciado por associações litológicas, metalogenéticas e estruturais, a exemplo do Lineamento Transbrasiliano-Kandi (Cordani et al., 2013; Figura 5).

Intrusões de granitoides de diferentes assinaturas geocronológicas e geoquímicas possuem papel chave para a compreensão dos eventos tectônicos que afetaram a Província Borborema (Neves et al., 2015). O primeiro evento intrusivo de maior destaque possui idade paleoproterozoica, estando relacionado ao amalgamento de blocos crustais mais antigos (Hollanda et al., 2011; Neves, 2015). Os processos tectono-magmáticos que ocorreram durante o início do Neoproterozoico são correlacionados ao Ciclo Cariris Velhos, que corresponde aos ambientes de arco continental e retro-arco (Santos et al., 2010; Brito Neves et al., 2014). O último evento orogenético é datado do fim do Neoproterozoico e ocorreu em

escala mais ampla, envolvendo a América do Sul e a África (Figura 5). Esta orogenia, nomeada de Ciclo Brasiliano (Schobbenhaus et al., 1984; Curto et al., 2014), é caracterizada pela implementação de um sistema transcorrente que possibilitou a formação de vários depósitos ao longo de zonas de cisalhamento neoformadas ou reativadas (Brito Neves & Fuck, 2014). As rochas magmáticas originadas em cada um destes eventos fornecem informações acerca de fontes para os minérios e sobre características dos fluidos mineralizantes (Santos et al., 2013).

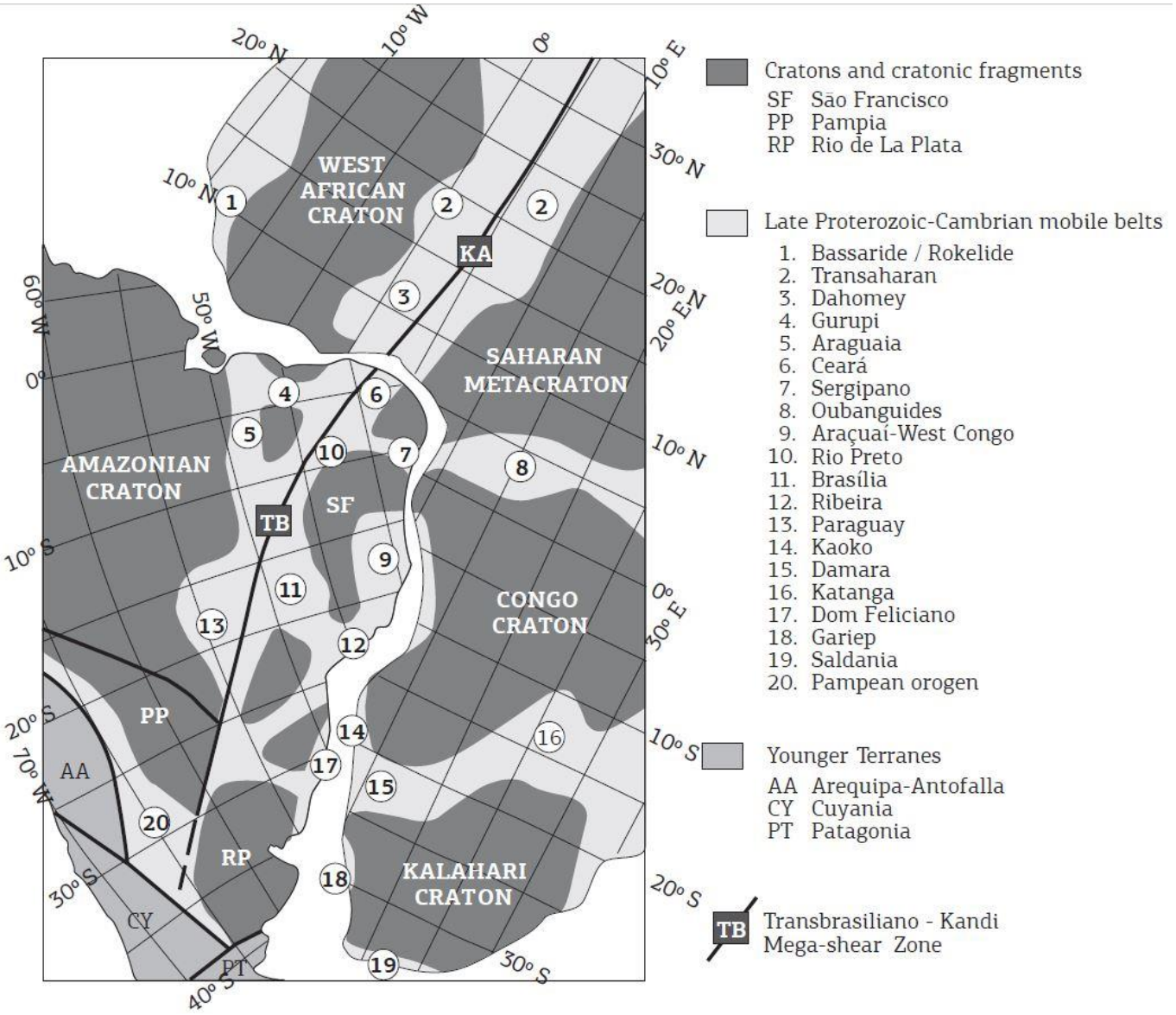

Figura 5. Figura esquemática regional modificada de Cordani et al. (2013). Nela, são evidenciadas as megazonas de cisalhamento Transbrasiliano e Kandi, bem como a disposição dos crátons e faixas móveis da América do Sul e da África. A área de estudo está localizada próximo ao número 6. Tais reconstruções têm se mostrado de suma importância para o entendimento do paleocontinente de Gondwana Ocidental.

O foco deste estudo está inserido no contexto da Faixa de Dobramentos Seridó, pertencente ao Domínio Rio Grande do Norte (Figuras 6 e 7). Ela é caracterizada por um embasamento gnáissico-migmatítico de idade Arqueana-Paleoproterozoica sobreposto pelas rochas neoproterozoicas do Grupo Seridó e intrusões graníticas associadas ao Ciclo Brasiliano (Van Schmus et al., 2003). Basicamente, afloram estreitas janelas de rochas arqueanas comumente associadas ao Maciço São José do Campestre (Souza & Dantas, 2008) em meio a um extenso domínio composto por rochas paleoproterozoicas pertencentes aos complexos Arábia e Caicó (Souza et al., 2007; Cavalcante et al., 2016). Importantes estudos no embasamento envolvem a região do Maciço São José do Campestre, em que os ortognaisses apresentam datações U-Pb em zircão de até 3.5 Ga e idades modelo Sm-Nd superiores a 3.7 Ga (Dantas et al., 2004). O Complexo Arábia é constituído por ortognaisses com idades siderianas superiores a 2.4 Ga

(Costa & Dantas, 2014). O Complexo Caicó, por sua vez, é caracterizado por ortognaisses e *augen* gnaisses com assinatura geoquímica calci-alcalina de alto potássio de afinidade meta- a peraluminosa, atribuídos a um evento colisional riaciano (Medeiros et al., 2012). Análises U-Pb em zircão indicam idades de 2.2 Ga e idades modelo por Sm-Nd de até 2.8 Ga, sugerindo que esta unidade litológica foi originada a partir da reciclagem de uma crosta mais antiga (Dantas et al., 2002; Hollanda et al., 2011).

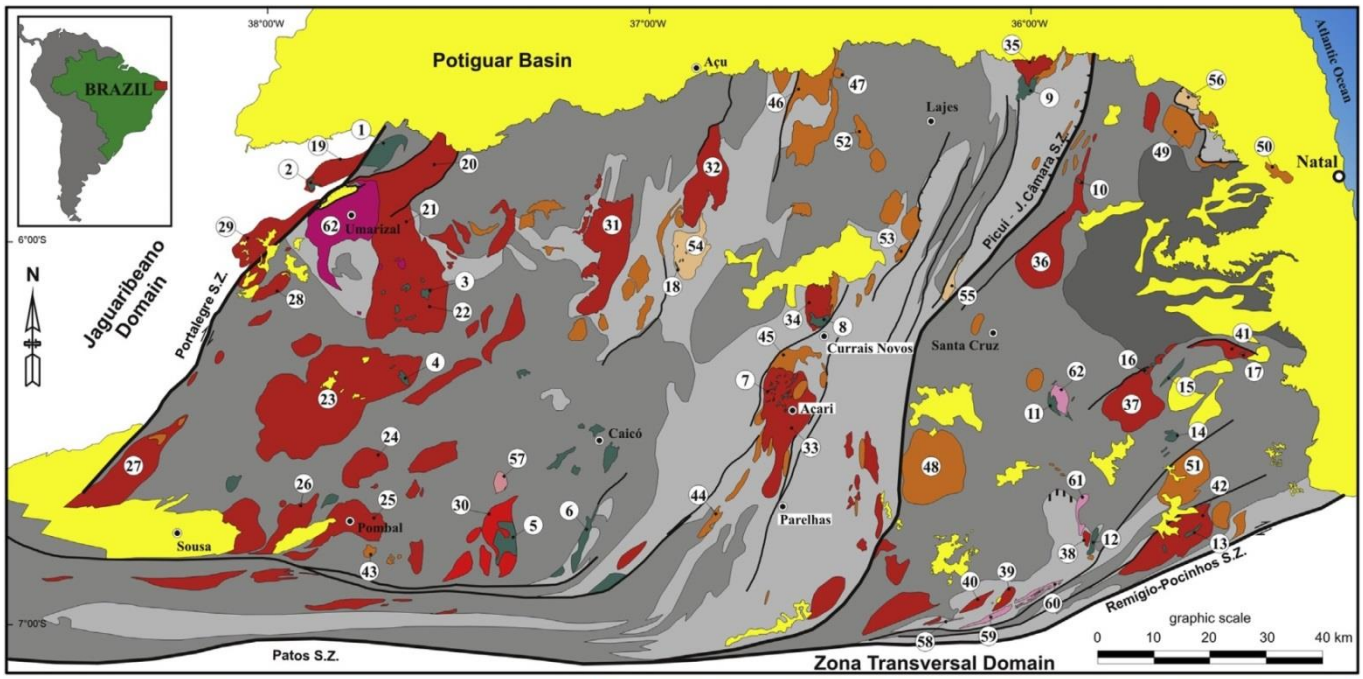

Shoshonitic Suite						Porphyritic High-K Calc-alkaline Suite											
1	Quixaba	7	Acari	13	Solânea	19	Prado	25	Pombal	31	Serra João do Vale	37	Monte das Gameleiras
2	Prado	8	Totoró	14	Riachão	20	Caraúbas	26	Pedregulho	32	São Rafael	38	Cabeçudo
3	Serra do Lima	9	Cardoso	15	Poço Verde	21	Tourão	27	Serra Branca	33	Acari	39	Jandaíra
4	Catolé do Rocha	10	Barcelona	16	Monte das Gameleiras	22	Serra do Lima	28	Serrinha dos Pintos	34	Totoró	40	Serra da Boa Vista
5	São José de Espinharas	11	Japi	17	Serrinha	23	Catolé do Rocha	29	Portalegre	35	Cardoso	41	Serrinha
6	São João do Sabugi	12	Casserengue	18	Serra da Garganta	24	Serra do Moleque	30	São José de Espinharas	36	Barcelona	42	Solânea

Equigranular High-K Calc-alkaline Suite						Calc-alkaline Suite		Alkaline Suite				Charnockite Alkaline Suite	
43	Capuxu	47	Flores	51	Dona Inês	54	Serra da Garganta	57	Serra Negra do Norte	61	Caxexa	62	Umarizal
44	Santa Luzia	48	Picuí	52	Caramuru	55	Serra Verde	58	Olho D´Água	62	Japi		
45	Acari	49	Taipu	53	Cerro Corá	56	Gameleira	59	Serra do Boqueirão				
46	Angicos	50	Macaíba					60	Serra do Algodão				

a b c d e f g h i j k l m n o

Figura 6. Mapa geológico do Domínio Rio Grande do Norte retirado de Nascimento et al. (2014). Nele, encontram-se destacadas intrusões de granitoides Brasilianos, foco deste trabalho, com diferenciação entre diversas suítes magmáticas. a: Coberturas Meso-Cenozoicas; b-g: Respectivamente suítes Shoshonítica, Calci-alcalina de Alto Potássio Porfirítica, Calci-alcalina de Alto Potássio Equigranular, Calci-alcalina, Alcalina e Charnoquítica Alcalina; h-i: Respectivamente embasamento gnáissico-migmatítico Arqueano e Paleoproterozoico; j: Grupo Seridó; k-m: Respectivamente zonas de cisalhamento Neoproterozoicas transcorrentes, transpressivas e extensionais; n: Cidades; o: Capitais.

Posteriormente, no fim do Neoproterozoico, ocorreu a deposição do Grupo Seridó num rifte intracontinental que evoluiu para uma margem passiva (Jardim de Sá, 1994; Hollanda et al., 2015). Neste contexto, estabeleceram-se as formações Serra dos Quintos, Jucurutu, Equador e Seridó, datadas através da técnica de U-Pb em cristais detríticos de zircão no intervalo entre 650 e 610 Ma (Van Schmus et al., 2003). Esta bacia sedimentar foi rapidamente sujeita à Orogênese Brasiliana, sendo deformada e metamorfizada sob fácies anfibolito (Jardim de Sá et al., 1995). O Ciclo Brasiliano desenvolveu, tanto no embasamento quanto nas supracrustais, zonas de cisalhamento subverticais, dextrais e de orientação N-NE (Archanjo & Bouchez, 1991).

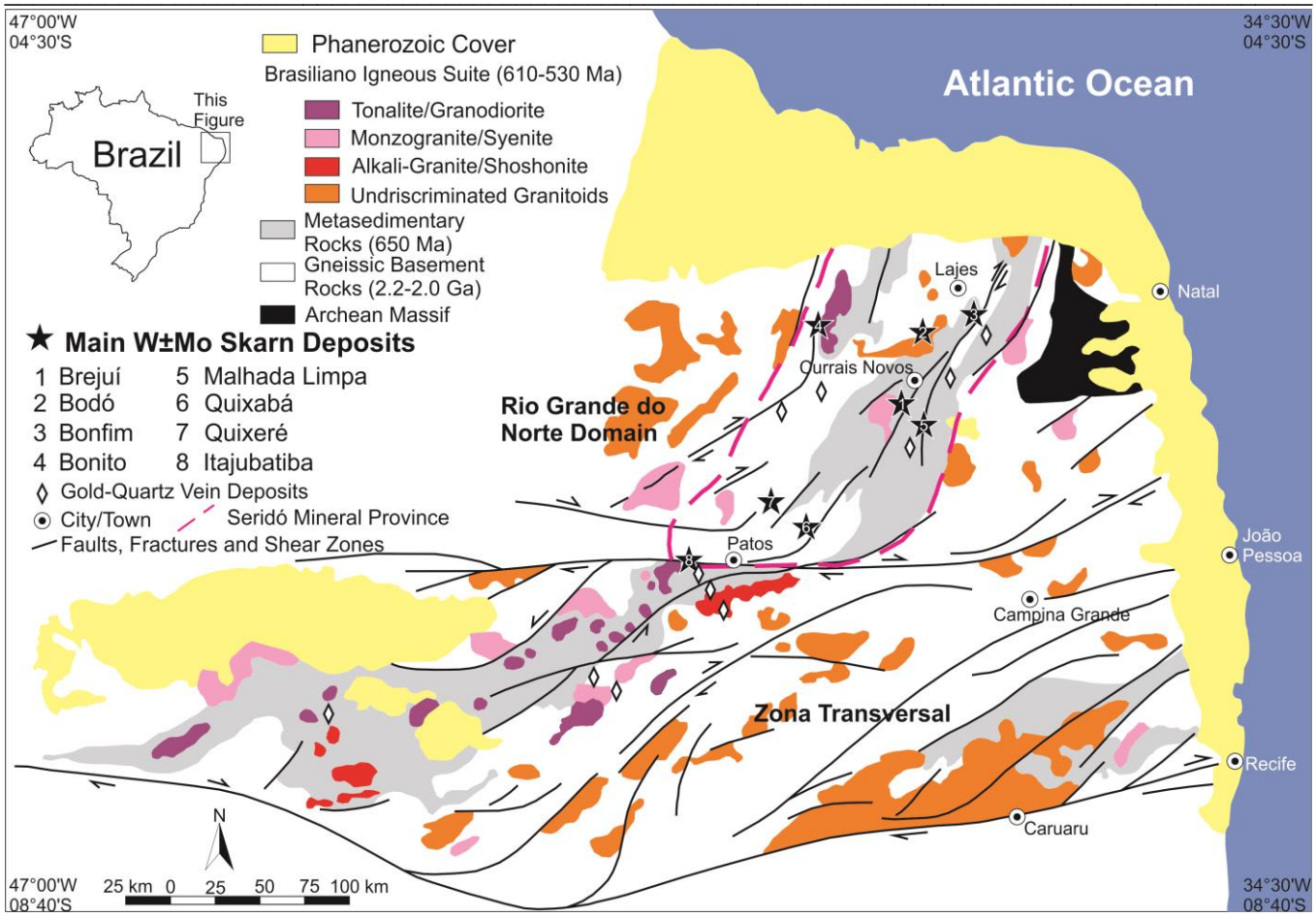

Figura 7. Mapa Geológico dos domínios Rio Grande do Norte e Zona Transversal adaptada de Archanjo et al. (2002) e Souza Neto et al. (2008). Nele, encontram-se os principais depósitos do tipo *skarn* da área a serem contemplados por este estudo, além dos depósitos auríferos.

Além de processos deformacionais, este evento desencadeou um plutonismo extensivo ao longo da Província Borborema (Sial, 1986; Santos & Medeiros, 1999; Neves et al., 2008; Santos et al., 2008; Araujo et al., 2014). No Domínio Rio Grande do Norte, seis suítes intrusivas afloram, classificadas por Nascimento et al. (2015) como Shoshonítica, Calci-alcalina de Alto Potássio Porfirítica, Calci-alcalina de Alto Potássio Equigranular, Calci-alcalina, Alcalina e Charnoquítica Alcalina (Figura 6). O espectro geocronológico destas rochas abrange o amplo intervalo de aproximadamente 100 milhões de anos, sendo uma das evidências de que o Evento Brasiliano ocorreu de forma contínua e multifásica. Com início em cerca de 600 Ma, seu pico se deu em 580 Ma e seus últimos pulsos ocorreram entre 530 Ma e 510 Ma (Hollanda et al., 2012; Archanjo et al., 2013; Beurlen et al., 2014). Nas fases mais tardias, alojaram-se rochas pegmatíticas, tanto na forma de pequenas intrusões quanto como *dykes* e *stocks* (Jardim de Sá, 1994; Ferreira et al., 1998; Baumgartner et al., 2006).

Por fim, esta Orogenia também levou à formação de depósitos minerais, tais como *skarns* de tungstênio, de onde são explorados tungstênio e molibdênio, ainda contando com ouro e bismuto em algumas localidades (Souza Neto et al., 2008; Figura 7). Como já mencionado, ao longo da Faixa Seridó, há mais de 700 registros de rochas contendo scheelita, o principal minério de W (Hollanda, et al., 2012). Depósitos e ocorrências desta variedade apresentam, em maior ou menor grau, associações espaciais e/ou temporais com corpos plutônicos brasilianos, bem como com estruturas (Santos et al., 2014; Figura 7). Datações Re-Os em molibdenita apontam idades para a mineralização variando entre 555 Ma e 510 Ma (Hollanda, 2012).

Estudos em alguns dos principais depósitos da região identificaram ao menos dois estágios para a mineralização, representados por um pulso inicial, de alta temperatura, e um tardio, de baixa temperatura

(Salim, 1993; Trindade, 2000). Tanto o mineral-minério quanto outros acessórios (i.e. sulfetos e magnetita) podem ocorrer em ambas as fases da alteração hidrotermal (Santos et al., 2014).

Para o caso das zonas de raiz do sistema de *skarns* do Seridó, não há muitos estudos disponíveis. Referências antigas, limitadas e de difícil acesso incluem Moeri & Kloechner (1979a,b), que interpretam estas rochas como produtos de metamorfismo em protólitos máficos, devido ao seu alto conteúdo de anfibólio e piroxênio. Quase quarenta anos mais tarde, este estudo propõe uma nova interpretação para esta assembleia litológica, associando-a como parte do zoneamento do sistema metalogenético, de maneira mais distal.

3. METODOLOGIA

O presente trabalho dedicou-se a cumprir os objetivos mencionados nas seções 1.1 e 1.2 do texto. Para tanto, serão listadas as técnicas utilizadas, ressaltando também a sua importância em termos de obtenção de resultados, bem como as interpretações que eles possibilitam realizar:

- **Mapeamento Regional:** Afloramentos rochosos e depósitos foram visitados e estudados, possibilitando obter medidas estruturais, fotografar e determinar a mineralogia e textura das rochas. Dentre as localidades visitadas, destacam-se o depósito de Bonfim e as ocorrências de Salgadinho, Recanto, Alívio, Espinheiro, Pedro Tomás, Caçador, Isidoro e Richão, a serem explicadas com maior detalhe nos Capítulos 2 e 3. Amostras de superfície e de subsuperfície (obtidas a partir de furos de sondagem) foram coletadas para análises. Além de imagens de sensoriamento remoto, esta etapa também contou com estudos de produtos geofísicos para fins de mapeamento, por ajudarem a correlacionar áreas anômalas com elementos geológicos, tais como falhas, fraturas, lineamentos, litologias e variações faciológicas. Imagens processadas de magnetometria e gamaespectrometria aérea foram fornecidos pelo Laboratório de Geofísica Aplicada da Universidade de Brasília (LGA-UnB), fruto dos levantamentos realizados e disponibilizados pelo Serviço Geológico do Brasil (CPRM).
- **Petrografia:** Observações feitas em mais de cinquenta lâminas delgadas polidas possibilitaram análises mais detalhadas da textura e mineralogia das rochas. Nesta etapa, foi realizada uma prévia determinação de paragêneses da alteração hidrotermal, bem como a observação de microtexturas, microestruturas e reações entre minerais. Fotomicrografias foram adquiridas nesta fase.
- **Química Mineral por Microssonda Eletrônica:** Após a definição das melhores lâminas e *mounts* para análises de química mineral, 1593 pontos tiveram sua composição química determinada (em porcentagem de massa para elementos maiores, traço e menores e em ppm para elementos terras-raras) em cristais de anfibólio, feldspato, piroxênio, titanita, apatita, magnetita, barita, minerais do grupo do epidoto, biotita e scheelita, com o fim de determinar suas características químicas e aspectos genéticos. As análises ocorreram no Laboratório de Microssonda Eletrônica da Universidade de Brasília utilizando um equipamento JEOL JXA-8230 operando a 20kV e 20 nA, com tempos de contagem de pico e *background* de 10 segundos e 5 segundos, respectivamente. A partir dos dados obtidos, foi calculada a fórmula de cada mineral, disposta em *atoms per formula unit* (apfu), e em seguida os resultados processados foram plotados em diagramas. Os procedimentos de cálculo específicos de cada mineral estão contidos no Capítulo 2.
- **Imageamento por Microscópio Eletrônico de Varredura (MEV):** Este aparato analítico foi utilizado exclusivamente em duas lâminas, com o fim de identificar variações nos teores de bário em aglomerados de feldspato e em alguns grãos de barita. O imageamento ocorreu no Laboratório de Geocronologia da Universidade de Brasília utilizando um MEV FEI QUANTA 450 acoplado a um *Energy Dispersive Spectrometer* (EDS) EDAX Apollo X, com o *software* EDAX TEAM EDS Suite, sob condições de alto vácuo. Os parâmetros de operação foram 25 kV, 12.1mm de *working distance* e tamanho de *spot* 6.

Os quatro itens citados acima compreendem o conteúdo do primeiro artigo do doutorado, referente ao Capítulo 2. Sua temática consiste em caracterizar as zonas de raiz da Província Scheelitífera Seridó e em propor modelos para a gênese da mineralização e das sequências paragenéticas, situando-as no arcabouço tectônico regional.

O *paper* seguinte, referente ao Capítulo 3, é pautado em análises de geoquímica de rocha total e geologia isotópica. Os dados de geoquímica possibilitaram uma melhor caracterização dos processos de alteração hidrotermal, envolvendo particionamento de elementos e definição de halos/estágios metassomáticos. A abordagem por isótopos estáveis de enxofre teve como objetivo identificar fontes para os minerais hidrotermais. As técnicas analíticas envolvendo geocronologia, por sua vez, objetivaram correlacionar o magmatismo brasiliano com a formação dos depósitos da área de estudo e de determinar a idade de suas rochas encaixantes. Para tanto, a pesquisa buscou datar as mineralizações nestas zonas de raiz ou em rochas associadas, com os métodos a serem descritos abaixo:

- **Geoquímica de Rocha Total:** Foram analisados dois lotes de amostras: O primeiro foi enviado à *ACME Analytical Laboratories LTD.*, enquanto o segundo foi encaminhado para a *ALS Global LTD*. Os lotes incluíram tanto amostras de rochas encaixantes quanto de hospedeiras. Elementos maiores foram analisados num ICP-AES, enquanto elementos traço foram determinados utilizando um ICP-MS.
- **Geocronologia U-Pb em Zircão por *Laser Ablation Inductively Coupled Plasma Mass Spectrometer* (LA-ICP-MS):** Realizada no Laboratório de Geocronologia da Universidade de Brasília. Foram utilizadas amostras dos pegmatitos com associação espacial e temporal aos halos de alteração, além de outras retiradas das próprias zonas hidrotermalizadas. O principal objetivo destas análises é datar, com precisão, tanto rochas encaixantes em que a mineralização está hospedada, quanto o magmatismo/metassomatismo associado à mineralização.
- **Imageamento de Catodoluminescência:** Esta etapa ocorreu exclusivamente para dar suporte às análises de U-Pb, imageando cristais de zircão com relações de núcleo-borda e outros grãos que possuíam relevância e representatividade em meio às assembleias coletadas. As análises ocorreram no Laboratório de Microssonda Eletrônica da Universidade de Brasília utilizando um equipamento JEOL JXA-8230 operando a 15kV e 15 nA, fazendo mapas com resolução de 1600x1200 pontos.
- **Isótopos Estáveis de S por Diluição em Molibdenita, Barita e Pirita:** Realizada no Laboratório de Geocronologia da Universidade de Brasília. Estas análises compreenderam minerais hidrotermais amostrados em diferentes localidades e contextos, de modo a apontar suas assinaturas isotópicas de diferentes estágios da mineralização. Em alguns casos, ainda que de maneira restrita, também foram efetuados estudos de termometria com base em pares minerais.

Unveiling the Root Zones of Tungsten-Bearing Skarn Systems:

An Example From The Seridó Mineral Province, Northeastern Brazil

CAPÍTULO II

1. ABSTRACT

Six W(±Mo±Au) deposits and occurrences in the Seridó Mineral Province represent metasomatic assemblages related to tungsten endowment processes, but differ from the sensu strictu skarns of the area. Unlike these garnet-diopside skarns, the studied deposits in this work show no spatial association with carbonate rocks or igneous intrusions, but are strongly controlled by regional-scale N20°E-trending shear zones formed during the Neoproterozoic-Ediacaran (ca. 615 Ma to 530 Ma) Brasiliano Cycle. Throughout the area, this orogenic event affected both basement and supracrustal rocks, forming scheelite-bearing rocks in both domains. The alteration process is characterized by three mineral associations: (1) diopside-amphibole-feldspars (DAF), (2) amphibole-feldspars (AF), and (3) biotite-rich (BR); which may occur alone or combined. Some of the studied locations are also spatially associated with the classic mineralized garnet-diopside skarns (MGDS) of the area, generally occurring tens to hundreds of meters below them. These associations represent a continuously evolving system that record changes in physicochemical properties over time. These changes are documented by mineral chemistry analyses for pyroxene, amphibole, feldspars, biotite, epidote group minerals, titanite and apatite. Earlier, higher temperature metasomatism enriched the system in Mg, Fe, Ca, Ba and REE, whereas later, lower temperature stages are characterized by an enrichment in Na, K, Si, W and Mo. The studied mines and occurrences provide important information on the distal, deeper hydrothermal alteration haloes of tungsten deposits in the Seridó Mineral Province.

2. INTRODUCTION

Skarn-like alteration may be present in several types of magmatic-hydrothermal deposits, such as porphyry, reduced intrusion-related gold systems (RIRGS) and IOCG (Dick & Hodgson, 1982; Pirajno, 1992; Robb, 2005; Reid et al., 2011). Skarn deposits are not simply the result of interaction between metasomatic fluids and carbonate rocks. During the metasomatic event, calc-silicate rocks are formed and host Fe, Au, Cu, Zn, W, Mo and/or Sn mineralization (Meinert, 1992). The presence of a carbonate contact is not a requirement for skarn development, and neither is the proximity to plutons (Meinert et al., 2005). Different deposits are developed depending on factors such as tectonic environment, source magma and wallrock compositions, mechanisms of fluid flow, depth of emplacement, temperature and oxygen fugacity (Lentz, 1998).

Among the most studied skarn modalities, W-skarns, which generally are synonymous with scheelite-skarns, are commonly associated with deep, reduced, meta- to weakly peraluminous, I-type, calc-alkaline batholiths in a thickened crust (Smirnov, 1976; Newberry & Swanson, 1986). These usually share several characteristics with Cu-skarns, but are associated with more evolved magmas and are emplaced at greater depths (Manning & Henderson, 1984; Newberry, 1987). Important tungsten districts include the Tintina Gold Province (Goldfarb et al., 2000), the South China Province (Ding et al., 2018) and the Seridó Mineral Province (Souza Neto et al., 2008).

Unlike the previous studies in the Seridó Mineral Province, this paper focuses on a calc-silicate metasomatic assemblage which is distal in relation to the classic W-skarns of the area. We interpret these assemblages as representatives of the root zones of the skarn system of the studied region. Root zones may be defined as areas beneath an orebody which were strongly affected by upward focused fluid flow, characterized by widespread wallrock alteration, dyke swarms and vein development (Seedorff et al., 2008). These are commonly characterized by calcic, sodic-calcic and/or sodic hydrothermal alteration haloes in IOCG and porphyry systems (Groves et al., 2010; Sillitoe, 2010; Richards & Mumin, 2013).

Regardless of the type of metal deposit, root zones form at depth, and hence are rarely exposed, recording complementary information about metals endowment processes (Carten, 1986). These regions

hold imprints from the earliest stages of the hydrothermal fluid formation, and therefore may help to track metal sources and identify pathways and metasomatic solution migration mechanisms (Audétat et al., 2000; Runyon et al., 2017).

This research proposes an unprecedented interpretation for these calc-silicate rocks, focusing primarily on mineral chemistry analyses to better characterize the whole system. This methodology shows minerals compositional variations, which are a reflex of the evolution of the environment of formation of the deposits and occurrences (Fonteilles et al., 1989; Seymour et al., 2009). The composition of the analyzed minerals records the chemical signature of each stage and zone, and will be detailed in the next sections.

Although the studied rocks in this paper also refer to tungsten mineralization processes in the Seridó Mineral Province, they present several differences from classic W-skarn textures, mineral assemblages and metallogenetic mechanisms. Among the main questions concerning the whole Seridó Mineral Province skarn system, some are: How and when does the metasomatism occur in the root zones? Are the calc-silicate rocks from the root zones cogenetic with the skarns? How are both deposit styles linked? Is the hydrothermal alteration a recurring process or was it formed from a single pulse and/or event? Is it chemically and/or mineralogically zoned? This paper focuses on some of these points, presenting data in various scales of observation.

3. REGIONAL GEOLOGIC SETTING

3.1. *Tectonic setting*

The Seridó Mobile Belt is part of the Borborema Structural Province, which was initially defined by Almeida et al. (1981) as a complex and polyphasic assemblage of crustal blocks. Following the classification scheme of Brito Neves et al. (2000) and Van Schmus et al. (2011), this Province is divided into six domains, named from northwest to southeast as Médio Coreaú, Ceará Central, Rio Grande do Norte, Zona Transversal, Pernambuco-Alagoas and Sul (Figure 1). These domains are separated from each other by regional-scale shear zones, which brought together crustal blocks with distinct evolution histories (Jardim de Sá, 1994; Dantas et al., 2003; Neves, 2003; Amaral et al., 2012).

The Seridó Fold Belt is situated in the Rio Grande do Norte Domain. This belt has attracted the interest of several researchers for two main reasons: i) it is a key area to understand the link between Brazil and Africa during the Western Gondwana collage, represented by the ca. 615 Ma to 530 Ma Brasiliano-Pan African Orogeny (Brito Neves et al., 2014; Araujo et al., 2016; Figure 1); and ii) its orogenic and polymetallic deposits, especially the W(±Au±Mo±Bi) association found in some of the skarns along this fold belt (Silva, 2000; Souza Neto et al., 2008). The rocks found along this terrane range from the Paleoarchean to the Ediacaran, showing a complex lithological assemblage (Ebert, 1970; Neves, 2015; Souza et al., 2016).

The oldest rocks found in the study area present zircon U-Pb ages up to 3.5 Ga and Sm-Nd TDM model ages higher than 3.7 Ga (Dantas et al., 2004). These lithologies are comprised of orthogneisses and are probably associated with the São José do Campestre Massif, a possibly detached terrane of an evolved craton located to the east of the study area (Dantas et al., 2013; Souza et al., 2016; Figure 2). These Paleoarchean rocks appear as fragments inside a much younger basement, named as Caicó Complex (Souza et al., 2007). This Complex is composed mainly of orthogneisses and augen gneisses with high-K calc-alkaline and meta- to peraluminous geochemical signature, produced during a Rhyacian collisional event (Medeiros et al., 2012). Zircon U-Pb analyses provide ages of ca. 2.2 Ga and Sm-Nd TDM model ages up to 2.8 Ga, suggesting that the Caicó Complex was formed by the recycling of an older crust (Dantas et al., 2002; Hollanda et al., 2011).

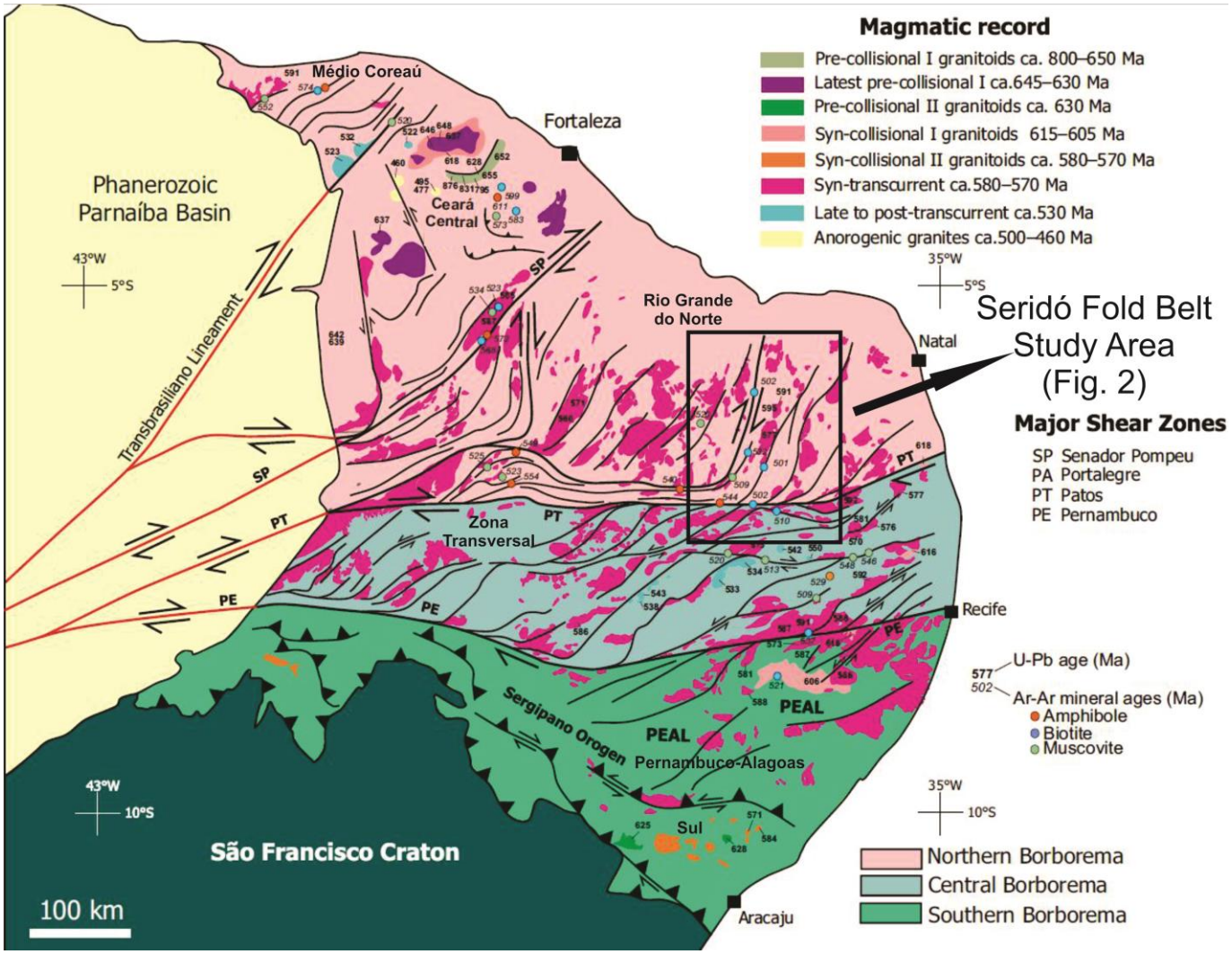

Figure 1. Regional Borborema Province map from Araujo et al. (2014), dividing the area in three main regions (Northern, Central and Southern Borborema), which may be subdivided in six domains, named as Médio Coreaú, Ceará Central, Rio Grande do Norte, Zona Transversal, Pernambuco-Alagoas and Sul (Van Schmus et al., 2011). The map also highlights the temporal and spatial distribution of the Brasiliano-related granitoids of the area. References for geochronological data are listed in Araujo et al. (2014).

During the Late Neoproterozoic, an extensional event led to the deposition of the Seridó Group in an intracontinental rift that evolved into a passive margin (Jardim de Sá, 1994; Hollanda et al., 2015). The Seridó Group is comprised of amphibolite facies metasedimentary rocks subdivided in the following formations: i) Serra dos Quintos, the basal unit constituted by paragneisses and micaschists; ii) Jucurutu, comprised of paragneisses, calc-silicate rocks and marbles; iii) Equador, composed of quartzites and metaconglomerates; iv) Seridó, the top unit, comprising mainly micaschists (Jardim de Sá et al., 1995; Angelim et al., 2006; Figure 2). U-Pb analyses of detrital zircons establish a deposition age in the interval between 650 and 610 Ma (Van Schmus et al., 2003). Later, the sedimentary basin was quickly compressed, deformed and metamorphosed during the Neoproterozoic-Ediacaran Brasiliano Cycle (Schobbenhaus et al., 1984; Brito Neves et al., 2000). This event was responsible for the development of a transcontinental strike-slip system with N-NE dextral subvertical shear zones in the basement and supracrustal rocks (Archanjo & Bouchez, 1991). It also led to the emplacement of several plutonic bodies and the formation of ore deposits.

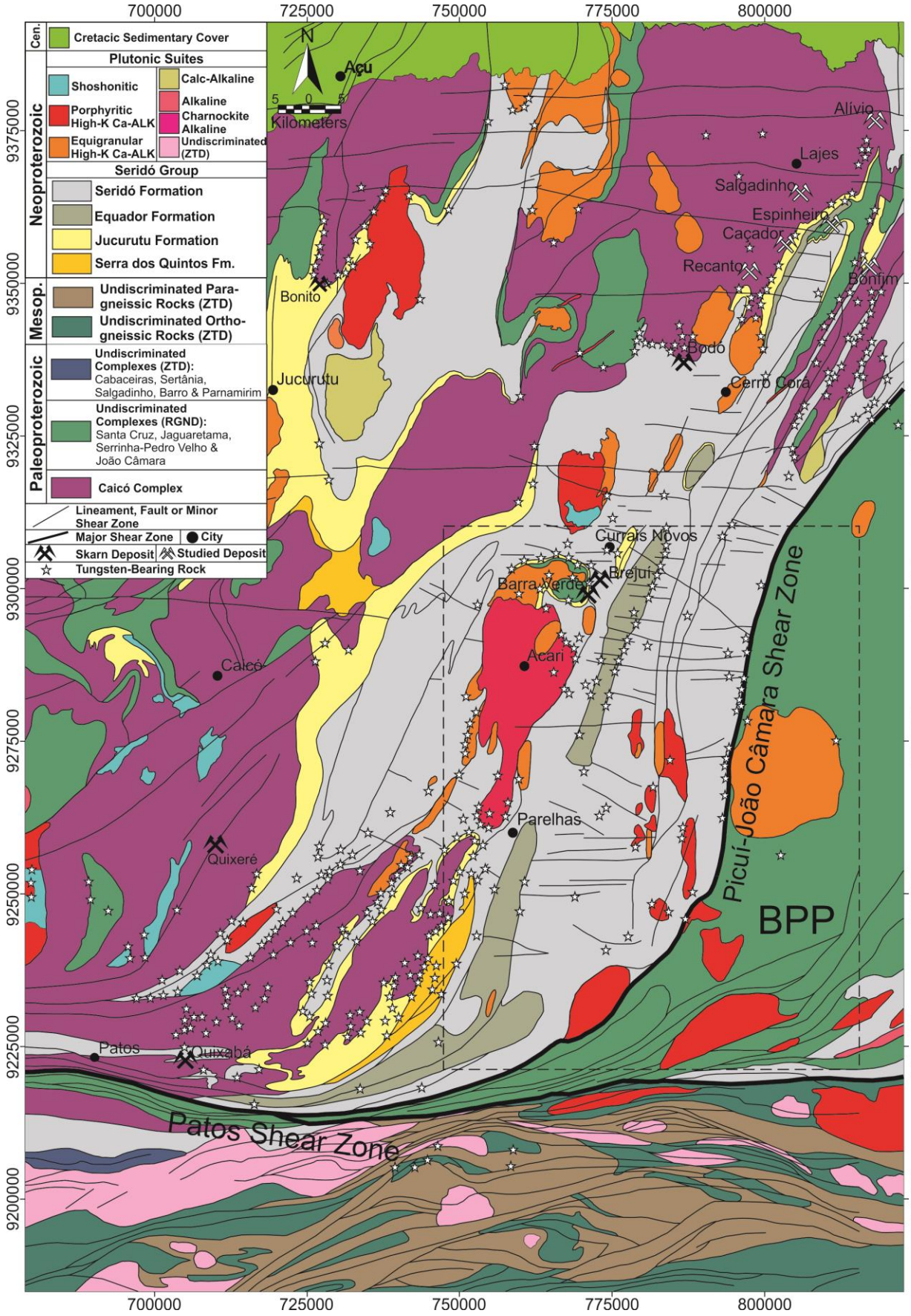

Figure 2. Simplified geological map of the study area formulated after the obtained field data from this research, geophysical and remote sensing imagery and the works of Angelim et al. (2004), Angelim et al. (2006), Souza Neto et al. (2008) and Nascimento et al. (2015). The abbreviations BPP, RGND and ZTD stand for "Borborema Pegmatite Province", "Rio Grande do Norte Domain" and "Zona Transversal Domain", respectively.

3.2. Neoproterozoic to Ediacaran Brasiliano Plutonism

Extensive magmatism occurred within the whole Borborema Province during the Brasiliano Cycle (Jardim de Sá, 1981; Sial, 1986; Santos & Medeiros, 1999; Neves et al., 2008; Santos et al., 2008; Araujo et al., 2014; Neves et al., 2015; Figures 1 and 2). Archanjo et al. (1992), based on structural criteria, identified two plutonism episodes, with the first intrusions being coeval with the building of the Seridó Belt, characterized by NS-trending low- to medium-angle shear planes; while the second are parallel to the regional trend of the belt, defined by dextral NE-SW-trending shear zones with high dip angle, associated with transfer zones caused by the Patos Lineament. The second phase is associated with the peak of the Brasiliano Orogeny, which occurred at ca. 580 Ma (Archanjo et al., 2013; Souza et al., 2016).

The thermal record of the Brasiliano Cycle, determined by $^{40}Ar/^{39}Ar$ analyses in amphibole, biotite, phlogopite and muscovite, points to a slow cooling history that lasted for more than 80 Ma. Ruiz et al. (2018) reported phlogopite $^{40}Ar/^{39}Ar$ ages in the 3.5 Ga Paleoarchean São Tomé layered mafic-ultramafic intrusion of 597±5 Ma and 517±6 Ma, which were attributed to the emplacement of local granites. The 523±1 Ma biotite $^{40}Ar/^{39}Ar$ age obtained by Araújo et al. (2005) in a pegmatite near Parelhas records late- to post-tectonic intrusive events. This long and unusual period of high temperature gradients enabled the formation of several magmatic suites, with their last pulses at ca. 500 Ma (Corsini, 1998).

Jardim de Sá et al. (1981; 1987), based on compositional, textural and structural parameters, divided two groups of Late Neoproterozoic granitoids, named as G3 for syn-tectonic porphyrytic and equigranular granodiorites and granites; and G4 for late- to post-tectonic equigranular granites/leucogranites/pegmatites that generally occur as dykes and stocks. Later, other classification schemes were proposed, adding more data from field observations, as well as petrographic, geochemical and isotopic analyses (Jardim de Sá, 1994; Ferreira et al., 1998).

More recently, Nascimento et al. (2015) defined six plutonic suites for the Rio Grande do Norte Domain, named as shoshonitic, porphyritic high-K calc-alkaline, equigranular high-K calc-alkaline, calc-alkaline, alkaline and charnockite alkaline. The shoshonitic suite is comprised of mafic to intermediate rocks with a mantle origin (Jardim de Sá, 1994). These rocks show the oldest ages, ranging from 600 to 580 Ma. The porphyritic high-K calc-alkaline suite may be slightly younger or contemporaneous with the shoshonitic suite, with ages in the interval between 580 and 550 Ma (Archanjo et al., 2013). The equigranular high-K calc-alkaline suite, as well as the porphyritic suite, shows a strong crustal component (Jardim de Sá, 1994), but seems to have been formed later than the porphyritic and shoshonitic suites, with ages ranging from 550 to 520 Ma (Hollanda et al., 2012). The geochronology of the alkaline, charnockite alkaline and calc-alkaline suites is not well constrained (Nascimento et al., 2015).

Another relevant feature of the Brasiliano Cycle is the Borborema Pegmatite Province (BPP), situated in the southeastern part of the Seridó Fold Belt (Beurlen et al., 2009a; Figure 2). Pegmatitic intrusions record the latest stages of the Brasiliano Cycle, ranging from 530 to 510 Ma (Baumgartner et al., 2006; Beurlen et al., 2009b). These rocks are potential targets for Be-Li-Nb-Ta-Sn-REE mineralizations and contain rare U-enriched minerals (Beurlen et al., 2008; Dill et al., 2013). Fluid inclusion studies point to isobaric crystallization conditions (ca. 3.8 kbar) between 580°C and 400°C, and geochemical analyses indicate their peraluminous nature, with their source possibly linked to basement gneisses and/or metasedimentary rocks of the Seridó Group (Beurlen et al., 2014; Sallet et al., 2015). The pegmatites occur as N50°E/N70°E-trending dyke swarms or filling N70°W/E-W extension fractures, occurring as: i) homogeneous pegmatites, which are less prominent and have mineral assemblage comprised mainly of quartz, feldspars and mica; ii) heterogenous pegmatites, which are mostly associated

with the N50°E/N70°E-trending dyke swarms, commonly contain minerals of economic interest such as beryl, tantalite, spodumene and tourmaline, and present a complex mineral zoning (Araújo et al., 2005). The recurring temporal and spatial associations between pegmatites and the rocks studied in this paper suggest that they may have contributed to the development of the W-skarns of the Seridó Mobile Belt.

3.3. Previous Studies of the Seridó Mineral Province

The Seridó Fold Belt hosts more than 700 documented occurrences of scheelite-bearing rocks and has produced around 60,000 t of WO3 for nearly a hundred years (Hollanda et al., 2012; Cavalcante et al., 2016; Table 1). Most deposits present several similarities with other tungsten skarns around the world (Dick & Hodgson, 1982; Bowman et al., 1985; Souza Neto et al., 2008; Soloviev, 2011).

The Seridó Mineral Province is a key area to understand the formation of W-skarns because, in most cases, the deposits are formed along marbles from the Jucurutu Formation of the Seridó Group, but there are reports of tungsten mineralization hosted in schists and gneisses from either the Seridó Group or the basement rocks (Salim, 1993; Souza Neto et al., 2008; Figure 2). Some of the main deposits include Brejuí, Bodó, Bonfim, Bonito, Malhada Limpa, Quixabá and Itajubatiba, with the metallogenetic association W±Au±Mo±Bi (Salim, 1993; Trindade, 2000; Souza Neto et al., 2012; Table 1).

The skarns are spatially and temporally associated with plutons formed during the Late Neoproterozoic Brasiliano Cycle, but specific intrusive bodies which could have acted as direct sources for W and associated metals have not been determined. In this sense, skarns are more controlled by shear zones, which acted as pathways for fluids and metals (Santos et al., 2014; Figure 3). Geochronological data by Re-Os in molybdenite from three mines provided ages of 555±2 Ma for Brejuí, 524±2 Ma for Bonfim and 510±2 Ma for Bodó, indicating that the skarns were formed during the latest stages of the Late Neoproterozoic Brasiliano Orogeny (Hollanda et al., 2017).

Like the Brejuí mine, most scheelite deposits of the studied area are dominantly oxidized W-skarns, based on the abundance of pyrite and magnetite and on the high contents of grossular and andradite molecules in garnet. Most deposits develop mineral zoning patterns: From the unaltered gneissic basement, distal amphibole-dominant skarns are formed, then clinopyroxene-dominant skarns, and finally proximal garnet-dominant skarns, until the marble front is reached (Salim, 1993). Chemical exchanges between elements inside the same minerals are a common feature (Souza Neto et al., 2012). At least two hydrothermal stages were identified, forming a prograde (early, high-temperature) paragenesis composed by almandine, diopside, anorthite, magnesiohornblende, titanite, apatite, allanite, zircon and monazite; while the retrograde (late, low-temperature) is comprised by alkali feldspar, clinozoisite-zoisite, sericite, epidote, calcite, vesuvianite and quartz (Trindade, 2000; Souza Neto et al., 2008; Hollanda, 2012; Hollanda et al., 2017). Sulfides (e.g., pyrite, pyrrhotite, chalcopyrite, molybdenite), magnetite and scheelite may occur at both stages (Santos et al., 2014).

Table 1. Tipology of scheelite occurrences according to wallrock alteration. References used include Salim (1979; 1993), Souza Neto et al. (2008), Cavalcante et al. (2016), Hollanda et al. (2017) and this work. * stands for the terminology used in this work, defined as the following abbreviations: Diopside-Amphibole-Feldspars (DAF), Amphibole-Feldspars (AF) and Biotite-Rich (BR) mineral associations and Mineralized Garnet-Diopside Skarns (MGDS). ** stands for data acquired by Corrêa et al. (Chapter 3).

Scheelite District	Type	Commodities	W Tonnage (Mt)	Grade (% WO3)	Host Rocks/Wallrocks	Primary Metasomatic Mineralogy	Morphology	Mineralization Control	Oxidation State	Age	Pressure/Temperature Conditions
Brejuí-Boca de Laje (Barra Verde, Olho D'Água, Saco dos Veados, Malhada Limpa, Juazeirinho, Machado, Zangarelhas, Cabeço de São Pedro)	MGDS*	W±Mo± ±Fe±Cu	11	0.5-1	Marbles, Metamafic Rocks and Biotite-Gneisses (Jucurutu Fm.)	Cpx (Hd30-60), Pl (An85–92), Grt (Ad19–49, Al+Sp2–7, Gr51–78), Amp (Hb), Ttn, Qz, K-Fsp	Lenticular, Stratiform, Stratabound	Reaction with Wallrocks	Oxidized	555±2 Ma	2-3 kb; 450-550°C (prograde), 200-450°C (retrograde)
					Gneisses (Caicó Complex)						
	DAF/AF/BR*		?	?	Ca-Si Rocks, Amphibolites	Hb, Pl, Cpx, Qz	Stratiform	Structural Traps, Quartz Veins, Reaction with Wallrocks	Reduced to Oxidized		
					Ca-Si Rocks, Pegmatites		Stratabound				
Bodó (Queimadas, Isidoro, Riachão, Baixios I & II, Dois Rios, Cafuca, Cinzas, Galo)	MGDS*	W±Mo	9	2	Ca-Si Rocks, Marbles (Jucurutu Fm.)	Px, Grt, Amp, Wo, Ttn, Fsp	Stratiform, Stratabound	Reaction with Wallrocks	Oxidized	510±2 Ma	?
					Gneisses and Schists (Caicó Complex)						
	BR*	W±Mo	?	?	Gneisses and Schists (Caicó Complex), Pegmatites	Bt, Qz, Fsp, Amp	Banded	Quartz Veins, Structural Control, Reaction with Wallrocks	Reduced	?	?
Bonfim (Morro do Careca, Amarante, Sulista, Queiroz, Catolé II, Gupiara-Oiticica, Pedra Preta, Mulungu, Feiticeiro, Matinha)	MGDS*	W±Au± ±Mo±Bi	>0.3	4,8	Schists (Seridó Formation)	Cpx (Hd11–48), Grt (Ad3–5, Al+Sp68–69, Gr21–22), Pl (An85–99), Amp (Tr-Hb), Ttn, Ap, Wo	Stratiform, Stratabound	Reaction with Wallrocks, Structural Control	Reduced	553±3 Ma**	2.5-4 kb; 500-580°C (prograde), 400-500°C (retrograde)
					Marbles (Jucurutu Formation)						
					Neoproterozoic Biotite-Granite					548±2 Ma**	
	DAF/BR*		?	?	Paleoarchean Granitoids	Cpx (Hd15-38), Amp (Prg-Hb-Tr), Pl (An01-53), K-Fsp, Bt, Ttn, Ap, Aln, Brt, Qz	Lenticular, Banded				
					Pegmatites					524±2 Ma	
					Neoproterozoic Biotite-Granite						
Quixabá-Malhada Vermelha	MGDS*	W	>2.5	0.5-1.4	Marbles (Jucurutu Formation?)	Grt, Px, Pl, Aln, Ap, Ttn, Scp	Lenticular, Stockwork	Reaction with Wallrocks	Reduced to Oxidized	?	?
	DAF/AF/BR*		?	?	Amphibolites, Pegmatites	Amp, Px, Qz					
Lajes (Salgadinho, Alívio, Recanto, Caçador, Espinheiro, Arara, Cacimba de Cima)	DAF/AF/BR*	W±Mo	?	?	Gneisses (Caicó Complex)	Px (Hd13-22), Amp (Prg-Hb-Tr), Pl (An01-56), K-Fsp, Bt, Ttn, Ap, Aln, Brt, Qz	Lenticular, Banded	Reaction with Wallrocks, Structural Control, Quartz Veins	Reduced	557±8 Ma**	?
	BR*		?	?	Neoproterozoic Granitoid/Pegmatite	Bt, Qz, Fsp, Amp				501±2 Ma**	
Itajubatiba	MGDS*	Au±Fe±Cu	No W	No W	Marbles (Jucurutu Formation?)	Px (Hd05-75), Amp (Tr-Hb), Ttn, Ap	Lenticular, Stratiform	Quartz Veins, Reaction with Wallrocks	Reduced	?	2.5-4 kb; 500-580°C (prograde), 400-500°C (retrograde)

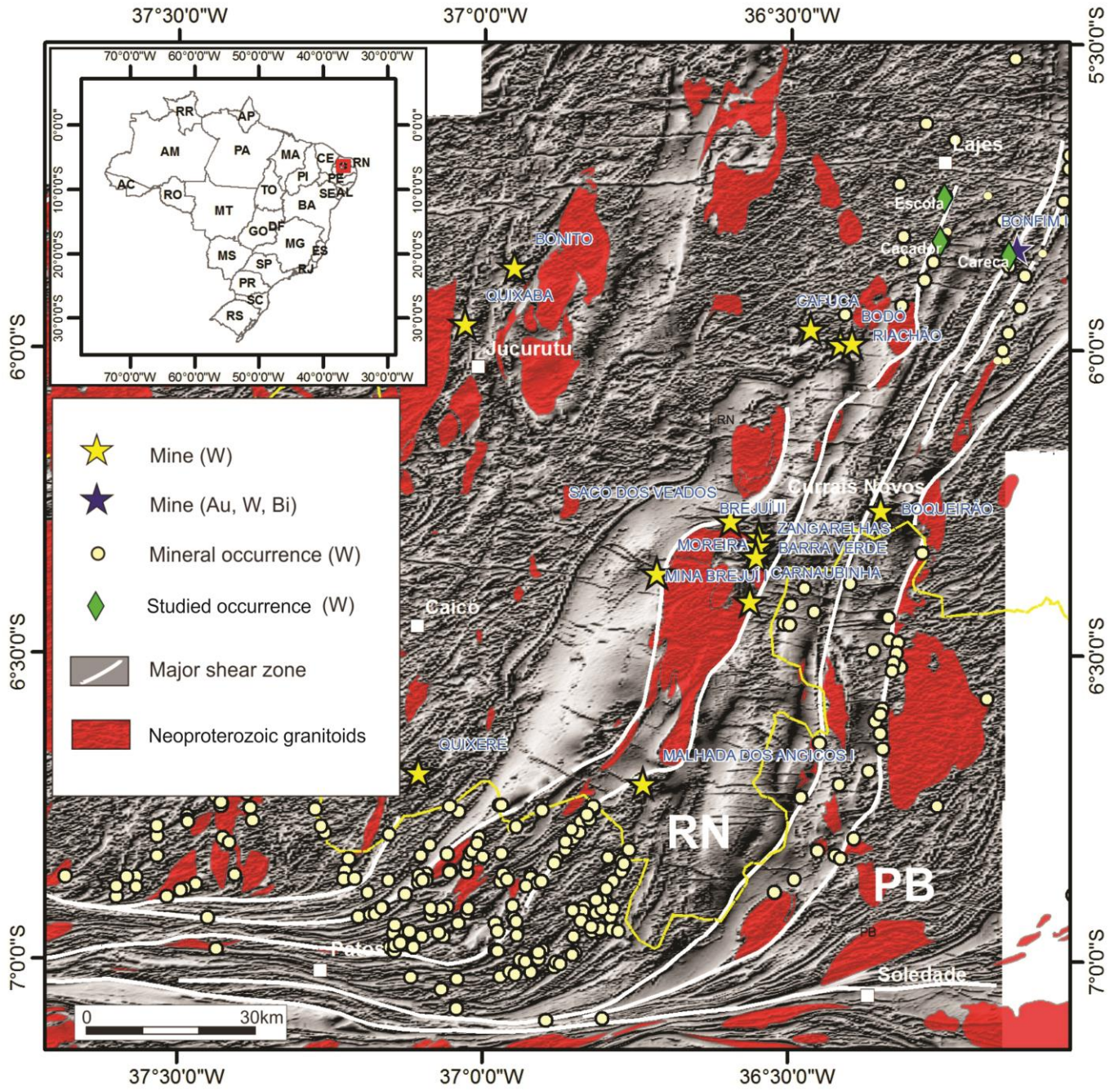

Figure 3. Tilt Derivative geophysical image of the study area. Several deposits and occurrences are highlighted, showing their spatial association with regional-scale shear zones and Neoproterozoic plutonic rocks. These lineaments acted as pathways for magmas emplacement and hydrothermal fluids migration. There is no distinction between the different types of W deposits/occurrences in the symbols used in this figure.

4. METHODS

Field work and geophysical and remote sensing analyses were used to acquire structural and lithological data. Well-known occurrences and deposits were visited and samples were collected. Micropetrographic observations in polished thin sections were conducted in order to identify mineralogical and textural characteristics, leading to the definition of paragenetic sequences and hydrothermal alteration haloes. The assemblages were classified by temporal and spatial relationships between minerals. In all figures, mineral abbreviations are displayed according to Whitney & Evans (2010).

Mineral chemistry analyses were conducted at the Electron Microprobe Laboratory of the University of Brasília using a JEOL JXA-8230 operating at 20 kV and 20 nA, with 10-second and 5-second peak and background counting times, respectively. Images using this equipment were acquired at 15 kV. A total of 1201 spots were analyzed in pyroxene, amphibole, feldspars, biotite, epidote group minerals, titanite and apatite to determine their composition. The data for all analyzed crystals are presented as oxide weight percentages (wt %) for all elements, and, when acquired, rare-earth elements (REE) are reported in parts per million (ppm) (Tables 2-8, available in the Supplementary Material section in the end of Chapter 2). From the analyzed weight percentages the atoms per formula unit (apfu) were calculated for each mineral (Deer et al., 2013) and plotted in binary and ternary diagrams, as well as spidergrams normalized to the chondrite (Sun & McDonough, 1989). The recalculation procedures for each mineral will be detailed in their respective topics.

Barium-containing minerals, such as hyalophane and barite, were imaged by a FEI QUANTA 450 Scanning Electron Microscope (SEM) coupled to an EDAX Apollo X Energy Dispersive Spectrometer (EDS) in the Geochronology Laboratory of the University of Brasília. Image acquisitions were done with the EDAX TEAM EDS Software Suite in two thin sections under high vacuum conditions. Operating parameters were 25 kV voltage and 12.1 mm working distance.

Finally, the processed data were interpreted and integrated, leading to conclusions concerning the mechanisms that led to the formation of the Seridó Mineral Province.

5. RESULTS

5.1. Field Work and Petrographic Observations

5.1.1. Descriptive Characterization of the Studied Deposits and Occurrences

Previously described as mafic/metamafic rocks (Moeri & Kloechner, 1979a, b), the studied calc-silicate rocks are generally characterized by garnet-lacking, diopside and amphibole-rich black to dark green rocks with feldspar-rich white domains that occur parallel to N-NE-trending map-scale shear zones (Figures 2, 3 and 4). All the rocks studied in this work occur along granitoid wallrocks, where most belong to the basement. In some locations, these zones are associated with strongly deformed biotite-rich bands. Their outcrops are relatively narrow, never reaching extensions higher than a hundred meters. These rocks show no clear association with marbles from the Jucurutu Formation or with Late Neoproterozoic plutons. Instead, as stated above, the main observable features associated with their origin are strike-slip structures, which control their spatial distribution. In the areas where these rocks occur, there are records of scheelite and barite extraction, such as the occurrences of Salgadinho, Alívio, Recanto, Espinheiro and Caçador.

Since the studied deposits and occurrences present many similarities between them, they were grouped following field and macroscopic criteria, leading to three distinct associations. The first includes the Alívio, Recanto and Espinheiro occurrences, which are composed of massive, coarse-grained calc-silicate rocks with different textures constituted mainly by diopside, amphibole and feldspars. The second is the Bonfim-Salgadinho association, which presents rocks with a somewhat similar mineralogy as the first group but also exhibits strongly foliated biotite-rich bands which are generally located at the borders of less deformed domains (Figure 4). The last is represented solely by the Caçador occurrence, mainly composed of strongly oriented biotite or biotite-amphibole rocks, with minor quantities of calc-silicate rocks. The different characteristics observed in these three groups suggest a temporal progression from the first association to the last, to be further explained in the following topics.

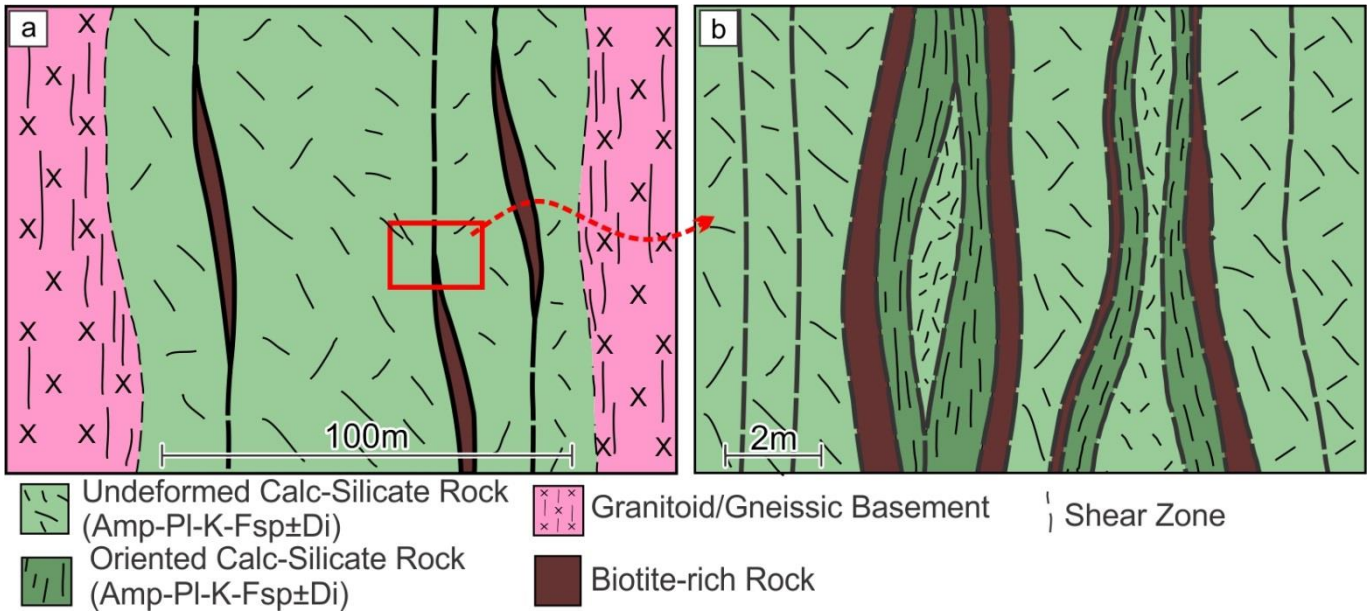

Figure 4. Schematic maps highlighting the structural and metallogenetic array of the study area. Although these images are from the Salgadinho occurrence, similar textures are seen in other locations. a: Map showing the Salgadinho occurrence, which is bordered by basement granitoids. In this location, zones with different deformational grades are observed, being controlled by N-trending shear zones. b: Outcrop-scale image representing all the described metasomatic rocks.

5.1.1.1. Bonfim W-Au(±Mo±Bi) Deposit

The Bonfim mine is possibly the most studied skarn deposit in the Seridó Mineral Province, summarized in the work of Souza Neto et al. (2008). It consists in a typical exoskarn mostly contained within Neoproterozoic marbles from the Jucurutu Formation, but skarn-like alterations also occur in biotite-schists from the Seridó Formation (Figure 5). In this location, skarns are diopside/hedenbergite-rich and garnet-poor, presenting with associated amphibole (tremolite-magnesiohornblende), titanite, magnetite and apatite. A diverse sulfide assemblage, composed of molybdenite, pyrrhotite, chalcopyrite, pyrite and arsenopyrite, occurs in association with scheelite. The main structures of this deposit are a kilometric antiform and steep-dipping NS/N30°E shear zones. Gold, along with Te- and Bi-bearing minerals, appear to be in late-stage phases, which are controlled by N70°W/EW-trending faults that crosscut the deposit rocks, and hence could be unrelated to the skarn formation process.

The W±Mo±Au±Bi skarns mentioned in the previous paragraph are different from the rocks studied in this work. The calc-silicate rocks from this paper present a distal characteristic in relation to the skarns, are garnet-lacking and have distinct mineral assemblages and textures. In the Bonfim deposit, these rocks occur beneath the skarn, as seen in the deepest portions of the underground mine and in several drill hole samples (Figure 5). Rocks with similar features occur in trenches and outcrops at the near-mine Morro do Careca occurrence, located approximately 1 km southwest of the Bonfim deposit, with mineral associations mainly composed of diopside-amphibole-feldspars (DAF), amphibole-feldspars (AF) and biotite (BR). Unless stated otherwise, in this paper the term “Bonfim” refers to the Bonfim mine along with its drill core samples and the Morro do Careca occurrence.

In Bonfim, the contact between the granitic wallrock and the melanocratic zones may be abrupt or transitional (Figure 5). Near their boundaries, the wallrock appears more deformed. When the contact is transitional, a discrete hydrothermal alteration is initially developed, characterized by the formation of discontinuous and anastomosing amphibole-rich centimeter-scale bands. Later, these tend to gather, forming larger bands parallel to the regional foliation trend. Amphibole is generally fine to medium-grained, occurring in association with plagioclase and diopside as the alteration process advances. Relict

granitic nuclei are commonly preserved along these domains. Barite-rich bands, which occur associated with other accessory minerals (e.g., titanite, magnetite, apatite), are common in these rocks.

Nearly monomineralic biotite bands also frequently appear in the borders of the amphibole-rich domain (Figures 4 and 5). These have a replacement-like character, evidenced by crosscutting relationships and mineral alteration processes, showing that they were formed from a superimposed process. Discordant N70°W-trending tabular pegmatitic dykes cut through all of the described altered mineral associations. Among other factors, a unique feature of this deposit is the presence of hyalophane, a Ba-containing feldspar. Further progression of the metasomatic alteration results in the formation of ore minerals, such as molybdenite and scheelite.

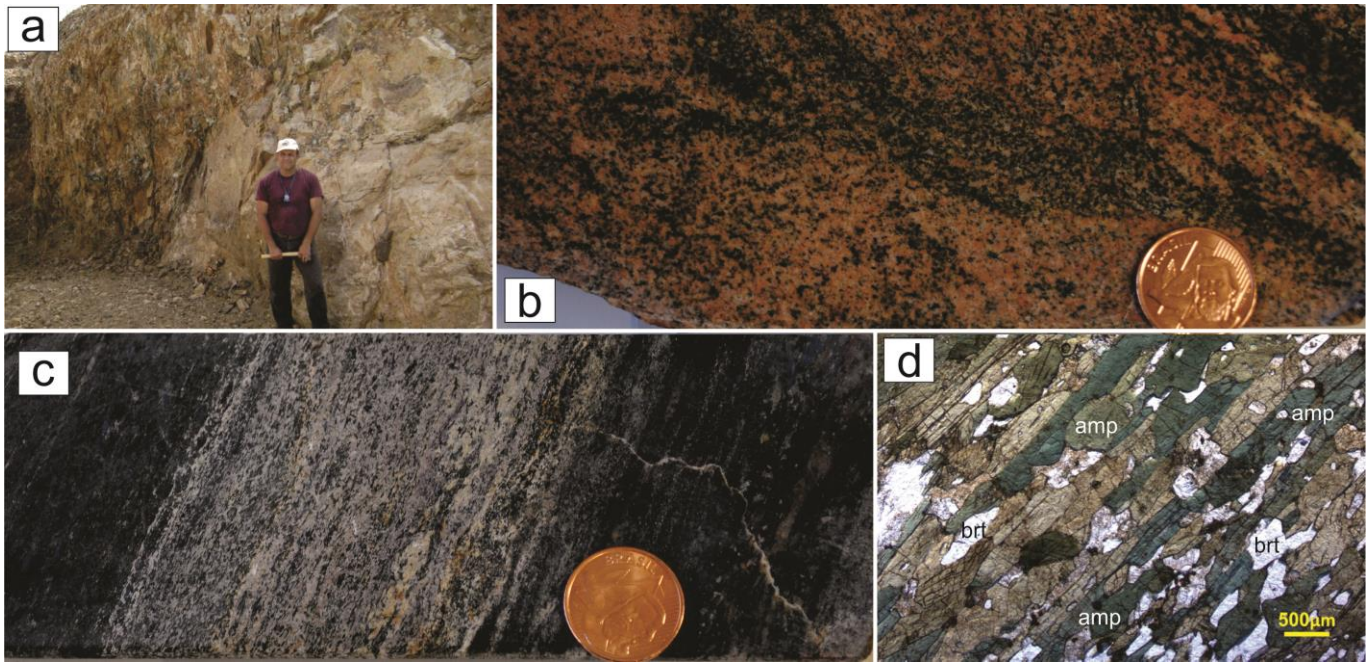

Figure 5. Plate from Bonfim. a: Contact between the studied calc-silicate rocks (left) and the granitic wallrock (right). b: Metasomatic amphibole bands subparallel to the foliation formed along the granitic wallrock, representing the beginning of the alteration process. c: Strongly-deformed barite-rich band (white) along an amphibole-rich rock (black). d: Photomicrography of the barite-rich band from Figure 5c.

5.1.1.2. Salgadinho W Occurrence

The Salgadinho occurrence exists in a 100-meter-wide pit limited by Caicó Complex basement granitoids, which appear deformed and aligned in parallel to the regional foliation trend (Figures 4 and 6). When less deformed, the granitoids still preserve their granular igneous texture.

As seen at the Bonfim deposit, this occurrence presents both amphibole-dominant and biotite-rich mineral assemblages, with the latter occurring in lesser quantities when compared with the Bonfim deposit (Figure 6). Differently from the previous locality, the amphibole-rich association in this occurrence presents very coarse amphibole grains, which generally occur as nonfoliated undeformed domains. These occur as nuclei that become more deformed at their borders, forming a strongly oriented texture. A second difference between Salgadinho and Bonfim is that the former presents more prominent feldspars contents, shown by larger white colored domains in the rocks (Figure 6). Like Bonfim, the biotite-rich (BR) bands also show signs that they were formed after the diopside-amphibole-feldspars (DAF) and amphibole-feldspars (AF) mineral associations.

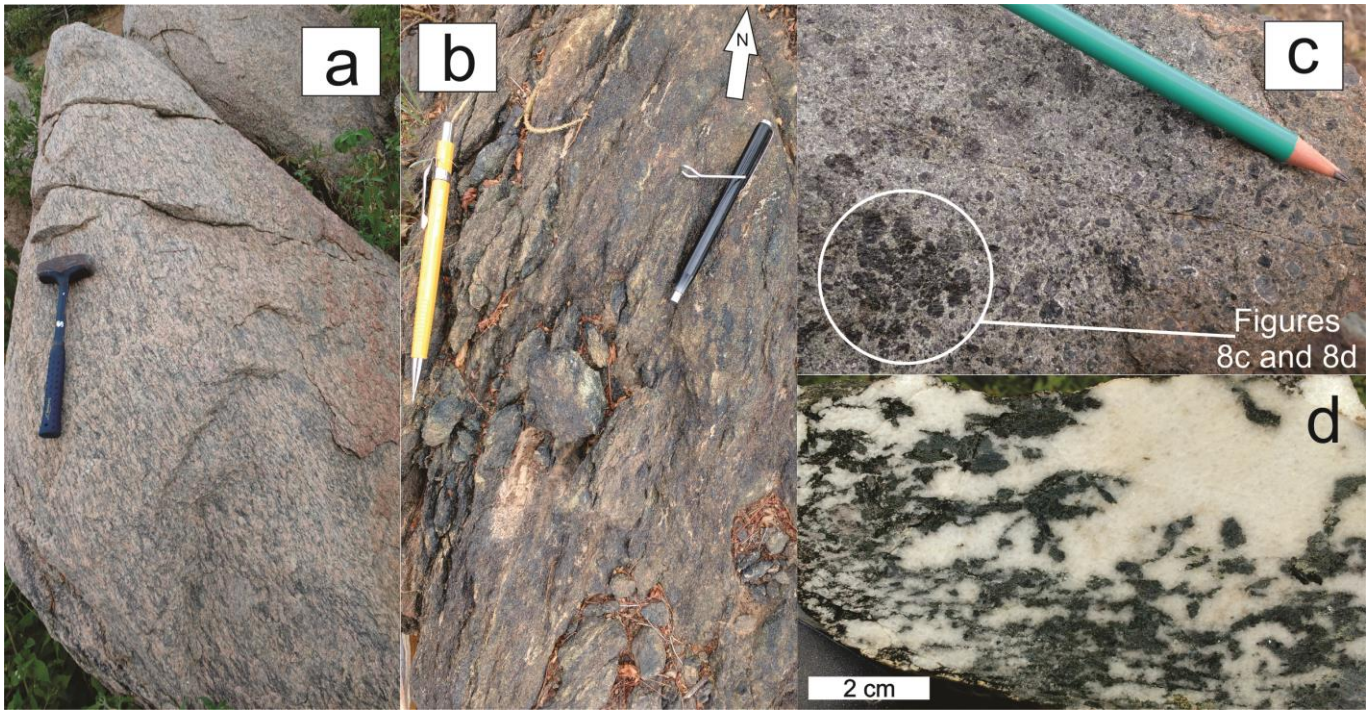

Figure 6. Plate from the Salgadinho occurrence. a: Outcrop showing a foliated granitic rock from the Paleoproterozoic basement bordering the hydrothermally altered domain. b: Metasomatic rock with coarse amphibole grains (black) oriented parallel to the regional N20°E-trending Brasiliano Cycle deformation. c: Calc-silicate sample presenting an undeformed texture with coarse amphibole crystals (black) being formed over older diopside grains (green). d: Calc-silicate rock showing anastomosing and discontinuous amphibole-rich and feldspar-rich bands, highlighting their synchronous character.

5.1.1.3. Alívio, Recanto and Espinheiro W Occurrences

The Alívio occurrence lacks the biotite-rich bands described above. Coarse-grained, nondeformed diopside-amphibole-feldspars-rich (DAF) and amphibole-feldspar-rich (AF) rocks characterize the Alívio occurrence (Figure 7). In this location, pegmatitic dykes also appear, showing similar alteration characteristics as the previously mentioned localities, such as the formation of diopside-epidote-quartz and amphibole clusters. Similar features appear at the Espinheiro occurrence. In the Recanto occurrence, as well as the Alívio, biotite-rich rocks are also absent. In this location, discordant N70°W-trending dyke swarms occur, crosscutting paragneisses possibly from the Jucurutu Formation (Figure 7).

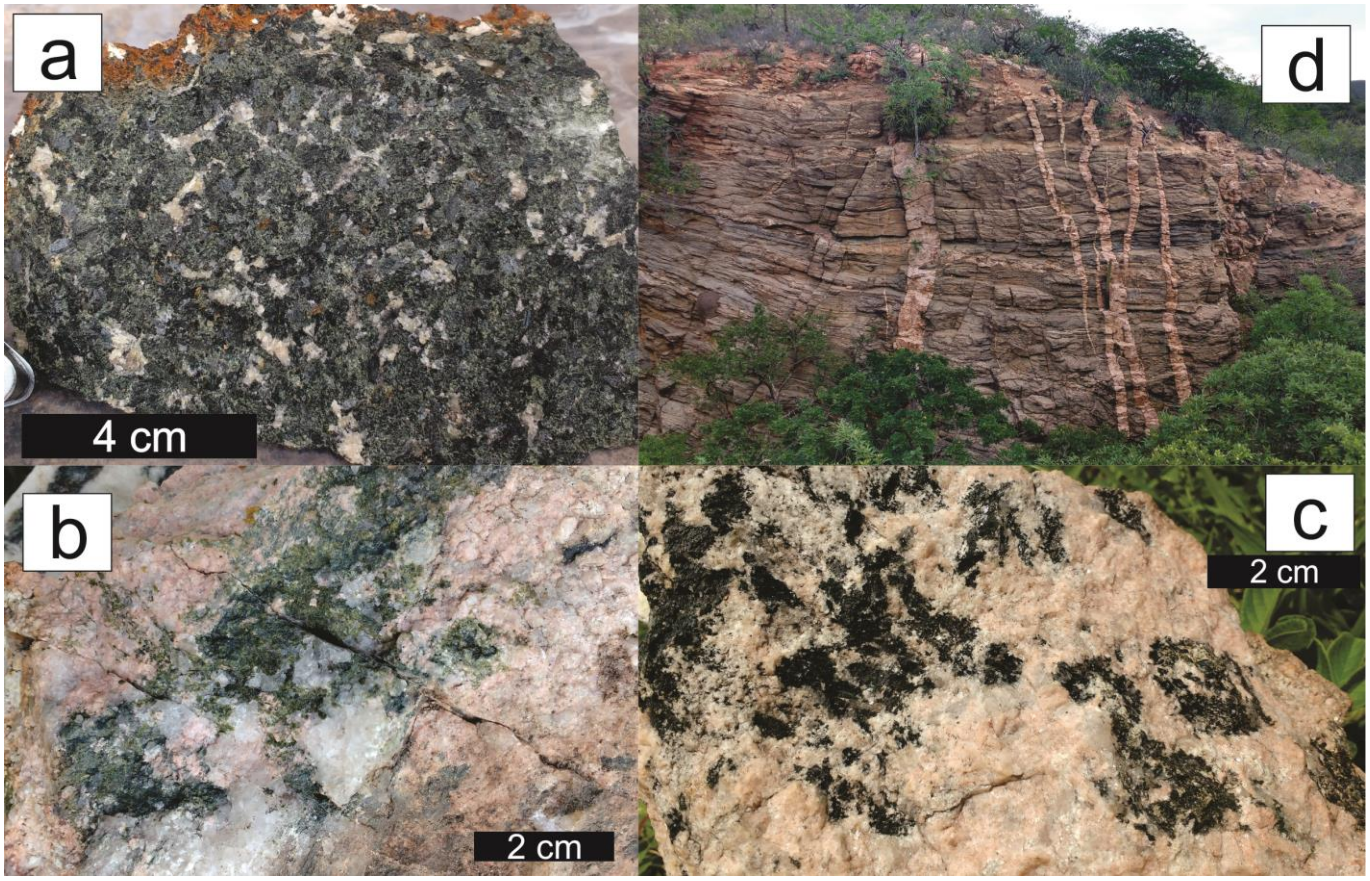

Figure 7. Plate from the Alívio (a-c) and Recanto (d) occurrences. a: Sample showing coarse grains of amphibole, diopside and feldspars. b-c: Diopside-epidote-quartz (b) and amphibole (c) clusters formed in a pegmatite sample. d: Subvertical N70°W-EW pegmatitic dyke swarm crosscutting paragneisses possibly from the Jucurutu Formation.

5.1.1.4. Caçador W(±Mo) Occurrence

The Caçador occurrence is composed of only biotite-rich (BR) associations (Figure 8) along a tens of meters wide open pit. However, in the vicinities of this occurrence there are diopside-amphibole-feldspars-rich calc-silicate rocks. Rocks from this location may be divided into biotite-only and biotite-amphibole assemblages. Unlike Bonfim and Salgadinho, biotite appears in textural equilibrium with amphibole.

Shear zones crosscut the whole occurrence, with quartz segregations commonly developing along them (Figure 8). Sulfides, such as molybdenite and pyrite, are generally precipitated at the biotite band/quartz segregation interface. Irregular pegmatitic injections appear both with discordant and subconcordant geometries. Disseminations of scheelite and molybdenite occur along the biotite-rich bands, as well as quartz veins/segregations and pegmatites (Figure 8).

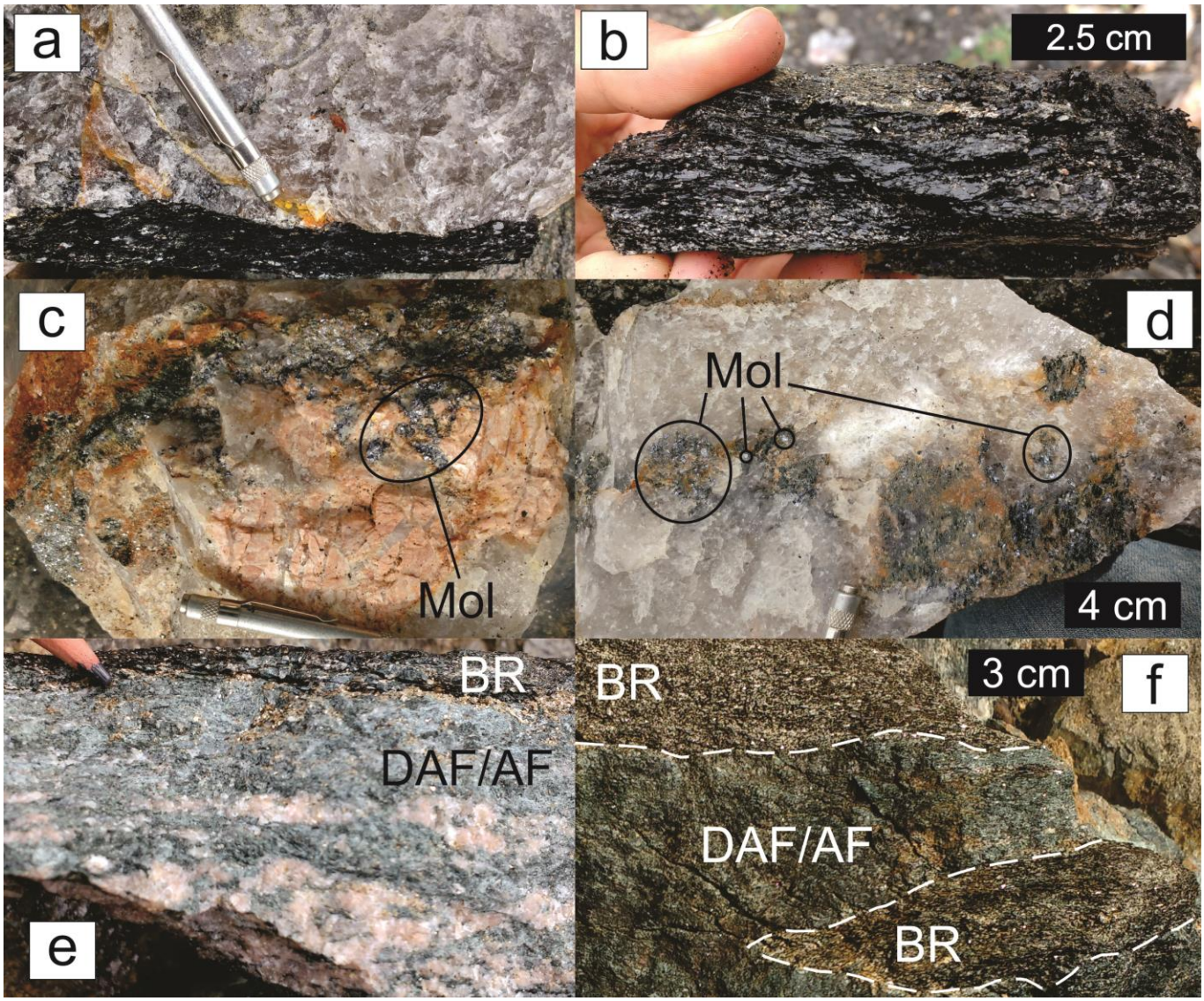

Figure 8. Plate from the Caçador occurrence (a-d) and Bonfim (e-f), showing the biotite-rich rocks. a: Association between a biotite-rich band and a thick quartz segregation. b: Hand sample showing the almost biotite-pure composition in some rocks. c-d: Association between the biotite-rich rocks, pegmatitic injections, quartz veins/segregations and molybdenite. e-f: At Bonfim, the biotite-rich mineral association (BR) is superimposed on the diopside-amphibole-feldspars (DAF) and amphibole-feldspars (AF) mineral associations. BR bands occur either at the borders (e) or overprinting (f) portions of the DAF/AF associations.

5.1.2. Pegmatitic Injections

On all studied deposits and occurrences, pegmatitic injections were observed directly associated with all observed mineral associations, or at least in their vicinities. They commonly occur as discordant N70°W-trending semitabular dykes that cut the studied rocks but also appear as subconcordant discontinuous injections. In some locations, pegmatitic bodies contain diopside and amphibole aggregates and are associated with quartz veins and molybdenite disseminations (Figures 7 and 8).

At Bonfim and Morro do Careca, two pegmatite types were identified, namely, a rose-colored, K-feldspar-rich rock that directly crosscuts the studied rocks and a distal white-colored, albite-rich rock. The proximal type presents a syn- to postkynematic character in regards to amphibole- and biotite-rich rocks, although space and time connects these zones and the white-colored pegmatite remain unclear. The rose-colored pegmatite is seen in other occurrences, such as at the Alívio, Recanto and Caçador occurrences, while the albite-rich pegmatite is not. Both rocks have a similar mineralogy, which is essentially composed of quartz, albite, K-feldspar, garnet, biotite and muscovite. The rose-colored pegmatite also contains magnetite.

5.1.3. The Diopside-Amphibole-Feldspars (DAF) and Amphibole-Feldspars (AF) Associations

Representatives of these mineral associations are found in all of the studied deposits and occurrences. The rocks are composed mainly of diopside, amphibole and plagioclase, with minor K-Ba-feldspar, titanite, epidote-allanite, apatite, magnetite, quartz, calcite, barite and scheelite (Figure 9). Locally, anomalous concentrations of titanite, magnetite, epidote-allanite, apatite, barite and scheelite may occur. These rocks are generally either undeformed, banded or foliated (Figure 4). In undeformed domains, the rocks are medium to very coarse-grained. When deformed, crystals are generally fine- to medium-grained, commonly presenting with a wavy extinction and/or microfracturing. Amphibole and titanite define the oriented texture, which is usually parallel to the main foliation. In some domains, leucocratic feldspar-rich and greenish melanocratic diopside-amphibole-rich bands are developed. Both DAF and AF are often spatially associated with quartz segregations.

Under micropetrographic observations, mineral alteration processes were identified, leading to the definition of paragenetic sequences (Figure 10). Initially, the DAF association is formed, and then it is replaced by AF, as observed in petrographic and mineral chemistry analyses.

DAF is represented by a wide variety of mineral species. Early diopside and allanite are formed and then consumed to produce hornblende, titanite and magnetite, which commonly occur along bands (Figure 9). Plagioclase tends to be more calcic, and the system becomes enriched in Ba, represented by hyalophane and barite, and REE-enriched minerals, such as allanite, titanite and apatite. Although still discrete, scheelite grains start to precipitate in this stage.

The AF association, which forms later than the DAF, is characterized by Na-rich plagioclase as well as the development of a hydrous assemblage, represented by coarse-grained zoisite/clinozoisite and interstitial muscovite and chlorite clusters. The chemical compositions of several minerals, such as amphibole and plagioclase, are altered as a consequence of changes to the physicochemical conditions of the system. Alteration processes such as saussuritization and sericitization of feldspars are common in this phase, and diopside is rare (Figure 9). This last pulse is generally responsible for the main ore-minerals deposition, corresponding with scheelite and molybdenite.

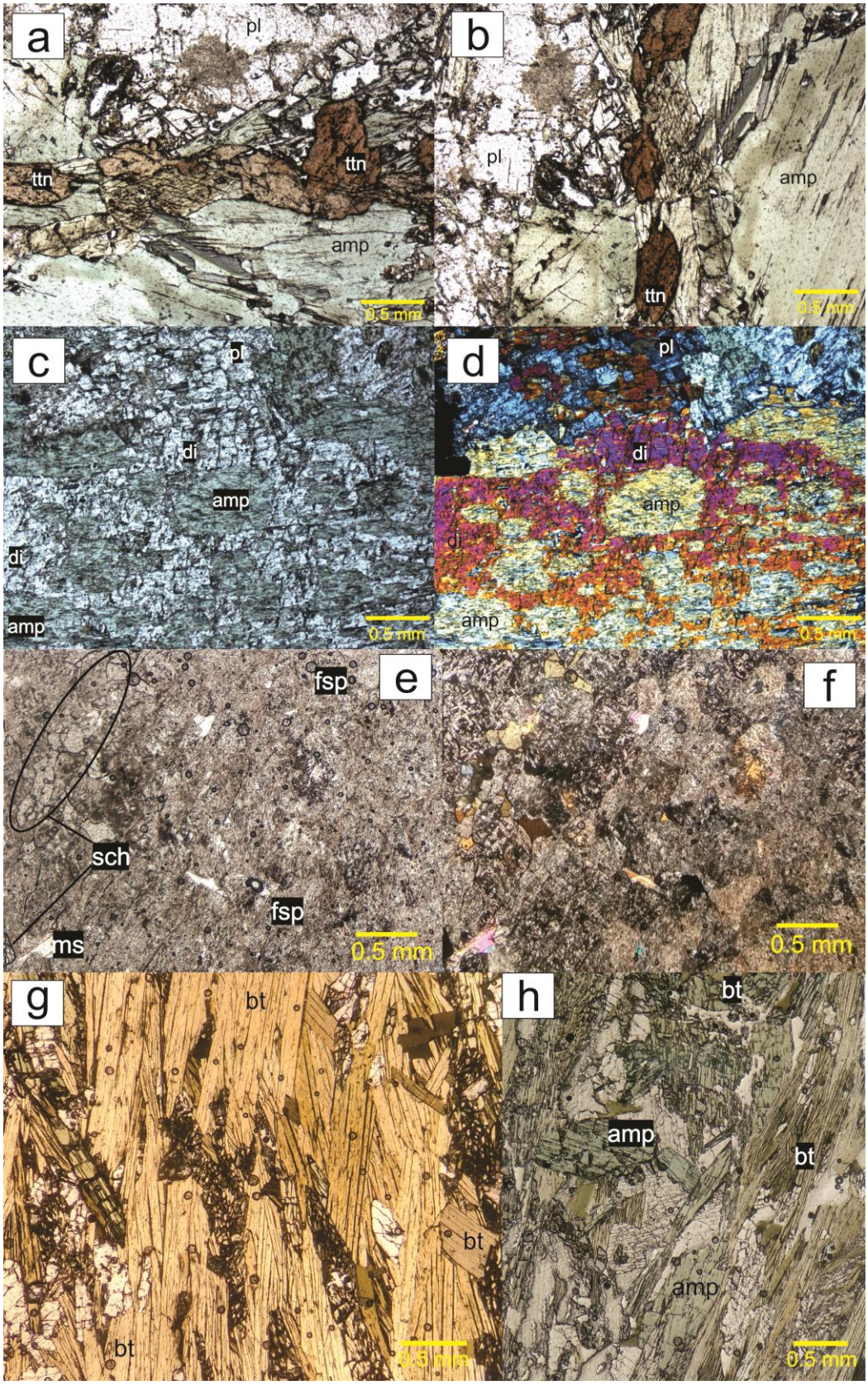

Figure 9. Metasomatic mineral associations plate. a-b: Sample from Salgadinho photomicrographs under parallel polarizers showing an oriented amphibole-titanite band from the DAF association, also highlighting pleochroic titanite crystals at 0° (a) and at 90° (b). c-d: Photomicrographs under parallel (c) and crossed (d) polarizers of the same sample from Salgadinho seen in Figure 6c. These show older metasomatic diopside crystals being altered to amphibole, representing the transition from DAF to AF. e-f: Photomicrographs under parallel (e) and crossed (f) polarizers of a sample from Bonfim showing scheelite with muscovite and altered feldspar (by saussuritization and sericitization processes), which are representatives of the AF association. g-h: Photomicrographs under parallel polarizers of a sample from Caçador presenting biotite and amphibole from the BR association.

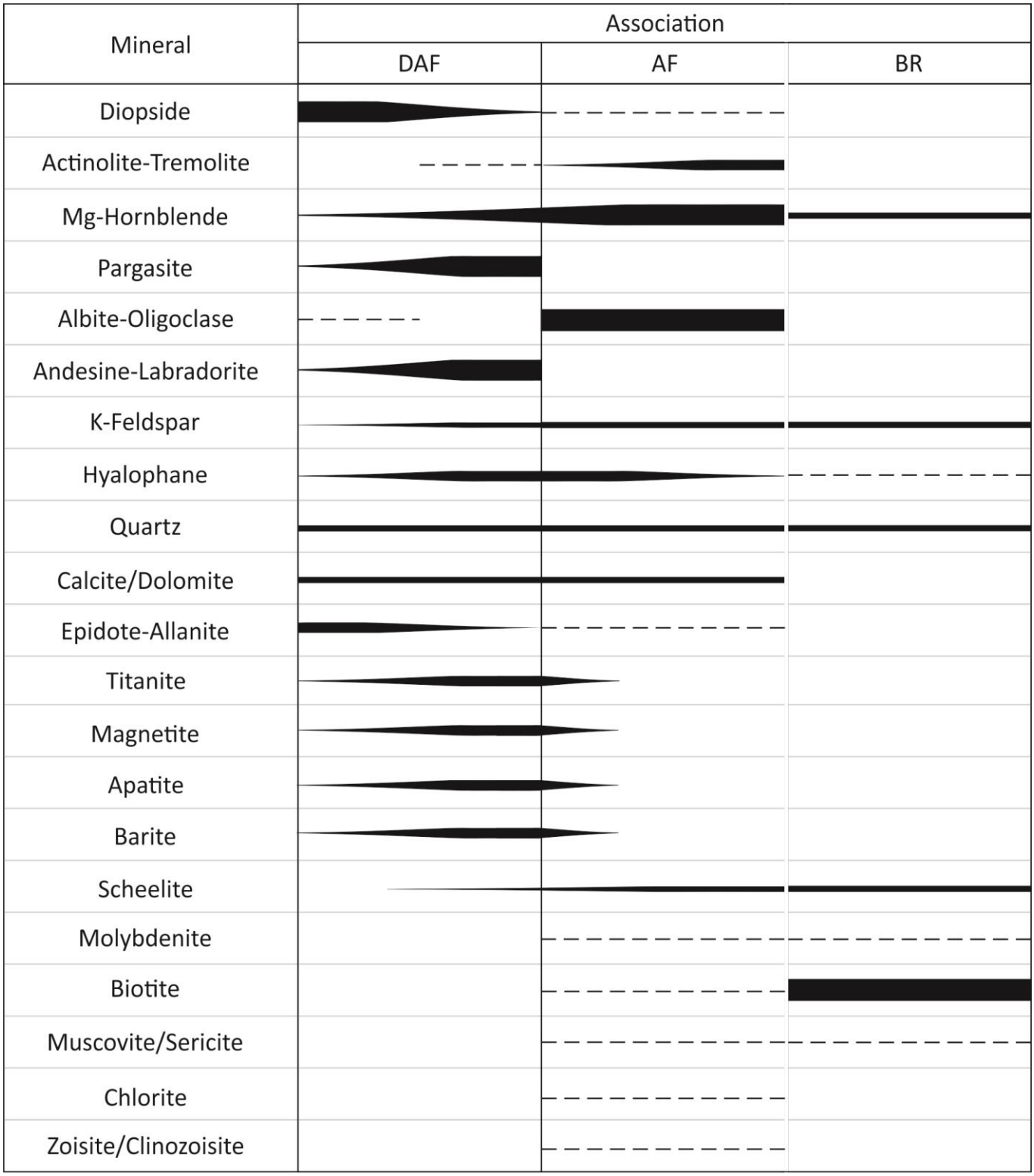

Figure 10. Paragenetic Sequences Chart. Assemblages are separated according to each mineral association (DAF, AF and BR). Each bar or line represents the occurrence rate of each mineral: blank spaces indicate absence, fine dashed lines rare, fine continuous lines uncommon and thick continuous lines common minerals. The vertical lines that divide DAF from AF and AF to BR are different because there is a continuous transition from DAF to AF, while from AF to BR there is a superimposition of processes.

5.1.4. The Biotite-Rich Association (BR)

In Salgadinho and Bonfim, these rocks appear as decimeter-scale bands that envelop the DAF/AF assemblages. As previously stated, the BR association occurs as a superimposed alteration over the DAF/AF associations in these localities (Figure 8). In the Caçador occurrence and in its vicinities, the BR

association appears as tens of meters-wide domains strongly associated with centimeter-scale quartz veins and segregations (Figure 8).

This association is essentially composed of biotite, accounting for more than 95 vol. % of the whole rock in some samples. In others, decreased amounts of this mineral occur in association with plagioclase, K-feldspar, quartz and hornblende, comprising a single paragenesis (Figures 9 and 10). The strong foliated texture formed by biotite lamellae with or without amphibole is a key feature of this domain. Ore minerals associated with this zone are scheelite and molybdenite.

5.2. Mineral Chemistry

5.2.1. Pyroxene

A total of 124 pyroxene spot analyses on 17 samples from the DAF/AF associations were done (Table 2). The obtained data was recalculated following the procedures of Morimoto et al. (1988) based on 6 oxygens. The results in atoms per formula unit (apfu) were then used to obtain the proportions of each end-member of the wollastonite-enstatite-ferrosilite (Wo-En-Fe) and diopside-hedenbergite-johannsenite (Di-Hd-Jo) systems and plotted on ternary diagrams (Figure 11). The data were also compared with data from other deposits (Salim, 1993; Souza Neto et al., 2008).

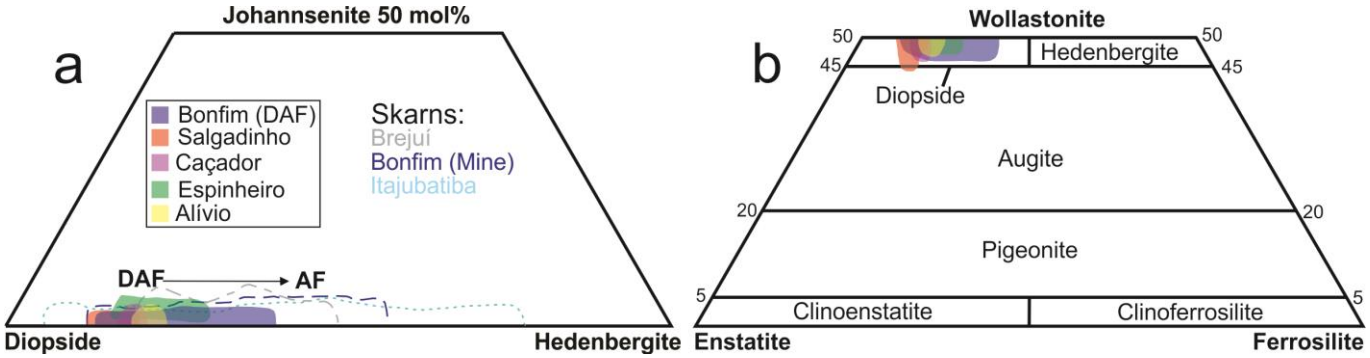

Figure 11. Pyroxene diagrams. a: Di-Hd-Jo diagram, presenting data from this work (fields) and from other deposits (dashed lines), such as Brejuí (Salim, 1993), Bonfim mine and Itajubatiba (Souza Neto et al., 2008). b: En-Fs-Wo diagram, showing that all acquired data plots in the diopside field.

Pyroxene appears either as coarse-grained crystals (DAF) or as fine relict grains scattered along deformed bands (AF). This mineral typically presents signs of alteration to amphibole (Figure 9). All pyroxene data plot in the diopside field, but there are some variations between some groups (Figure 11). Early diopside from the DAF association is richer in Mg and Mn and slightly poorer in alkalis. As this phase advances to AF, diopside becomes more hedenbergitic, enriched in iron and poorer in Mn. This fact may be explained by Mg consumption during alteration to amphibole, which makes the crystals enriched in Fe in the AF association.

Although the pyroxene chemistry data from the literature belongs to the classic skarns of the Seridó Mineral Province, they still share chemical characteristics with the pyroxene crystals studied in this paper (Figure 11). These previous works cite “hornblende-clinopyroxene-skarns” or “amphibolites”, which could be related to the rocks studied in this paper since the pyroxene analyses plot at exactly the same field (Salim, 1993; Souza Neto et al., 2008). In localities which present both diopside-skarns and garnet-skarns, the pyroxene composition shows a larger range between the diopside and hedenbergite molecules.

5.2.2. Amphibole

Amphibole from the DAF/AF and BR associations were studied, totaling 404 spot analyses on 28 samples (Table 3). The results were processed following the classification scheme of Hawthorne et al. (2012) with the aid of the recalculation spreadsheet of Locock (2014) based on 24 anions (OH, F, Cl, O),

where at least 22 of these account for O. The H_2O-OH component was not measured but estimated following the same procedures. Then, the data were used to classify the different amphibole minerals in each group, subgroup and species and to indicate their chemical correlations with each mineral paragenesis (Figure 12). The data were also compared with data from other deposits (Salim, 1993; Souza Neto et al., 2008).

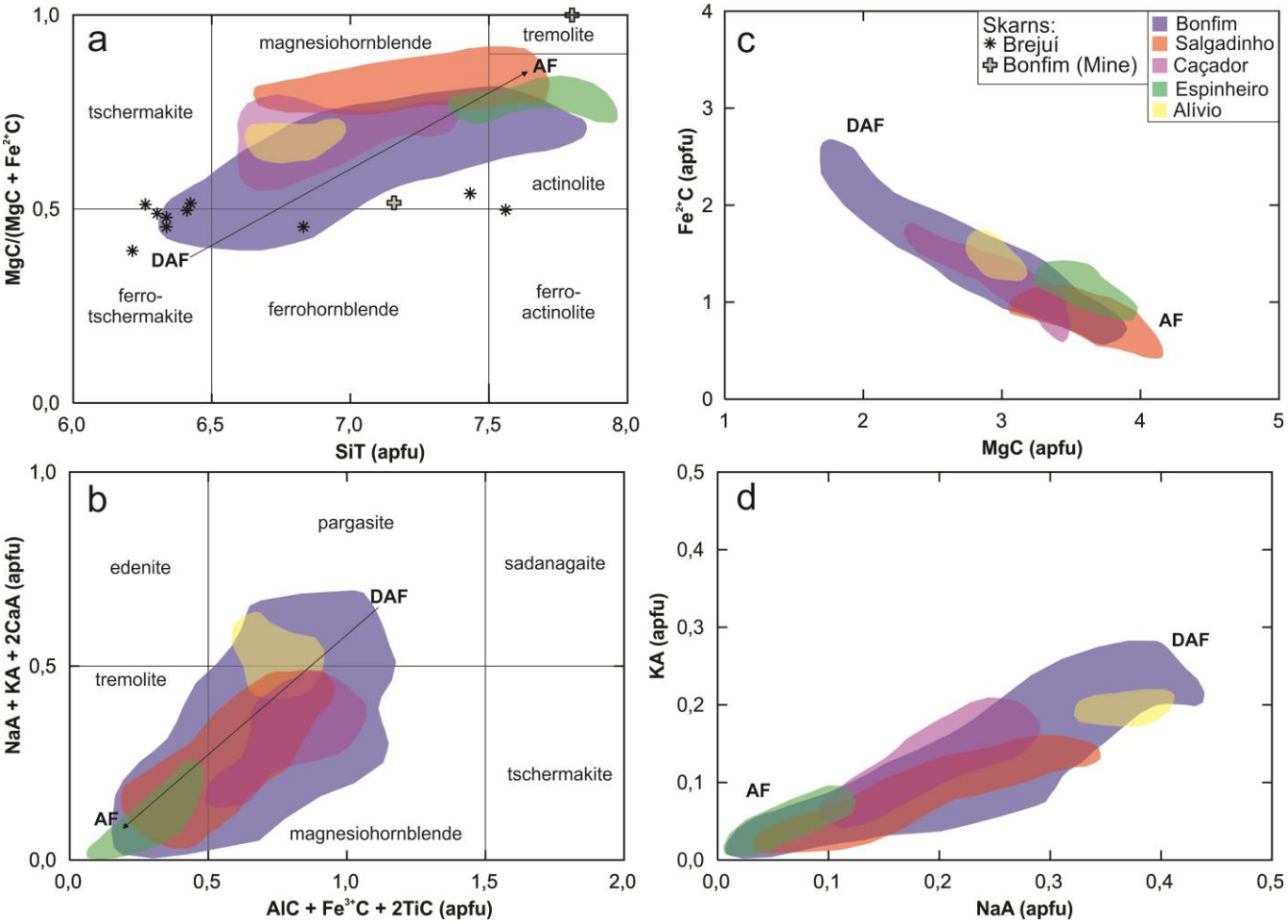

Figure 12. Amphibole diagrams presenting data from this work and from skarn deposits, such as Brejuí (Salim, 1993) and Bonfim (Souza Neto et al., 2008). The transition between the DAF and AF associations is represented by arrows. a: Si in the T site vs Mg/(Mg+Fe^{2+}) in the C site diagram, following the classification scheme of Leake et al. (1997). It is important to note that part of the analyses have Na+K in the A site > 0.5, and hence may not be plotted in this diagram, being classified as pargasite. b: Al+Fe^{3+}+2*Ti in the C site vs Na+K+2*Ca in the A site classification diagram proposed by Hawthorne et al. (2012). The acquired data range from tremolite to pargasite, but most analyses plot in the magnesiohornblende domain. c: Mg in the C site vs Fe^{2+} in the C site diagram, showing the cationic exchanges between these elements during the metasomatic processes. d: Na in the A site vs K in the A site diagram, highlighting the association between alkalis.

Analyzed amphibole grains from all mineral assemblages belong to the OH-F-Cl group and to the calcic subgroup. There are, however, relevant differences between crystals from each mineral association. Under microscopic observations, two amphibole groups were identified based on their pleochroism colors. The first species presented with brown to dark green pleochroism, corresponding to magnesiohornblende and pargasite associated with DAF. The second species showed light brown to pale bluish green pleochroism, corresponding to actinolite-tremolite attributed to AF (Figure 12). The microprobe analyses confirmed this distinction, presenting a wide chemical range between actinolite-tremolite, magnesiohornblende and pargasite (Figure 12).

The DAF and AF associations have amphibole analyses that represent all of the previously mentioned mineral phases. Early amphibole formed during the DAF association plots in the pargasite-

magnesiohornblende field, while grains from AF plot in the actinolite-tremolite domain. Nevertheless, the majority of the analyzed grains plot in the magnesiohornblende field. The DAF assemblage is composed of amphibole with high Al, Fe^{2+}, Fe^{3+} and Ti contents on the C site, low Si on the T site and high Na and K on the A site. The AF association, on the other hand, is characterized by crystals with high Mg and low Al, Fe^{2+}, Fe^{3+} and Ti on the C site, high tetrahedral Si and low alkalis content on the A site (Figure 12). It is hard to graphically delimit one association from the other because their fields overlap with each other.

The BR association is represented by a smaller quantity of samples from the Caçador occurrence in which biotite coexists with amphibole. These minerals show petrographic and chemical features that are more similar to AF, suggesting the late-stage character of both AF and BR mineral associations (Figure 12).

When compared, the studied deposits present some differences between their amphibole analyses. The ones from the Salgadinho occurrence are richer in Mg and poorer in Fe^{2+} on the C site and in K on the A site than the other deposits. Data from Alívio present higher alkali contents on the A site than most deposits. Amphibole from the Bonfim deposit are responsible for the wide compositional dispersion shown in Figure 12, and in general present the lowest [MgC/(MgC+Fe^{2+}C)] ratios among all analyses. When compared with data from the Brejuí and Bonfim skarn deposits, grains from skarns are richer in Fe than those from the studied rocks, presenting balanced contents of Mg and Fe.

5.2.3. Feldspars

A total of 298 feldspar analyses were done on 32 samples from the DAF/AF and BR associations, including plagioclase, K-feldspar and hyalophane – a Ba-rich K-feldspar (Table 4). The results were processed following Deer et al. (2013) based on 8 oxygens in the mineral formula. Finally, the recalculated data was used to obtain the proportions of each end-member in the systems albite-anorthite-orthoclase (Ab-An-Or) and albite-orthoclase-celsian (Ab-Or-Cn) and plotted on ternary diagrams. A petrographic distinction between K-feldspar and hyalophane is not always simple, so the criteria for assigning each analyzed mineral to one of the systems was based on their CaO and BaO wt% contents, which are almost always mutually exclusive (i.e., when one of them prevails, the other is nearly zero). The data were also compared with data from other deposits (Salim, 1993; Souza Neto et al., 2008).

5.2.3.1. Plagioclase

Plagioclase is one of the most common minerals of the DAF/AF associations (Figure 13). Plagioclase from the DAF association is characterized by Ca-enriched crystals, reaching up to An56 contents and plotting in the andesine-labradorite field. Plagioclase associated with the AF association tends to become more sodic and plots in the albite-oligoclase field (Figures 13 and 14). Crystals from both mineral associations are petrographically coeval with amphibole formations (Figures 9 and 10). Compositions of the DAF and AF feldspars overlap.

At the Brejuí and Bonfim skarn deposits, plagioclase reaches nearly pure anorthite compositions (An_{97}). In Brejuí, there is a population that presents similar An contents as the studied rocks (Figure 14).

5.2.3.2. K-feldspar and Hyalophane

These minerals are not as abundant as plagioclase but were present in the majority of studied samples. Analyzed crystals from the DAF/AF and BR associations show a large variance between them, including the anorthoclase and K-feldspar fields, as well as the orthoclase-celsian interval (Figures 13 and 14). Analyses from the Brejuí skarn deposit present nearly pure K-feldspar compositions.

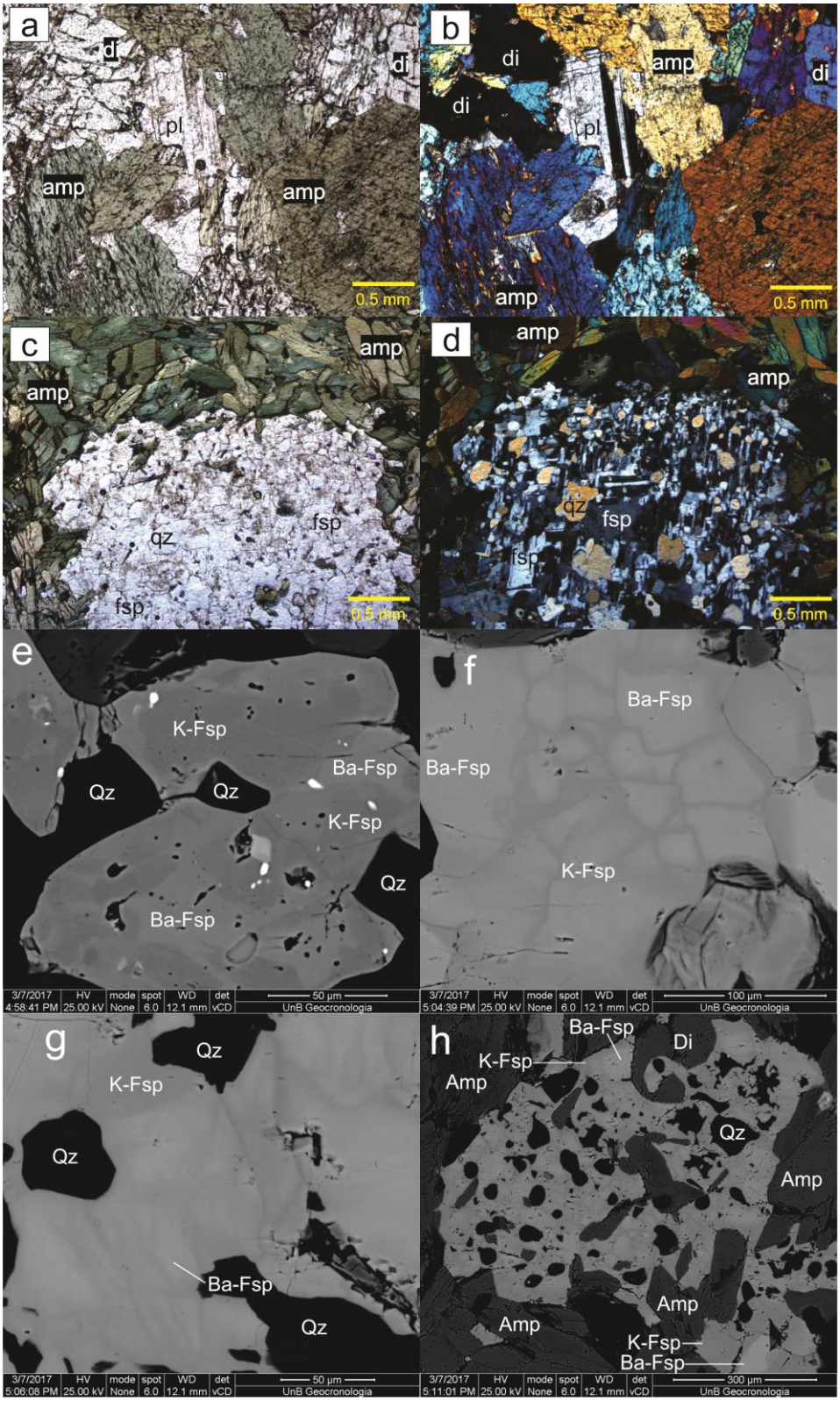

Figure 13. Feldspars plate, acquired by petrographic microscope (a-d) and SEM (e-h). a-b: Association between plagioclase, diopside and amphibole with an isotropic texture from the DAF association under parallel (a) and crossed (b) polarizers. c-d: Hornfels-like texture presenting a quartz-feldspar cluster comprised mainly by hyalophane bordered by amphibole crystals under parallel (c) and crossed (d) polarizers. e: Hyalophane grain showing Ba-rich domains being replaced by K-rich domains. This pattern of Ba-depletion/alkali-enrichment is associated with the transition from DAF to AF. f: Hyalophane grain presenting a homogeneous Ba-rich domain at the upper left portion (lighter), while to right a polygonal substitution occurs, resembling a blocky texture. This texture may be associated with the alteration happening along cleavage plans or with a cluster of altered crystals. g: Curvilinear banded alteration showing an orientation which could be related to deformational processes. h: Hyalophane crystal with quartz, diopside and amphibole inclusions, showing that they are coeval. Inside the feldspar grain, lighter areas represent domains richer in Ba, which are bordered by darker areas that are richer in alkalis.

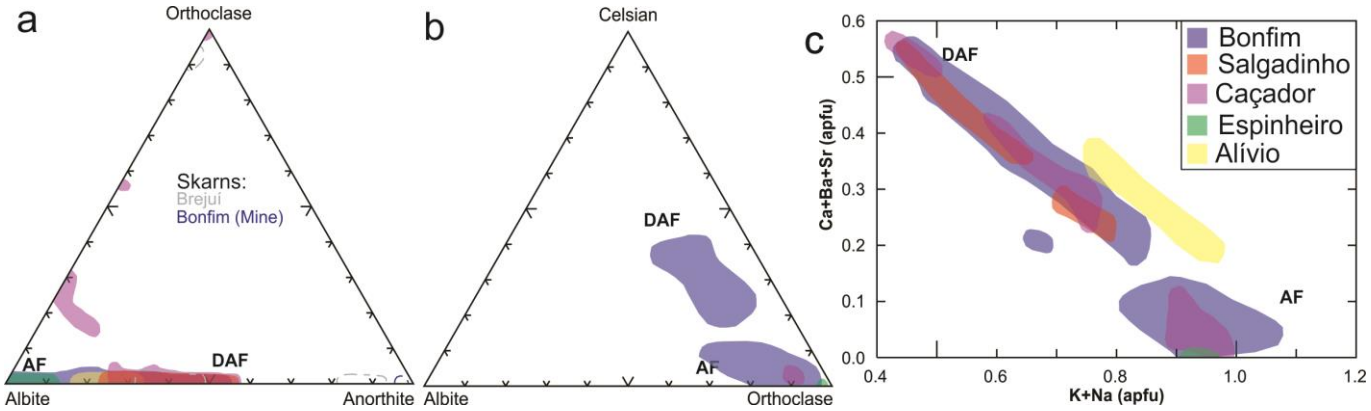

Figure 14. Feldspar diagrams, presenting data from this work and from the literature for Brejuí (Salim, 1993) and Bonfim (Souza Neto et al., 2008). a: Ab-An-Or diagram, presenting a wide chemical range for plagioclase and alkali-feldspar compositions. b: Ab-Or-Cn diagram, showing two distinct populations of Ba-feldspar. c: Monovalent vs Divalent cations binary diagram for feldspar compositions.

Under petrographic observations, K-feldspar tends to form crystals in a similar way to plagioclase. Both feldspars form along leucocratic undeformed bands. Hyalophane, on the other hand, may appear as fine-grained clusters together with plagioclase, K-feldspar and quartz, producing a texture that resembles a hornfelsic fabric (Figure 13). Another population of the Ba-feldspars is nearly indistinguishable from K-Feldspar, being identifiable only by microprobe and SEM analyses.

Basically, there are two Ba-feldspar populations in the analyzed samples. The first, from DAF, is composed of crystals with celsian molecular contents between 20% and 40% and that also have SrO contents approximately 0.5% (Figure 14). The formation of these high-Ba grains is texturally coeval with barite precipitation. The second Ba-feldspar population is correlated with the AF association and has lower Ba amounts ($<Cn_{20}$). In the AF association there is also a loss of Na accompanying the Ba depletion, which produces purer K-feldspar grains.

The monovalent vs divalent graphic from Figure 14 highlights the cationic exchanges that occur during the hydrothermal alteration stages. In DAF, Ca- and Ba-rich feldspars are more abundant, while in AF they become enriched in K and Na. Sr is an element that at DAF fills vacancies both in plagioclase and hyalophane.

Although the BR association, represented mainly by the Caçador occurrence, does not contain significant quantities of Ba-feldspars, it contains the only alkali-feldspars which are not nearly pure albite or pure K-feldspar, with data ranging from Ab_{80} to Ab_0 (Figure 14). Since this association is related to a narrower timespan compared to the DAF/AF associations, the huge discrepancies between the Na-K contents of the analyzed grains do not represent the chemical characteristics of this paragenesis. Instead, they may be explained by processes of alkali addition/depletion in an open system, which produced this broad interval. In the BR association, Ba-feldspars, when present, always have low barium contents (i.e., up to 5% of the celsian molecule).

5.2.4. Biotite

Biotite from the AF and BR associations of Bonfim and Caçador, respectively, were studied, totaling 42 spot analyses on 3 samples (Table 5). The results were recalculated following Tindle & Webb (1990), Tischendorf et al. (2004) and Nachit et al. (2005) based on 22 oxygens. No Li calculation was applied. The processed data was plotted in binary and ternary diagrams to indicate their chemical correlations with each paragenetic stage (Figure 15). The data was also compared with analyses from Salim (1993), with studied minerals from “biotite-hornblende skarns” from the Brejuí mine.

Biotite crystals are strongly oriented parallel to the main foliation trend. In the BR association, when occurring with amphibole, this mineral is texturally and chemically associated with amphibole from the AF association. Independent of the association where it occurs, lamellae are generally fine to medium grained, with coarser varieties appearing together with amphibole (Figures 8 and 9).

Biotite from the AF association in the Bonfim deposit show higher contents of Mg and Al, with the same content of K_2O of crystals from the BR association, represented by the Caçador occurrence. Grains from the BR association present higher contents of Fe and Ti, as well as K (apfu) contents closer to 2, which is the ideal theoretical value for this mineral. Discrete chemical discrepancies are seen between samples with "biotite-only" and "amphibole-biotite" associations, with the latter showing slightly enriched TiO_2 contents. When compared with the data presented by Salim (1993), the results for the "biotite-hornblende-skarns" of the Brejuí deposit present chemical similarities with the AF association in the K_2O-FeO-MgO diagram, while in the Al_2O_3-FeO-MgO they plot in the same area of the analyzed grains from the BR association.

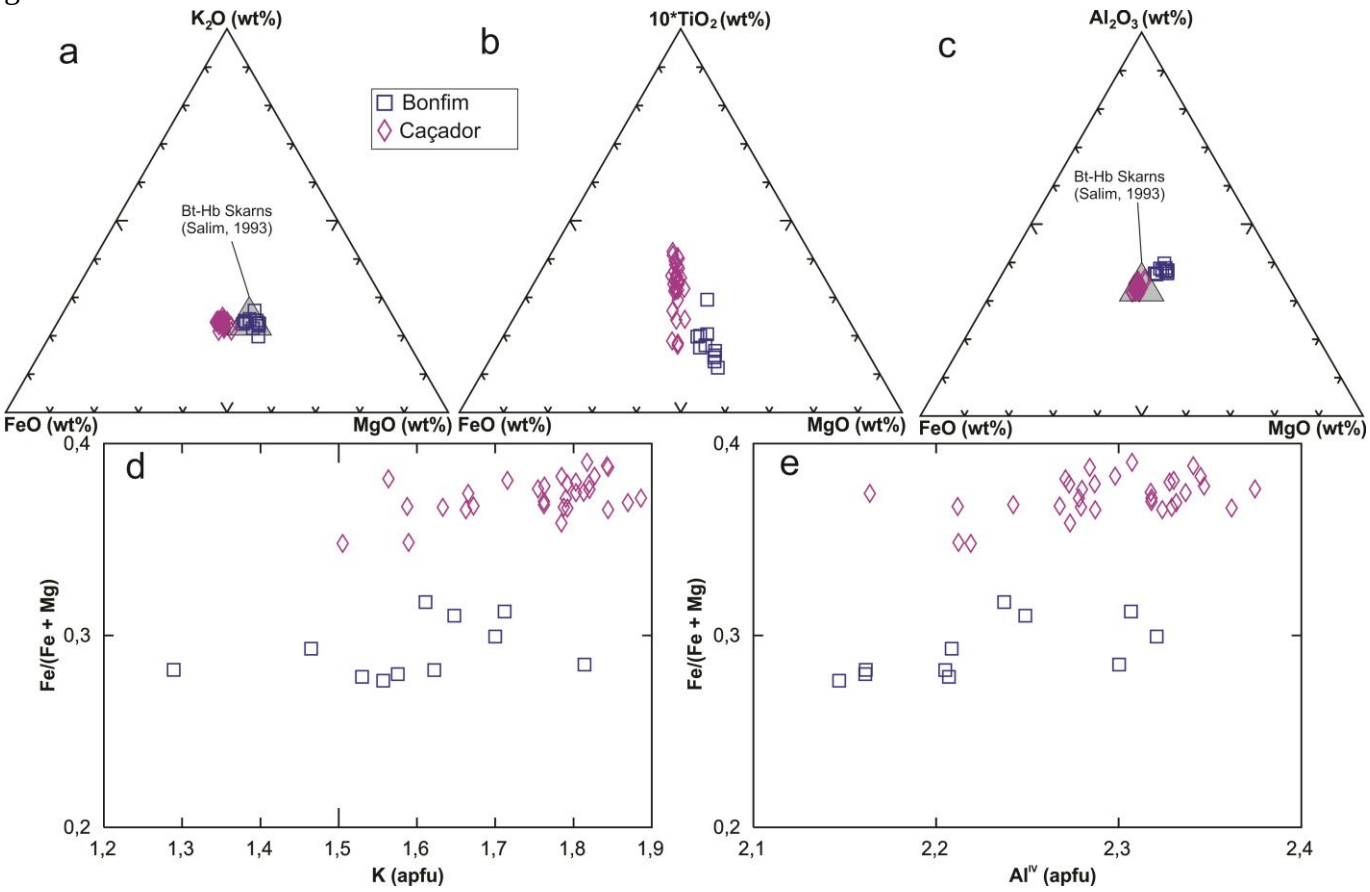

Figure 15. Biotite diagrams, also comparing with data from biotite-hornblende skarns from Brejuí (Salim, 1993). a-c: FeO vs MgO vs K_2O, FeO vs MgO vs 10*TiO_2 and FeO vs MgO vs Al_2O_3 ternary diagrams. d-e: K vs Fe/(Fe+Mg) and Al^{IV} vs Fe/(Fe+Mg) binary diagrams.

5.2.5. Epidote Group Minerals

A total of 89 spot analyses were done on 9 samples from the DAF/AF associations, including epidote, allanite and zoisite/clinozoisite (Table 6). The obtained data in oxides wt% was processed following the procedures of Ercit (2002) based on 12.5 oxygens. According to the binary diagram of Petrik et al. (1995) and Gieré & Sorensen (2004), the ratio Fe^{3+}/ Fe* was estimated and defined as 0.6 (Figure 16). Out of the 89 spot analyses, 41 studied grains were analyzed for their REE contents. The processed results were plotted on a ternary classification diagram and in spidergrams to better define the chemical characteristics between DAF and AF.

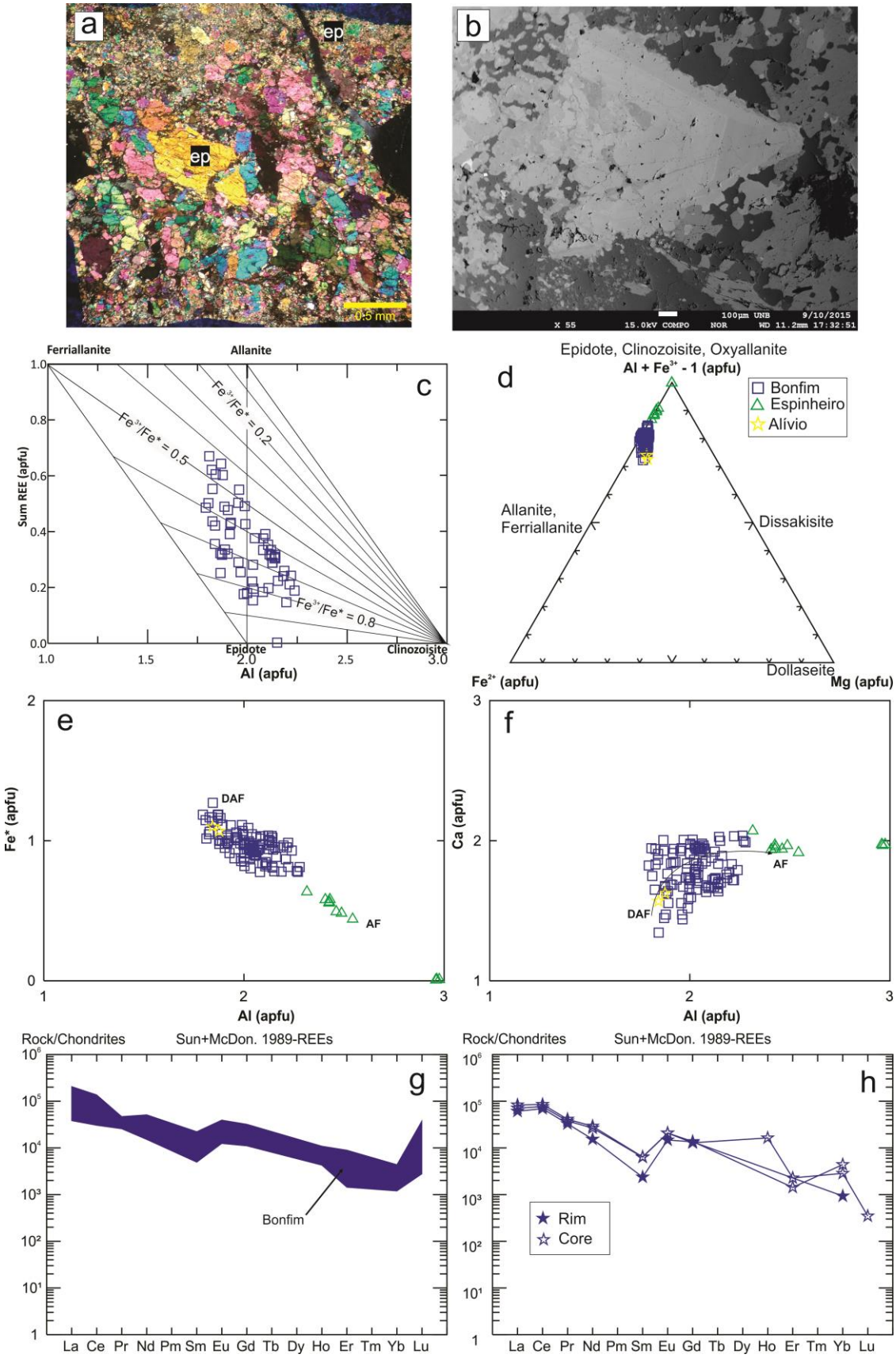

Figure 16. Epidote Group Minerals plate. a: Pure epidote veinlet showing coarse grains at the center and fine-grained crystals at the border. b: Sample from Bonfim showing a zoned allanite megacryst with consumed borders. Image acquired by the microprobe used in this work. c: Fe^{3+}/Fe^* ratio estimation diagram, proposed by Petrik et al. (1995). d: Epidote group minerals classification diagram. e: Al vs Fe* diagram, showing the cationic exchanges between these elements. f: Al vs Ca diagram. g-h: REE spidergrams normalized to the chondrite (Sun & McDonough, 1989) with all the data from the Bonfim deposit (g) and rim and core relations from the crystal shown in Figure 16b (h).

5.2.5.1. Epidote-Allanite

These minerals present a fairly continuous trend based on their total REE count and Fe^{2+}-Fe^{3+} cationic exchanges, so it is not always possible to discern one from the other. Petrographically, though, epidote appears to be associated with AF associations, while allanite is related to DAF associations (Figure 16).

Initially, in DAF, best represented by the Bonfim deposit, early allanite is produced, appearing either as coarse zoned crystals or as fine to medium grains that occur in association with diopside. It presents the lowest Ca and Al contents, along with the highest Fe amounts. This mineral is enriched in LREE, especially in Ce, also exhibiting slightly positive anomalies for Eu and Lu.

In the AF association, allanite is consumed, becoming poorer in Fe* and richer in Ca and Al compared to the crystals from DAF. Analyses on a single zoned grain suggest that the transition from DAF to AF depletes allanite in REE, especially Nd, Sm and Yb (Figure 16). Epidote is also produced during this AF, occuring as monomineralic late- to postkinematic discordant veinlets.

5.2.5.2. Zoisite-Clinozoisite

This mineral is restricted to the AF association, represented by samples from Espinheiro, and appearing as subhedral grains which are generally associated with the alteration of plagioclase or epidote. Chemically, it is easily distinguishable from epidote and allanite by an intense increase in Al and Ca and due to exhibiting the lowest Fe* contents (Figure 16).

5.2.6. Titanite

181 spot analyses in titanite on 24 samples from the DAF/AF associations in 3 deposits were made (Table 7). The results were processed following Harlov et al. (2006) and Deer et al. (2013) based on 1 Si. All FeO* data was converted to Fe_2O_3* and OH was estimated by the formula $OH=Al+Fe^{3+}-F$. Out of the 181 spot analyses, 97 were analyzed for their REE contents and minor elements (Nb, Ta, Y, Ba, Sr, Cr, V, Hf, Zr, U, Th and Pb). The processed data was plotted in binary and ternary diagrams and spidergrams to better characterize the DAF and AF associations (Figure 17).

Titanite appears in several different forms. In samples from the Salgadinho occurrence, it appears as medium-grained crystals oriented subparallel to the main foliation along with amphibole and magnetite. Grains from this location show a strong pleochroism, alternating from pale brown to reddish brown, which may be related to higher Ti and Nb contents (Figures 9 and 17). In other locations, it appears as abundant (i.e., modal compositions higher than 20%) fine-grained euhedral prismatic crystals which also follow the structural trend. Less frequent occurrences include associations with barite, zircon and allanite, which suggests that they are cogenetic. Titanite also occurs precipitated along the cleavage plans of amphibole grains, probably caused by cooling processes during the formation of the AF association, leaching Ca, Ti and Si from amphibole (Figure 17).

Chemical analyses point to the nearly stoichiometric character of this mineral, presenting almost the same contents of Ca, Ti and Si in apfu (Figure 17). Grains from DAF tend to present the highest contents of Fe^{3+}, Al and REE, as well as noteworthy contents of Nb, Ta and Y (up to 2.8 in oxide wt%). Using the classification diagram of Stepanov et al. (2012), the analyses plot in the titanite field. Crystals from AF present lower contents of Al, Fe^{3+}, REE, Nb, Ta and Y.

In REE spidergrams, when single analyses are overviewed, crystals present several discrepancies between them. When all titanite data are combined though, very clear patterns are observed, pointing to an almost flat REE fractionation pattern between LREE and HREE in the Bonfim samples, while in Salgadinho a slight enrichment in HREE occurs. In both cases, contents vary by more than one order of magnitude (Figure 17).

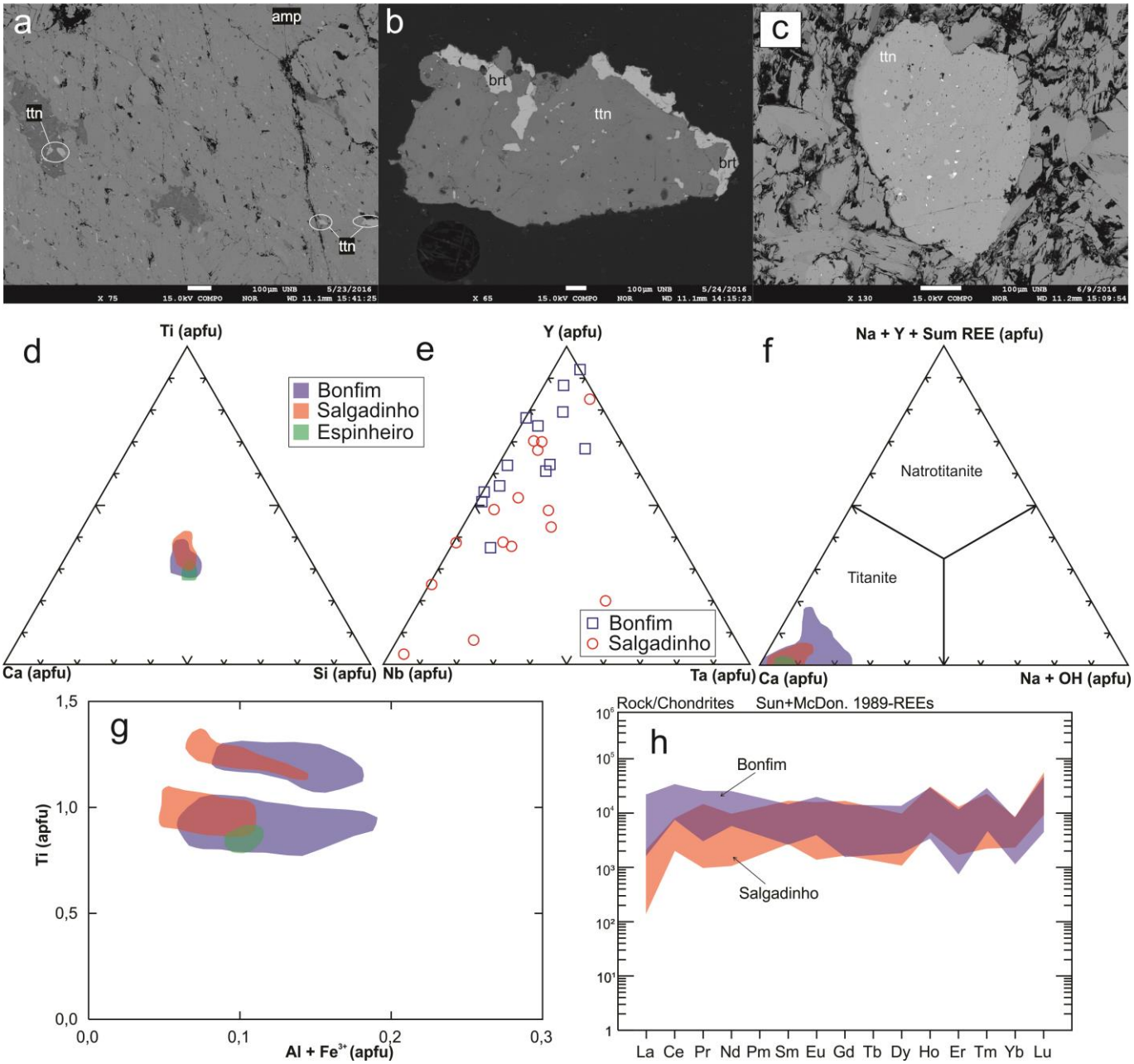

Figure 17. Titanite compositional diagrams and images acquired by the microprobe used in this work. All images are from Bonfim samples. a: Titanite grains distributed along the cleavage plans of an amphibole crystal. b: Barite inclusions in titanite, showing that these minerals were formed together. c: Titanite grain with zircon, allanite and quartz inclusions. d: Ca-Si-Ti diagram. e: Nb-Ta-Y diagram. f: Classification diagram of Stepanov et al. (2012). g: Al+Fe^{3+} vs Ti diagram. h: REE spidergram normalized to the chondrite (Sun & McDonough, 1989).

5.2.7. Apatite

63 apatite spot analyses on 9 samples from the DAF/AF associations in 3 deposits were done in order to better characterize their chemical signature according to each mineral association (Table 8). Out of the 63 spot analyses, 33 crystals were analyzed for their REE contents. The acquired data was recalculated following the procedures of Deer et al. (2013) based on 26 oxygens. The components OH and CO_3 were not measured, and OH was estimated by the formula OH=2-F-Cl. The results were then plotted in binary diagrams and spidergrams (Figure 18).

Apatite often occurs in association with amphibole, magnetite, barite, titanite and scheelite, appearing as subhedral fine to medium crystals. Crystals from the DAF assemblage are richer in Ca and OH and poorer in P and F, while the ones from AF are poorer in Ca and OH and richer in P and F (Figure

18). Similar to titanite, single analyses observed in REE spidergrams do not present a pattern, but when all data are combined, a slight fractionation trend showing an enrichment in HREE contents is observed, as well as positive anomalies of Pr, Ho and Lu. The majority of the analyzed grains are classified as hydroxyl-fluorapatites in the DAF assemblage and fluorapatites in AF rocks.

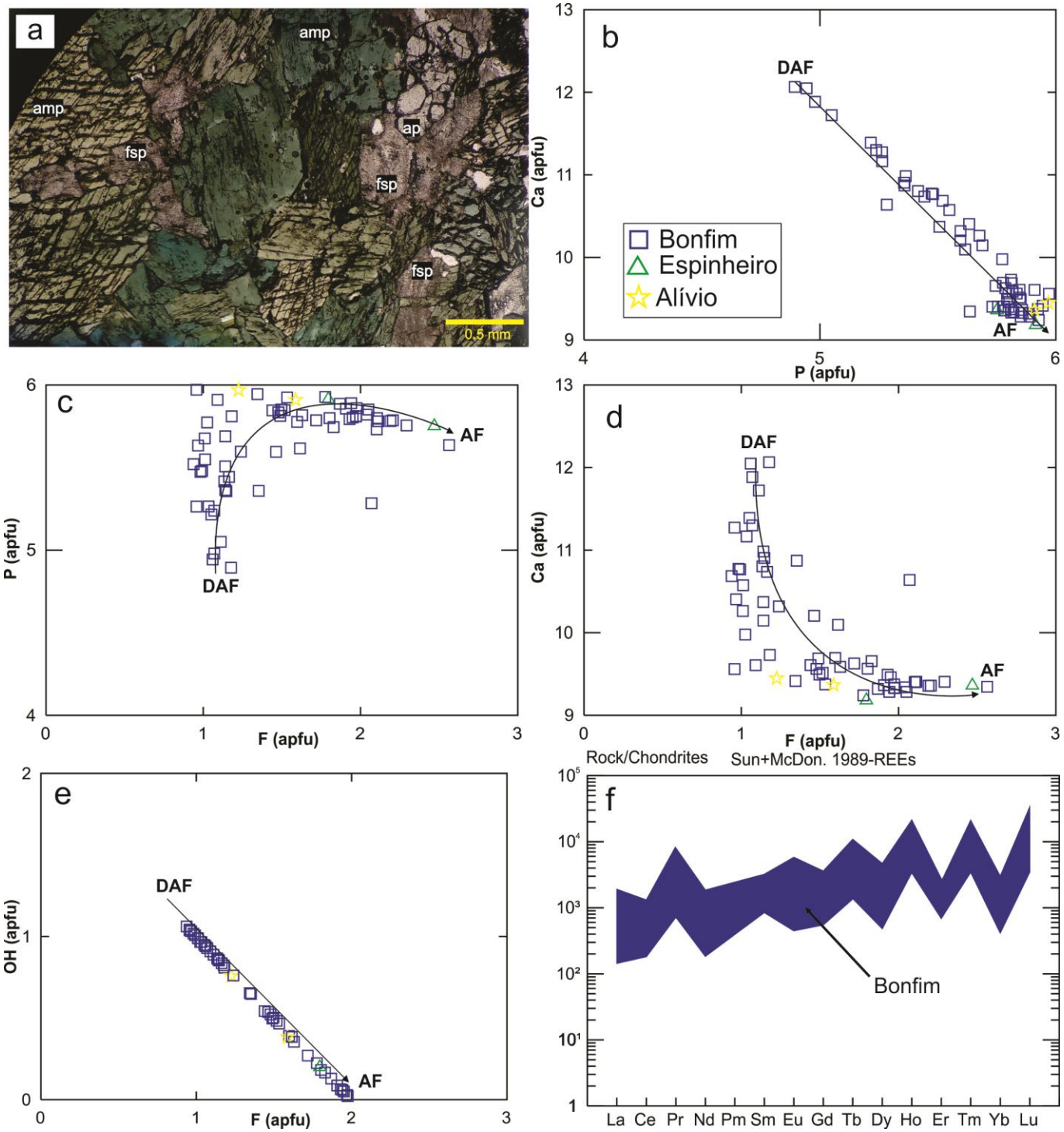

Figure 18. Apatite photomicrograph and diagrams. Paths from DAF to AF are indicated by arrows. a: Apatite crystal along with amphibole and altered feldspar grains. b-e: P vs Ca, F vs P, F vs Ca and F vs OH binary diagrams, showing the correlations between these elements. f: REE spidergram normalized to the chondrite (Sun & McDonough, 1989).

6. DISCUSSION

6.1. Differences Between the DAF/AF/BR Metasomatic Assemblages and the Stricto Sensu Skarns (MGDS)

The over 700 deposits and occurrences of the Seridó Fold Belt share many characteristics, allowing them to be integrated into a single W-Mo-endowed system. Occurrences related to the DAF/AF/BR associations described above and deposits linked with the mineralized garnet-diopside-skarns (to be referred as MGDS) may be distinguished based on mineralogical, textural, lithological and structural criteria.

A key aspect that concerns these different modalities are their controlling mechanisms. MGDS-type deposits are mostly associated with carbonate-bearing wallrocks, either in marbles from the Jucurutu Formation or along lithological boundaries between marbles and schists or gneisses. The MGDS occur as exoskarns, presenting a zoned alteration front between proximal marbles and distal wallrocks (Salim, 1993). A common feature among MGDS deposits is that the highest tungsten grades are concentrated along fold hinges (Souza Neto et al., 2008). Deposits and occurrences associated with the DAF/AF and BR associations, however, have no clear signs of interaction with carbonate rocks. They are aligned and connected by N20°E-trending lineaments, evidenced by remote sensing, geophysical and structural data, and altering granitic-gneissic basement wallrocks without carbonate rocks. They also commonly occur in association with pegmatitic injections that crosscut both DAF/AF/BR associations and wallrocks.

In this sense, wallrock composition is a determining factor for the formation of the DAF/AF/BR and MGDS types. Concerning the differences between marble and granitoid wallrocks, the former represents more reactive, Ca±Mg±Fe-rich rocks. Their association with Al-rich rocks, such as biotite-schists from the Seridó Formation, could be responsible for the formation of metasomatic garnet, since Al is an element with generally low mobility. On the other hand, garnet is absent in the DAF/AF/BR associations, and amphibole is the most abundant mineral phase. They occur along plutonic felsic wallrocks, which in turn are Si-, alkali- and REE-rich, possibly having contributed to the diverse calc-silicate mineral assemblage of the DAF, AF and BR associations. These mineralogical differences between the MGDS and the mineral associations may have implications for their formation conditions, such as H_2O and Al availability, which could also be a reflex of the wallrock composition. Chemical differences between same minerals from distinct deposits/occurrences may also be influenced by wallrock compositions, affecting Mg-Fe and K-Na chemical exchanges and Ba, P and REE contents in the minerals.

The MGDS have estimated formation depths between 10 to 15 km at 400 to 580°C and 2 to 4 kbars (Souza Neto et al., 2008 and references therein). Similar P-T conditions are indicated for pegmatites crystallization, set between 580°C and 400°C ca. 3.8 kbar by fluid inclusion studies (Beurlen et al., 2001). The spatial association between the DAF/AF/BR associations with both MGDS and pegmatitic rocks suggests that, apart from their distal character in relation to the main mineralization, the DAF/AF/BR associations were formed at the same crustal level and at similar temperatures as the MGDS and pegmatites.

6.2. Processes that Led to the Formation of the DAF/AF/BR Associations

Both DAF/AF/BR and MGDS deposits were formed by a long-lived magmatic-hydrothermal system that precipitated metasomatic minerals at continuously changing pressure, temperature, pH, water activity and oxygen fugacity conditions. In conformity with W-skarn genetic models (Newberry & Swanson, 1986; Meinert et al., 2005), the Late Neoproterozoic Brasiliano Cycle promoted thick crustal conditions for this part of the Borborema Province, reaching Curie depths higher than 30 km (Correa et al., 2016). This Neoproterozoic orogenic event also developed and/or reactivated deep regional-scale shear zones, where magmas and W-Mo-bearing metasomatic fluids migrated and ascended through the thickened crust.

Throughout the Seridó Mineral Province, several granitoid intrusions have been suggested to have acted as a source for the MGDS formation, but these assumptions usually present geochronological

inconsistencies (e.g., the Acari Pluton). Geochronological data from Hollanda et al. (2017) and Ruiz et al. (2018) indicate that postmetamorphic peak plutons (i.e., younger than 575 Ma) represent the potential sources for W-enriched fluids. Hence, tungsten mineralization in the Seridó Mineral Province was probably derived from a deeply hidden reduced magma formed in a late- to postcollisional setting during the latest stages of the Late Neoproterozoic Brasiliano Event, possibly coeval with rocks from the Borborema Pegmatite Province, which present with ages in the 550 Ma to 510 Ma interval (Beurlen et al., 2014; Hollanda et al., 2017; Figure 19). Since most deposits and occurrences are more closely linked to structures than with specific plutons, the W±Mo-enriched hydrothermal fluid may have been formed from more than one source magma. Although pegmatites did not necessarily add W±Mo to the system, these rocks are acknowledged for acting as suppliers of volatiles (Goldfarb et al., 2005; Rasmussen et al., 2011). In addition, the formation of metasomatic amphibole and diopside-epidote-quartz clusters in the pegmatite from Alívio (Figure 7) and the precipitation of molybdenite in the pegmatite from Caçador (Figure 8) also suggest that they are related to the mineralization. Although pegmatites appear to be younger by crosscutting relationships, they may have contributed to the ore-forming processes, being either contemporaneous with the mineralization or by promoting W-Mo remobilization, with a late- to postmineralization character.

The produced magmatic-hydrothermal solution started to accumulate in the borders and/or cupolas of the igneous intrusions and ascended through the thickened crust along the deep and subvertical Late Neoproterozoic Brasiliano Cycle shear zone system. The magmatic-hydrothermal fluids interacted with different wallrocks, but consistently developed similar hydrothermal alteration mineral associations in several locations (Figure 19). In the Bonfim deposit, both DAF/AF and BR associations were formed in the Archean granitic basement. The same pattern occurred in Salgadinho, Recanto and Alívio, with one or all associations being formed in Paleoproterozoic granites, gneisses and schists from the Caicó Complex. At Alívio, the alteration also occurred in a Late Neoproterozoic-Ediacaran pegmatitic rock, being the only case that could potentially represent an endoskarn (Figure 7).

Along these structures, the mineralizing fluid interacted with the wallrocks, producing several metasomatic haloes and stages in a continuously evolving system. In distal environments in relation to the skarns, DAF/AF and BR associations were produced, defined as the root zones of the system. These rocks are generally structurally controlled, occurring as lenticular bodies aligned in parallel to the regional N-N20°E trend. In proximal areas in relation to the main mineralization the interaction between the hydrothermal solution and sedimentary (mostly carbonate) rocks promoted the development of MGDS-type skarns, which commonly occur along lithological boundaries, as lenses, as continuous stratiform domains, and controlled by structures. The DAF/AF, BR and MGDS types are synchronous and cogenetic, having been formed by similar mechanisms but under different physicochemical and elemental mobility conditions (Figure 19).

At the Bonfim deposit, a clear spatial association between the DAF/AF and BR and the MGDS is verified in the lowest levels of the underground mine and in drill hole samples, showing that the DAF/AF and BR associations occur beneath the MGDS. At the other studied locations, there is no direct evidence that suggests that the DAF/AF and BR associations are the root zones of the MGDS. The root zones interpretation is extended to the other studied occurrences and deposits due to the similarities between the rocks, concerning their mineral assemblages, as well as textural and compositional aspects. The absence of MGDS in the northeastern part of the Seridó Fold Belt, where Salgadinho, Alívio, Caçador and Recanto are located (Figure 2), may be explained by the following factors: i) MGDS-type deposits were formed during the Late Neoproterozoic Brasiliano Cycle but were eroded, exposing the Paleoproterozoic basement rocks of the Caicó Complex along with the DAF, AF and BR associations, or ii) there were no carbonate rocks near these locations, and hence the MGDS were not formed. Concerning this second hypothesis, the interaction between hydrothermal fluids and highly reactive carbonate rocks represent an efficient process for skarns, leading to higher ore contents and concentrations. The root zones, on the other hand, represent a less efficient case, where a W-endowed hydrothermal fluid interacted with granitic wallrocks, producing a disseminated mineralization pattern. In this sense, Salgadinho, Alívio, Caçador and Recanto may represent a “preskarn” assemblage that never reached carbonate wallrocks.

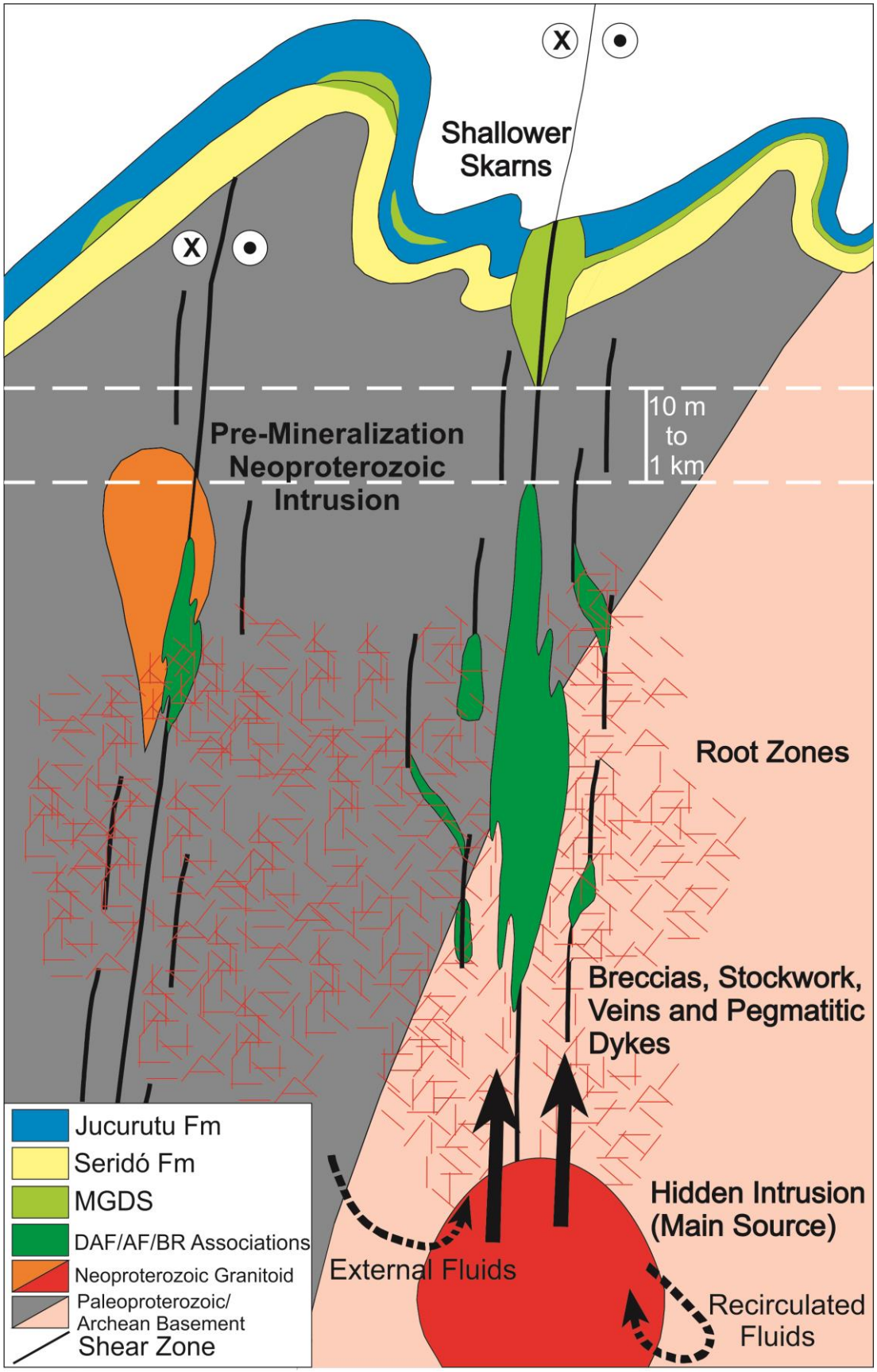

Figure 19. Metallogenetic model proposed for the studied mineral associations and skarns of the Seridó Mineral Province. Magmatic-derived hydrothermal fluids from a hidden source migrated along deep, subvertical and active shear zones that crosscut both basement and supracrustal wallrocks. At distal locations in relation to the skarns, the root zones of the system were developed, comprising rocks of the DAF/AF/BR associations. At proximal areas, the interaction between the hydrothermal solution with metasedimentary rocks developed the MGDS.

The DAF association corresponds to a mineral assemblage that was formed in the beginning of the hydrothermal alteration process. The AF association, on the other hand, is related to the latest stages of the metasomatic event. The transition from DAF to AF is verified by petrographic observations, SEM imaging and microprobe analyses.

The DAF association is characterized by higher temperature conditions, inferred from the mineralogical assemblage associated with this stage, represented by diopside, andesine-labradorite, magnesiohornblende-pargasite, K-feldspar, hyalophane, allanite, magnetite, apatite and barite. Chemically, this phase is represented by an enrichment in Ca, Mg, Fe, Na, K, Ba and REE.

The AF association presents a mineralogical association composed of primarily magnesiohornblende-tremolite, albite-oligoclase, epidote, zoisite/clinozoisite, quartz, muscovite/sericite, chlorite, biotite, molybdenite and scheelite. In the BR association, where some minerals are compositionally similar to the AF association, the paragenesis is composed mainly of biotite, magnesiohornblende, albite-oligoclase, K-feldspar, quartz, scheelite and molybdenite. Both AF and BR associations appear to have occurred in the final stages of the mineralization event, which correspond to the period of highest W-Mo deposition. These parageneses are indicative of lower temperature conditions. Regardless of the hydrothermal mineralogical association in which they occur, both AF and BR associations are chemically characterized by an enrichment in Na, K, Si, W and Mo.

6.3. The Origin of Barium-Enriched Minerals in the Metasomatic System

In a mafic magma, the natural Bowen's continuous reaction series implies the formation of calcic plagioclase, among other minerals (Bowen, 1928). In addition to Ca, Sr and Eu also present high partition coefficient values in these conditions, and hence are commonly substituted for Ca in Ca-rich plagioclase. Another element which presents somewhat similar chemical properties (i.e., ionic radius and charge) to Sr and Ca is Ba, but it is generally incompatible in this environment (Rollinson, 1993).

In felsic magmas, on the other hand, plagioclase becomes increasingly richer in Na, forming a complete solid solution between pure albite and pure K-feldspar at high temperatures. In this totally different context, Sr and Ca are not as compatible as in the first example, and Ba is much more available, although still incompatible for most minerals, with the exception of alkali-feldspars (Winter, 2010). Barium-feldspars, such as celsian and hyalophane, are very rare in this environment, being more commonly associated with ferromanganese BIFs and other sedimentary-derived Cu-Pb-Zn deposits (McSwiggen et al., 1994).

Since most available Ba concentrates are in the liquid phase due to their somewhat incompatible character in felsic magma, a deep granitic source may have exsolved reduced Ba-rich hydrothermal fluids during the high temperature alteration. Then, changes in the hydrothermal solution REDOX state, which could be caused by fluid mixing and/or reaction with wallrocks, would lead to the precipitation of sulfate (barite) and Fe^{3+}-bearing minerals (magnetite and epidote-allanite) under more oxidizing conditions.

At this time, the metasomatic alteration promoted a chemical partitioning of the system for feldspars, with the associations Ca-Na-K and Ba-Na-K. The first group is characterized by pure K-feldspar and Ca-rich plagioclase (i.e., up to An_{56}), while the second is constituted by K-feldspar and hyalophane, with up to 40% of celsian molecular contents. Both systems present an association with Sr, containing more than 1% SrO in some analyses. In this way, the high temperature alteration led to chemical substitutions between Ca, Na, K and Ba in the feldspar assemblage. When barite is considered, the high temperature alteration also exhibits an association between barium and sulfur.

The low temperature alteration is mainly characterized by Ba and Ca depletions, enriching the feldspar assemblage in K and Na independently of the chemical association. The alteration occurred mainly as substitutions, as evidenced by SEM images, where Ba-rich nuclei are bordered by Na- and/or K-rich domains inside the same feldspar crystal (Figure 13). This process may appear along irregular polygonal textures, forming straight planar boundaries, while in other cases it occurs as irregular curvilinear bands. Regardless of their form, they always show that the Ba-rich areas are older, associated with high temperature alterations and that the K/Na-rich domains are younger, being associated with low temperature alterations. A complementary observation is that divalent cations, such as Ca, Sr and Ba, are

more associated with the high temperature alteration, while monovalent cations (i.e., alkalis) are representative of the low temperature alteration.

6.4. Correlations with the Root Zones of other Ore Deposit Types

Magmatic-hydrothermal systems, which include Porphyry, IOCG, RIRGS, Skarn and Greisen deposits, are formed in distinct tectonic settings, pressure, temperature, pH and REDOX conditions (Pirajno, 2009). At depth, though, in their root zones, commonly Ca, Na and/or Na-Ca hydrothermal alteration haloes are developed. In the root zones of the Yerington porphyry deposit, Carten (1986) reports that: i) Sodic-calcic alteration is coeval with the formation of the potassic halo; ii) the main hydrothermal reactions are the replacement of primary K-feldspar and biotite by oligoclase and actinolite, respectively. Stable isotope studies on a Na-Ca halo from the Cloncurry District by Mark & Foster (2000) suggest that: i) the hydrothermal fluid that formed this halo was magmatic-derived,; ii) the Na-Ca alteration occurred between 450°C and 550°C. Richards & Mumin (2013) propose several different formation conditions for S-rich Cu±Mo±Au porphyry and S-poor IOCG deposits, but show that at their deepest portions they tend to form similar Na±Ca hydrothermal alteration haloes. This work also reports the formation of similar mineral associations in a regional-scale skarn system.

One of the main divergent aspects concerning magmatic-hydrothermal deposits are the classification criteria for their metasomatic rocks: Some haloes are defined based on their chemistry (e.g., Sodic±calcic, potassic); others follow associations of index minerals (e.g., propylitic, argilic); some are based on temporal relationships (e.g., metasomatic prograde and retrograde stages); and some are classified based upon alteration processes (e.g., hydrolytic, chloritization). In this sense, similar alteration processes are commonly treated as different mechanisms. For example, an albitization alteration may be a synonym for a sodic halo; and a sericitic halo may refer to hydrolytic or retrograde alteration. Comparisons between the hydrothermal alteration haloes of several magmatic-hydrothermal deposits are listed in Table 9.

Table 9. General comparisons between the main alteration features of Porphyry, IOCG and skarn deposits.

Description	Main Minerals	Spatial Distribution	Corresponding Metasomatism		
			Pophyry	IOCG	Skarn
Early, high temperature alteration with Na-Ca metasomatism	Cpx-Amp-Pl±Scp±Grt	Distal	Na±Ca	Na±Ca	DAF/AF Skarnoid
Fe, Mg, Na, CO_2 and H_2O metasomatism	Ep-Cal-Chl-Ab	Distal to Proximal	Propylitic	Propylitic	Prograde
High temperature paragenesis, K metasomatism	K-Fsp±Bt	Proximal	K Alteration	K Alteration	Prograde
Late-stage, low temperature, K alteration	Bt	Distal			BR/Retrograde
Late-stage, low temperature, H_2O alteration	Ser-Qz±Ms	Distal	Sericitic	Chloritization Hydrolytic	Retrograde

In this paper, due to the chemical nature of the parageneses of each hydrothermal association, the investigated DAF association may be interpreted, in fact, to a calcic or Ca-Ba halo due to the calc-silicate mineral assemblage associated with barite and hyalophane. The AF association, due to the presence of albite and the calc-silicate mineral assemblage, may be interpreted as a sodic-calcic halo. Finally, the BR association may be interpreted as a potassic (K) halo due to the presence of biotite and K-feldspar. These three associations are more or less similar to the hydrothermal zoning of Porphyry and IOCG deposits, which commonly present calcic, sodic-calcic and potassic haloes (Seedorff et al., 2005; Williams et al., 2005; Table 9).

A second interpretation is more closely linked to the typical classification of skarn deposits (Robb, 2005; Meinert et al., 2005). When the DAF and AF associations are seen as part of the same evolving system, the DAF association may be linked to a prograde stage, while the AF may be interpreted as a retrograde phase. Chronologically, the BR association appears to be coeval with the retrograde stage.

We state that the classification of the DAF, AF and BR associations concerns similar processes studied from different perspectives. The studied root zones from the Seridó Mineral Province share chemical and mineralogical characteristics with the root zones of Pophyry, IOCG and RIRGS systems, which are usually hidden (Hart, 2007; Seedorff et al., 2008; Groves et al., 2010). The Ca-Ba, Na-Ca and K hydrothermal alteration haloes at Seridó are representatives of "pre-skarn" assemblages, in the sense that they are part of the skarn-formation system, but cannot be classified as skarns. These haloes were formed from a more pure (i.e., unmixed) magmatic-hydrothermal solution, less influenced by carbonate wallrocks. The distal, deeper and less mixed character of the root zones may explain why metasomatic calc-silicate and K-enriched assemblages are developed along such diverse environments. Furthermore, classification diagrams of whole-rock geochemistry, mineral chemistry, trace elements and stable isotopes analyses generally present a great overlap between the fields of magmatic-hydrothermal deposits (Meinert et al., 2005; Dare et al., 2014; Nadoll et al., 2014; Nadoll et al., 2015; Canil et al., 2016).

7. CONCLUSIONS

The presented work, with its field, petrographic and mineral chemistry data and interpretations, in contrast with the previous mafic/metamafic rocks, hornblende±clinopyroxene±biotite-skarns and calc-silicate gneisses classifications, suggests a new approach for the whole Seridó Mineral Province metallogenetic system. When the poorly studied occurrences of this paper are linked with the better-known MGDS deposits and occurrences, several implications may be highlighted:

- The distribution of chemical elements and metasomatic processes in distal locations from the classic skarns of the area are documented, defining the root zones of the W-Mo skarn system of the Seridó Mineral Province.
- The whole system is characterized by multiple mineral assemblages. Earlier, higher temperature processes formed the DAF association, with diopside, amphibole and Ca-Ba-rich feldspars as the most common minerals. Later, cooling of the system produced the AF association, which altered the previous DAF association. The lower temperature alteration also led to the formation of the nearly monomineralic BR association.
- Chemically, the high temperature DAF association is characterized by the formation of REE-rich minerals, such as allanite-epidote, titanite and apatite. It is also represented by barium-bearing minerals, such as hyalophane and barite. The low temperature AF and BR associations, on the contrary, are characterized by the leaching of these previously mentioned elements and are more closely associated with the scheelite precipitation process.
- In the literature, there is not always a direct association between Late Neoproterozoic granitoids and MGDS deposits or occurrences in the Seridó Mineral Province. As observed in satellite and geophysical immagery, as well as during field work, the mineralization in the root zones is strongly linked to structures, and its source may come from a deeper intrusion or may have more than one source. Regardless of their origin, the observed alteration features in some granitic and pegmatitic rocks record the beginning of these hydrothermal processes.
- Pegmatitic rocks generally present a spatial association with the mineralization. These injections could have acted as tungsten, molybdenum or barium sources and/or have supplied fluids to the system.
- Finally, there are several similarities between the root zones of the Seridó Mineral Province and the hydrothermal alteration haloes of other deposit classes, such as IOCG, Porphyry and RIRGS. While still respecting the genetic differences between each deposit type (e.g., tectonic setting, depth, physicochemical conditions, etc.), the development of similar alteration haloes in distinct magmatic-hydrothermal systems may be explained through the study of root zones.

8. SUPPLEMENTARY MATERIAL

Table 2. Selected Pyroxene Microprobe Analyses.

Stage	DAF			AF		
SiO2	53,301	53,780	53,411	52,609	51,842	52,409
TiO2	0,068	0,101	0,080	0,000	0,118	0,000
Al2O3	0,517	0,844	0,849	1,011	1,017	1,133
FeO*	5,054	5,277	5,132	11,066	11,110	12,197
MnO	0,392	0,255	0,287	0,451	0,597	0,360
MgO	15,889	15,597	15,550	11,441	11,411	10,728
CaO	24,375	24,362	24,014	23,174	22,855	22,993
Na2O	0,253	0,396	0,401	0,462	0,559	0,678
K2O	0,018	0,000	0,000	0,035	0,000	0,046
Total	99,867	100,612	99,724	100,249	99,509	100,544
Si	1,973	1,991	1,977	1,948	1,919	1,940
Ti	0,000	0,003	0,002	0,000	0,003	0,000
Al	0,018	0,037	0,037	0,044	0,044	0,049
Fe*	0,174	0,163	0,159	0,343	0,344	0,378
Mn	0,007	0,008	0,009	0,014	0,019	0,011
Mg	0,853	0,861	0,858	0,631	0,630	0,592
Ca	0,960	0,966	0,953	0,919	0,907	0,912
Na	0,015	0,028	0,029	0,033	0,040	0,049
K	0,000	0,000	0,000	0,002	0,000	0,002
Wo	47,977	48,317	47,626	45,960	45,328	45,601
En	42,647	43,039	42,909	31,571	31,488	29,603
Fs	8,686	8,169	7,944	17,130	17,199	18,881
Di	82,552	83,396	83,638	63,898	63,455	60,355
Hd	16,813	15,829	15,485	34,671	34,659	38,495
Jo	0,634	0,775	0,877	1,431	1,886	1,151

Table 3. Selected Amphibole Microprobe Analyses. N.A. stands for "Not Analyzed".

Stage	**DAF**			**AF**			**BR**		
SiO2	43,093	41,862	44,351	46,915	47,431	55,026	48,387	46,996	50,051
TiO2	0,842	0,792	0,528	0,886	0,697	0,117	0,000	0,421	0,398
Al2O3	9,984	10,409	9,514	8,103	8,316	1,658	6,963	8,175	5,441
MnO	0,243	0,556	0,271	0,242	0,328	0,600	0,695	0,298	0,371
FeO*	20,023	21,228	18,953	13,078	13,320	12,439	15,315	15,046	12,746
MgO	9,489	8,670	10,105	13,711	14,251	15,879	13,123	13,078	14,953
CaO	11,691	11,605	11,735	11,699	12,267	12,351	12,242	11,965	11,942
Na2O	1,540	1,311	1,580	1,216	1,100	0,326	0,803	1,014	0,627
K2O	1,116	1,305	1,098	0,858	0,565	0,035	0,411	0,706	0,403
F	0,043	N.A.	0,022	0,020	0,063	0,000	N.A.	0,182	0,175
Cl	0,044	0,023	0,025	0,111	0,054	0,000	0,000	0,011	0,004
Total	98,108	97,761	98,182	96,839	98,392	98,431	97,939	97,892	97,111
T Site									
Si	6,496	6,359	6,647	6,911	6,824	7,834	7,045	6,860	7,252
Al	1,504	1,641	1,353	1,087	1,176	0,166	0,955	1,140	0,748
Ti									
Fe3+									
C Site									
Ti	0,095	0,091	0,060	0,098	0,075	0,013		0,046	0,043
Al	0,269	0,223	0,327	0,320	0,234	0,112	0,240	0,266	0,181
Mn3+									
Fe3+	0,499	0,712	0,361	0,162	0,455	0,068	0,494	0,489	0,366
Mn2+		0,020				0,024	0,047		
Fe2+	2,004	1,985	1,994	1,386	1,137	1,413	1,371	1,324	1,156
Mg	2,132	1,963	2,258	3,011	3,057	3,370	2,848	2,846	3,230
B Site									
Mn2+	0,031	0,051	0,034	0,030	0,040	0,048	0,039	0,037	0,046
Fe2+	0,021		0,020	0,063	0,011			0,023	0,023
Mg									
Ca	1,888	1,889	1,884	1,847	1,891	1,884	1,910	1,871	1,854
Na	0,060	0,059	0,062	0,061	0,058	0,068	0,045	0,069	0,078
A Site									
Ca									
Na	0,390	0,327	0,397	0,287	0,249	0,022	0,182	0,218	0,098
K	0,215	0,253	0,210	0,161	0,104	0,006	0,076	0,131	0,074
W Site									
OH	1,968	1,994	1,983	1,963	1,958	2,000	2,000	1,913	1,919
F	0,020	N.A.	0,010	0,009	0,029		N.A.	0,084	0,080
Cl	0,011	0,006	0,006	0,028	0,013			0,003	0,001

Table 4. Selected Feldspar Microprobe Analyses. N.A. stands for "Not Analyzed".

Stage	**DAF**			**AF**			**BR**		
Mineral	**PL**	**KFS**	**Ba-FSP**	**PL**	**KFS**	**Ba-FSP**	**PL**	**KFS**	**Ba-FSP**
SiO2	53,817	63,037	50,556	63,615	64,039	48,989	63,366	66,775	65,204
TiO2	0,044	0,000	0,047	0,000	0,000	0,000	0,060	0,000	0,000
Al2O3	29,752	17,667	22,573	22,336	18,625	24,752	23,801	19,006	18,655
FeO*	0,079	0,055	0,229	0,029	0,000	0,035	0,345	0,062	0,001
MnO	0,006	N.A.	0,000	0,022	0,029	0,000	0,000	0,000	0,034
MgO	0,013	0,004	0,016	0,014	0,000	0,000	0,107	0,033	0,004
CaO	11,499	0,028	0,109	3,329	0,000	0,046	0,656	0,319	0,015
BaO	N.A.	1,713	16,697	0,000	1,694	17,488	0,000	0,123	1,388
SrO	N.A.	0,052	0,778	0,211	N.A.	1,394	N.A.	N.A.	N.A.
Na2O	5,045	0,320	1,856	9,312	1,011	1,690	7,912	4,956	0,856
K2O	0,120	15,767	6,648	0,102	14,996	7,234	3,605	9,742	15,672
Total	100,375	98,643	99,509	99,034	100,405	101,628	99,876	101,041	101,829
Si	2,407	3,211	2,575	2,888	2,864	2,708	2,834	2,986	2,916
Ti	0,001	0,000	0,002	0,000	0,000	0,000	0,002	0,000	0,000
Al	1,568	1,061	1,355	1,195	0,982	1,412	1,254	1,002	0,983
Fe2	0,003	0,002	0,010	0,001	0,000	0,000	0,013	0,002	0,000
Mn	0,000	N.A.	0,000	0,001	0,001	0,000	0,000	0,000	0,001
Mg	0,001	0,000	0,001	0,001	0,000	0,001	0,007	0,002	0,000
Ca	0,551	0,002	0,006	0,162	0,000	0,001	0,031	0,015	0,001
Ba	N.A.	0,034	0,333	0,000	0,030	0,250	0,000	0,002	0,024
Sr	N.A.	0,002	0,023	0,006	N.A.	0,018	N.A.	N.A.	N.A.
Na	0,437	0,032	0,183	0,820	0,088	0,188	0,686	0,430	0,074
K	0,007	1,025	0,432	0,006	0,855	0,596	0,206	0,556	0,894
An	55,360	-	-	16,398	-	-	3,405	1,527	-
Ab	43,952	2,898	17,719	83,004	9,010	18,195	74,315	42,938	7,477
Or	0,688	93,966	45,728	0,598	87,938	57,628	22,280	55,535	90,073
Cn	-	2,694	36,929	-	2,450	18,687	-	-	2,925

Table 5. Selected Biotite Microprobe Analyses.

Sample	DAF/AF		BR			
			Biotite-only		Amphibole-Biotite	
SiO2	39,215	38,989	38,143	37,493	37,933	38,436
TiO2	0,475	0,530	1,406	1,439	2,229	2,120
Al2O3	16,640	16,406	16,060	16,034	14,769	14,945
FeO	11,119	11,301	15,596	15,656	16,395	16,042
MnO	0,185	0,238	0,319	0,227	0,308	0,336
MgO	16,057	16,436	14,624	14,559	14,484	15,565
CaO	0,083	0,148	0,028	0,072	0,000	0,024
Na2O	0,326	0,813	0,082	0,088	0,114	0,105
K2O	8,296	8,073	9,521	9,169	9,684	9,579
BaO	0,273	0,097	0,037	0,144	0,071	0,177
F	0,323	0,333	0,489	0,364	0,540	0,711
Cl	0,027	0,086	0,009	0,031	0,000	0,009
Total	93,019	93,450	96,314	95,276	96,527	98,049
Si	5,839	5,793	5,663	5,625	5,659	5,638
Ti	0,053	0,059	0,157	0,162	0,250	0,234
Al iv	2,161	2,207	2,337	2,375	2,341	2,362
Al vi	0,759	0,666	0,474	0,461	0,256	0,222
Fe2+	1,385	1,404	1,937	1,965	2,046	1,968
Mn	0,023	0,030	0,040	0,029	0,039	0,042
Mg	3,564	3,640	3,237	3,256	3,221	3,404
Ca	0,013	0,024	0,004	0,012	0,000	0,004
Na	0,094	0,234	0,024	0,026	0,033	0,030
K	1,576	1,530	1,803	1,755	1,843	1,792
Ba	0,016	0,006	0,002	0,008	0,004	0,010
F	0,152	0,156	0,230	0,173	0,255	0,330
Cl	0,007	0,022	0,002	0,008	0,000	0,002
OH*	3,841	3,822	3,768	3,819	3,745	3,668
TOTAL	19,483	19,593	19,688	19,682	19,721	19,737
Y total	5,784	5,800	5,854	5,882	5,841	5,901
X total	1,699	1,793	1,833	1,800	1,880	1,836
Al total	2,920	2,873	2,811	2,836	2,597	2,584
Fe/Fe+Mg	0,280	0,278	0,374	0,376	0,388	0,366

Table 6. Selected Epidote Group Minerals Microprobe Analyses. N.A. stands for "Not Analyzed".

Stage	DAF		AF	
Mineral	**Ep-Aln**	**Ep-Aln**	**Ep-Aln**	**Zo-Czo**
SiO2	33,324	34,273	35,492	40,308
TiO2	0,123	0,123	0,067	0,111
Al2O3	18,322	19,442	20,559	33,375
FeO*	13,250	12,670	12,875	0,082
MnO	0,000	0,000	0,236	0,058
MgO	0,582	0,432	0,255	0,002
CaO	15,781	16,987	19,996	24,477
Na2O	0,000	0,000	0,000	0,000
K2O	0,000	0,000	0,006	0,004
La2O3	5,750	4,492	1,255	N.A
Ce2O3	9,828	8,524	3,433	N.A
Pr2O3	0,523	0,442	0,283	N.A
Nd2O3	1,336	1,318	1,132	N.A
Sm2O3	0,087	0,095	0,232	N.A
Eu2O3	0,128	0,171	0,153	N.A
Gd2O3	0,458	0,379	0,327	N.A
Tb2O3	0,000	0,000	0,000	N.A
Dy2O3	0,000	0,000	0,050	N.A
Ho2O3	0,057	0,030	0,028	N.A
Er2O3	0,000	0,064	0,118	N.A
Tm2O3	0,000	0,000	0,000	N.A
Yb2O3	0,000	0,000	0,031	N.A
Lu2O3	0,000	0,017	0,000	N.A
Total	99,549	99,459	96,528	98,417
Si	2,902	2,928	3,370	3,032
Ti	0,008	0,008	0,000	0,006
Al	1,880	1,957	1,986	2,959
Fe2+*	1,003	0,939	0,854	0,005
Fe3+ Calc	0,702	0,657	0,513	0,003
Fe2+ Calc	0,301	0,282	0,342	0,002
Mn	0,000	0,000	0,000	0,004
Mg	0,076	0,055	0,020	0,000
Ca	1,472	1,555	1,837	1,973
Na	0,000	0,000	0,000	0,000
K	0,000	0,000	0,001	0,000
Sum of REE (apfu)	0,600	0,502	0,000	N.A
La	49027,967	38301,501	0,000	N.A
Ce	83906,770	72773,841	0,000	N.A

Pr	4468,940	3776,809	0,000	N.A
Nd	11454,047	11299,726	0,000	N.A
Sm	750,259	819,248	0,000	N.A
Eu	1105,450	1476,811	0,000	N.A
Gd	3973,625	3288,218	0,000	N.A
Tb	0,000	0,000	0,000	N.A
Dy	0,000	0,000	0,000	N.A
Ho	497,599	261,894	0,000	N.A
Er	0,000	559,685	0,000	N.A
Tm	0,000	0,000	0,000	N.A
Yb	0,000	0,000	0,000	N.A
Lu	0,000	149,503	0,000	N.A

Table 7. Selected Titanite Microprobe Analyses.

Sample	**DAF**		**AF**	
SiO2	26,554	28,362	25,695	25,815
TiO2	33,251	32,952	42,045	41,315
Al2O3	2,551	1,592	1,401	1,330
Fe2O3*	2,196	3,580	0,391072	0,783255
MnO	0,050	0,046	0,042	0,258
MgO	0,000	0,000	0,000	0,000
CaO	27,642	24,171	26,845	27,621
Na2O	0,027	0,095	0,029	0,000
K2O	0,012	0,005	0,001	0,000
F	1,002	0,049	0,024	0,078
Cl	0,000	0,000	0,000	0,000
Nb2O5	0,000	0,711	0,353	0,000
P2O5	0,011	0,006	0,103	0,115
SrO	0,039	0,076	0,023	0,032
BaO	0,061	0,026	0,027	0,030
UO2	0,000	0,000	0,000	0,000
ThO2	0,013	0,043	0,031	0,000
PbO	0,000	0,014	0,000	0,000
HfO2	0,028	0,189	0,160	0,000
ZrO2	0,116	0,335	0,000	0,000
Y2O3	0,320	2,099	0,321	0,186
Ta2O5	0,018	0,011	0,076	0,000
La2O3	0,311	0,241	0,000	0,015
Ce2O3	2,042	2,068	0,290	0,045
Pr2O3	0,124	0,196	0,003	0,000
Nd2O3	0,567	0,945	0,120	0,013
Sm2O3	0,113	0,278	0,087	0,083
Eu2O3	0,043	0,118	0,000	0,024
Gd2O3	0,119	0,437	0,031	0,000
Tb2O3	0,000	0,000	0,000	0,000
Dy2O3	0,000	0,238	0,000	0,039

Ho2O3	0,000	0,063	0,024	0,000
Er2O3	0,033	0,165	0,035	0,084
Tm2O3	0,000	0,063	0,000	0,000
Yb2O3	0,000	0,181	0,007	0,026
Lu2O3	0,044	0,051	0,000	0,001
Total wt%	97,287	99,406	98,125	97,815
Si	1,000	1,000	1,000	1,000
Ti	0,942	0,874	1,231	1,204
Al	0,113	0,066	0,064	0,061
Fe3+	0,062	0,095	0,011	0,023
V	0,000	0,000	0,000	0,000
Cr	0,000	0,000	0,000	0,000
Fe2+	0,000	0,000	0,000	0,000
Mn	0,002	0,001	0,001	0,008
Mg	0,000	0,000	0,000	0,000
Ca	1,115	0,913	1,119	1,146
Na	0,002	0,006	0,002	0,000
K	0,001	0,000	0,000	0,000
F	0,119	0,005	0,003	0,010
Cl	0,000	0,000	0,000	0,000
Nb	0,000	0,011	0,006	0,000
P	0,000	0,000	0,003	0,004
Sr	0,001	0,002	0,001	0,001
Ba	0,001	0,000	0,000	0,000
U	0,000	0,000	0,000	0,000
Th	0,000	0,000	0,000	0,000
Pb	0,000	0,000	0,000	0,000
Hf	0,000	0,002	0,002	0,000
Zr	0,002	0,006	0,000	0,000
Y	0,006	0,039	0,007	0,004
Ta	0,000	0,000	0,001	0,000
La apfu	0,004	0,003	0,000	0,000
Ce apfu	0,028	0,027	0,004	0,001
Pr apfu	0,002	0,003	0,000	0,000
Nd apfu	0,008	0,012	0,002	0,000
Sm apfu	0,001	0,003	0,001	0,001
Eu apfu	0,001	0,001	0,000	0,000
Gd apfu	0,001	0,005	0,000	0,000
Tb apfu	0,000	0,000	0,000	0,000
Dy apfu	0,000	0,003	0,000	0,000
Ho apfu	0,000	0,001	0,000	0,000
Er apfu	0,000	0,002	0,000	0,001
Tm apfu	0,000	0,001	0,000	0,000
Yb apfu	0,000	0,002	0,000	0,000

Lu apfu	0,001	0,001	0,000	0,000
OH	0,056	0,156	0,073	0,074
Total apfu	3,470	3,241	3,533	3,539
Total REE apfu	0,045303	0,056852	0,007409	0,002944
La ppm	3647,102	2826,211	0,000	175,905
Ce ppm	23917,673	24222,208	3396,731	527,079
Pr ppm	1451,111	2293,691	35,108	0,000
Nd ppm	6613,415	11022,358	1399,664	151,630
Sm ppm	1310,367	3223,735	1008,867	962,482
Eu ppm	497,924	1366,396	0,000	277,911
Sm ppm	1310,367	3223,735	1008,867	962,482
Gd ppm	1371,622	5036,963	357,313	0,000
Tb ppm	0,000	0,000	0,000	0,000
Dy ppm	0,000	2731,508	0,000	447,600
Ho ppm	0,000	721,675	274,924	0,000
Er ppm	377,349	1886,747	400,219	960,526
Tm ppm	0,000	719,505	0,000	0,000
Yb ppm	0,000	2061,068	79,710	296,065
Lu ppm	500,345	579,946	0,000	11,371
Total REE ppm	39686,908	58692,010	6952,536	3810,570

Table 8. Selected Apatite Microprobe Analyses. N.A. stands for "Not Analyzed".

Stage	**DAF**		**AF**	
P2O5	40,906	39,296	41,953	39,913
SiO2	0,172	0,040	0,308	0,121
FeO*	0,083	0,031	0,156	0,015
MnO	N.A	0,010	N.A	0,020
CaO	55,869	56,141	51,464	51,408
Na2O	0,031	0,108	0,000	0,044
F	1,944	1,872	3,410	3,591
Cl	0,030	N.A	0,017	N.A
La2O3	N.A	0,039	N.A	0,001
Ce2O3	N.A	0,012	N.A	0,000
Pr2O3	N.A	0,019	N.A	0,000
Nd2O3	N.A	0,011	N.A	0,062
Pm2O3	N.A	N.A	N.A	N.A
Sm2O3	N.A	0,001	N.A	0,035
Eu2O3	N.A	0,000	N.A	0,025
Gd2O3	N.A	0,000	N.A	0,024
Tb2O3	N.A	0,000	N.A	0,007
	N.A	0,000	N.A	0,022

Dy2O3				
Ho2O3	N.A	0,002	N.A	0,009
Er2O3	N.A	0,003	N.A	0,071
Tm2O3	N.A	0,000	N.A	0,000
Yb2O3	N.A	0,000	N.A	0,000
Lu2O3	N.A	0,000	N.A	0,011
Total	99,035	97,585	97,291	95,379
P	6,004	5,903	6,151	6,035
Si	0,030	0,007	0,053	0,022
Fe	0,004	0,016	0,000	0,007
Mn	0,012	0,005	0,023	0,002
Ca	10,377	10,673	9,549	9,837
Na	0,000	0,003	0,017	0,007
F	1,066	1,050	1,867	2,028
Cl	0,009	0,000	0,005	0,000
OH	0,925	0,950	0,128	0,000
La apfu	0,000	0,003	0,000	0,000
Ce apfu	0,000	0,001	0,000	0,000
Pr apfu	0,000	0,001	0,000	0,000
Nd apfu	0,000	0,001	0,000	0,004
Total	17,427	17,612	16,793	16,913
La pmm	N.A.	332,538	N.A.	8,527
Ce pmm	N.A.	102,450	N.A.	0,000
Pr pmm	N.A.	162,352	N.A.	0,000
Nd pmm	N.A.	94,307	N.A.	531,550
Pm pmm	N.A.	N.A.	N.A.	N.A.
Sm pmm	N.A.	8,624	N.A.	301,828
Eu pmm	N.A.	0,000	N.A.	215,908
Gd pmm	N.A.	0,000	N.A.	208,225
Tb pmm	N.A.	0,000	N.A.	60,817
Dy pmm	N.A.	0,000	N.A.	191,688
Ho pmm	N.A.	17,460	N.A.	78,568
Er pmm	N.A.	26,235	N.A.	620,901
Tm pmm	N.A.	0,000	N.A.	0,000
Yb pmm	N.A.	0,000	N.A.	0,000
Lu pmm	N.A.	0,000	N.A.	96,737

W-Mo and Au Zoning in Skarn and Intrusion-Related Systems,

Seridó Mineral Province, Northeastern Brazil

CAPÍTULO III

1. ABSTRACT

In the literature, skarn deposits have their genesis commonly explained by the interaction between a magmatic-hydrothermal fluid and carbonate rocks. There is, however, a large number of exceptions to this rule. One of the best examples may be the Seridó Mineral Province, where more than 700 scheelite occurrences have been documented. Important deposits, such as Bonfim, Brejuí, Bodó and Barra Verde, develop classic skarn alteration in the contact with marbles, forming diopside- and/or garnet-dominant parageneses. Other types of occurrences account for amphibole- and/or biotite-dominant assemblages interpreted as Ca-Ba and K hydrothermal alteration rocks that occur along granitoid basement rocks. Apart from pegmatitic dykes, the Ca-Ba and K metasomatic rocks do not show any clear association with carbonate rocks and/or plutonic bodies. Instead, most of these W-bearing rocks are strongly associated with subvertical N20°E-trending shear zones, being more structurally controlled than lithologically dependent. Some of the most representative skarn, Ca-Ba and K alteration deposits and occurrences of the area, which occur in different geological units, were studied in this work.

Metasomatic rocks from the Ca-Ba alteration are constituted by a vast mineralogical assemblage, comprising diopside, magnesiohornblende-pargasite, andesine-labradorite, K-feldspar and hyalophane, with minor contents of titanite, epidote-allanite, barite, magnetite, carbonate, quartz, molybdenite, and scheelite. Both whole rock geochemistry and mineral chemistry analyses point to an enrichment in Ca, Mg, Fe, Ba, Na and REE. Deposits and occurrences which are representative of the Ca-Ba alteration in this study are Bonfim, Morro do Careca, Salgadinho, Alívio, Recanto, Espinheiro and Pedro Tomás.

Rocks from the K alteration are comprised primarily of strongly-oriented biotite-rich bands, with minor amounts of magnesiohornblende, albite-oligoclase, K-feldspar, quartz, muscovite/sericite, chlorite, molybdenite, pyrite and scheelite. Rocks from this domain are characterized by an enrichment in Na, K, Si, Mo and W and are associated with quartz segregations and subconcordant pegmatitic dykes. Occurrences which are representative of the K alteration in this study are Caçador, Salgadinho, Morro do Careca, Isidoro and Riachão.

Zircon U-Pb analyses provided basement granitoid wallrock ages through inherited grains collected from host rock samples. In the Bonfim deposit, relict Paleoarchean zircon grains yielded an age of 3324±33 Ma; Neoarchean crystals yielded an age of 2699±11 Ma in Pedro Tomás; relict Paleoproterozoic grains from Salgadinho held ages of 2217±6 Ma and 2177±16 Ma; and a Paleoproterozoic age of 2194±31 Ma was verified in the Caçador occurrence. In the Salgadinho occurrence, the core of a single grain along with the borders of some crystals provided concordant ages of 575±3 Ma, 558±4 Ma and 536±3 Ma, which may be correlated to peak orogenic and metasomatic events. Results of similar age were identified by 40Ar/39Ar analyses in hydrothermal minerals, such as amphibole, with the ages 553±3 Ma and 548±2 Ma for Bonfim and 557±7 Ma for Salgadinho; and biotite, which yielded the ages 498±2 Ma and 501±2 Ma for Caçador. These Neoproterozoic-Ediacaran ages, along with field and petrographic observations, reflect the importance of the end of the Brasiliano Cycle for the tungsten endowment in the Seridó Mineral Province.

Following a new model for the area, the rocks studied in this work are interpreted as the root zones of the W-skarns, presenting spatial and temporal associations with them. The Ca-Ba and K alteration rocks along with skarns are part of the same system, but formed under different pressure, temperature, chemical, pH and REDOX conditions, as well as distinct fluid/rock ratios and hydrothermal solution and wallrock compositions.

These metasomatic rocks may also be correlated with similar alteration patterns in other magmatic-hydrothermal systems, which may help in the discovery of new deposits by identifying and

delimiting their root zones. The regional-scale zoning between W-Mo and Au deposits in the Seridó Mineral Province also suggests an association with Intrusion-Related systems.

2. INTRODUCTION

W-skarns, where the main ore mineral is generally scheelite, are commonly related to deep reduced meta- to weakly peraluminous I-type calc-alkaline batholiths emplaced in thickened crustal conditions (Smirnov, 1976; Newberry & Swanson, 1986). These plutonic bodies exsolve magmatic-hydrothermal fluids which migrate along structures (e.g., faults, fractures, shear zones) until a precipitation site is reached, which generally occurs due to interactions with wallrocks (Lentz, 1998; Seymour et al., 2009; Lecumberri-Sanchez et al., 2017). In the hydrothermal solution, tungsten tends to form oxyanionic complexes, achieving optimal solubilities with high temperatures (reaching more than 600°C in some cases) and low pH, also commonly presenting an aqueous±CO_2 nature with variable salinities (Manning & Henderson, 1984; Newberry, 1987; Wood & Samson, 2000; Zajacz et al., 2008; Pokrovski et al., 2013). A recurrent feature in most skarn deposits is that the mineralization tends to form in several pulses, developing different hydrothermal zoning and/or stages, spatially with distal pyroxene and proximal garnet in relation to the high-grade mineralization. Chronologically, they commonly show an early, high temperature phase, followed by a late, lower temperature stage (Meinert, 1992; Robb, 2005; Pirajno, 2009).

Despite the well-constrained genetic model, skarns were originally used as a descriptive term based upon the mineralogy of "odd dark rocks" which were associated with ore minerals along a feldspar-poor felsic volcanic environment (Törnebohm, 1875). Nowadays, skarns are classically defined as pyroxene- and/or garnet-rich calc-silicate rocks produced by the interaction between magmatic-hydrothermal fluids and carbonate rocks (Dick & Hodgson, 1982; Pirajno, 1992; Robb, 2005). Although the original skarn definition also concerned rocks with a similar mineralogy, these rocks present no clear association with plutonic bodies or limestones (Meinert et al., 2005). In this sense, the case of this study is more closely related with the original skarn meaning than with its commonly used genetic model.

This research accounts for rocks which are set in a skarn formation environment, but differ from the classic genetic models: In a previous study, Corrêa et al. (Chapter 2), based on mineral chemistry analyses, suggested that these rocks may be interpreted as the root zones of the W-skarns of the Seridó Mineral Province. Root zones may be defined as distal, but cogenetic zones from an orebody where commonly calcic and/or sodic-calcic hydrothermal alteration are developed, generally accompanied by dyke swarms and veins (Carten, 1986; Seedorff et al., 2008). Early metasomatism occurs generally at temperatures above 500°C and may occur as a regional, widespread alteration (Mark & Foster, 2000; Garcia, 2018). These areas are rarely exposed, but have been ocasionally reported in other magmatic-hydrothermal deposits, such as porphyry, IOCG and intrusion-related (Pollard, 2001; Candela & Piccoli, 2005; Richards & Mumin, 2013).

Among suggestions, interpretations and conclusions concerning the Seridó Mineral Province W-bearing system, this paper focuses in answering the following questions: What is the temporal relation between the root zones and the skarns? Was the hydrothermal alteration a continuous event that lasted for some time or did it occur as a short-lived pulse? What are the chemical characteristics of the host rocks and how do they reflect metasomatic processes? What is the influence of wallrocks and pegmatites for the formation of the root zones? What is the main source of the hydrothermal fluid? This paper suggests new genetic and prospective models for the skarn formation system of the Seridó Mineral Province based on fieldwork observations, mineral association studies and whole-rock geochemistry and isotopic analyses, aiming to answer the aforementioned questions.

3. REGIONAL GEOLOGIC SETTING

3.1. Geologic Framework

The Borborema Province is characterized by the amalgamation of crustal blocks of different origins, set apart from each other by regional-scale shear zones (Jardim de Sá, 1994; Hackspacher et al., 1997; Dantas et al., 2003). According to Brito Neves et al. (2000) and Van Schmus (2011), these blocks are divided in six domains, named from northwest to southeast as Médio Coreaú, Ceará Central, Rio Grande do Norte, Zona Transversal, Pernambuco-Alagoas and Sul. The Rio Grande do Norte Domain (RGND) comprises massifs and mobile belts and their respective basement rocks (Ebert, 1970; Almeida et al., 1981). The study area is located in the Seridó Fold Belt, one of the mobile belts inside the RGND (Figure 1).

The Seridó Fold Belt is the most studied terrane from the RGND due to its connection to Africa during the Late Neoproterozoic-Ediacaran Western Gondwana collage, named as Brasiliano-Pan African Orogeny (Neves, 2003; Van Schmus et al., 2008; Brito Neves et al., 2014; Neves, 2015; Araujo et al., 2016). During this orogenic cycle, several ore deposits were formed, including lode gold (Coutinho, 1994; Silva, 2000; Trindade, 2000), Ta±Be±Sn±Li±REE-bearing pegmatites (Baumgartner et al., 2006; Beurlen et al., 2008; Beurlen et al., 2014) and a skarn and skarnoid W±Au±Mo±Bi±Cu polymetallic association (Salim, 1993; Cavalcanti Neto, 2008; Souza Neto et al., 2008).

The basement rocks of the area comprise a Paleoproterozoic assemblage constituted by orthogneisses and augen gneisses with high-K calc-alkaline and meta- to peraluminous geochemical signature, named as Caicó Complex (Souza et al., 2007; Medeiros et al., 2012; Figure 1). Zircon U-Pb analyses point to Rhyacian igneous crystallization ages around 2.2 Ga, while Sm-Nd TDM model ages up to 2.8 Ga suggest that this lithological unit was formed from older reworked crustal rocks (Dantas et al., 2002; Hollanda et al., 2011). Outcrops from the oldest rocks in the area correspond to localized Archean nucleii which may be correlated with the São José do Campestre Massif, presenting zircon U-Pb ages up to 3.5 Ga and Sm-Nd TDM model ages higher than 3.7 Ga (Dantas et al., 2004; Dantas et al., 2013; Souza et al., 2016; Ruiz et al., In Press).

The supracrustal rocks of the study area are represented by the Seridó Group (Jardim de Sá, 1994; Van Schmus et al., 2003; Hollanda et al., 2015; Figure 1). Its basal unit is named Serra dos Quintos Formation, constituted mainly by paragneisses and micaschists (Angelim et al., 2006). Above, the Jucurutu Formation comprises paragneisses, calc-silicate rocks and marbles, generally being the main controlling agent for the skarn occurrences of the area (Santos et al., 2014). Then, the Equador Formation is constituted by quartzites and metaconglomerates. On the top, the Seridó Formation comprises mainly micaschists with lesser amounts of carbonate and mafic metavolcanic rocks (Jardim de Sá et al., 1995; Angelim et al., 2004). U-Pb analyses in detrital zircon grains revealed deposition ages between 650 and 610 Ma, and both Jucurutu and Seridó formations were dated by SHRIMP zircon U-Pb analyses, yielding ages of 634 Ma and 628 Ma, respectively (Van Schmus et al., 2003; Angelim et al., 2006).

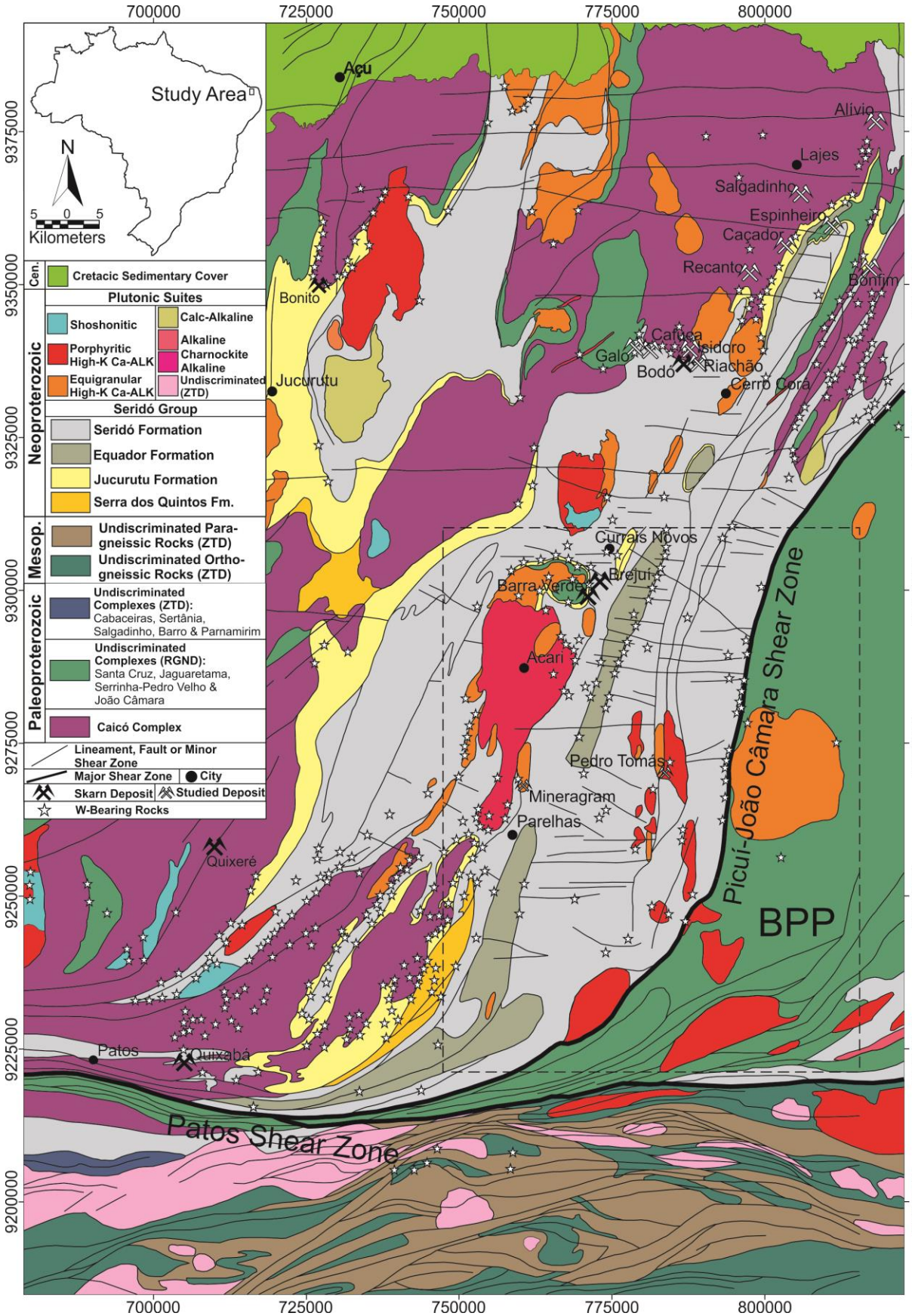

Figure 1. Simplified geological map of the study area slightly adapted from Corrêa et al. (Chapter 2) and references therein, also including data from Cavalcante et al. (2016). The abbreviations BPP, RGND and ZTD stand for "Borborema Pegmatite Province", "Rio Grande do Norte Domain" and "Zona Transversal Domain", respectively. The location map is slightly adapted from Archanjo et al. (2013) and the abbreviations WA, A, C and K stand for the West African, Amazonia, Congo and Kalahari cratons, respectively.

During the Brasiliano Cycle, basement and supracrustal rocks were deformed and metamorphosed under amphibolite facies conditions (Jardim de Sá et al., 1995; Brito Neves et al., 2000). This orogeny also developed a transcontinental syn-collisional environment that evolved to a strike-slip system with dextral subvertical N-NE-trending shear zones, as well as extensive plutonic activity and ore deposits formation (Jardim de Sá, 1981; Sial, 1986; Archanjo & Bouchez, 1991; Hackspacher et al., 1997; Santos & Medeiros, 1999; Santos et al., 2008; Araujo et al., 2014; Neves et al., 2015; Chagas, 2017). Syn-peak intrusions are generally parallel to the regional foliation trend, presenting ages of ca. 580 Ma (Jardim de Sá et al., 1987; Archanjo et al., 1992; Archanjo et al., 2013; Souza et al., 2016; Hollanda et al., 2017). As recorded by 39Ar/40Ar data in amphibole, biotite, muscovite and phlogopite grains, this slow cooling history promoted a long-lived magmatic activity that lasted for more than 80 Ma (Corsini, 1998; Araújo et al., 2005; Ruiz et al., 2018). Throughout this period, six plutonic suites have been identified by Nascimento et al. (2015) in the Rio Grande do Norte Domain based on their geochemical and geochronological data. Late- to post-tectonic magmatic rocks are also widely spread across the Seridó Fold Belt, commonly occurring as N50°E/N70°E-trending dyke swarms (Jardim de Sá et al., 1987; Ferreira et al., 1998). An important representative of this phase is the Borborema Pegmatite Province (BPP), with most rocks dating from 530 Ma to 510 Ma (Beurlen et al., 2009a, 2009b; Baumgartner et al., 2006; Figure 1).

3.2. Seridó Mineral Province

More than 700 tungsten mineralization deposits and occurrences have been documented, commonly located along regional-scale lineaments and basement highs along the Seridó Mobile Belt. W-bearing rocks are generally associated with the last pulses of the Neoproterozoic-Ediacaran Brasiliano Cycle (Hollanda, 2012). Some of the most studied deposits, which include Brejuí, Bodó, Bonfim, Barra Verde, Bonito, Malhada Limpa, Quixabá, Quixeré and Itajubatiba, are in accordance with the classic skarn model (Eugster, 1985; Newberry & Swanson, 1986; Lentz, 1998; Meinert et al., 2005), in which magma-derived hydrothermal fluids reacted with carbonate rocks, leading to ore precipitation. In this sense, the Brasiliano Orogeny promoted a unique tectonic environment where an intense plutonic activity allied with a strike-slip system could interact with different wallrocks, producing skarns along a 200 km-wide belt (Salim, 1993; Souza Neto et al., 2012; Santos et al., 2014; Figure 1). The main scheelite districts of the area are described in Table 1.

Corrêa et al. (Chapter 2) defined the proximal well-known skarn deposits of the area as Mineralized Garnet-Diopside Skarns (to be referred in this paper as MGDS), while distal W-bearing rocks unrelated to carbonate rocks and/or plutons were divided in the Diopside-Amphibole-Feldspars, Amphibole-Feldspars and Biotite-Rich mineral associations (to be referred from now on as DAF, AF and BR, respectively). DAF and AF are associated with a Ca-Ba alteration (regardless of timing relations), while BR corresponds to a K alteration.

Table 1. Tipology of scheelite occurrences according to wallrock alteration from Corrêa et al. (Chapter 2). References used include Salim (1979; 1993), Souza Neto et al. (2008), Cavalcante et al. (2016), Hollanda et al. (2017), Corrêa et al. (Chapter 2) and this work.

Scheelite District	Type	Commodities	W Tonnage (Mt)	Grade (% WO3)	Host Rocks/Wallrocks	Primary Metasomatic Mineralogy	Morphology	Mineralization Control	Oxidation State	Age	Pressure/Temperature Conditions
Brejuí-Boca de Laje (Barra Verde, Olho D'Água, Saco dos Veados, Malhada Limpa, Juazeirinho, Machado, Zangarelhas, Cabeço de São Pedro)	MGDS	W±Mo± ±Fe±Cu	11	0.5-1	Marbles, Metamafic Rocks and Biotite-Gneisses (Jucurutu Fm.)	Cpx (Hd30-60), Pl (An85–92), Grt (Ad19–49, Al+Sp2–7, Gr51–78), Amp (Hb), Ttn, Qz, K-Fsp	Lenticular, Stratiform, Stratabound	Reaction with Wallrocks	Oxidized	555±2 Ma	2-3 kb; 450-550°C (prograde), 200-450°C (retrograde)
					Gneisses (Caicó Complex)						
	DAF/BR		?	?	Ca-Si Rocks, Amphibolites	Hb, Pl, Cpx, Qz	Stratiform	Structural Traps, Quartz Veins, Reaction with Wallrocks	Reduced to Oxidized		
					Ca-Si Rocks, Pegmatites		Stratabound				
Bodó (Queimadas, Isidoro, Riachão, Baixios I & II, Dois Rios, Cafuca, Cinzas, Galo)	MGDS	W±Mo	9	2	Ca-Si Rocks, Marbles (Jucurutu Fm.)	Px, Grt, Amp, Wo, Ttn, Fsp	Stratiform, Stratabound	Reaction with Wallrocks	Oxidized	510±2 Ma	?
					Gneisses and Schists (Caicó Complex)						
	BR	W±Mo	?	?	Gneisses and Schists (Caicó Complex), Pegmatites	Bt, Qz, Fsp, Amp	Banded	Quartz Veins, Structural Control, Reaction with Wallrocks	Reduced	?	?
Bonfim (Morro do Careca, Amarante, Sulista, Queiroz, Catolé II, Gupiara-Oiticica, Pedra Preta, Mulungu, Feiticeiro, Matinha)	MGDS	W±Au± ±Mo±Bi	>0.3	4,8	Schists (Seridó Formation)	Cpx (Hd11–48), Grt (Ad3–5, Al+Sp68–69, Gr21–22), Pl (An85–99), Amp (Tr-Hb), Ttn, Ap, Wo	Stratiform, Stratabound	Reaction with Wallrocks, Structural Control	Reduced	553±3 Ma*	2.5-4 kb; 500-580°C (prograde), 400-500°C (retrograde)
					Marbles (Jucurutu Formation)						
					Neoproterozoic Biotite-Granite					548± 2 Ma*	
	DAF/BR		?	?	Paleoarchean Granitoids	Cpx (Hd15-38), Amp (Prg-Hb-Tr), Pl (An01-53), K-Fsp, Bt, Ttn, Ap, Aln, Brt, Qz	Lenticular, Banded				
					Pegmatites					524±2 Ma	
					Neoproterozoic Biotite-Granite						
Quixabá-Malhada Vermelha	MGDS	W	>2.5	0.5-1.4	Marbles (Jucurutu Formation?)	Grt, Px, Pl, Aln, Ap, Ttn, Scp	Lenticular, Stockwork	Reaction with Wallrocks	Reduced to Oxidized	?	?
	DAF/BR		?	?	Amphibolites, Pegmatites	Amp, Px, Qz					
Lajes (Salgadinho, Alívio, Recanto, Caçador, Espinheiro, Arara, Cacimba de Cima)	DAF/BR	W±Mo	?	?	Gneisses (Caicó Complex)	Px (Hd13-22), Amp (Prg-Hb-Tr), Pl (An01-56), K-Fsp, Bt, Ttn, Ap, Aln, Brt, Qz	Lenticular, Banded	Reaction with Wallrocks, Structural Control, Quartz Veins	Reduced	557±7 Ma*	?
	BR		?	?	Neoproterozoic Granitoid/Pegmatite	Bt, Qz, Fsp, Amp				501±2 Ma*	
Itajubatiba	MGDS	Au±Fe±Cu	No W	No W	Marbles (Jucurutu Formation?)	Px (Hd05-75), Amp (Tr-Hb), Ttn, Ap	Lenticular, Stratiform	Quartz Veins, Reaction with Wallrocks	Reduced	?	2.5-4 kb; 500-580°C (prograde), 400-500°C (retrograde)

MGDS-type deposits and occurrences are typically exoskarns controlled by carbonate-bearing wallrocks, usually hosted in Jucurutu Formation marbles or along lithological contacts between marbles and other wallrocks. Exceptions are not uncommon, since there are exoskarns in rocks either of the Seridó Group (e.g., biotite-schists and gneisses) or the basement (e.g., orthogneisses and augen gneisses), and even endoskarns formed along Brasiliano granitoids (Brito Neves et al., 2000; Souza Neto et al., 2008). In the Brejuí mine, Salim (1993) reported a zoned alteration front between proximal marbles and distal wallrocks. Scheelite ore shoots are commonly concentrated along fold hinges (Souza Neto et al., 2008). Most MGDS deposits show features that allow them to be classified as oxidized W-skarns (with the exception of Bonfim and Itajubatiba), also presenting prograde (early, high-temperature) and retrograde (late, low-temperature) phases (Trindade, 2000; Souza Neto et al., 2008).

The DAF/AF/BR have been previously described as mafic/metamafic rocks (Moeri & Kloechner, 1979a,b); hornblende-, clinopyroxene- and/or biotite- skarns (Salim, 1993); and calc-silicate gneisses (Cavalcante et al., 2016). These rocks are generally defined as black or green garnet-lacking, diopside-amphibole-rich, molybdenite-scheelite-bearing lithotypes with leucocratic quartz-feldspar domains. The DAF, AF and BR mineral associations are distal to the MGDS and are commonly unrelated to carbonate rocks or Late Neoproterozoic Brasiliano intrusions. Instead, these mineral associations occur along basement wallrocks, mostly from the Paleoproterozoic Caicó Complex (Figure 1).

In some locations, a clear spatial association between the DAF/AF/BR mineral associations and the MGDS is verified. In the Bonfim deposit, for example, DAF/AF/BR rocks occur beneath the skarns, as seen in the deepest levels of the underground mine and in drill hole samples. Similar rocks (i.e., in terms of texture, mineral assemblages and composition) were identified in other localities and were correlated with the ones from the Bonfim deposit, interpreted as having been formed by the same processes, regardless if they present a clear spatial association with MGDS or not.

DAF/AF rocks generally occur along N-NE-trending shear zones, where BR bands may also be present as envelopes or crosscutting the DAF/AF rocks. Pegmatitic rocks are also commonly associated with the DAF/AF/BR rocks, occurring either as subconcordant anastomosing injections or as discordant subvertical N70°W-trending tabular dykes. Deformation partitioning produced undeformed to strongly foliated textures. Common ore minerals in these rocks are scheelite, molybdenite and barite.

The DAF/AF associations represent two hydrothermal alteration stages, characterized by an early high-temperature prograde paragenesis, comprising hedenbergitic diopside, epidote-allanite, magnesiohornblende-pargasite, titanite, magnetite, Ca-rich plagioclase, hyalophane, barite and apatite in the DAF association; and a late, lower-temperature retrograde assemblage presenting sericite, zoisite-clinozoisite, chlorite, magnesiohornblende-tremolite, Na-rich plagioclase, K-feldspar, molybdenite and scheelite in the AF association. The transition from DAF to AF is best represented by the alteration of early diopside and allanite, forming amphibole, titanite and magnetite bands. The BR association is comprised of biotite, magnesiohornblende, K-feldspar, quartz, molybdenite and scheelite; and most minerals show similar chemical signatures with the AF association, which corroborate with their late-stage character interpretation (Corrêa et al., Chapter 2).

Souza Neto et al. (2008) and references therein presented formation condition estimates for the MGDS between 10 to 15 km of depth at 400°C to 580°C, with pressures between 2 kbars and 4 kbars. Beurlen et al. (2001) also verified similar P-T conditions estimates for pegmatitic rocks, set between 400°C and 580°C at ca. 3.8 kbars. The correlation between the DAF/AF/BR rocks with both MGDS and pegmatites suggest that they were formed at similar conditions, despite their distal character in relation to the skarns.

Apart from the W-Mo-bearing rocks, several gold deposits occur in the Seridó Mineral Province, such as São Francisco, Simpático and Ponta da Serra (Trindade, 2000). The ore is typically hosted in quartz veins related to Brasiliano strike-slip structures (Araújo et al., 2002). 40Ar/39Ar analyses in muscovite and biotite lamellae from these veins yielded ages in the 520-500 Ma interval (Araújo et al., 2005).

3.3. Studied Deposits and Occurrences

Mesoscopic, macroscopic and microscopic features from Bonfim, Morro do Careca, Salgadinho, Recanto, Espinheiro, Alívio and Caçador are documented in Corrêa et al. (Chapter 2) and will only be briefly summarized in this paper. Other deposits and occurrences included in this work account for recently discovered localities which are representatives of the Ca-Ba and K alteration, the MGDS and a pegmatoid granite outcrop.

The Bonfim mine is one of the most important deposits of the area and represents a typical exoskarn hosted in marbles from the Jucurutu Formation which are located in the flank of an antiform. NS/N30°E-trending shear zones are also present along the exposures. Skarns are comprised of garnet, diopside, amphibole, titanite, magnetite and apatite along with sulfides and scheelite. In the contact zone between skarns and marbles, reaction aureoles are formed (Figure 2). In the underground mine and drill core samples, Ca-Ba and potassic alteration rocks are observed, revealing that the studied metasomatic calc-silicate rocks occur beneath the skarns. In these samples, granitoid wallrocks are gradually altered to Ca-Ba and K metasomatic rocks (Figure 3).

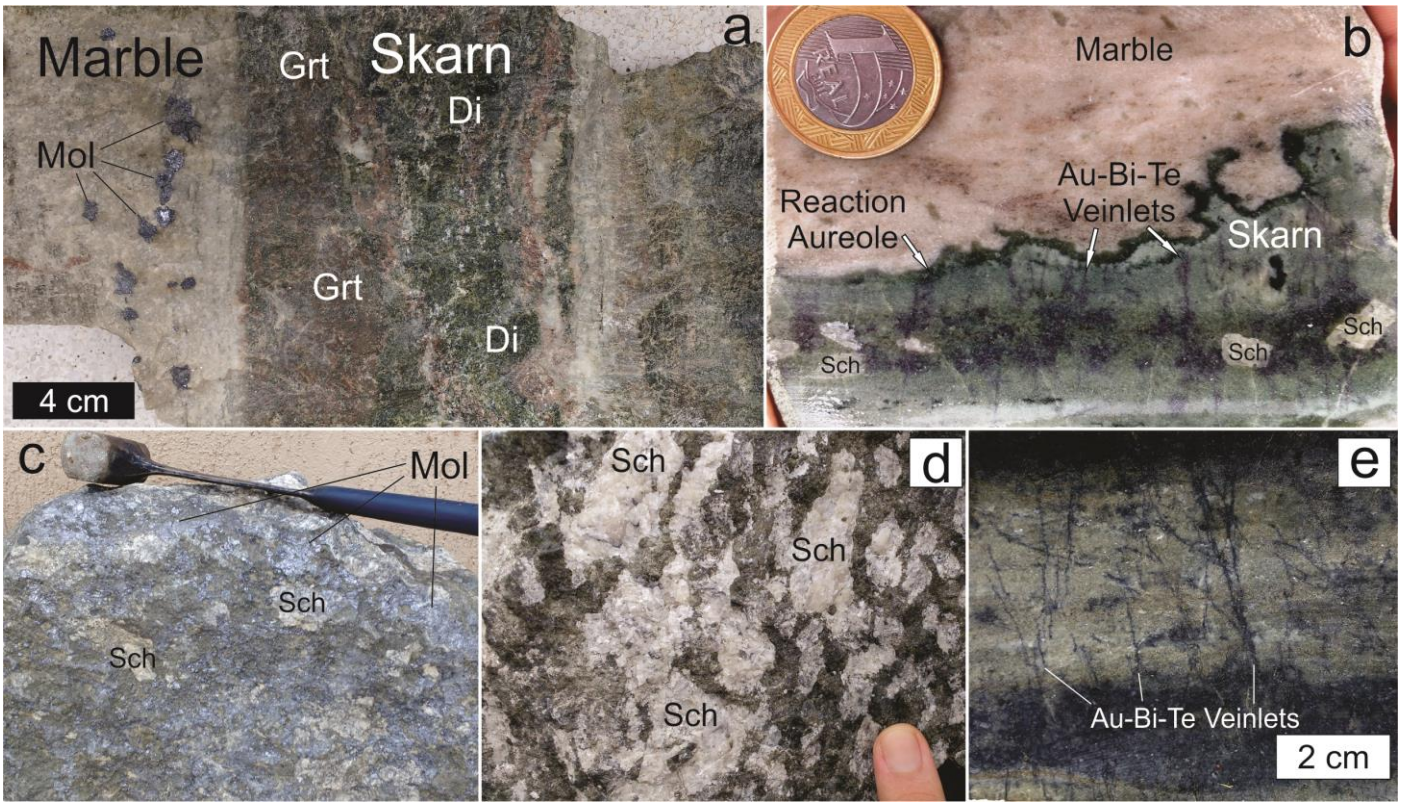

Figure 2. Plate with samples from the Bonfim deposit area. Mineral abbreviations, when present, are in accordance with Whitney & Evans (2010). a: Stratiform garnet-diopside skarn in contact with a molybdenite-bearing marble rock in a sample from the Serra do Feiticeiro occurrence, which is located near Bonfim. b: Skarn altering marble, showing: an irregular reaction aureole, centimeter-scale scheelite crystals aligned parallel to the the main foliation, and discordant auriferous brittle-ductile veinlets. c: Extensive molybdenite precipitation in a skarn sample. d: Coarse-grained scheelite dissemination in a skarn sample. e: Late-stage brittle-ductile Au-Bi-Te veinlets that crosscut the skarns from Bonfim..

Morro do Careca is a near-mine occurrence located approximately 1 km southwest of the Bonfim deposit. In this location, abrupt and transitional contacts between the granitoid wallrocks and the Ca-Ba and K altered rocks are verified (Figure 3). REE-rich minerals, such as allanite, titanite and apatite, and Ba-

bearing minerals, such as barite and hyalophane, occur in large amounts in some domains. In this location, the potassic alteration, represented by nearly monomineralic biotite-rich bands, is superimposed on the Ca-Ba rocks, showing a replacement-like character evidenced by crosscutting relationships.

The Salgadinho occurrence is a 100 meters wide pit comprising both Ca-Ba and potassic alteration rocks that occur along granitoid basement rocks. The Ca-Ba alteration rocks appear as undeformed nuclei that become strongly-oriented to the rims, and are commonly bordered and/or crosscutted by the potassic alteration. In the nuclei, very coarse amphibole crystals occur (Figure 4), usually replacing previously formed diopside grains. Leucocratic quartz-feldspar rocks, which are also part of the Ca-Ba alteration, are developed either as bands or irregular domains inside the melanocratic diopside- and/or amphibole-dominant rocks (Figure 4).

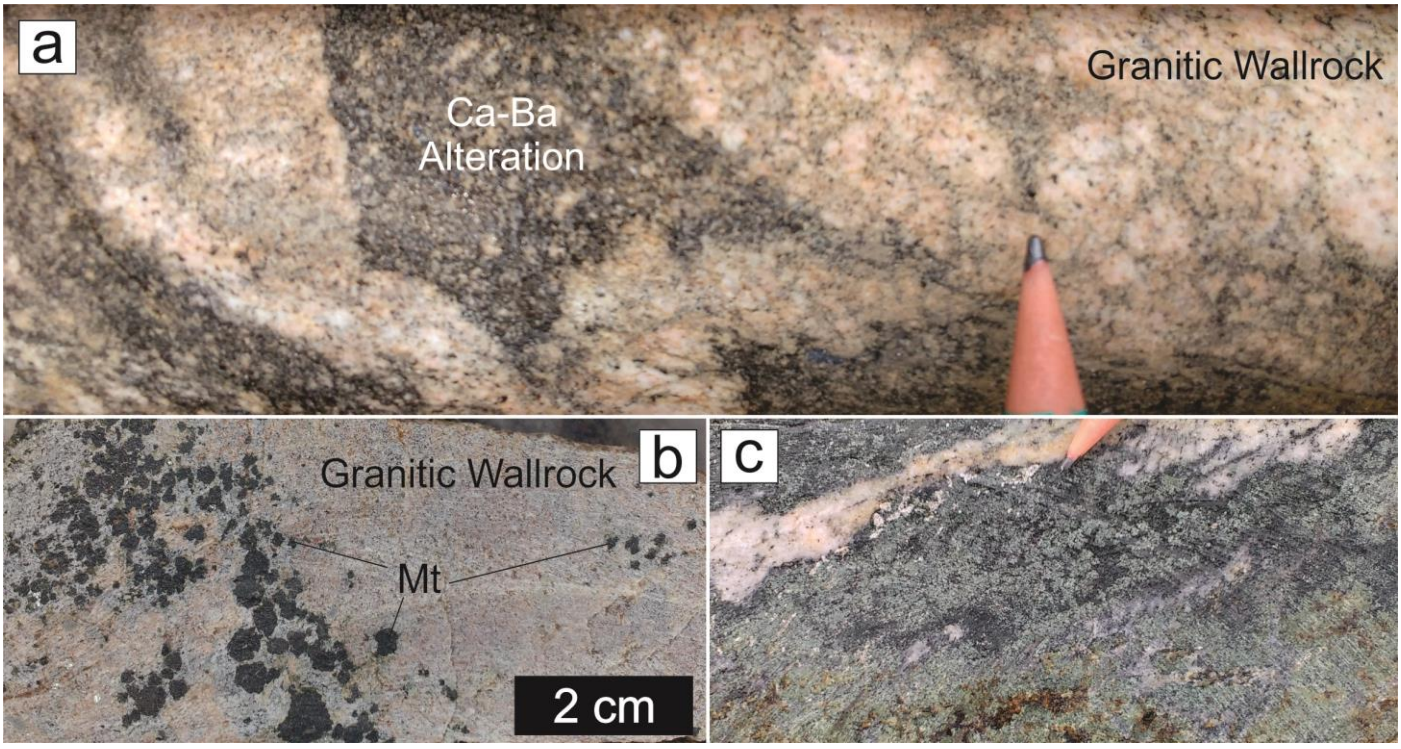

Figure 3. Ca-Ba alteration plate with samples from the Bonfim deposit. a: Drill hole sample showing the Ca-Ba alteration being formed in a granitic wallrock. b: Drill hole sample showing metasomatic magnetite clusters being formed in a granitic wallrock. c:. Drill hole sample showing relict granitic lenses along the Ca-Ba alteration.

The Alívio, Recanto and Espinheiro occurrences do not show rocks related to the potassic alteration. Like in the Salgadinho occurrence, these localities present coarse-grained diopside- and/or amphibole-rich domains associated with feldspar-rich bands and quartz segregations that alter granitoid basement wallrocks (Figure 4). In the Alívio occurrence, a pegmatite sample presented metasomatic amphibole and diopside-epidote-quartz clusters.

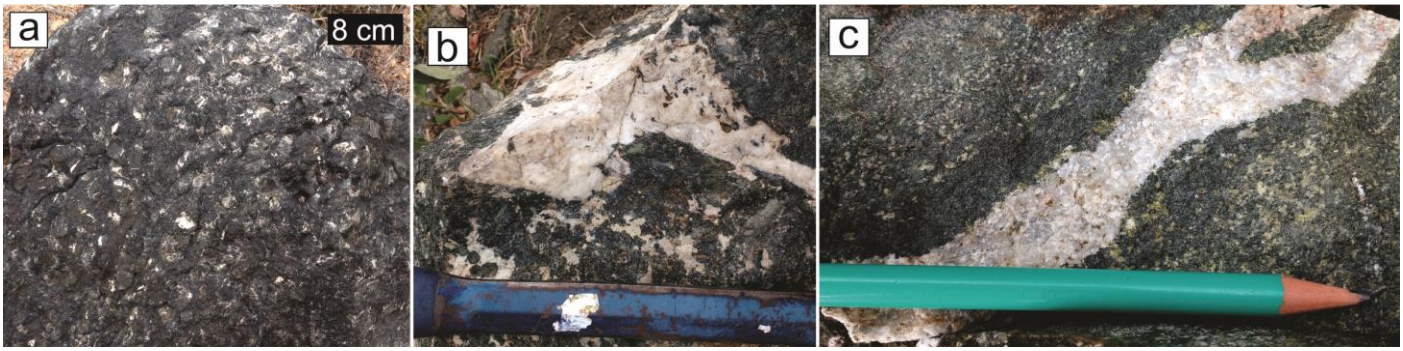

Figure 4. Plate with Ca-Ba and K alteration samples. a-b: Samples from the Salgadinho occurrence. a: Typical Ca-Ba alteration sample with undeformed coarse-grained amphibole crystals, which occur associated with diopside and feldspars. b: Feldspars±quartz-rich bands formed along diopside-amphibole-rich domains. c: Quartz segregation in the Ca-Ba alteration from the Alívio occurrence.

The Caçador occurrence consists in a tens of meters wide open pit that only presents the potassic alteration along basement granitoid wallrocks, although Ca-Ba rocks appear in its vicinities. There is an association of N-N20°E-trending shear zones, subconcordant pegmatitic injections and quartz segregations, leading to molybdenite-scheelite precipitation along the foliation plans. In this location, biotite appears in textural equilibrium with amphibole.

The Pedro Tomás occurrence contains typical rocks of the Ca-Ba alteration but is located more than 100 km away from the other Ca-Ba occurrences (Figure 5). This fact highlights the regional character of the occurrence of these root zone-related rocks. The basement granitic wallrock appears strongly foliated, exhibiting bands of metasomatic magnetite, which record the beginning of the hydrothermal alteration process (Figure 5). The whole occurrence is controlled by subvertical shear zones with S and C foliation trends of N30°W and N50°E, respectively. These rocks tend to form amphibole-rich clusters inside epidote-diopside-rich or feldspar-rich domains (Figure 5). In this occurrence, centimeter-scale domains are developed, even on small hand samples, as seen in Figure 5.

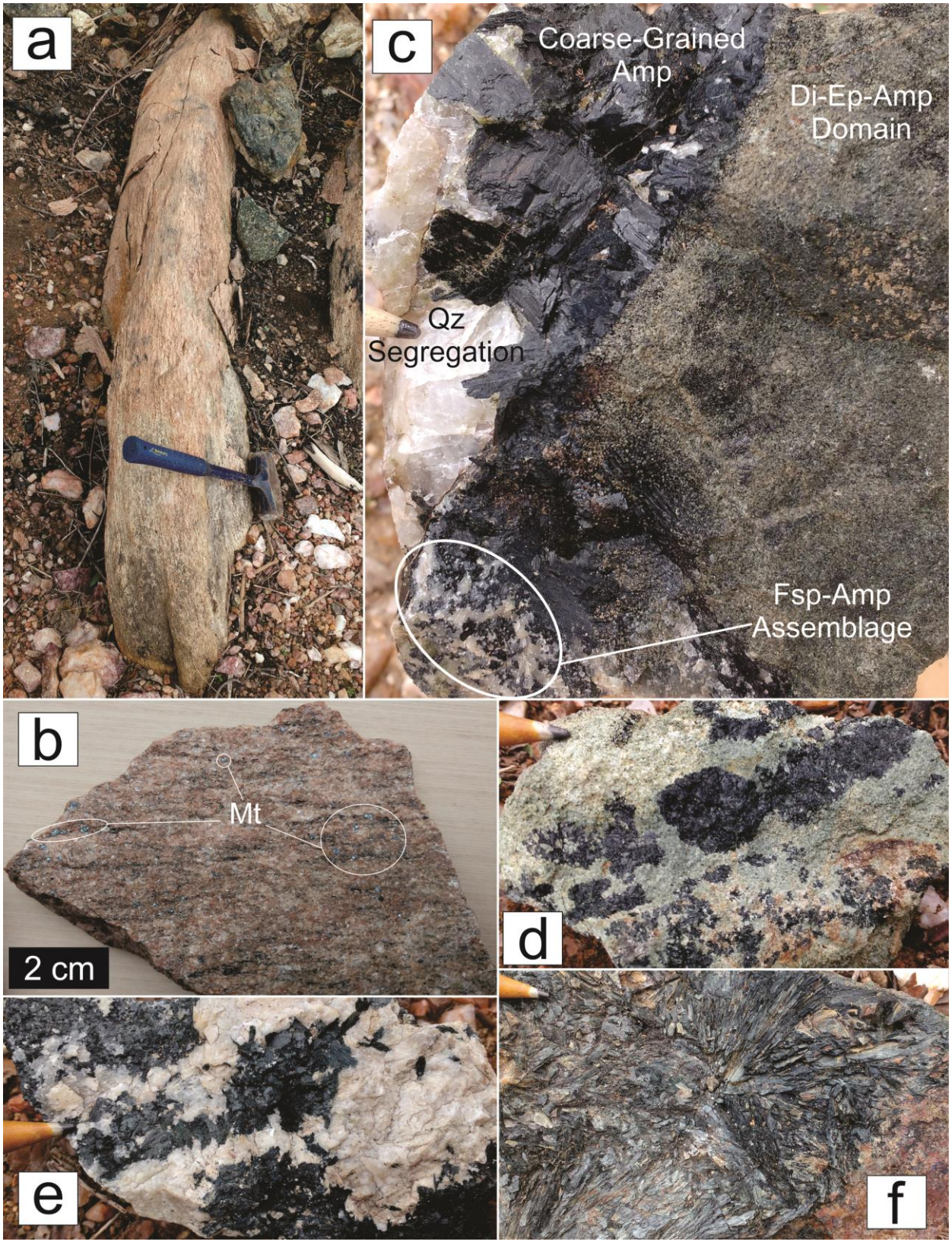

Figure 5. Samples of the Ca-Ba halo from Pedro Tomás. a: N50°E-trending strongly foliated granitic wallrock. b: Magnetite crystals being formed along the granitic wallrock foliation plans. c: Mineral and textural zoning in a hand sample. d: Monomineralic amphibole agglomerates bordered by diopside-epidote-rich domains. e: Amphibole-feldspar association. f: Coarse-grained radiating amphibole crystals.

Occurrences which are representatives of the potassic alteration studied in this paper are Isidoro and Riachão, which are located near the Bodó mine and alter basement granitoid wallrocks. These are dominated by N20°E-trending faults, where quartz±feldspar-rich boudins occur (Figure 6). On the borders of these boudins, biotite-rich bands are formed, being also associated with rose-colored pegmatites that occur either as folded lenses or as discordant anastomosed N20°W-trending dykes.

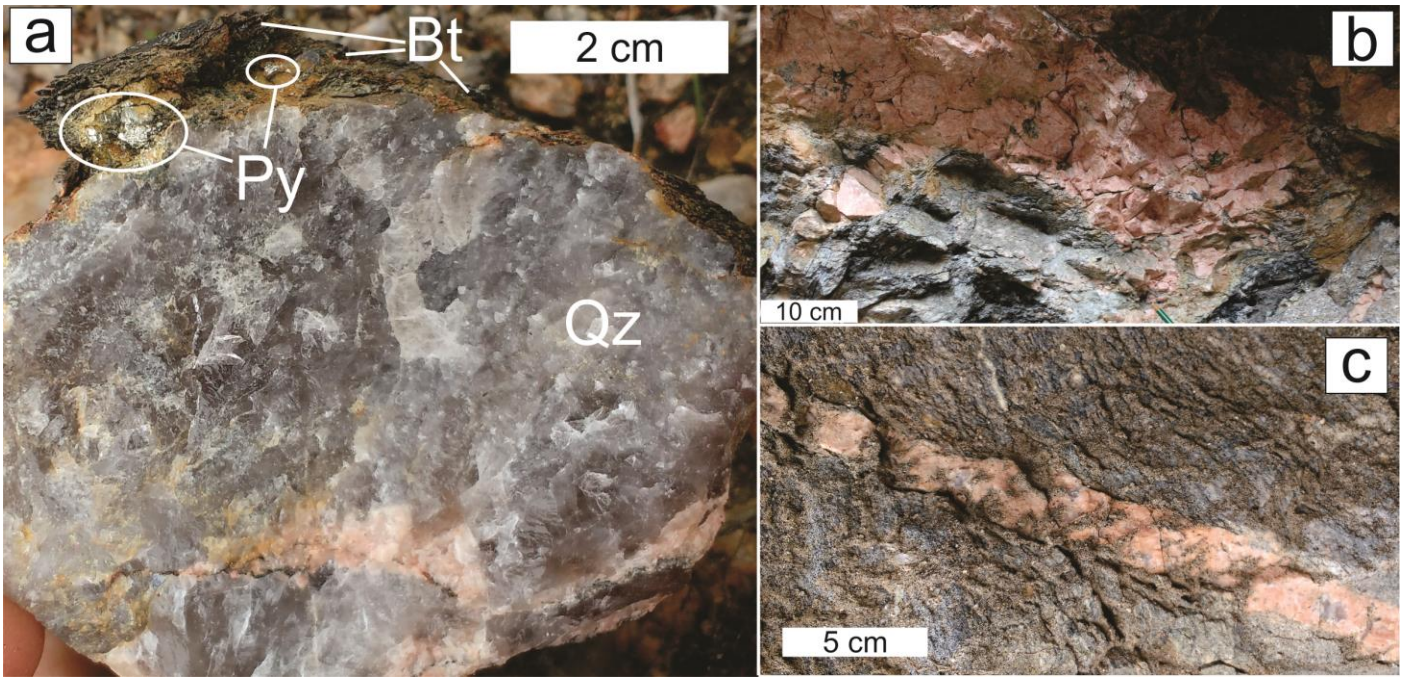

Figure 6. Potassic halo plate from the Isidoro and Riachão occurrences. a: Quartz±feldspar segregation bordered by biotite-rich bands. Pyrite grains are precipitated in the interface between these two domains. b: Contact between the folded biotite-rich bands and the subconcordant pegmatitic dykes. c: Detail of a pegmatitic dyke along the potassic alteration.

Pyrite and molybdenite are the most common sulfides in these locations, occurring i) at the intersection between quartz segregations and biotite-rich bands, ii) as disseminated crystals along biotite-rich rocks, also appearing with scheelite, and iii) as euhedral coarse-grained clusters inside quartz±feldspar boudins (Figure 6).

The Galo occurrence and the Cafuca mine correspond with MGDS near the Bodó mine. These occur in the contact between marbles and schists from the Seridó Group, preferably forming diopside-epidote-rich rocks along N40°E-trending fold hinges (Figure 7). A quartz and quartz-feldspar veinlet system is developed with EW and N60°W trends. These are folded, discontinuous and anastomosing, producing boxwork-like textures. Molybdenite is generally subparallel to the main foliation trend, disseminated along the epidote-diopside-rich matrix.

The Mineragram mine accounts for an undeformed pegmatitic granite containing quartz, K-feldspar, albite, biotite, muscovite, garnet and tourmaline which is used as a construction material (Figure 8). This rock presents in oriented domains with coarser and finer crystals, which may be correlated with differences in volatile availability and magmatic flux textures. Biotite-schist xenoliths from the Seridó Formation are common, showing curved contacts with the granite. The pegmatoid rock also cuts the xenoliths, forming both parallel and discordant bands (Figure 8).

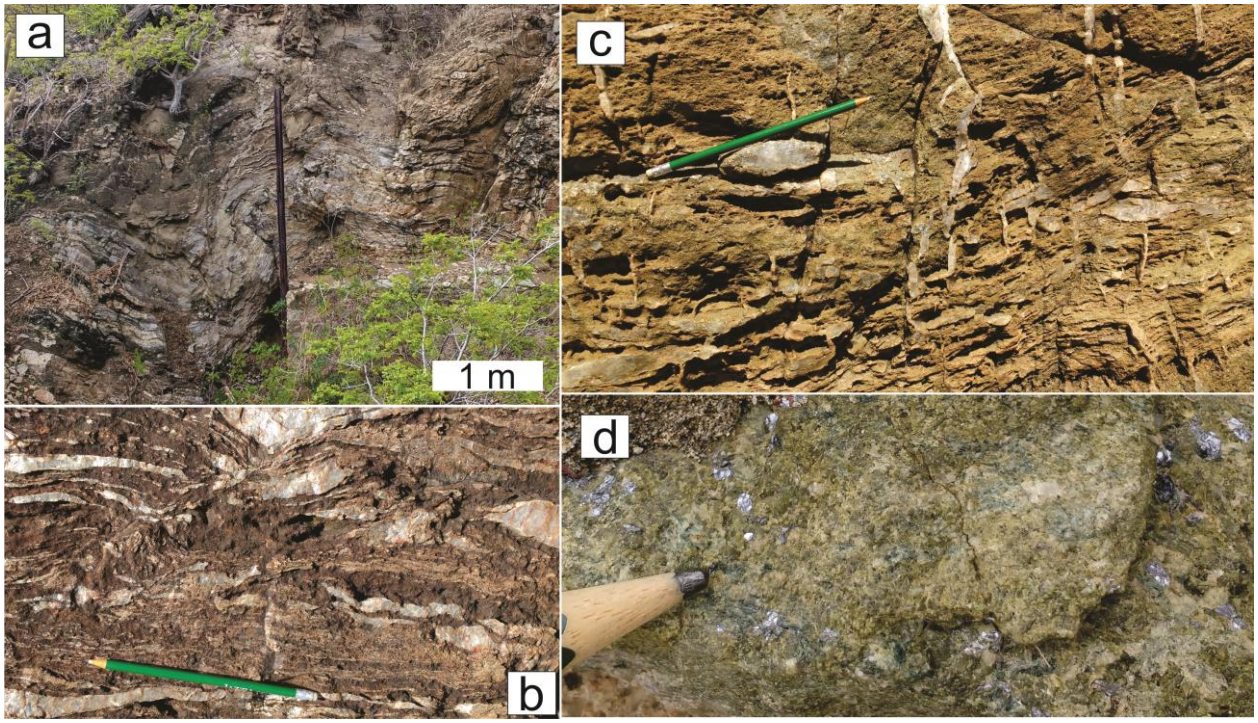

Figure 7. MGDS plate from Galo and Cafuca. a: Outcrop showing a folded contact between marbles and skarns. b-c: Quartz segregations and boxwork-like vein system. d: Extensive molybdenite formation in a epidote-diopside skarn.

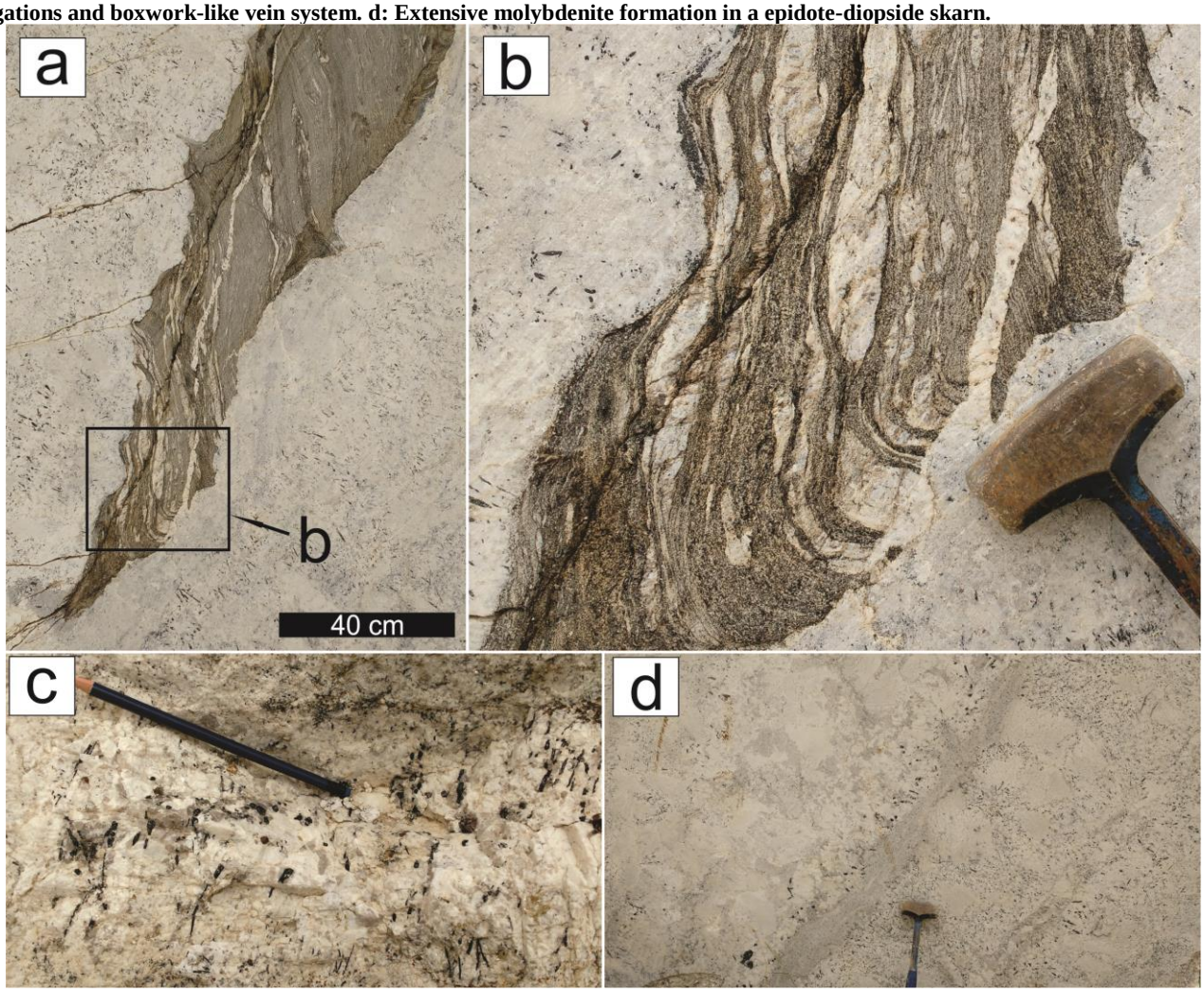

Figure 8. Mineragram outcrop. a: Pegmatoid granite with a biotite-schist xenolith. b: Detail of image a, where the pegmatitic injections intrude the xenolith. c: Slightly oriented tourmaline prisms along with garnet, muscovite, quartz and feldspar grains. d: Magmatic flux texture, forming domains with coarser and finer crystals.

4. METHODS

A consistent bibliographic review allied with geophysical products and satellite images helped to define deposits and occurrences to be studied during the field works. During this stage, structural and lithological data were acquired and samples were collected from the following locations: Bonfim, Morro do Careca, Salgadinho, Pedro Tomás, Alívio, Recanto, Espinheiro, Caçador, Isidoro, Riachão, Galo, Cafuca and Mineragram. Collected samples included skarn, Ca-Ba and K alteration rocks, as well as wallrocks from all the aforementioned deposits and occurrences.

In order to better characterize the processes that led to W precipitation in a variety of host rocks, geochemical, geochronological and stable isotopes analyses were conducted in this research. Whole rock geochemistry was applied to better characterize the chemical signature of both wallrocks and host rocks, as well as to point out the processes of enrichment and leaching of elements during the metasomatism. Geochronological analyses were done to determine the age of W-Mo mineralization and to compare the formation age of MGDS and Ca-Ba/K rocks, as well as prograde and retrograde stages. Sulfur isotopic analyses were conducted to identify S sources, which have a direct impact on mineralization constraints. The acquired data were integrated and led to the formulation of a model for the tungsten metallogenesis in the Seridó Mineral Province. Tables 2-13 are available in the Supplementary Material section in the end of Chapter 3.

4.1. Whole Rock Geochemistry

Geochemical analyses were performed on ten Ca-Ba samples from Bonfim and Morro do Careca (BONFIM CARECA, SEB-295 34.70m, SEB-299 14.45m, SEB-316 21.30m and MC-BF-01), Salgadinho (SALG-01, SALG-02 and SALG-03), Alívio (AL-01) and Recanto (REC-01); one K alteration sample from Caçador (CC-01); and five wallrock samples from the Bonfim deposit (POT-3, SEB-295 10.80m, SEB-295 13.60m, SEB-295 25.30m and SEB-295 42.30m), totaling 16 samples (Table 2). In order to prevent W contamination, samples were powdered in an agate vibratory ring and puck mill. The major elements count (presented in oxide wt%) was determined in the pulverized rock samples by ICP-AES, while trace elements (shown in ppb for gold and in ppm for the rest) were analyzed by ICP-MS. Part of the analyses was held at ACME Analytical Laboratories LTD. (First nine samples of Table 2) and part at ALS Global LTD. (Last seven samples of Table 2). In general, samples presented loss on ignition (LOI) values below 2%, with few exceptions that are probably caused by higher OH-bearing minerals contents.

The obtained data was plotted in binary, ternary and spider diagrams to identify elements mobility processes, which are consequences of fluid-wallrock interactions, transitions between hydrothermal alteration stages and development of different metasomatic rocks. Different sets of samples were used in the diagrams in order to highlight geochemical mobility characteristics and/or processes. Results from this work were also compared with data from the literature (Cunha de Souza, 1987; Salim, 1993) aiming to better characterize and discern the Ca-Ba and K alteration from the MGDS skarns of the Brejuí deposit. REE spidergrams were normalized to the chondrite (Sun & McDonough, 1989) and multi-elements spidergrams were normalized to the primordial mantle (Wood et al., 1979).

4.2. Geochronology

4.2.1. U-Pb Analyses

Six zircon mounts were used for U-Pb analyses. Grains from the host rocks (i.e., Ca-Ba/K alteration) were analyzed aiming to identify magmatic, metamorphic and/or metasomatic processes. Analyses for the Ca-Ba alteration were held in one sample from a drill hole in the Bonfim deposit (Table 3), one sample from Pedro Tomás (Table 4) and three samples from Salgadinho (Tables 5-7), while one sample from the K alteration in the Caçador occurrence was analyzed (Table 8).

Zircon U-Pb analyses were performed in the Geochronology Laboratory of the University of Brasília using a Multicollector LA-ICP-MS Thermo-Finnigan Neptune coupled to a 213 nm New Wave laser. Used standards were the GJ-1 and 91500 zircon crystals. Operation parameters were 10 Hz frequency, 30 µm spot width, 4.00 J/cm² average fluence (65%), 0.97 L/min Ar gas and 0.38 L/min He gas average volumetric flow rates. Subsequently, the acquired data was processed using the Chronus 2.0 and Isoplot 4.15 softwares to produce Concordia diagrams (Ludwig, 2008; Oliveira, 2015).

Cathodoluminescence imaging in selected zircon grains was performed in the Electron Microprobe Laboratory of the University of Brasília using a JEOL JXA-8230. Operating parameters were 15 kV and 15 nA, producing maps with a 1600x1200 resolution. Imaged crystals included some with different core-rim ratios, as well as some that were representative for some samples.

4.2.2. $^{40}Ar/^{39}Ar$ Analyses

$^{40}Ar/^{39}Ar$ dating was performed in amphibole and biotite crystals in order to determine the age of the metasomatism in the root zones of the Seridó Mineral Province (Tables 9-12). A total of four samples were analyzed, comprising pargasite from Morro do Careca (aliquots MCBF-1 and MCBF-3), tremolite from Salgadinho (SALGA-1), biotite from Salgadinho (aliquots SALGB-1 and SALGB-2) and biotite from Caçador (aliquots CC-1 and CC-2). Amphibole analyses correspond to the Ca-Ba alteration, while biotite samples are from the K alteration.

Analyses were performed at the Geochronological Research Center of the University of São Paulo following the procedures of Vasconcelos et al. (2002). The standard used was the Fish Canyon sanidine. All samples were irradiated in the cadmium lined in-core (CLICIT) facility at the Oregon State University TRIGA reactor and then loaded in a Cu-disk. These were step-heated by a solid-state Nd: YVO4 (532 nm) Verdi 6 W Coherent laser and analyzed in an ARGUS VI Thermo Scientific system.

The obtained data were processed using the Ar/ArCALC 2.5.2 software, where corrections for nuclear interferences were applied, as well as background and mass discrimination (Koppers, 2002). The J parameter corresponds to the value J=0.00330800±0.00000400. The $^{40}Ar/^{39}Ar$ ages were determined based on their plateau ages, with the exception of the sample SALGB, which only yielded total fusion ages.

4.3. S Isotopes

Eight Sulfide samples from MGDS and Ca-Ba/K alterations were analyzed in order to determine their source (Allègre, 2008; Table 13). Samples CC-MOLY stand for molybdenite from Caçador (three samples), SALG-MOLY and SALG-PY stand for molybdenite and pyrite from Salgadinho (one sample of each mineral), and BF-MOLY stand for molybdenite from the Bonfim skarns (three samples).

Measurements were done using a Thermo Scientific MAT 253 continuous flow isotopic ratio mass spectrometer with a magnetic sector gas source and the Vienna-Canyon Diablo Troilite (V-CDT) standard (Ding et al., 2001). Samples were heated at 1020°C and the obtained SO_2 was analyzed based on the molecular masses 64, 65 and 66. Data was processed using the software Isodat 3.0 and the mass fractionation ($\delta^{34}S$) was calculated for sulfur. All data present an associated error of 0.2‰.

5. RESULTS

5.1. Geochemistry Data

The analyzed metasomatic samples present several discrepancies between their chemical signatures. Comparisons between hydrothermally altered rocks and stages may be seen in the binary diagrams of Figure 9. Ca-Ba samples show the highest values for CaO, Fe_2O_3*, MgO, P_2O_5 and REE, while the potassic alteration has the highest alkalis and Al_2O_3 contents. In the Ca-Ba domain, the prograde stage is characterized by an enrichment in CaO, Fe_2O_3*, MgO, P_2O_5 and REE, while the retrograde stage exhibits higher Na_2O, Al_2O_3 and SiO_2 values. The enrichment in CaO in the CaO/Al_2O_3 ratio suggests Ca

metasomatism. A positive correlation is verified between P_2O_5 and HREE, likely due to apatite formation during the prograde stage. LREE displays the same trend but are mostly related to epidote-allanite and titanite crystallization.

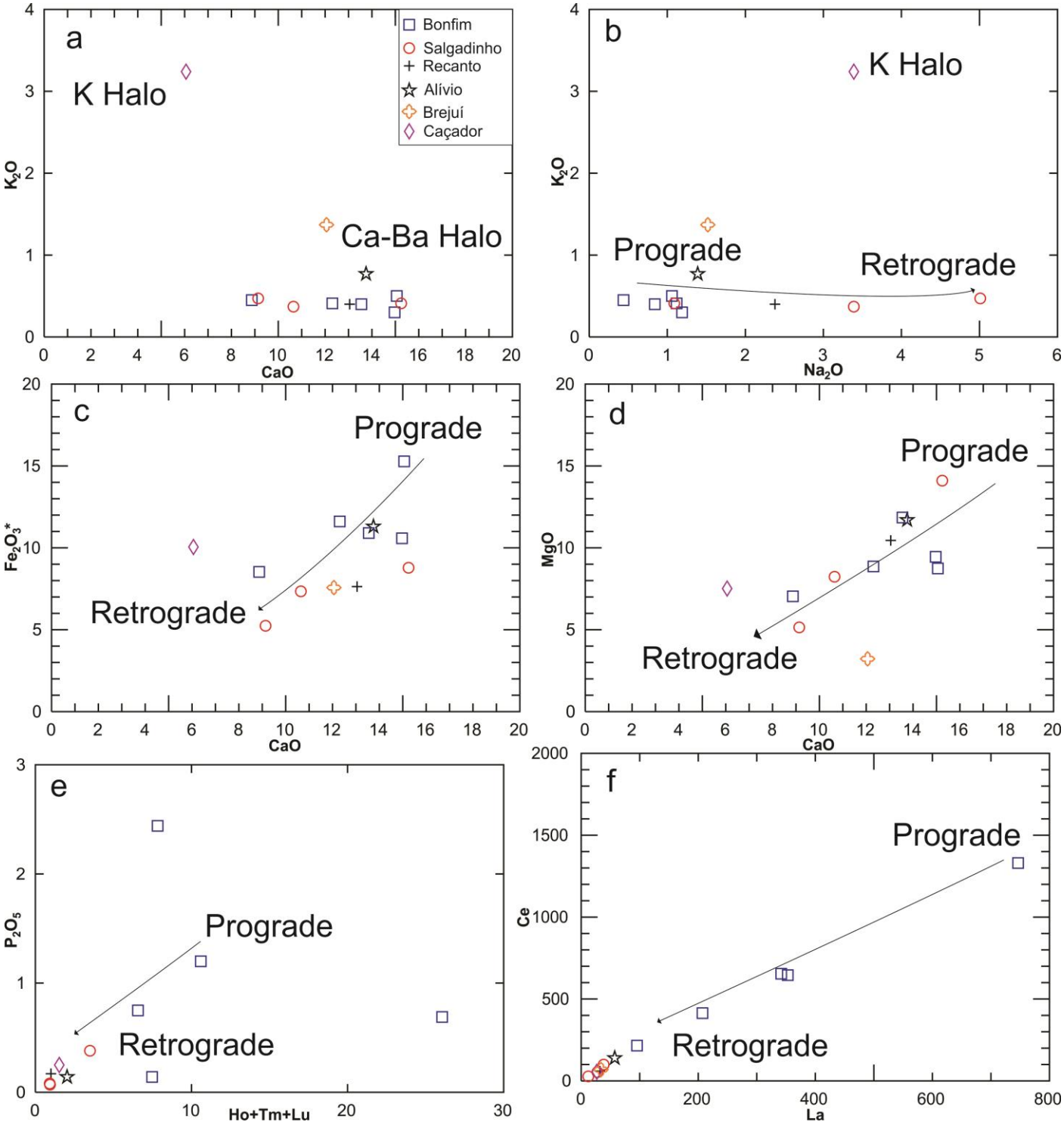

Figure 9. Whole rock geochemistry binary diagrams, highlighting the different chemical signatures of the Ca-Ba and K haloes and of the prograde and retrograde stages. Data from the Brejuí deposit (Salim, 1993) is also included. a: CaO vs K_2O diagram. b: Na_2O vs K_2O diagram. c: CaO vs Fe_2O_3* diagram. d: Cao vs MgO diagram. e: Ho+Tm+Lu vs P_2O_5 diagram. f: La vs Ce diagram.

Concerning MgO and Fe_2O_3* chemical exchanges, differences between Bonfim (Fe-rich) and Salgadinho (Mg-rich) samples may be explained by distinct wallrock compositions. MGDS samples become progressively enriched in CaO the closer they get to the marble front (Figure 10). This fact contrasts with

rocks from the root zones of the system because these are mostly affected by silicification processes, especially during the retrograde phase.

When compared with the data from Brejuí (Salim, 1993), the studied rocks plot in the horblende±clinopyroxene-skarns and clinopyroxe±garnet-skarns fields, matching field, petrographic and geochemical criteria, with the exception that garnet was absent in all Ca-Ba and K occurrences studied in this paper. In the SiO_2-W-Ba diagram, the prograde stage is represented by Ba-rich rocks, while the retrograde stage shows high W values in mineralized and higher SiO_2 contents in barren samples (Figure 10).

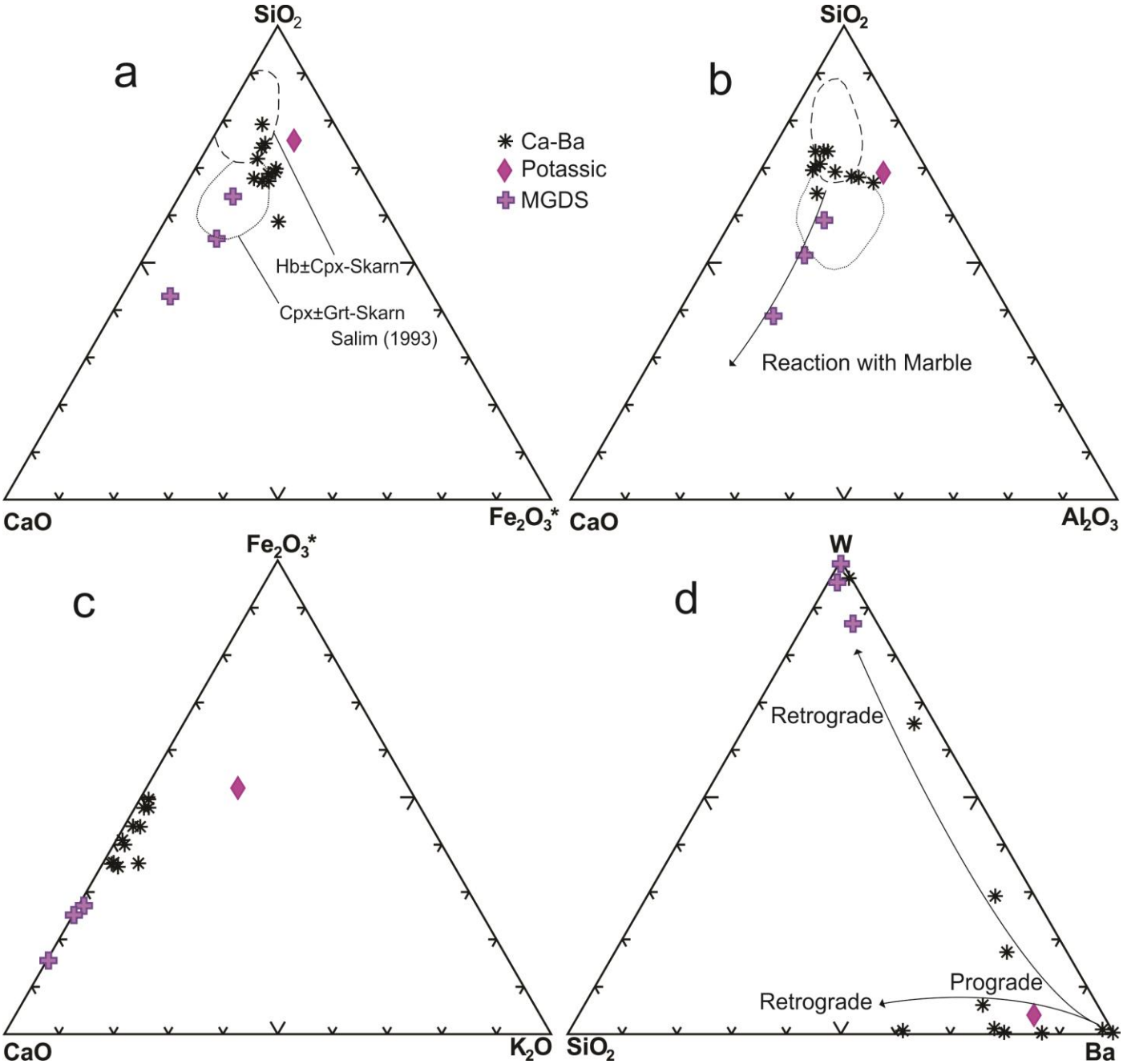

Figure 10. Whole rock geochemistry ternary diagrams. a-b: CaO vs SiO_2 vs Fe_2O_3* and CaO vs SiO_2 vs Al_2O_3 diagrams. Delimited domains correspond to the rocks studied by Salim (1993) in the Brejuí deposit. c: CaO vs Fe_2O_3* vs K_2O diagram, showing the chemical differences between the three studied haloes. d: SiO_2 vs W vs Ba diagram, comparing rocks from the prograde and retrograde stages.

In REE spidergrams, the studied rocks present a slight slope from LREE towards HREE, having, in most cases, more than ten times LREE than HREE contents in the same sample (Figure 11). Furthermore, most analyzed rocks present (La+Ce)/(Yb+Lu) ratios above 50. These may also show discrete negative Eu

and positive Tm anomalies. Rocks from the Ca-Ba alteration in the Bonfim deposit possess the highest REE sum, reaching 3159 ppm, while the average sum for the other studied deposits and occurrences is 176.7 ppm. In addition, samples from the prograde stage have higher REE values than those from the retrograde phase. These observations are compatible with the presence of REE-bearing minerals, such as apatite, epidote-allanite and titanite in these rocks, especially in the Ca-Ba alteration.

In the Brejuí deposit (data from Salim, 1993), MGDS rocks present gradually lower REE contents the closer they get to the marble front (Figure 11). REE-enriched distal rocks, such as hornblende-clinopyroxene skarns, undergo an increasing REE leaching process towards proximal, REE-poor assemblages, such as garnet-skarns. The same pattern was observed in other deposits/occurrences, where the prograde stage from the Ca-Ba alteration presents the highest REE values, then the retrograde phase, including both Ca-Ba and K rocks, and finally the MGDS.

A more focused analysis was held at the Bonfim deposit by comparing the REE signatures between host rocks (Ca-Ba alteration) and wallrocks (calc-alkaline meta- to peraluminous granitoids). Wallrock samples include POT-3, an unaltered wallrock; and fairly preserved samples from different depths of a same drill hole, which correspond to SEB-295 10.80m, SEB-295 13.60m, SEB-295 25.30m and SEB-295 42.30m. In general, both rock types display the same pattern, with LREE-enriched and HREE-depleted values and a discrete negative Eu anomaly, but the metasomatic samples contain REE contents nearly two orders of magnitude higher than the magmatic ones (Figure 11). POT-3 presents a positive Eu anomaly, along with the lowest REE values, presenting a distinct pattern from the SEB-295 samples. In these samples, REE values tend to decrease with depth, but then reach the highest values in the depth of 42.30m after being altered by the Ca-Ba alteration, represented by sample SEB-295 34.70m.

In multielement diagrams, samples from all deposits present a discrete enrichment in LILE and a depletion in HFSE, especially Ti (Figure 12). Locally, positive anomalies for Cs, Ba and LREE also occur. These chemical characteristics are an obvious reflex of the mineralogy of each hydrothermal alteration nature, with the Ca-Ba assemblage presenting higher REE, Nb, Y, U, Th and P contents due to the formation of accessory minerals such as apatite, epidote-allanite and titanite, and Ba due to the hyalophane-barite association. The potassic domain, on the other hand, presents with higher amounts of Cs, Rb and K due to its extensive biotite formation.

In the Salgadinho deposit, three samples with different textures were selected, namely, i) an undeformed amphibole-diopside-rich rock, ii) a banded rock with feldspar-rich and amphibole-diopside-rich domains, and iii) an amphibole-rich rock with a foliated texture. The sample with the highest values in the multielement diagram is the banded rock, followed by the one with the foliated texture, and finally the undeformed rock (Figure 12). This fact may not be associated with hydrothermal alteration stages, but rather with deformational processes. The banded sample is characterized by higher values of Cs, Th, U, Ta, Nb, Sr, Sm and Tb, which become gradually depleted in the other samples.

The transition between the prograde and retrograde hydrothermal stages in the Ca-Ba alteration is highlighted in the data from the Bonfim deposit (Figure 12). Samples related to the prograde stage are enriched in Ba, Ta, Nb, REE and Y, while the ones from the retrograde phase become poorer in these elements.

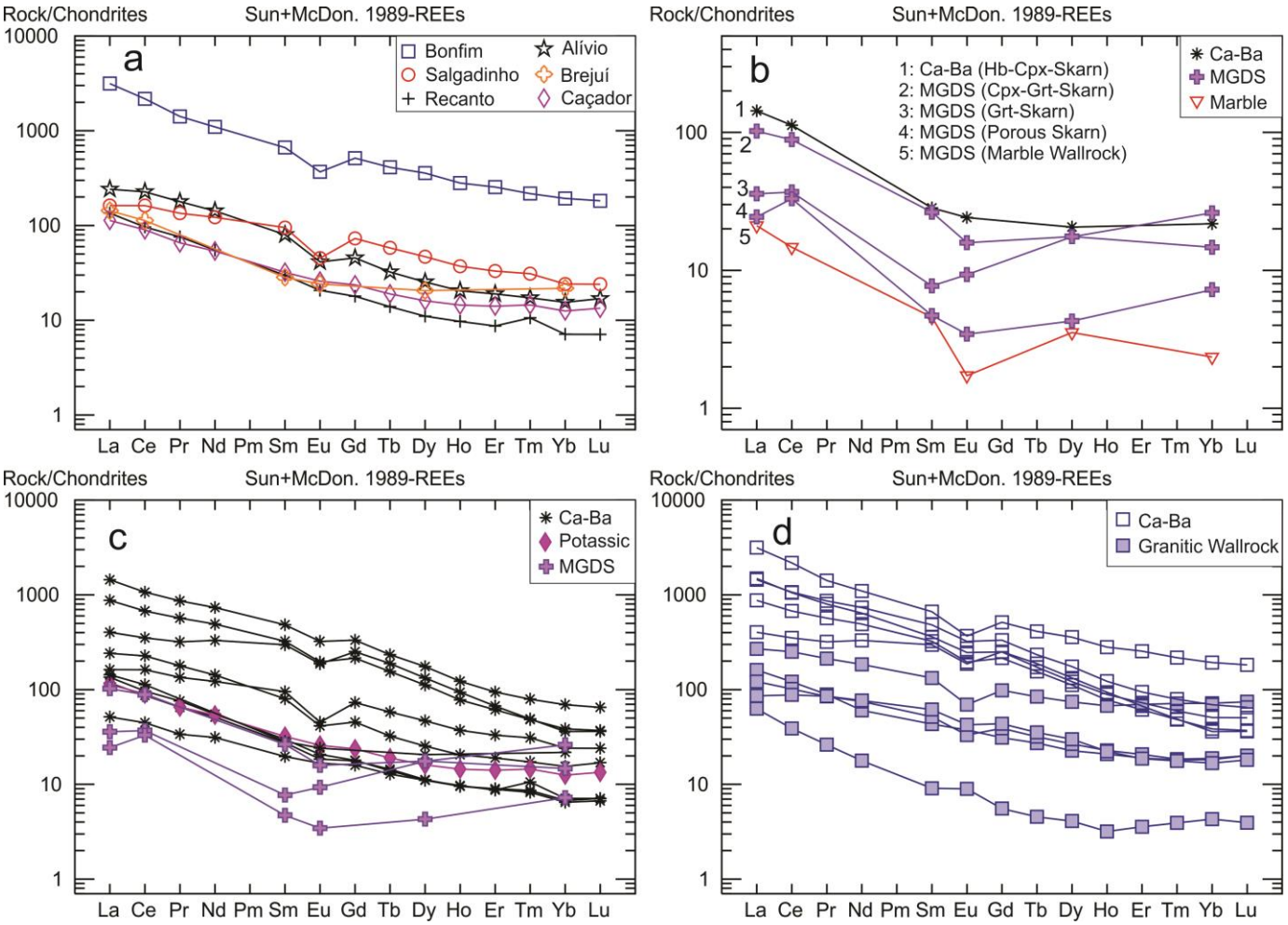

Figure 11. Whole rock geochemistry REE spidergrams, including data from the Brejuí deposit (Salim, 1993). a: Diagram with selected samples from each deposit. b: Progression of the interaction with marble wallrocks along the alteration front in the Brejuí deposit. c: Differences between the three studied haloes. d: Comparison between the Ca-Ba halo and the granitic wallrock in the Bonfim deposit.

5.2. Geochronology Data

5.2.1. U-Pb Dating

In cathodoluminescence images from all analyzed samples, zircon crystals present textural features showing that they were deeply affected by events after their formation, which may include metamorphic, deformational and hydrothermal processes. This fact is highlighted by fractures, which often appear filled by other minerals, mineral inclusions, erratic heterogeneous compositional domains and resorption/alteration borders. Nevertheless, some grains preserve their primary characteristics, such as oscillatory crystal zoning. Representative images of zircon grains from each sample are presented in Figure 13.

At the Bonfim deposit, 29 zircon grains were analyzed in the SEB-295 Ca-Ba alteration sample (Figure 13). The processed results produced a discordia diagram using the data from 16 crystals, showing Paleoarchean and Neoproterozoic upper and lower intercepts of 3324±33 Ma and 547±33 Ma, respectively.

At Pedro Tomás, one sample (PEDRO TOMÁS) from the granitic wallrock was collected and 32 zircon crystals were analyzed. Apart from its granitic nature, this rock is characterized by hydrothermal magnetite-rich bands which are subparallel to the main foliation (Figure 5). The produced discordia diagram based on 32 analyses yielded a Neoarchean age of 2699±11 Ma on its upper intercept. The lower intercept points to a Neoproterozoic-Ediacaran age of 530±42 Ma.

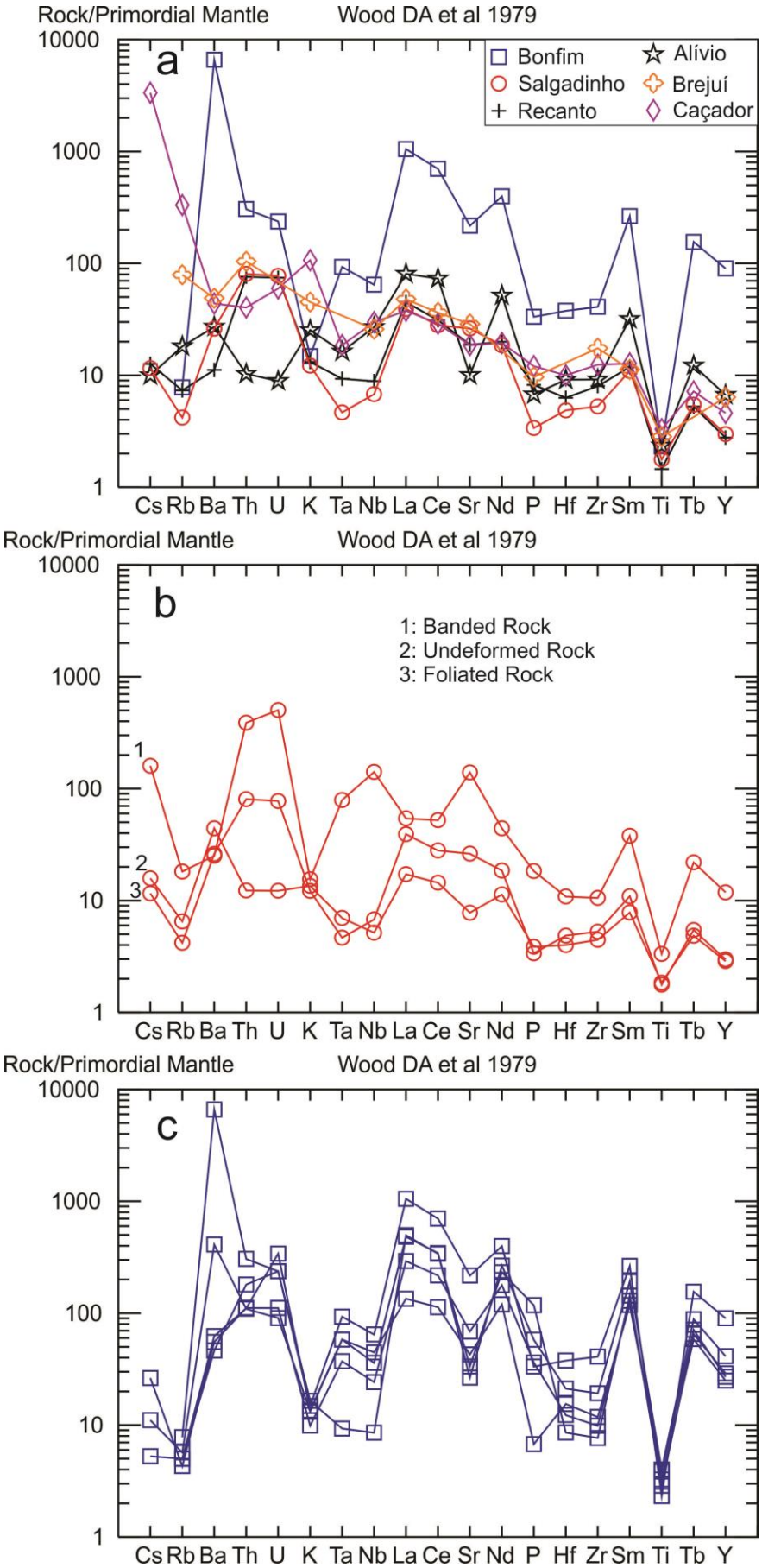

Figure 12. Whole rock geochemistry multi-element diagrams. a: Diagram with selected samples from each deposit. b: Comparison between three samples from the Salgadinho deposit. c: Comparison between Ca-Ba samples from the Bonfim deposit.

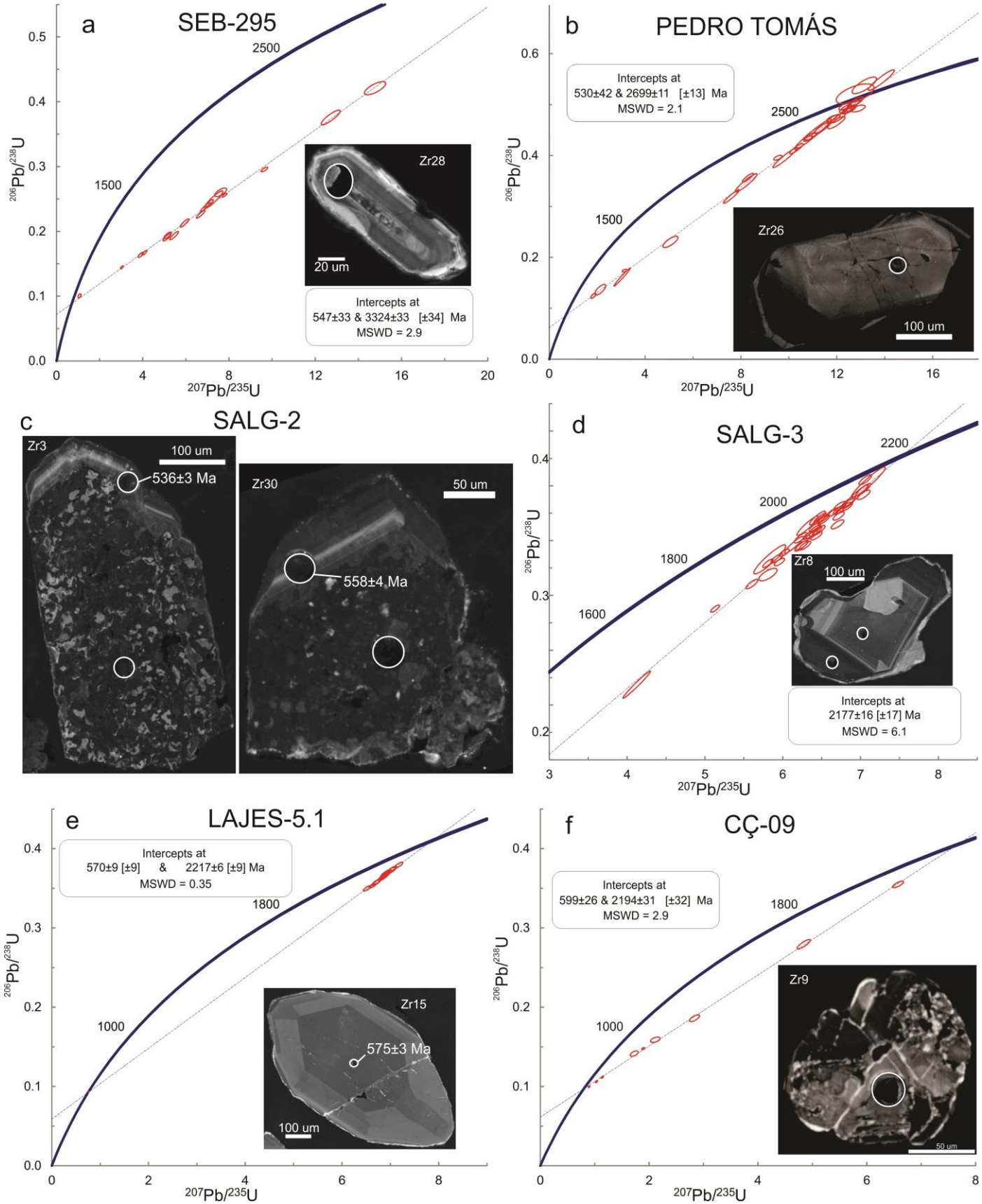

Figure 13. Zircon U-Pb analyses plate including Discordia diagrams and cathodoluminescence images. a: Discordia diagram from the Bonfim deposit. b: Discordia diagram from the Pedro Tomás occurence. c: Cathodoluminescence images of two concordant zircon grains with concordant borders from Salgadinho. d: Discordia diagram from other sample of Salgadinho. e: Discordia age of a third sample from Salgadinho along with a single concordant zircon grain. f: Discordia diagram from Caçador.

At the Salgadinho occurrence, three samples from the Ca-Ba alteration were analyzed. 30 zircon crystals were analyzed in each sample, and 10, 29 and 17 analyses were used to build discordia diagrams in samples SALG-2, SALG-3 and LAJES-5.1, respectively (Figure 13). All samples present Rhyacian Paleoproterozoic ages on their upper intercepts, dated as 2163±160 Ma (SALG-2), 2177±16 Ma (SALG-3) and 2217±6 Ma (LAJES-5.1). Two lower intercepts point to the Late Neoproterozoic-Ediacaran, with ages of 509±64 Ma (SALG-2) and 570±9 Ma (LAJES-5.1), while SALG-3 presents a large error and lacks a clear geological meaning.

At the Caçador occurrence, 19 zircon grains were anayzed in the CÇ-09 potassic alteration sample. 9 analyses were processed, producing a discordia diagram with Paleoproterozoic and Neoproterozoic upper and lower intercepts of 2194±31 Ma and 599±26 Ma, respectively (Figure 13).

While the Rhyacian ages in the Salgadinho and Caçador samples are fairly constrained by the discordia diagrams with ages of ca. 2.2 Ga, the Neoproterozoic-Ediacaran lower intercept ages are not due to their large errors and disperse results. Concerning younger ages, two of the three analyzed samples from Salgadinho (SALG-2 and LAJES-5.1) presented concordant zircon grains which are interpreted as better representatives of this event than the obtained lower intercepts. In the sample LAJES-5.1, the core of one possibly recrystallized or neoformed grain yielded a concordant age of 575±3 Ma (Figure 13; Table 7). In the sample SALG-2, both grains presented strongly altered cores, while their rims were clearly formed later (Figure 13; Table 5). In this sample, one of the crystals produced a concordant age of 558±4 Ma, while the second presented a concordia age of 536±3 Ma.

5.2.2. $^{40}Ar/^{39}Ar$ Data

In Morro do Careca, two aliquots of a pargasite sample were analyzed (Figure 14). This mineral is representative of the high temperature paragenesis of the Ca-Ba alteration, yielding ages of 553±3 Ma and 548±2 Ma. These analyses only produced small plateaus, with less than 50% of released 39Ar, which could be related to a partial resetting of the isotopic system.

In the Salgadinho occurrence, one sample of tremolite from the Ca-Ba alteration and one sample of biotite from the potassic alteration were analyzed (Figure 14). Tremolite, as an alkali-poor calcic amphibole, presented a K/Ca ratio lower than 0.04, which produced a larger error when compared with the other 40Ar/39Ar analyses. The tremolite 40Ar/39Ar analysis yielded an age of 557±7 Ma, which is similar to the data obtained for Morro do Careca.

Two aliquots from a biotite sample from the Salgadinho occurrence were also analyzed. Both results were affected by a heating event that occurred after the mineral's crystallization, and hence plateau ages were not produced. Nearly unreliable total fusion ages of 563±3 Ma and 499±2 Ma were obtained for aliquots SALGB-2 and SALGB-1, respectively.

Finally, biotite of the potassic alteration from Caçador was also analyzed, yielding consistent ages of 498±2 Ma and 501±2 Ma for aliquots CC-1 and CC-2, respectively (Figure 15).

When all data are compared, two age intervals become evident. The first, approximately between 560 to 550 Ma, is clearly defined for the hydrothermal amphibole formation in the Ca-Ba alteration, regardless of the stage. One of the total fusion ages for biotite in Salgadinho may also be related to this timespan. The second age interval is set ca. 500 Ma, representing hydrothermal biotite formation in the K alteration.

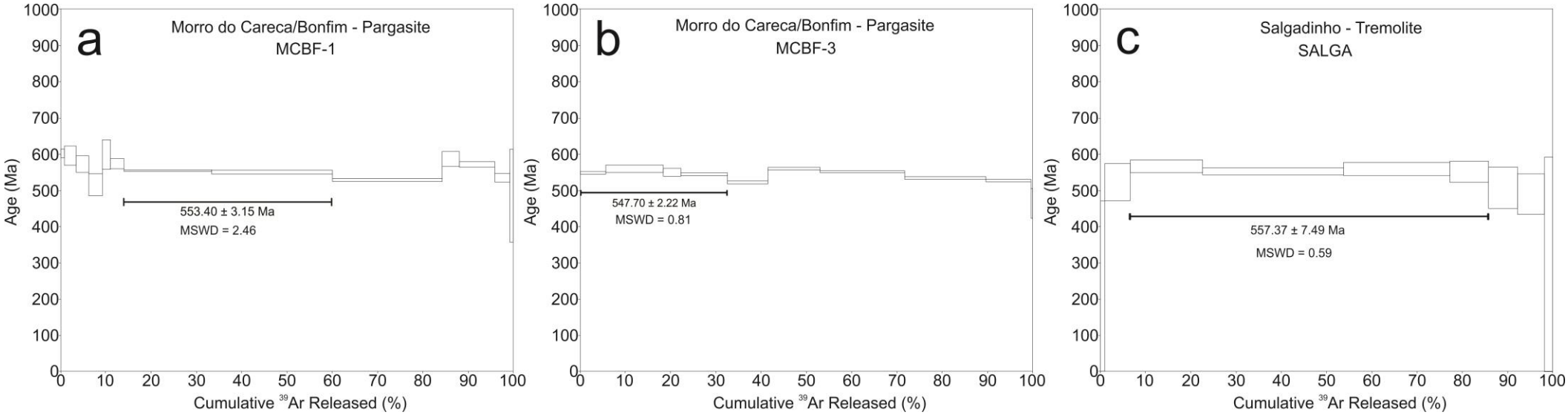

Figure 14. Amphibole ^{40}Ar-^{39}Ar step heating ages plate. a: Diagram for Morro do Careca/Bonfim, aliquot 1. b: Diagram for Morro do Careca/Bonfim, aliquot 2. c: Diagram for Salgadinho.

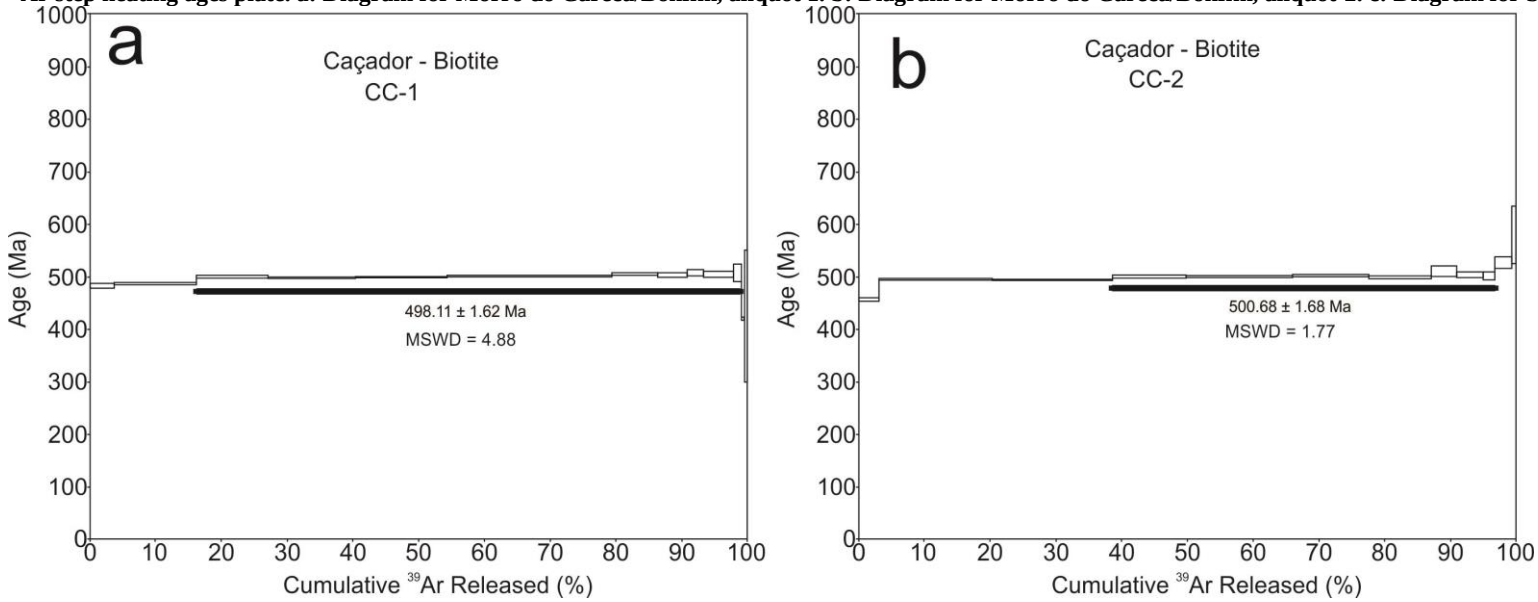

Figure 15. Biotite^{40}Ar-^{39}Ar step heating ages plate for Caçador, containing aliquots 1 (a) and 2 (b).

5.3. Sulfur Stable Isotopes Data

Sulfur stable isotopes analyses were conducted to determine the source of the hydrothermal fluid by comparing the obtained results with other geological materials (Hoefs, 2009; Figure 16; Table 13). The δ34S data show a low variation between samples from the same deposits/occurrences (i.e., less than 1‰). However, when samples from distinct locations are compared, sulfides present a wider δ34S range (6.77‰). Molybdenite grains from the K alteration in Caçador were the only analyses that yielded negative values, from -2.50‰ to –1.86‰. Molybdenite and pyrite from the Ca-Ba alteration in Salgadinho produced similar results, corresponding to 3.29‰ and 3.46‰, respectively. Molybdenite grains from the skarns of the Bonfim mine yielded δ34S values between 4.17‰ and 4.27‰.

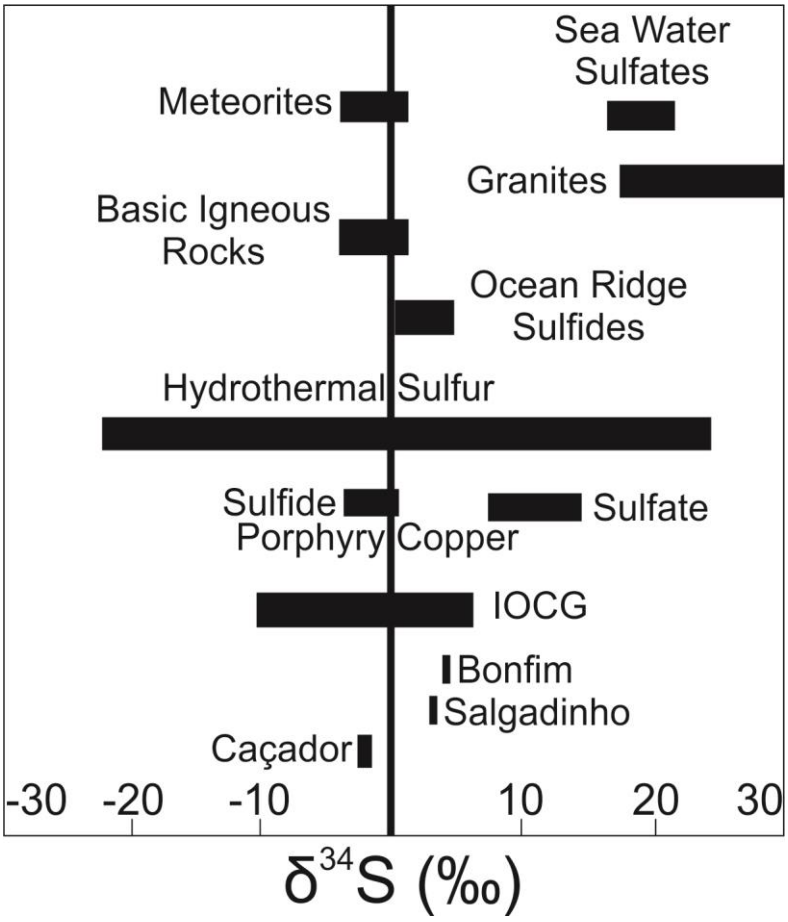

Figure 16. Sulfur isotopes data for sulfide samples from Salgadinho (molybdenite and pyrite), Caçador (molybdenite) and Bonfim (molybdenite). The fields for other geological materials are also shown for comparison (data from Allègre, 2008).

The obtained data for sulfides present values near 0‰, showing low S isotopic fractionation. Negative values may be associated with barite precipitation, leading to a more prominent fractionation between sulfides and sulfates.

6. DISCUSSION

6.1. Age and Tectonic Setting of the Wallrocks

This work identified distinct zircon U-Pb ages for some of the studied deposits and occurrences. The Bonfim deposit sample presented a Paleoarchean age of 3324±33 Ma, the Pedro Tomás occurrence sample showed a Neoarchean age of 2699±11 Ma, Salgadinho samples yielded Paleoproterozoic ages of 2177±16 and 2216.9±5.6 Ma, and Caçador presented a Paleoproterozoic age of 2194±31 Ma. Cathodoluminescence images from the analyzed crystals show that they were affected by later events unrelated to their formation (Figure 13). These results lead to the conclusion that the analyzed zircon samples correspond with inherited grains from the wallrocks.

In all studied deposits and occurrences, wallrocks correspond to granitoid or orthogneissic rocks, which are representative of at least three different basements of Paleoarchean, Neoarchean and Paleoproterozoic ages. The Paleoarchean rock from the Bonfim deposit could be associated with the Paleo- to Neoarchean São José do Campestre Massif, and may also be related with the 3.5 Ga São Tomé mafic-ultramafic layered intrusion, since it is close (i.e., approximately 10 km) to the Bonfim mine (Dantas et al., 2004; Ruiz et al., 2018; Figure 17).

The Neoarchean Pedro Tomás wallrock sample could represent an extension of the Archean lithologies from Bonfim and São Tomé, since these locations are linked by the same lineament (Ruiz et al., 2018; Figures 1, 13 and 17). According to Dantas et al. (2013), rocks from the São José do Campestre Massif were formed in a convergent tectonic setting, where subducted oceanic crust and the mantle wedge were the main sources for the magmas, which were formed through the recycling of older crust and successive episodes of arc accretion.

Regardless of the alteration type, the Paleoproterozoic ages from Salgadinho and Caçador samples are associated with the Caicó Complex (Souza et al., 2007). Data from Souza et al. (2016) for this basement unit record arc and collisional tectonic settings with mostly juvenile signatures between 2.4 and 2.2. Ga (Souza et al., 2016).

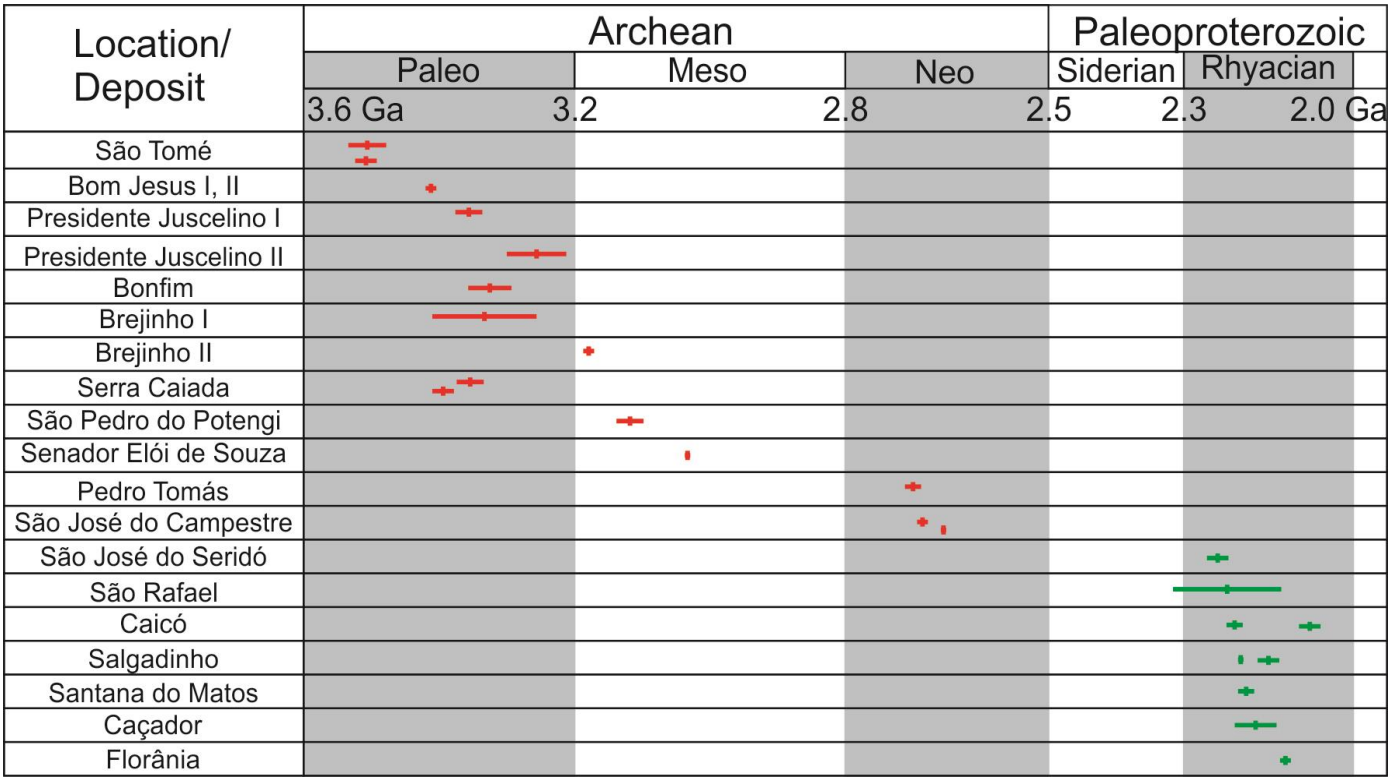

Figure 17. Archean and Paleoproterozoic geochronological data for the Seridó Fold Belt based on U-Pb analyses. Used references include Dantas (1996), Dantas et al. (2004, 2013), Souza et al. (2016), Ruiz et al. (2018) and this work for the São José do Campestre/Archean basement rocks of the Seridó Mobile Belt (in red); Hollanda et al. (2011), Souza et al. (2007, 2016) and this work for the Paleoproterozoic G2 granitoids and Caicó Complex (in green).

6.2. Constraining the W-Mo Mineralization

Multiple episodes of partial melting of the old continental crust of the Seridó Mineral Province with subsequent fractional crystallization processes led to an anomalous geological background for tungsten in both basement and supracrustal rocks. W and Mo geochemical data from igneous, metamorphic and sedimentary rocks of the Seridó Mobile Belt (data from Cunha de Souza, 1987; Salim, 1993; and this work) commonly show values more than ten times higher than the average crust composition (data from Parker, 1967).

The Neoproterozoic-Ediacaran Brasiliano Orogeny led to the formation of a transcontinental strike-slip system with associated regional metamorphism and plutonic activity. This collisional event contributed for the formation of a thick continental crust in the Seridó Fold Belt, reaching Curie depths greater than 30 km (Correa et al., 2016). Furthermore, Brasiliano granitoids present crustal recycling isotopic signatures (Archanjo et al., 2013; Souza et al., 2016; Hollanda et al., 2017). In accordance with data from the literature, which is represented in Figure 18, this work identified several zircon U-Pb ages correlated with this event, which were interpreted as i) syn-peak representatives of this orogeny between 600 Ma and 570 Ma, ii) regional metamorphism or initial/early metasomatism representatives between 560 Ma and 550 Ma, and iii) tardi-tectonic processes representatives between 536 Ma and 530 Ma.

Tungsten and associated metals have possibly been incorporated into this continental crust since the early Archean, but it was probably only during the Late Neoproterozoic-Ediacaran Brasiliano collisional event that they became more concentrated. During the latest stages of the Brasiliano cycle, partial melting of this thick, W±Mo-endowed, constantly reworked crust in deep environments produced I- and S-type granitoids, which further remobilized and concentrated these elements in the magma. Later, upwards migration of the magma coupled with differentiation processes led to the exsolution of a reduced metalliferous volatile-rich phase. All sulfur stable isotopes results for sulfides corroborate with this assumption, since they indicate a magmatic-derived origin for the metasomatic process.

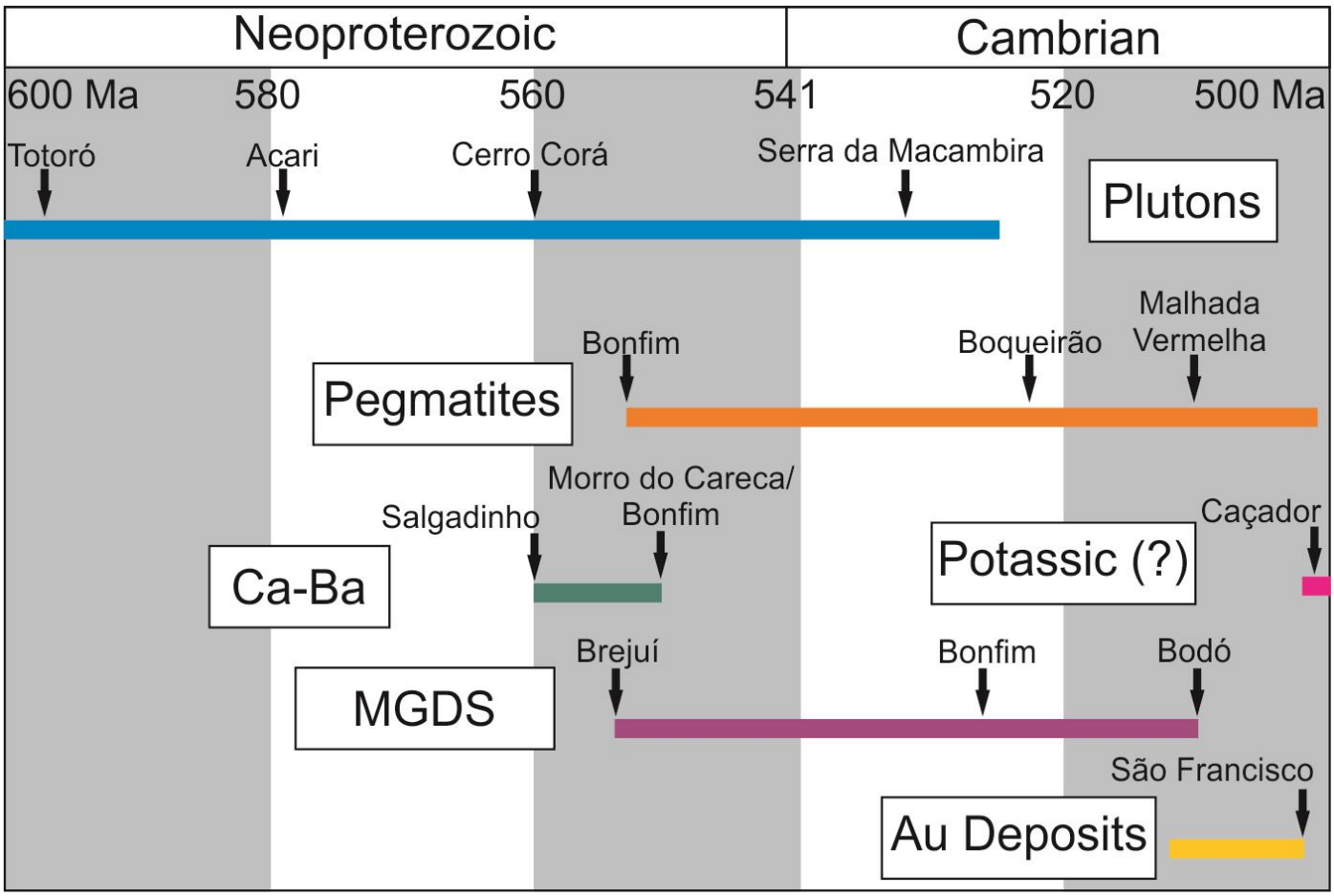

Figure 18. Neoproterozoic and Cambrian geochronological data for the Seridó Fold Belt based on U-Pb, Ar-Ar and Re-Os analyses. Used references include Jardim de Sá (1994), Brito Neves et al. (2003), Baumgartner et al. (2006), Souza Neto et al. (2008), Archanjo et al. (2013), Nascimento et al. (2015), Souza et al. (2016), Hollanda et al. (2017), Ruiz et al. (2018) and this work for Brasiliano plutons; Araújo et al. (2005), Baumgartner et al. (2006), Beurlen et al. (2009, 2014) for the Borborema Pegmatite Province; this work for Ca-Ba and K haloes; Hollanda et al. (2017) for W mineralization in the MGDS; and Araújo et al. (2005) for lode gold mineralization events. A possible true age of the potassic alteration is discussed in the main text.

Similar processes probably occurred in several rocks both vertically and horizontally, forming more than 700 scheelite occurrences in the Seridó Fold Belt and basement inliers. This assumption also implies that there is likely more than one tungsten source in the area. Most of these occurrences are linked and controlled by subvertical shear zones and lineaments, which acted as pathways for a channelized hydrothermal fluid flow. The metasomatic solution interacted with several granitoid wallrocks from the basement, forming the Ca-Ba and K alteration in the root zones of the Seridó Mineral Province (Figure 19).

Hydrothermal alteration occurred in two main phases. The early, high temperature prograde stage of the Ca-Ba alteration produced metasomatic minerals along wallrocks with fairly preserved primary textures. The progression of this alteration style, along with deformational processes, fully obliterated the wallrock features, forming the diopside-amphibole-feldspar (DAF) assemblage. Later, the retrograde stage of the Ca-Ba alteration re-equilibrated the older paragenesis to lower temperature conditions, producing the amphibole-feldspar (AF) association. The retrograde stage of the Ca-Ba alteration is characterized by an enrichment in CaO, MgO, Fe_2O_3* Ba and REE, and a depletion in SiO_2, Al_2O_3, K_2O and Na_2O.

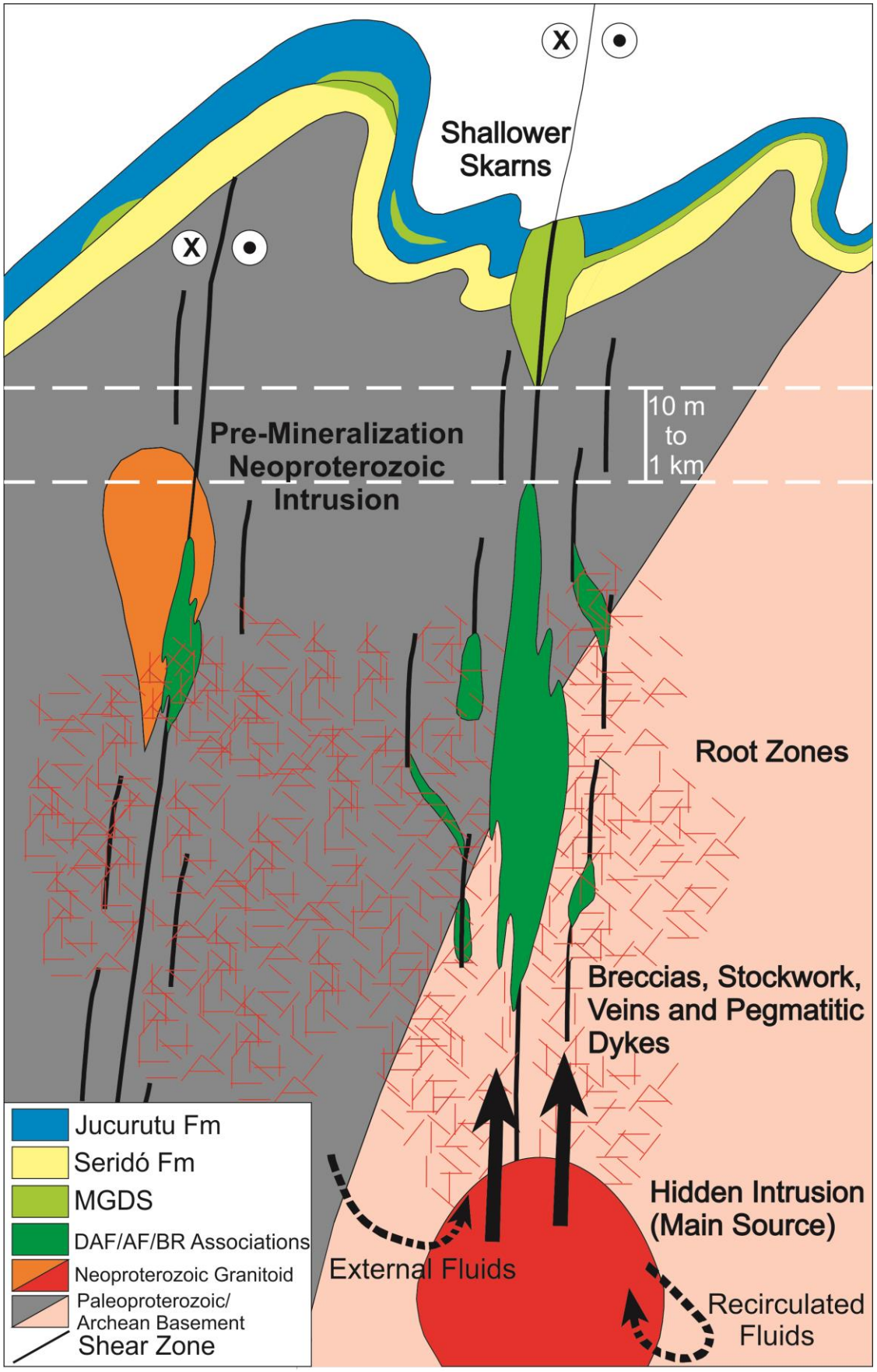

Figure 19. Schematic metallogenetic model for W-Mo mineralization in the Seridó Mineral Province from Corrêa et al. (Chapter 2). During the Neoproterozoic-Ediacarian Brasiliano Cycle, deep intrusive bodies, which are possibly hidden, exsolved metalliferous hydrothermal fluids that migrated along subvertical structures from the strike-slip system. The metasomatic solution interacted with different wallrocks, producing Ca-Ba, K and MGDS rocks, precipitating scheelite and associated minerals along them.

Just as the U-Pb data, the $^{40}Ar/^{39}Ar$ results point to a complex formation history for both Ca-Ba and K metasomatic rocks. Amphibole and biotite $^{40}Ar/^{39}Ar$ data from these hydrothermally altered rocks have implications for the ages of hydrothermal processes, as well as mineralization events, all of which occurred during the Late Neoproterozoic-Ediacaran interval. The amphibole $^{40}Ar/^{39}Ar$ analyses from this work effectively defined the age of formation for the Ca-Ba alteration as ca. 560-550 Ma, with the results obtained for Bonfim and Salgadinho (Figure 18). The molybdenite Re-Os age of 555±2 Ma obtained by Hollanda et al. (2017) for the Brejuí deposit is also in accordance with the ages from this work, suggesting that the root zones and skarns formation was coeval. The younger molybdenite Re-Os ages of 524±2 Ma and 510±2 Ma for the Bonfim and Bodó deposits obtained by the same work may be either products of remobilization processes or evidences that the root zones/skarns formation event lasted for at least 40 Ma.

The potassic alteration presents a tardi-tectonic, syn-mineralization character, being correlated texturally, mineralogically and chemically with the retrograde stage of the Ca-Ba alteration. This alteration style is represented by strongly foliated biotite-rich bands with subordinate amphibole that commonly appears at the borders of the Ca-Ba domain as a superimposed alteration. Rocks from the K alteration commonly appear with disseminated scheelite and sulfides, as well as pegmatitic injections. This domain is characterized by an enrichment in K_2O, Na_2O, SiO_2, Cs, Rb, Mo and W.

The biotite $^{40}Ar/^{39}Ar$ ages for the K alteration from this work in Caçador and Salgadinho appear to be at ca. 500 Ma (Figure 18). Although a 50 Ma gap between the formation of the Ca-Ba and K alteration is possible, these ages may be better explained by two interpretations. The first suggests that biotite may have been produced after amphibole (by millions or tens of millions of years), and then remobilized by tardi-tectonic processes, exemplified by pegmatitic intrusions, plutonic activity and strain intensification along structures. The second is based on differences in mineral closure temperatures. When these are considered, hornblende, molybdenite and biotite tend to close their isotopic systems approximately 550°C for K-Ar, 500°C for Re-Os and 300°C for K-Ar, respectively (Suzuki & Masuda, 1996; Ganguly & Tirone, 2009). The 50 Ma interval could in turn represent the regional-scale tectonic cooling history, recording a decrease of the geothermal gradients by ca. 250°C during this period.

The association of both Ca-Ba and K hydrothermal alteration domains with pegmatites may be reflexive of their emplacement in deeper crustal levels. The Neoproterozoic Brasiliano Cycle extensive magmatism increased the regional geothermal gradient, maintaining temperatures above 500°C in the vicinities of intrusive granitoids and pegmatitic bodies. Depth calculations for these rocks position them in the 5 to 15 km interval (Beurlen et al., 2014; Chagas, 2017). These conditions are similar to those calculated for the MGDS deposits (Souza Neto et al., 2008 and references therein). These thermobarometric parameters promoted the ideal conditions for fluid circulation, consequently carrying metals with them. In this sense, the root zones underwent similar processes to lead to the formation of the W-skarns of the Seridó Mineral Province.

Some samples from the root zones in this work presented highly anomalous values for W and Ba, which were, in some cases, even above the detection limit. These results highlight that these were areas of focused fluid flow that resulted in high metal concentrations along the Transbrasiliano strike-slip system (Figure 19). Initially, the hydrothermal solution was probably hot and reduced, which would allow the transportation of Ba, among other elements. In the root zones, processes of fluid mixing or reaction with wallrocks could change the REDOX stability of the system, leading to the precipitation of sulfate (barite) and Fe^{3+}-bearing minerals (magnetite and epidote-allanite) under more oxidizing conditions. Then, the following retrograde alteration was the main phase for sulfides and scheelite precipitation.

From the root zones, where basement granitoid wallrocks occur, the hydrothermal fluid migrated further upwards and interacted with the highly reactive marbles from the Jucurutu Formation, as well as other lithologies from the Seridó Group, forming the well-known MGDS deposits. Since the highest sulfide $\delta^{34}S$ values occur in the Bonfim skarn samples, they could represent the interaction between magmatic-hydrothermal fluids and metasedimentary rocks. It is likely that the fluid-wallrock reaction was the most efficient scheelite precipitation mechanism, since the ore is usually hosted in lithological boundaries between carbonates and other rocks. This process abruptly lowered the temperature and simultaneously increased the pH of the system.

6.3. The Effect of Similar Alteration Processes on Different Wallrocks in the Root Zones

Data from this research have shown that both Ca-Ba and K metasomatic rocks are developed in Paleoarchean, Neoarchean and Paleoproterozoic granitoid wallrocks. Regardless of the studied location, similar alteration patterns, parageneses and textures were produced during the Neoproterozoic-Ediacaran Brasiliano Cycle, suggesting that these hydrothermally altered rocks, representative of the root zones of the whole W-enriched system, were formed under similar physicochemical conditions. While these rocks share characteristics in a macroscopic scale, distinct features between deposits and occurrences may be recognized in microscopic observations and by whole rock and mineral chemistry analyses.

Major and trace elements signatures point to discrepancies between deposits. For example, Bonfim and Morro do Careca, the only locations where mineralization occurs in Paleoarchean wallrocks, present very high values of P2O5 and REE when compared with the other studied occurrences. This observation leads to the conclusion that apatite and other REE-bearing minerals were produced after the remobilization and concentration of these elements from an already anomalous wallrock. Hence, while W is most certainly derived from a magmatic source, migrating as an oxyanionic complex along the hydrothermal fluid, REE, P2O5 and other elements may be more dependent on the wallrock composition. However, this proposition does not state that the only source of these elements are the wallrocks themselves, since apatite and REE-bearing minerals occur in most studied locations, but that the wallrock composition may play a decisive role in achieving the highest observed concentrations.

Concerning the mineral chemistry analyses from Corrêa et al. (Chapter 2), other possibly wallrock-dependent features observed in minerals are seen in the differences between Fe2+ and Mg contents, as seen in pyroxene and amphibole grains. While samples from Salgadinho present Mg-rich diopside and magnesiohornblende, those from Bonfim are richer in Fe2+. For amphibole, the Alívio deposit presents with crystals of higher alkali contents than most deposits. Furthermore, titanite grains from Salgadinho are pleochroic, being enriched in HREE, while crystals from Bonfim are richer in LREE. Biotite from Caçador is richer in FeO and TiO2, while grains from Bonfim exhibit higher MgO values. Mineral chemistry analyses are effective for tracking partitioning processes between elements, but in this case, they also show that minerals with different chemical signatures may be produced based on distinct wallrock compositions.

Although the different wallrocks affected the chemical characteristics of the host rocks of the studied deposits and occurrences, the hydrothermal fluid was the most important factor for the formation of the Ca-Ba and K alteration rocks. The hydrothermal processes that culminated in W mineralization led to extensive amphibole and biotite formation in the root zones of this system.

6.4. The Formation of Pyroxene and Amphibole in the Root Zones

Although the wallrocks from the studied deposits present different ages, all of them correspond to granitoids. Considering this fact, how can felsic rocks be transformed into lithologies with such a large quantity of mafic minerals (e.g., pyroxene, amphibole and biotite)? An interesting observation is that the average amphibole composition for the Ca-Ba alteration (data from Corrêa et al., Chapter 2) is similar to the

average whole rock geochemical data for these hydrothermally altered rocks. This implies that the metasomatic fluid transported some elements from one or more hidden sources, while others were extracted from the wallrocks.

The amphibole supergroup is composed of minerals which may contain a wide variety of chemical elements, including alkalis, alkaline earth metals, Fe, Si, Al and OH (Leake et al., 1997; Hawthorne et al., 2012). The calculated P-T parameters for the prograde alteration in the Bonfim, Itajubatiba and Brejuí skarns are above 500°C and 2 kb (Salim, 1993; Souza Neto et al., 2008), which are physicochemical conditions where amphibole enters the system as a stable mineral phase. Hence, this mineral could form in the root zones after the interaction between a Ca-, Mg-, Fe- and OH-rich fluid with a Na- and K-rich granitoid wallrock (obviously, alkalis could have also been transported in the fluid). The same logic may be applied to diopside, as well for other metasomatic minerals in these domains.

Further implications of the hydrothermal fluid may be applied based on different metasomatic parageneses. Concerning the Ca-Ba alteration, the early prograde stage is characterized by a diopside-rich paragenesis, a higher temperature and anhydrous minerals. Then, the mineralogical assemblage becomes amphibole-dominant (pargasite-magnesiohornblende), which, as a hydrated mineral, represents a stronger influx of metasomatic fluid. Later, the retrograde stage, while still characterized by an amphibole-dominant assemblage (magnesiohornblende-tremolite), presents a lower temperature paragenesis. Both field observations and chemical data point to the fact that the potassic alteration is a late alteration style, correlated with the retrograde stage.

One of the main controlling agents for the formation of different textural/mineralogical domains may be distinct fluid/rock ratios, as seen in Figure 5c. Quartz segregations represent areas of focused fluid flow. On its borders, coarse-grained non-oriented amphibole crystals are formed due to the high hydrothermal solution availability. These are followed by medium- to fine-grained feldspar-amphibole-rich domains. Finally, in lower fluid/rock ratio zones, medium- to fine-grained epidote-diopside-amphibole-rich areas are developed.

Geochemical and fluid inclusion analyses from the MGDS of Brejuí (Salim, 1993) highlight the reaction between the hydrothermal fluid and carbonate wallrocks, producing a H_2O-poor and CO_2-rich solution. The carbonic/aqueous-carbonic fluid produced an anhydrous paragenesis where diopside and/or garnet are the prevailing mineral phases.

Since it is formed from a possibly hidden intrusion, through fluid migration along subvertical shear zones and finally reaching the various ore deposition sites, the W-Mo-endowed metasomatic solution experienced several compositional changes. Nevertheless, sulfur isotopic analyses for sulfides show that they preserved their essentially magmatic signature (i.e., nearly 0‰), as seen in Figure 16.

6.5. The Importance of the Borborema Pegmatite Province for W-Mo Endowment

In the literature, although Hollanda et al. (2017) suggest that the regional W-Mo mineralization may be coeval to pegmatitic intrusions, no clear association between MGDS and pegmatites has been observed in the Seridó Mineral Province. In the root zones, though, their relationship is much clearer. Discordant and/or subconcordant pegmatitic dykes were present in all studied locations, especially those where potassic alteration occurs. Their common presence in the root zones and typical absence in the MGDS may be evidence for different emplacement levels for these deposit modalities, positioning the pegmatites and Ca-Ba and K metasomatic rocks in deeper environments and the MGDS in shallower environments (by tens to hundreds of meters).

Analytical data also corroborate with possible correlations between these lithologies. U-Pb, Re-Os and $^{40}Ar/^{39}Ar$ dating for pegmatites (Araújo et al., 2005; Baumgartner et al., 2006) and W-bearing rocks

(Hollanda et al., 2017; Ruiz et al., 2018; this work) point to postpeak Brasiliano ages, mostly in the 550-500 Ma interval (Figure 18). Hence, even if pegmatitic rocks and W-Mo mineralization are unrelated, they are synchronic.

Classic models in the literature for tungsten deposits point to magmatic S- or I-type granites which interacted with continental crust rocks as potential sources for W (Newberry & Swanson, 1986; Pirajno, 2009; Sharma & Srivastava, 2014). Thickened crust conditions were achieved during the Neoproterozoic Brasiliano Collage, reaching Curie depths above 30 km in this region (Correa et al., 2016), allowing for interactions between possible I-type magmas and continental crust material. Pegmatites from the Borborema Pegmatite Province are associated with S-type granitic sources due to their peraluminous nature, highlighted by their mineralogy and geochemical signature (Beurlen et al., 2014, Corrêa et al., Chapter 2; this work). Both I- and S-granite types could be produced in these conditions, showing that the pegmatites and W-bearing rocks could have common sources. Furthermore, pegmatites are acknowledged for providing volatiles to the hydrothermal fluid, which could also aid in metallogenetic processes (Hart, 2007; Rasmussen et al., 2011).

Among the studied rocks in this paper, Mineragram is the only outcrop that presents characteristics which appear to be transitional between granites and pegmatites. Containing two micas, garnet and tourmaline, this rock also exhibits a peraluminous nature. Furthermore, biotite-schist xenoliths from the Seridó Formation, which show injections from the pegmatoid granite (Figure 8), suggest that this rock could have been produced after the partial melting of the sedimentary rocks from the Seridó Group. This suggestion leads to the hypothesis that the pegmatitic granite from Mineragram is representative of a possible source for the Borborema Pegmatite Province. Hence, it could also be a representative of a source rock for tungsten and associated metals in the Seridó Mineral Province

6.6. Regional-Scale W-Mo and Au Zoning: The Relation Between Skarns and Intrusion-Related Deposits

The Seridó Mineral Province presents distinct metalliferous associations, where an earlier W±Mo system is superimposed by an Au±Bi±Te system. These are easily distinguished by rheological and structural criteria, as seen in the Bonfim mine. The W±Mo association occurs in the ductile domain, represented by N30°E-trending shear zones and folds, while the Au±Bi±Te system is associated with brittle or brittle-ductile N70°W-trending faults and veins that crosscut the skarns (Souza Neto et al., 2008; this work). Lode gold-only deposits are typically hosted in amphibolite facies rocks mostly controlled by NE-trending shear zones, as a result of a late- to posttectonic reactivation that led to mineralization (Araújo et al., 2005; Figure 18).

The spatial distribution of the W-Mo and Au metalliferous associations is shown at Figure 20. The types of occurrences and/or deposits cited in the previous paragraph are mostly associated with shear zones and Brasiliano plutons (Silva, 2000; Araújo et al., 2002; Santos et al., 2014). The main W±Mo skarn deposits of the Seridó Mineral Province, such as Brejuí, Bodó, Bonfim, Bonito, Malhada Limpa, Quixabá and Quixeré, occur to the west, while the São Francisco Au mine is located to the east, defining a schematic and arbitrary limit between W-Mo and Au trends. As one of the major structures in the study area, the Patos shear zone is displaced by both lithological units and metalliferous trends by at least 50 km in the EW direction (Figures 1 and 20). South of the Patos shear zone, in the Zona Transversal Domain, gold-quartz vein deposits and occurrences prevail, while W-Mo deposits and occurrences become more restricted.

When considering the deposit's horizontal distribution, a resembling regional-scale zoning is verified in the Reduced Intrusion-Related Gold System (RIRGS) of the Tintina Gold Province, where typical RIRGS, such as Fort Knox and Dublin Gulch, are formed near and/or associated with W-skarns, such as Mactung and Cantung, being controlled by plutonic activity and/or structures (Dick & Hodgson, 1982;

Mathieson & Clark, 1984; Goldfarb et al., 2000; Goldfarb et al., 2005). Major faults, such as Tintina and Denali, displace RIRGS deposits that belong to the Tombstone Belt and separate RIRGS from deposits of controversial origins (Hart, 2007).

Deposits from both provinces show that the mineralization occurred under similar physicochemical conditions. In the Tintina Gold Province, anhydrous W-skarns were formed in earlier, hotter temperatures (from ca. 500°C to 650°C), followed by the Au-Bi-Te association in later, cooler conditions, generally in the 300°C to 350°C interval (Goldfarb et al., 2000; Hart, 2007). In the Seridó Mineral Province, W-Mo skarns were formed at temperatures between 450°C and 580°C and pressures in the 2-4 kb interval (Table 1 and references therein), while the mineralization in gold-only deposits occurred at 270-350°C and 1-3.4 kb (Coutinho, 1994).

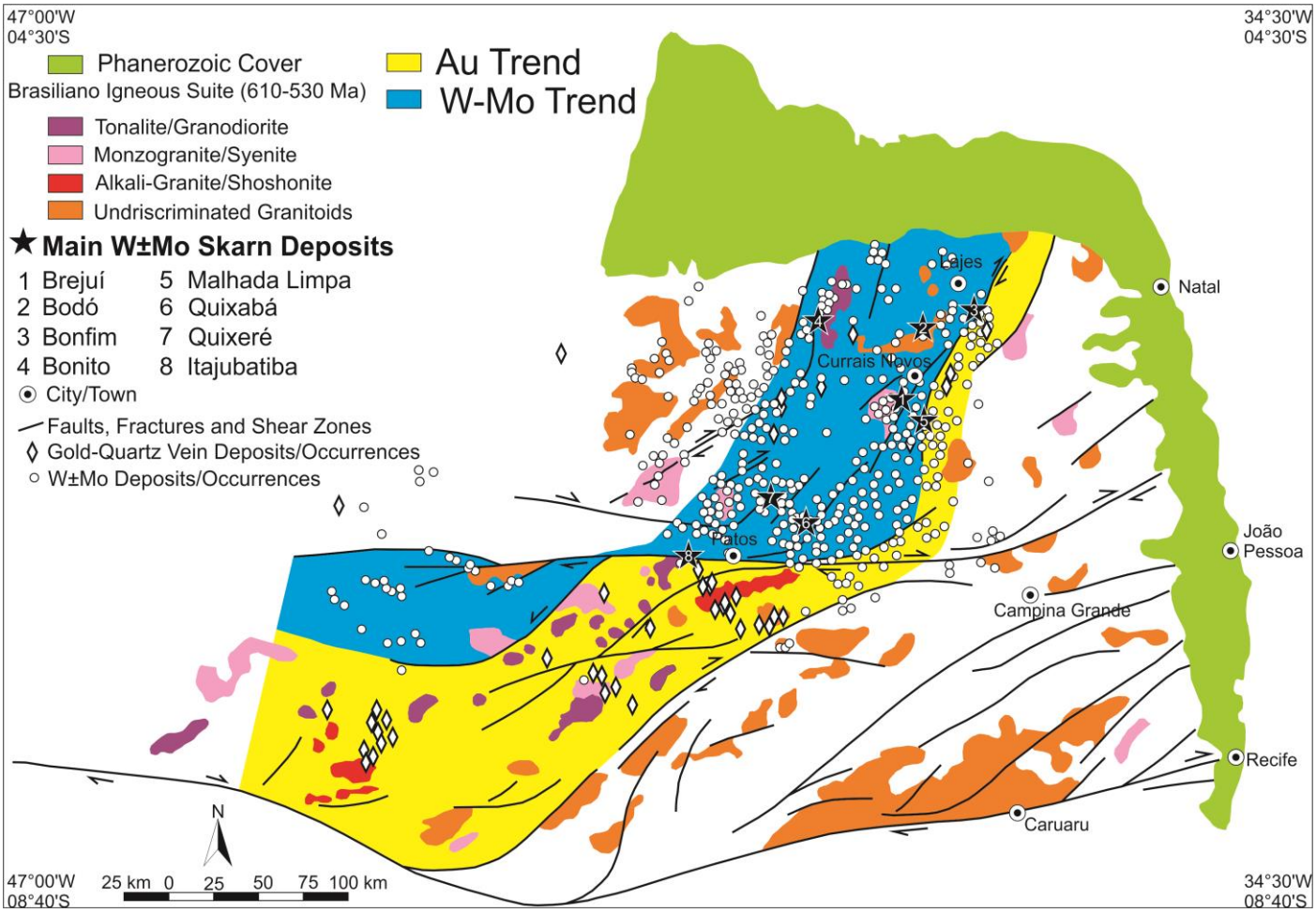

Figure 20. Regional-scale metalliferous zoning of W-Mo and Au deposits/occurrences. The map was adapted from Archanjo et al. (2002) and Souza Neto et al. (2008), and the areas for each trend were arbitrarily delimited based on the locations of deposits and occurrences, but also respecting lithological boundaries and major structures. Several lithological units were removed in order to highlight the metalliferous trends and the influence of shear zones and Brasiliano intrusions.

In the Seridó Mineral Province, scheelite-molybdenite-bearing rocks, such as the MGDS and Ca-Ba/K alteration, and gold deposits, such as Ponta da Serra, Simpático and São Francisco, are mostly controlled by strike-slip shear zones and/or intrusive bodies (Araújo et al., 2002; Araújo et al., 2005; Souza Neto et al., 2008, Figure 20). Coutinho (1994) suggested a magmatic-hydrothermal origin for the lode gold deposits of the study area, based on the anomalous contents of K, Ba, Rb, Bi, Te, Mo, F and B in hydrothermally altered rocks. In this sense, W-Mo skarns and auriferous lode deposits from the study area may belong to the same system, rather than having been formed from distinct processes, allowing them to be hypothetically classified as Intrusion-Related, showing a strong spatial zoning between Au-bearing quartz veins and W-skarns.

6.7. How Are the Different Magmatic-Hydrothermal Deposits Correlated?

The term "magmatic-hydrothermal" refers to a wide variety of deposits where a causative pluton (i.e., source of metals and/or volatiles) exsolves a hot fluid enriched in incompatible elements and ligands (Robb, 2005; Pokrovski et al., 2013). Intrusive bodies are also acknowledged for increasing the local geothermal gradient, as well as shear zones (Camacho et al., 2001). These deposits may form in proximal locations such as cupolas (e.g., Porphyry, Greisen), or the hydrothermal solution may migrate along structures (e.g., IOCG, Intrusion-Related) until a precipitation site is reached, such as carbonate lenses (e.g., Skarn). These deposits are produced under different physicochemical conditions, tectonic settings and epochs and present distinct metallogenetic associations, but still share many characteristics (Table 14).

Table 14. Characteristics of different magmatic-hydrothermal deposits. References used include Newbery & Swanson (1986), Lang & Baker (2001), Williams et al. (2005), Meinert et al. (2005), Seedorff et al. (2005), Candela & Piccoli (2005), Hart (2007), Pirajno (2009), Groves et al. (2010), Rasmussen et al. (2011), Hronsky et al. (2012), Richards & Mumin (2013), Sharma & Srivastava (2014), Ismail et al. (2014) and Soloviev (2014).

Deposit Class	Commodity	Tectonic Setting	Associated Pluton	Physicochemical Conditions (REDOX, Depth, T)	Fluid Characteristics	Hydrothermal Alteration Haloes
IOCG	Fe-Cu-Au	Cratonic Border, Distal Continental Arc, Thickened Continental Crust	Ultramafic to Felsic (Mixing)	Oxidized, 1-10 km, 300-600°C	H_2O-CO_2, High Salinity	Na, Na-Ca, K-Fe
Porphyry	Cu±Au± ±Mo±W±Sn	Continental Arc	Intermediate to Felsic	Oxidized, 1-6 km, 400-550°C	H_2O, High Salinity	Na-Ca, K, Propylitic, Sericitic, Argilic
RIRGS	Au±W± ±Bi±Te	Collisional, Accretionary Orogens, Thickened Continental Crust	Intermediate	Reduced, 5-7 km, 300-400°C	H_2O-CO_2, Low Salinity	Vein System Development
W-Skarn	W±Mo± ±Cu±Sn	Collisional, Accretionary Orogens, Thickened Continental Crust	Intermediate to Felsic	Reduced to Oxidized, 5-15 km, 400-650°C	H_2O, High Salinity	Ca ± (Ca-Ba, K)

Concerning skarn deposits, generally only the "end-members" of the system are studied, which account for calc-silicatic host rocks produced by the reaction between a hydrothermal fluid and carbonate wallrocks (Souza Neto et al., 2008; Soloviev, 2011, 2014; Rasmussen & Mortensen, 2013; Ismail et al., 2014; Xia et al., 2015; Yang et al., 2015; Zheng et al., 2015; Zheng et al., 2017; Cao et al., 2017). In this sense, the Ca-Ba and K metasomatic rocks from the root zones of the Seridó Mineral Province differ from these classic occurrences because they represent a preskarn assemblage, without any interaction with carbonate rocks. Since fluid-rock reactions are considered the main mechanism for tungsten precipitation (Lecumberri-Sanchez et al., 2017), this explains the contrast between disseminated scheelite-molybdenite in the root zones, with the fluid interacting with less reactive granitoids, and concentrated ore shoots formation controlled by fold hinges along lithological boundaries in the MGDS, where the hydrothermal solution interacted with highly reactive carbonate rocks (Souza Neto et al., 2008).

Although these classes cannot be grouped into a single genetic model, the deeper and hotter portions of these deposits possess more similarities than the shallower ones (Richards & Mumin, 2013). Calcic±sodic alteration is a diagnostic feature in IOCG deposits but is also verified in Porphyry deposits. The same situation applies for potassic alteration, which is a distinctive characteristic of Porphyry deposits but also

appears in IOCG deposits. The rocks from this study also present both alteration types, which occur along more than 100 km of the Seridó Mobile Belt (Figure 1). These represent a regional enrichment in tungsten that leads to the following question: How would the MGDS be classified if the hydrothermal fluid never reached carbonate rocks? They could possibly form structurally-controlled deposits and occurrences with disseminated scheelite-molybdenite crystals along quartz veins, similarly to rocks found in some intrusion-related deposits.

Magmatic-hydrothermal deposits must be treated as dynamic systems where a continuously changing hydrothermal fluid produces different metasomatic rocks when subjected to distinct physicochemical conditions. Hydrothermal zoning with different chemical signatures is controlled by the diffusion of chemical elements along alteration fronts (Pirajno, 2009). Smirnov (1976) created the following four groups of elements/complexes based on their mobility, from the most to the least mobile: i) H2O and CO2, ii) S, Cl, K and Na, iii) O, Si, Ca, Mg and Fe, and iv) P, W and Al. This scheme may explain why early, hotter and deeper alterations (including those formed in the root zones) tend to be richer in Ca, Fe and Mg, while later, lower temperature and shallower alterations become enriched in alkalis and sulfides. Furthermore, this classification also explains the abundance of P-, F-, Ti-, Ba- and LREE-bearing accessory minerals in the root zones of these deposits, which accounts for apatite, titanite, barite and hyalophane and epidote-allanite, respectively (Pirajno, 1992; Williams et al., 2005; Groves et al., 2010; Corriveau et al., 2016; Corrêa et al., Chapter 2, this work).

7. CONCLUSIONS

By highlighting the importance of these deep, reduced regions of intense metasomatic alteration, this study may contribute to prospective campaigns concerning the whole magmatic-hydrothermal system, which includes skarn, IOCG, porphyry and RIRGS deposits. The identification and characterization of the root zones of the Seridó Mineral Province was better described in this work by geochemical and isotopic analyses. The main results and interpretations of this research will be listed below:

- The DAF, AF and BR associations are interpreted as the root zones of the Seridó Mineral Province, being chronologically and chemically linked with the MGDS occurrences. Furthermore, due to their mineralogical and chemical nature, the DAF/AF associations are correlated with a calcic or calcic-barium (Ca-Ba) alteration, while the BR association is correlated with a potassic (K) alteration.
- The Ca-Ba and K metasomatic rocks were produced after a multistage metasomatic event that changed its physicochemical properties over time. The Ca-Ba alteration presents a high temperature paragenesis which is representative of the prograde stage. Samples from this stage tend to present higher CaO, MgO, Fe2O3*, REE and Ba values. 40Ar/39Ar dating in amphibole set the formation age of this alteration at ca. 550 Ma. Hence, the Late Neoproterozoic-Ediacaran transition represents a metallogenetic epoch in the Seridó Mineral Province.
- In the Ca-Ba and K metasomatic rocks, the early, higher temperature alteration is overprinted by the retrograde phase. Samples from this stage are generally characterized by leaching of the previously mentioned elements, and then become enriched in alkalis and SiO2. The main precipitation of sulfides and scheelite occurred during this phase.
- The most important controlling agents for developing the aforementioned alteration styles are changes in the physicochemical conditions of the system and different element mobilities, wallrock compositions and fluid/rock ratios.
- The Re-Os mineralization ages obtained by Hollanda et al. (2017) in the MGDS are relatively synchronic with the U-Pb and Ar-Ar ages obtained for the root zones in this work.

- Zircon U-Pb analyses point that the root zones were formed in different granitoid wallrocks of Paleoarchean, Neoarchean and Paleoproterozoic ages during the Neoproterozoic-Ediacaran Brasiliano Cycle. The metasomatism is strongly linked to structures and pegmatitic injections, which are probably synchronous with tungsten mineralization.

A regional-scale zoning between W-Mo and Au is verified between the Rio Grande do Norte and Zona Transversal domains. The Patos shear zone plays a major role in this process by displacing lithological units and deposits/occurrences for more than 50 km in the EW direction. A similar pattern is verified in the Tintina Gold Province, where RIRGS and skarns are spatially associated (Hart, 2007).

8. SUPPLEMENTARY MATERIAL

Table 2. Whole rock geochemical analyses. "N.A." stands for "Not Analyzed".

Sample	BONFIM CARECA	POT-3	SEB-295 10.80m	SEB-295 13.60m	SEB-295 25.30m	SEB-295 34.70m	SEB-295 42.30m	SEB-299 14.45m	SEB-316 21.30m	AL-01	REC-01	MC-BF-01	SALG-01	SALG-02	SALG-03	CC-01
SiO2	52.14	74.12	61.27	67.99	65.46	40.23	75.60	43.00	53.42	51.3	53	53.8	50.5	54.7	54.4	50.4
TiO2	0.83	0.05	0.31	0.35	0.53	0.59	0.27	0.73	1.02	0.6	0.37	0.98	0.47	0.85	0.45	0.84
Al2O3	7.16	14.16	18.85	14.93	15.13	5.64	9.96	8.48	6.92	7.39	10.6	5.91	6.92	17.95	14.95	16.6
Fe2O3*	10.58	0.73	2.26	2.58	3.62	8.53	4.68	15.28	11.61	11.3	7.63	10.9	8.78	5.24	7.34	10.05
Cr2O3	<0.002	<0.002	<0.002	<0.002	<0.002	0.003	0.005	0.003	<0.002	0.09	0.12	<0.01	0.12	0.06	0.01	0.05
MnO	0.38	0.01	0.02	0.06	0.06	0.16	0.05	0.47	0.50	0.22	0.14	0.36	0.15	0.12	0.11	0.2
MgO	9.45	0.45	2.18	0.64	0.98	7.04	3.03	8.74	8.86	11.7	10.45	11.85	14.1	5.14	8.23	7.51
CaO	14.97	1.04	1.58	3.33	2.16	8.87	0.36	15.06	12.31	13.75	13.05	13.55	15.25	9.14	10.65	6.06
BaO	N.A.	N.A.	N.A.	N.A.	N.A.	N.A.	N.A.	N.A.	N.A.	0.02	0.01	0.37	0.04	0.02	0.02	0.04
SrO	N.A.	N.A.	N.A.	N.A.	N.A.	N.A.	N.A.	N.A.	N.A.	0.03	0.05	0.11	0.02	0.37	0.07	0.05
Na2O	1.19	4.68	3.41	4.25	2.49	0.44	0.55	1.06	1.12	1.39	2.38	0.84	1.09	5.01	3.39	3.39
K2O	0.30	3.61	7.34	1.84	7.76	0.45	3.39	0.50	0.41	0.77	0.4	0.4	0.41	0.47	0.37	3.24
P2O5	0.75	0.02	0.04	0.12	0.13	0.69	0.03	2.44	1.20	0.14	0.17	0.14	0.08	0.38	0.07	0.25
C	0.05	0.06	0.02	<0.02	0.02	0.21	0.04	0.02	0.02	0.12	0.05	0.03	0.08	0.08	0.03	0.05
S	<0.02	<0.02	<0.02	1.13	<0.02	3.76	0.11	<0.02	<0.02	0.01	<0.01	<0.01	0.01	<0.01	0.01	0.01
LOI	1.5	0.9	1.2	2.1	0.5	3.9	1.7	1.6	2.0	1.33	0.95	0.98	0.95	0.8	0.77	0.91
Total	99.28	99.74	98.48	98.20	98.84	76.55	99.61	97.41	99.39	100.03	99.32	100.19	98.88	100.25	100.83	99.59
Li	N.A.	N.A.	N.A.	N.A.	N.A.	N.A.	N.A.	N.A.	N.A.	20	20	30	20	20	20	60
Be	6	3	2	1	1	3	3	5	2	N.A.	N.A.	N.A.	N.A.	N.A.	N.A.	N.A.
Sc	24	1	4	6	9	5	4	41	56	41	29	22	46	19	27	15
V	168	11	42	36	64	207	<8	217	185	158	111	171	188	84	162	145
Cr	N.A.	N.A.	N.A.	N.A.	N.A.	N.A.	N.A.	N.A.	N.A.	680	880	20	890	470	40	360
Co	65.9	107.4	52.6	101.4	56.7	34.6	79.7	29.3	32.9	40	39	24	49	26	37	39
Ni	2.5	3.7	6.8	2.2	4.6	31	5.2	4.3	4.4	395	171	6	265	154	91	216

Cu	18.4	6.4	5.4	265.0	22.1	380.6	21.0	101.1	13.3	10	2	12	128	3	44	1
Zn	63	11	34	37	18	13	157	110	89	108	84	288	83	61	58	169
Ga	18.4	15.0	17.8	13.7	14.6	14.9	22.5	24.4	19.2	15.2	12.9	16.7	9.7	21	15.1	24.9
Rb	3.7	40.7	83.2	12.2	102.3	6.7	86.3	4.3	4.3	15.6	6.3	4.9	5.6	15.6	3.6	285
Sr	1577.7	124.4	628.5	1243.5	1099.6	4991.5	24.9	769.0	609.3	231	431	984	179	3210	603	427
Y	121.5	6.5	31.5	36.2	32.8	438.6	100.8	141.0	200.8	32.5	13.5	131.5	14	57.6	14.5	22.4
Zr	108.4	57.4	418.2	66.8	29.5	450.1	615.8	84.3	211.4	101	88	130	49	116	58	137
Nb	15.0	3.1	9.4	19.0	16.7	40.0	27.0	5.3	22.3	16.7	5.5	27.7	3.2	87.3	4.2	18.5
Cs	0.5	0.3	3.4	0.4	0.9	<0.1	3.9	0.1	<0.1	0.19	0.24	0.21	0.3	3.04	0.22	63.5
Ba	418	915	11460	13544	8254	>50000	669	350	472	205	84.4	3100	334	190	197.5	331
La	207.3	14.9	38.2	28.8	20.4	746.4	63.8	353.0	341.8	57.3	32	95.5	12.2	38.5	27.8	26.8
Ce	413.3	23.8	74.1	62.2	53.8	1329.8	153.5	645.2	654.1	139	59	215	27.4	99.3	53.2	55.1
Pr	54.00	2.49	8.43	8.04	8.11	134.48	20.16	76.01	82.10	16.95	7.21	30.3	3.21	12.8	6.18	6.23
Nd	229.6	8.3	28.2	35.0	35.8	512.4	86.2	299.1	343.2	66.6	25.7	154.5	14.6	57	23.9	25.1
Sm	49.58	1.39	6.62	7.91	9.43	101.78	20.30	55.22	73.89	12.25	4.57	45.5	3.01	14.55	4.21	4.91
Eu	11.34	0.52	2.17	1.92	2.47	21.36	4.02	14.28	18.75	2.4	1.2	10.85	0.97	2.62	1.07	1.5
Gd	44.18	1.14	6.39	8.01	8.96	105.55	20.19	51.36	68.29	9.34	3.68	51.6	3.27	15	3.64	4.86
Tb	5.81	0.17	1.02	1.19	1.32	15.39	3.15	6.45	8.74	1.21	0.52	7.04	0.48	2.17	0.54	0.71
Dy	28.37	1.04	5.76	6.77	7.60	90.85	18.86	30.79	44.42	6.44	2.8	33.7	2.8	11.9	2.85	4.08
Ho	4.40	0.18	1.18	1.29	1.26	15.89	3.82	5.03	6.93	1.16	0.55	5.31	0.54	2.1	0.54	0.82
Er	10.14	0.59	3.14	3.43	3.09	42.11	11.55	12.00	15.60	3.14	1.44	11.1	1.47	5.47	1.49	2.33
Tm	1.23	0.10	0.46	0.47	0.45	5.54	1.82	1.52	2.02	0.44	0.27	1.25	0.21	0.79	0.22	0.37
Yb	6.55	0.73	3.10	3.20	2.85	32.80	12.20	8.63	11.79	2.63	1.21	6.13	1.1	4.1	1.15	2.13
Lu	0.94	0.10	0.51	0.51	0.46	4.63	1.89	1.28	1.65	0.43	0.18	0.92	0.17	0.61	0.18	0.34
Hf	4.3	1.6	10.3	2.3	1.1	13.2	21.2	3.0	7.4	3.2	2.2	5.4	1.4	3.8	1.7	3.5
Ta	1.6	0.7	0.7	1.5	1.5	4.0	1.8	0.4	2.5	0.7	0.4	2.5	0.3	3.4	0.2	0.8
U	3.0	0.6	1.6	1.2	0.9	6.4	2.2	6.4	9.2	0.24	2.01	2.44	0.33	13.6	2.09	1.61
Th	10.7	4.4	9.2	3.3	2.8	29.3	11.9	17.3	10.6	0.99	7.29	10.5	1.18	37.3	7.73	3.87
Pb	3.1	9.2	4.2	7.7	7.0	4.6	2.5	4.0	1.6	10	10	10	3	11	6	15

Ge	N.A.	N.A.	N.A.	N.A.	N.A.	N.A.	N.A.	N.A.	N.A.	<5	<5	<5	<5	<5	<5	<5
In	N.A.	N.A.	N.A.	N.A.	N.A.	N.A.	N.A.	N.A.	N.A.	0.014	<0.005	0.15	0.008	0.017	0.006	0.024
Re	N.A.	N.A.	N.A.	N.A.	N.A.	N.A.	N.A.	N.A.	N.A.	<0.001	<0.001	0.001	<0.001	<0.001	<0.001	0.001
Te	N.A.	N.A.	N.A.	N.A.	N.A.	N.A.	N.A.	N.A.	N.A.	0.01	<0.01	0.02	0.05	0.01	0.01	<0.01
Sn	23	<1	1	5	3	13	6	33	29	3	1	20	1	9	1	4
W	893.3	847.2	308.1	356.2	343.3	152.4	700.8	>10000.0	216.0	1	1	31	1	16	3	16
Ag	<0.1	<0.1	<0.1	0.2	<0.1	<0.1	<0.1	<0.1	<0.1	<0.5	<0.5	<0.5	<0.5	<0.5	<0.5	<0.5
As	1.9	<0.5	<0.5	<0.5	0.5	0.6	<0.5	4.9	2.0	0.3	0.3	0.3	0.2	0.3	0.1	0.1
Au	0.9	3.1	1.6	1.0	<0.5	7.1	1.1	10.6	1.9	N.A.	N.A.	N.A.	N.A.	N.A.	N.A.	N.A.
Bi	45.5	<0.1	<0.1	17.4	0.7	1.1	0.2	45.1	2.1	0.05	0.04	46.4	0.25	0.61	0.1	0.24
Cd	0.1	<0.1	<0.1	0.1	<0.1	<0.1	<0.1	<0.1	0.1	<0.5	<0.5	<0.5	<0.5	<0.5	<0.5	<0.5
Hg	N.A.	<0.01	<0.01	N.A.	<0.01	<0.01	<0.01	N.A.	<0.01	<0.005	<0.005	0.014	0.005	0.014	0.008	0.009
Mo	2.8	<0.1	<0.1	0.2	0.1	1.0	1.1	60.3	0.1	<1	<1	1	<1	<1	<1	<1
Sb	<0.1	<0.1	<0.1	<0.1	<0.1	<0.1	<0.1	<0.1	<0.1	<0.05	<0.05	0.05	<0.05	<0.05	<0.05	<0.05
Se	<0.5	<0.5	<0.5	<0.5	<0.5	<0.5	<0.5	<0.5	<0.5	<0.2	<0.2	<0.2	<0.2	<0.2	<0.2	0.2
Tl	<0.1	<0.1	0.3	<0.1	<0.1	<0.1	0.3	<0.1	<0.1	<0.02	<0.02	<0.02	<0.02	0.02	<0.02	1.38

Table 3. Zircon U-Pb data for the sample SEB-295.

Crystal ID	^{204}Pb cps	^{206}Pb mV	Th/U	^{206}Pb/^{204}Pb	1s%	^{207}Pb/^{235}U	1s %	^{206}Pb/^{238}U	1s %	Rho	^{207}Pb/^{206}Pb	2s abs	^{206}Pb/^{238}U	2s abs	^{207}Pb/^{235}U	2s abs	% U-Pb disc
004-ZirR01	37	0.0026	0.180	25758	40.11	12.717	2.30	0.3757	2.00	0.87	3156	34	2056	70	2659	43	34.84
005-ZirR02	23	0.0027	0.237	50610	29.50	7.614	2.43	0.2602	1.69	0.69	2923	55	1491	45	2187	43	49.00
007-ZirR04	164	0.0042	0.094	1684	5.37	3.035	1.42	0.1444	1.04	0.73	2373	30	870	17	1417	22	63.35
009-ZirR06	160	0.0060	0.087	2599	6.34	5.455	2.46	0.1934	2.20	0.89	2863	34	1140	46	1894	42	60.19
013-ZirR08	37	0.0083	0.141	115623	32.46	7.792	0.96	0.2557	0.76	0.79	2988	15	1468	20	2207	17	50.86
014-ZirR09	20	0.0039	0.107	262574	78.44	7.089	1.73	0.2435	1.48	0.85	2914	26	1405	37	2123	31	51.79
015-ZirR10	41	0.0081	0.143	36733	38.93	7.287	3.90	0.2489	3.60	0.92	2923	46	1433	92	2147	68	50.99
017-ZirR12	35	0.0030	0.152	39095	44.35	14.776	2.21	0.4208	1.59	0.72	3214	46	2264	61	2801	42	29.54
019-ZirR14	67	0.0060	0.173	22645	53.47	6.896	2.13	0.2372	1.99	0.93	2912	22	1372	49	2098	38	52.89
020-ZirR15	157	0.0104	0.155	4336	5.89	5.155	2.18	0.1938	1.73	0.79	2767	42	1142	36	1845	37	58.74

025-ZirR17	27	0.0140	0.157	193347	27.82	9.643	1.07	0.2955	0.83	0.78	3098	18	1669	24	2401	20	46.13
028-ZirR20	78	0.0071	0.160	6989	10.94	6.690	1.96	0.2263	1.78	0.91	2939	24	1315	42	2071	34	55.25
034-ZirR24	40	0.0064	0.166	35854	53.66	5.125	2.37	0.1909	1.96	0.83	2782	41	1126	41	1840	40	59.51
037-ZirR27	59	0.0041	0.198	14539	33.04	5.941	2.23	0.2128	1.98	0.89	2846	31	1244	45	1967	38	56.30
038-ZirR28	82	0.0062	0.159	5106	5.74	4.084	1.75	0.1669	1.42	0.81	2629	32	995	26	1651	28	62.15
039-ZirR29	37	0.0039	0.165	33426	50.60	3.908	2.05	0.1636	1.58	0.77	2589	41	977	29	1615	33	62.27

Table 4. Zircon U-Pb data for the sample PEDRO TOMÁS

Crystal ID	^{204}Pb cps	^{206}Pb mV	Th/U	$^{206}Pb/^{204}Pb$	1s%	$^{207}Pb/^{235}U$	1s %	$^{206}Pb/^{238}U$	1s %	Rho	$^{207}Pb/^{206}Pb$	2s abs	$^{206}Pb/^{238}U$	2s abs	$^{207}Pb/^{235}U$	2s abs	% U-Pb disc
003-ZR01	16	0.0064	0.460	198164	15.46	7.602	2.84	0.3193	2.70	0.95	2583	27	1786	84	2185	50	30.85
004-ZR02	14	0.0082	0.367	222059	17.04	10.796	1.13	0.4333	0.82	0.73	2659	22	2321	32	2506	21	12.73
005-ZR03	529	0.0092	0.330	1136	3.30	2.132	6.93	0.1364	5.05	0.73	1854	166	824	78	1159	94	55.53
006-ZR04	33	0.0044	0.395	32237	30.92	10.317	1.80	0.4134	1.60	0.89	2662	24	2230	60	2464	33	16.22
007-ZR05	184	0.0108	0.415	11015	65.69	5.061	4.13	0.2304	3.17	0.77	2448	87	1336	76	1830	69	45.42
008-ZR06	244	0.0093	0.298	2713	6.60	3.143	2.04	0.1739	1.01	0.49	2112	60	1034	19	1443	31	51.07
009-ZR07	10	0.0062	0.447	224605	16.14	12.698	1.32	0.5016	1.05	0.80	2686	23	2621	45	2658	25	2.42
010-ZR08	13	0.0036	0.333	87579	18.19	10.910	1.43	0.4376	1.10	0.76	2660	28	2340	43	2515	27	12.03
013-ZR09	14	0.0070	0.427	203748	18.47	11.358	1.79	0.4540	1.58	0.88	2666	25	2413	63	2553	33	9.48
014-ZR10	497	0.0127	0.125	1662	3.56	1.843	3.83	0.1245	2.67	0.70	1755	98	757	38	1061	50	56.88
015-ZR11	11	0.0033	0.365	137883	14.88	12.362	1.33	0.4922	1.09	0.82	2672	22	2580	46	2632	25	3.46
016-ZR12	20	0.0045	0.587	91145	20.15	12.396	1.03	0.4873	0.75	0.73	2693	20	2559	32	2635	19	4.99
017-ZR13	25	0.0076	0.088	80330	22.28	3.042	7.39	0.1612	7.26	0.98	2188	44	963	129	1418	110	55.96
018-ZR14	37	0.0087	0.477	72974	34.08	11.347	2.39	0.4522	2.21	0.93	2671	27	2405	89	2552	44	9.96
019-ZR15	14	0.0042	0.457	178186	14.52	12.759	1.18	0.5032	0.85	0.72	2688	24	2628	37	2662	22	2.26
020-ZR16	50	0.0078	0.483	112580	25.16	9.846	3.43	0.3960	3.29	0.96	2656	29	2150	120	2420	62	19.04
023-ZR17	47	0.0045	0.446	49992	33.66	11.986	2.00	0.4646	1.71	0.86	2717	31	2460	70	2603	37	9.45
024-ZR18	52	0.0031	0.322	33868	37.36	11.003	4.61	0.4418	4.46	0.97	2658	36	2359	175	2523	84	11.27
025-ZR19	510	0.0024	0.657	840	13.25	12.765	4.08	0.5211	2.48	0.61	2631	105	2704	109	2662	75	-2.75
026-ZR20	123	0.0051	0.714	71760	30.63	13.150	2.56	0.5378	2.01	0.78	2628	51	2774	90	2690	48	-5.56

027-ZR21	13	0.0041	0.442	176402	26.93	11.797	1.17	0.4729	0.84	0.72	2661	24	2496	35	2588	22	6.19
028-ZR22	40	0.0080	0.473	62397	34.35	8.216	3.67	0.3462	3.43	0.93	2578	42	1916	113	2255	65	25.67
029-ZR23	28	0.0042	0.432	132072	20.07	12.351	1.41	0.4971	1.04	0.74	2655	29	2601	44	2631	26	2.01
030-ZR24	17	0.0076	0.394	182493	20.42	9.543	1.21	0.3957	0.78	0.65	2605	28	2149	29	2392	22	17.51
033-ZR25	35	0.0035	0.520	67641	22.45	13.859	2.60	0.5482	2.43	0.94	2683	28	2818	111	2740	49	-5.00
034-ZR26	13	0.0038	0.338	101823	17.50	12.078	1.63	0.4743	1.40	0.86	2695	25	2502	58	2611	30	7.17
035-ZR27	8	0.0033	0.382	112577	13.55	12.573	1.17	0.4926	0.83	0.71	2699	24	2582	35	2648	22	4.33
036-ZR28	35	0.0029	0.394	53696	26.51	8.288	1.82	0.3563	1.61	0.88	2545	26	1964	54	2263	33	22.81
037-ZR29	17	0.0023	0.332	228528	75.56	12.548	1.50	0.4910	1.18	0.79	2701	28	2575	50	2646	28	4.66
038-ZR30	15	0.0033	0.377	93265	15.90	11.863	1.54	0.4720	1.23	0.80	2674	28	2492	51	2594	29	6.78
039-ZR31	128	0.0047	0.545	31658	40.68	12.886	1.55	0.4923	0.89	0.58	2741	40	2580	38	2671	29	5.85
040-ZR32	34	0.0053	0.481	119948	22.37	12.807	1.58	0.5058	1.25	0.79	2686	29	2638	54	2666	30	1.77

Table 5. Zircon U-Pb data for the sample SALG-2.

Crystal ID	^{204}Pb cps	^{206}Pb mV	Th/U	^{206}Pb/^{204}Pb	1s%	^{207}Pb/^{206}Pb	1s %	^{207}Pb/^{235}U	1s %	^{206}Pb/^{238}U	1s %	Rho	^{207}Pb/^{206}Pb	2s abs	^{206}Pb/^{238}U	2s abs	^{207}Pb/^{235}U	2s abs	% U-Pb disc
006-ZR3R	181	0.0222	0.068	10517	9.47	0.05857	0.61	0.699	0.94	0.0866	0.60	0.64	551	27	535	6	538	8	2.86
015-ZR8	409	0.0306	0.030	26155	76.92	0.07029	5.38	0.899	8.51	0.0928	6.58	0.77	937	213	572	72	651	80	38.97
019-ZR12	2082	0.0638	0.028	2113	5.35	0.08871	2.75	1.233	16.42	0.1008	16.18	0.99	1398	104	619	190	816	176	55.72
025-ZR15R	743	0.0565	0.027	5323	5.83	0.11653	0.69	3.456	2.37	0.2150	2.23	0.94	1904	25	1256	51	1517	37	34.04
027-ZR17	2039	0.0890	0.027	3367	11.95	0.07026	1.78	1.036	4.39	0.1069	3.99	0.91	936	72	655	50	722	45	30.05
028-ZR18	933	0.0504	0.035	4312	10.13	0.07570	1.61	1.184	4.00	0.1134	3.64	0.91	1087	64	693	48	793	44	36.29
030-ZR20	12725	0.0907	0.489	459518	38.22	0.15667	7.48	4.191	7.86	0.1940	2.39	0.30	2420	243	1143	50	1672	125	52.77
033-ZR21	2170	0.0951	0.049	3084	4.72	0.08972	0.77	1.721	9.03	0.1391	8.99	1.00	1420	29	840	141	1017	113	40.84
035-ZR23	629	0.1167	0.046	11706	1.51	0.11700	0.34	3.728	0.83	0.2311	0.65	0.79	1911	12	1340	16	1577	13	29.87
046-ZR30R	37	0.0176	0.015	283811	23.91	0.05878	0.80	0.733	1.14	0.0904	0.72	0.63	559	35	558	8	558	10	0.17

Table 6. Zircon U-Pb data for the sample SALG-3.

Crystal ID	^{204}Pb cps	^{206}Pb mV	Th/U	^{206}Pb/^{204}Pb	1s%	^{207}Pb/^{206}Pb	1s %	^{207}Pb/^{235}U	1s %	^{206}Pb/^{238}U	1s %	Rho	^{207}Pb/^{206}Pb	2s abs	^{206}Pb/^{238}U	2s abs	^{207}Pb/^{235}U	2s abs	% U-Pb disc
004-ZR2	22	0.0195	0.426	510333	17.67	0.13434	0.26	6.422	0.82	0.3467	0.69	0.84	2155	9	1919	23	2035	14	10.98
006-ZR3R	36	0.0447	0.383	394129	31.75	0.13027	0.19	5.809	0.75	0.3234	0.63	0.83	2102	7	1806	20	1948	13	14.05
007-ZR4R	17	0.0144	0.427	419284	16.27	0.13615	0.27	6.719	0.72	0.3579	0.55	0.77	2179	9	1972	19	2075	13	9.49
008-ZR4C	37	0.0575	0.593	330926	37.35	0.13387	0.26	6.665	0.72	0.3611	0.56	0.78	2149	9	1987	19	2068	13	7.54
010-ZR6C	20	0.0238	0.478	478283	21.03	0.13432	0.26	6.374	0.76	0.3441	0.61	0.80	2155	9	1907	20	2029	13	11.54
015-ZR8C	429	0.0624	0.598	9208	3.60	0.13485	0.22	6.841	0.89	0.3679	0.78	0.87	2162	8	2019	27	2091	16	6.59
017-ZR9C	20	0.0281	0.479	584049	19.38	0.13359	0.27	6.333	0.73	0.3438	0.57	0.78	2146	9	1905	19	2023	13	11.22
018-ZR9R	18	0.0221	0.487	628576	28.20	0.13371	0.24	6.425	0.68	0.3485	0.52	0.76	2147	8	1927	17	2036	12	10.24
019-ZR10C	45	0.0513	0.716	165580	23.68	0.13356	0.25	6.640	0.71	0.3605	0.54	0.77	2145	9	1985	19	2065	12	7.48
020-ZR10R	108	0.1022	0.589	66400	6.72	0.13203	0.31	6.480	0.89	0.3559	0.75	0.84	2125	11	1963	25	2043	16	7.63
023-ZR11	72	0.0193	0.451	78906	49.68	0.13494	0.24	6.462	0.83	0.3473	0.71	0.85	2163	8	1922	24	2041	15	11.16
030-ZR17	22	0.0318	0.441	827173	18.59	0.13292	0.27	6.410	0.72	0.3497	0.55	0.77	2137	9	1933	18	2034	13	9.52
031-ZR18	22	0.0377	0.415	1431974	28.25	0.13184	0.30	6.021	0.70	0.3312	0.52	0.74	2123	10	1844	17	1979	12	13.11
034-ZR19	32	0.0249	0.372	543589	24.10	0.13516	0.26	6.841	0.76	0.3671	0.61	0.80	2166	9	2016	21	2091	13	6.95
035-ZR20R	289	0.0949	0.746	22805	8.34	0.13113	0.26	6.446	1.03	0.3565	0.93	0.90	2113	9	1965	31	2039	18	6.99
036-ZR20C	833	0.0623	0.655	5568	7.60	0.13820	0.37	6.704	0.81	0.3518	0.62	0.77	2205	13	1943	21	2073	14	11.87
040-ZR23C	49	0.0825	0.051	385603	40.47	0.13139	0.34	5.924	0.85	0.3270	0.69	0.81	2117	12	1824	22	1965	15	13.84
041-ZR23O1	158	0.0283	0.328	262573	38.16	0.13372	0.85	5.811	1.33	0.3152	0.96	0.72	2147	30	1766	30	1948	23	17.75

045-ZR23O3	11	0.0187	0.436	744739	12.17	0.13557	0.30	6.286	0.78	0.3363	0.62	0.79	2171	10	1869	20	2017	14	13.93
047-ZR24	29	0.0314	0.607	453720	25.26	0.13324	0.30	5.958	0.73	0.3243	0.56	0.76	2141	11	1811	18	1970	13	15.43
048-ZR25C	36	0.1113	0.944	828373	34.20	0.13261	0.26	6.510	0.70	0.3560	0.54	0.77	2133	9	1963	18	2047	12	7.94
049-ZR25R	10	0.0158	0.376	502795	15.46	0.13582	0.28	6.433	0.76	0.3435	0.60	0.79	2175	10	1904	20	2037	13	12.46
050-ZR26C	29	0.1024	0.625	1683527	30.06	0.13321	0.28	6.524	0.77	0.3552	0.61	0.80	2141	10	1959	21	2049	13	8.47
051-ZR26R	15	0.0265	0.396	658254	19.16	0.13448	0.42	6.240	0.83	0.3365	0.61	0.74	2157	14	1870	20	2010	14	13.32
054-ZR27C	64	0.0271	0.418	234457	32.37	0.13183	0.36	5.604	0.90	0.3083	0.74	0.82	2122	13	1732	22	1917	15	18.39
055-ZR27R	14	0.0138	0.335	448198	14.69	0.13466	0.30	6.241	0.91	0.3361	0.78	0.85	2160	10	1868	25	2010	16	13.51
056-ZR28R	250	0.0686	0.354	19305	7.24	0.13212	0.31	6.230	0.88	0.3420	0.73	0.83	2126	11	1896	24	2009	15	10.83
060-ZR30C	21	0.0218	0.448	537975	18.59	0.13553	0.36	6.816	0.78	0.3647	0.59	0.75	2171	12	2004	20	2088	14	7.67
061-ZR30O1	30	0.0343	0.669	464547	28.55	0.13384	0.39	6.741	0.81	0.3653	0.61	0.75	2149	14	2007	21	2078	14	6.60

Table 7. Zircon U-Pb data for the sample LAJES-5.1.

Crystal ID	**^{204}Pb cps**	**^{206}Pb mV**	**Th/U**	**^{206}Pb/^{204}Pb**	**1s%**	**^{207}Pb/^{235}U**	**1s %**	**^{206}Pb/^{238}U**	**1s %**	**Rho**	**^{207}Pb/^{206}Pb**	**2s abs**	**^{206}Pb/^{238}U**	**2s abs**	**^{207}Pb/^{235}U**	**2s abs**	**% U-Pb disc**
004-ZirR01	18	0.0067	0.302	104294	18.01	6.899	0.95	0.3674	0.70	0.74	2179	18	2017	24	2098	17	7.41
005-ZirR02	15	0.0058	0.619	309027	18.64	7.057	0.74	0.3748	0.53	0.72	2184	12	2052	19	2119	13	6.06
009-ZirR04	33	0.0242	0.282	462632	26.20	6.706	0.89	0.3571	0.71	0.79	2179	14	1968	24	2073	16	9.68
010-ZirR05	25	0.0385	0.442	489093	26.46	6.937	0.77	0.3702	0.59	0.76	2175	12	2031	20	2103	14	6.66
011-ZirR06	22	0.0049	0.436	96008	22.99	7.016	0.91	0.3725	0.68	0.75	2184	17	2041	24	2113	16	6.56
015-ZirR08	29	0.0081	0.502	124442	35.01	6.840	0.85	0.3634	0.66	0.77	2183	14	1998	23	2091	15	8.47

023-ZirR14	33	0.0356	0.756	309815	30.08	6.717	0.78	0.3580	0.61	0.79	2178	10	1973	21	2075	14	9.40
024-ZirR15	21	0.0209	0.027	366931	28.70	0.767	0.84	0.0931	0.63	0.75	594	18	574	7	578	7	3.47
028-ZirR16	34	0.0130	0.261	157495	34.15	6.917	0.82	0.3679	0.61	0.74	2182	14	2019	21	2101	15	7.43
030-ZirR18	25	0.0287	0.450	404627	28.03	6.900	0.79	0.3685	0.59	0.75	2174	13	2022	20	2099	14	7.01
035-ZirR21	29	0.0279	0.476	402019	28.09	7.171	0.82	0.3791	0.65	0.80	2192	11	2072	23	2133	14	5.46
039-ZirR23	23	0.0049	0.591	111110	20.92	6.867	0.92	0.3648	0.71	0.78	2183	15	2005	25	2094	16	8.18
040-ZirR24	19	0.0071	0.417	111654	29.48	6.880	0.80	0.3668	0.58	0.72	2177	14	2014	20	2096	14	7.48
042-ZirR26	21	0.0201	0.473	457226	21.31	6.872	0.77	0.3653	0.55	0.71	2182	14	2007	19	2095	14	8.02
045-ZirR27	16	0.0177	0.488	488017	21.32	6.630	0.71	0.3532	0.51	0.73	2179	11	1950	17	2063	12	10.50
047-ZirR29	19	0.0174	0.360	412202	24.78	6.824	0.78	0.3627	0.59	0.75	2183	12	1995	20	2089	14	8.61
048-ZirR30	20	0.0182	0.330	451666	19.91	6.520	0.80	0.3498	0.62	0.78	2166	12	1934	21	2049	14	10.74

Table 8. Zircon U-Pb data for the sample CÇ-09.

Crystal ID	**^{204}Pb cps**	**^{206}Pb mV**	**Th/U**	**^{206}Pb/^{204}Pb**	**1s%**	**^{207}Pb/^{235}U**	**1s %**	**^{206}Pb/^{238}U**	**1s %**	**Rho**	**^{207}Pb/^{206}Pb**	**2s abs**	**^{206}Pb/^{238}U**	**2s abs**	**^{207}Pb/^{235}U**	**2s abs**	**% U-Pb disc**
005-ZR3	104	0.0038	0.465	2525	7.79	2.114	2.78	0.1588	1.39	0.50	1558	88	950	24	1153	38	38.99
006-ZR4	120	0.0074	0.423	3921	4.86	1.033	1.23	0.1060	0.80	0.65	949	35	649	10	721	13	31.58
012-ZR8	32	0.0041	0.427	53394	37.07	2.834	2.16	0.1860	1.52	0.70	1808	54	1099	31	1365	32	39.19
013-ZR9	7	0.0069	0.114	295029	12.93	6.574	1.02	0.3548	0.76	0.75	2156	20	1958	26	2056	18	9.20
017-ZR13	86	0.0045	0.689	3669	7.14	0.898	1.18	0.0996	0.69	0.59	787	37	612	8	651	11	22.22
021-ZR15	66	0.0036	0.166	38934	45.79	1.726	2.84	0.1414	1.58	0.55	1395	88	852	25	1018	36	38.88
022-ZR16	21	0.0059	0.289	62978	35.40	4.841	1.67	0.2793	1.42	0.85	2039	28	1588	40	1792	28	22.13
024-ZR18	101	0.0051	0.260	3364	6.54	1.141	1.19	0.1116	0.86	0.72	1045	30	682	11	773	13	34.71
025-ZR19	87	0.0059	0.314	4760	8.28	1.890	0.96	0.1477	0.61	0.64	1484	24	888	10	1078	13	40.15

Table 9. Amphibole ^{40}Ar /^{39}Ar data for the sample MCBF (aliquots 1 and 3).

Step	Laser Power	% 40Ar	% Mol 39Ar	Cum. %	Age (Ma)	± 2s	K/Ca	± 2s
MCBF-1A	0.10	107.86	0.00	0.00	0.00	60726.53	0.01	0.23
MCBF-1B	0.20	55.24	0.04	0.04	3550.52	1254.60	0.23	0.37
MCBF-1C	0.30	37.85	0.05	0.09	2290.40	1313.72	0.27	0.42
MCBF-1D	0.40	77.95	0.07	0.16	3029.01	1457.97	0.03	0.03
MCBF-1E	0.50	51.16	0.69	0.85	602.11	11.95	0.05	0.00
MCBF-1F	0.60	91.33	2.55	3.40	595.65	26.61	0.04	0.00
MCBF-1G	0.70	91.35	2.82	6.22	572.59	22.89	0.04	0.00
MCBF-1H	0.80	94.02	3.02	9.24	514.72	29.95	0.04	0.00
MCBF-1I	0.90	95.06	1.72	10.96	598.33	40.72	0.04	0.00
MCBF-1J	1.00	99.94	3.07	14.03	573.42	14.12	0.03	0.00
MCBF-1K	1.20	95.06	19.32	33.35	554.07	2.05	0.03	0.00
MCBF-1L	1.40	99.71	26.65	59.99	550.22	4.47	0.03	0.00
MCBF-1M	1.60	100.13	24.28	84.28	528.42	4.13	0.03	0.00
MCBF-1N	1.80	99.84	3.83	88.11	586.36	20.92	0.03	0.00
MCBF-1O	2.00	100.44	7.81	95.92	570.71	7.78	0.04	0.00
MCBF-1P	2.20	86.10	3.27	99.19	534.65	12.07	0.03	0.00
MCBF-1Q	2.40	90.04	0.45	99.64	484.57	128.93	0.03	0.00
MCBF-1R	2.60	59.70	0.14	99.77	1138.23	1475.30	0.01	0.01
MCBF-1S	2.80	14.58	0.01	99.78	1002.59	23283.04	0.01	0.11
MCBF-1T	3.00	12.02	0.22	100.00	37.97	368.02	0.07	0.00
Step	Laser Power	% 40Ar	% Mol 39Ar	Cum. %	Age (Ma)	± 1s	K/Ca	± 1s
MCBF-3A	0.20	67.21	0.07	0.07	3513.46	946.53	0.02	0.01
MCBF-3B	0.40	70.49	0.16	0.22	2403.40	477.01	0.06	0.02
MCBF-3C	0.60	82.77	5.42	5.64	547.96	3.07	0.03	0.00
MCBF-3D	0.80	96.95	12.59	18.23	560.51	9.01	0.03	0.00
MCBF-3E	1.00	96.01	3.91	22.14	548.57	10.12	0.03	0.00
MCBF-3F	1.20	97.43	10.27	32.41	545.57	3.33	0.03	0.00
MCBF-3G	1.40	98.45	9.00	41.40	520.68	3.62	0.04	0.00
MCBF-3H	1.60	98.09	11.42	52.82	559.51	3.05	0.03	0.00
MCBF-3I	1.80	98.74	18.75	71.57	551.56	1.86	0.04	0.00
MCBF-3J	2.00	99.44	17.93	89.50	533.49	1.97	0.03	0.00
MCBF-3K	2.20	98.04	9.91	99.41	527.09	2.91	0.03	0.00
MCBF-3L	2.40	86.49	0.59	100.00	463.96	39.52	0.03	0.00

Table 10. Amphibole $^{40}Ar/^{39}Ar$ data for the sample SALGA.

Step	Laser Power	% 40Ar	% Mol 39Ar	Cum. %	Age (Ma)	± 2s	K/Ca	± 2s
SALGA-1A	0.10	125.92	-0.02	-0.02	2614.51	9307.26	0.06	0.38
SALGA-1B	0.20	89.91	0.02	-0.01	4017.22	23511.28	0.02	0.26
SALGA-1C	0.30	90.15	0.06	0.06	0.00	23437.11	0.25	1.12
SALGA-1D	0.40	110.35	-0.02	0.03	0.00	19844.89	0.00	0.03
SALGA-1E	0.50	87.61	0.10	0.14	2552.81	15490.91	0.84	7.47
SALGA-1F	0.60	35.68	-0.23	-0.09	249.66	1321.94	0.36	0.92
SALGA-1G	0.70	130.43	0.96	0.86	669.63	114.61	0.17	0.09
SALGA-1H	0.80	101.43	5.58	6.44	524.17	51.67	0.05	0.00
SALGA-1I	0.90	101.42	15.95	22.39	567.40	17.67	0.04	0.00
SALGA-1J	1.00	101.31	31.38	53.78	554.41	9.71	0.04	0.00
SALGA-1K	1.20	102.66	23.59	77.37	558.87	17.50	0.04	0.00
SALGA-1L	1.40	102.18	8.52	85.89	552.89	28.98	0.04	0.00
SALGA-1M	1.60	94.12	6.38	92.27	507.20	57.19	0.04	0.00
SALGA-1N	1.80	96.08	5.97	98.24	490.46	56.27	0.04	0.00
SALGA-1O	2.00	105.49	0.41	98.65	1132.60	1061.70	0.02	0.02
SALGA-1P	2.20	334.96	0.07	98.72	0.00	7716.50	0.02	0.06
SALGA-1Q	2.40	31.16	0.15	98.87	662.64	1671.27	0.01	0.03
SALGA-1R	2.60	109.28	0.23	99.09	1124.20	1228.09	0.05	0.07
SALGA-1S	2.80	43.30	0.76	99.85	100.81	493.30	0.64	0.54
SALGA-1T	3.00	32.22	0.15	100.00	384.28	1344.20	0.06	0.10

Table 11. Biotite ^{40}Ar /^{39}Ar data for the sample SALGB (aliquots 1 and 2).

Step	Laser Power	% 40Ar	% Mol 39Ar	Cum. %	Age (Ma)	± 2s	K/Ca	± 2s
SALGB-1A	0.10	21.22	4.71	4.71	284.61	13.59	7.53	2.93
SALGB-1B	0.20	65.64	7.10	11.81	383.95	4.97	6.39	2.33
SALGB-1C	0.30	76.70	8.25	20.07	457.94	5.61	7.42	0.80
SALGB-1D	0.40	81.10	9.64	29.71	493.51	2.13	3.07	0.15
SALGB-1E	0.50	84.62	14.66	44.37	509.13	2.52	2.83	0.13
SALGB-1F	0.60	90.01	26.63	71.00	451.17	1.32	2.98	0.12
SALGB-1G	0.70	94.27	12.49	83.49	579.37	1.82	3.35	0.28
SALGB-1H	0.80	96.70	8.23	91.72	600.52	12.94	10.74	9.20
SALGB-1I	0.90	98.30	3.75	95.47	631.47	15.55	9.15	8.66
SALGB-1J	1.00	100.75	1.80	97.27	683.21	35.50	1.99	1.90
SALGB-1K	1.20	99.09	1.75	99.02	641.23	23.91	1.83	0.29
SALGB-1L	1.40	99.13	0.81	99.83	701.93	68.27	5.27	7.61
SALGB-1M	1.60	53.69	0.05	99.88	466.23	836.92	1.11	6.81
SALGB-1N	1.80	78.57	0.07	99.96	664.92	900.37	1.27	7.53
SALGB-1O	2.00	143.81	0.04	100.00	1301.09	1173.94	0.57	1.96
Step	Laser Power	% 40Ar	% Mol 39Ar	Cum. %	Age (Ma)	± 2s	K/Ca	± 2s
SALGB-2A	0.10	24.43	2.78	2.78	256.78	20.92	21.09	78.35
SALGB-2B	0.20	53.04	11.96	14.74	350.18	2.34	7.32	0.48
SALGB-2C	0.30	76.97	11.28	26.02	485.29	3.41	7.00	0.78
SALGB-2D	0.40	88.19	18.59	44.62	546.04	2.84	6.92	0.55
SALGB-2E	0.50	92.55	15.03	59.64	603.59	2.71	7.70	0.53
SALGB-2F	0.60	94.33	12.88	72.52	636.90	2.34	11.17	4.62
SALGB-2G	0.70	93.24	11.46	83.98	637.95	3.63	10.82	5.49
SALGB-2H	0.80	94.67	5.43	89.41	647.67	15.75	10.83	8.07
SALGB-2I	0.90	97.29	3.76	93.17	653.95	23.62	9.78	7.70
SALGB-2J	1.00	98.10	4.02	97.19	681.40	22.61	1.90	0.15
SALGB-2K	1.20	101.25	1.07	98.26	708.05	40.75	7.10	14.04
SALGB-2L	1.40	91.92	1.27	99.53	685.15	51.57	0.39	0.02
SALGB-2M	1.60	131.55	0.02	99.56	2398.15	3484.50	0.31	1.32
SALGB-2N	1.80	96.30	0.15	99.70	1229.10	789.16	1.00	2.55
SALGB-2O	2.00	99.05	0.32	100.02	659.05	178.03	2.60	7.62
SALGB-2P	2.20	6.59	-0.02	100.00	55.22	3371.95	-0.03	0.07

Table 12. Biotite ^{40}Ar /^{39}Ar data for the sample CC (aliquots 1 and 2).

Step	Laser Power	% 40Ar	% Mol 39Ar	Cum. %	Age (Ma)	± 2s	K/Ca	± 2s
CC-1A	0.10	124.68	0.04	0.04	897.13	759.14	2.54	9.20
CC-1B	0.20	100.11	3.43	3.47	480.51	4.60	184.50	965.62
CC-1C	0.30	100.25	12.54	16.01	485.24	2.10	147.09	133.52
CC-1D	0.40	100.00	11.02	27.03	498.01	2.48	483.71	1188.14
CC-1E	0.50	99.85	13.29	40.33	496.28	1.08	146.77	256.67
CC-1F	0.60	99.83	13.99	54.32	496.80	1.31	818.18	6444.86
CC-1G	0.70	100.00	10.32	64.64	498.99	1.24	13.51	1.44
CC-1H	0.80	99.94	14.94	79.58	499.04	1.20	55.77	9.16
CC-1I	0.90	100.18	6.98	86.56	502.79	2.89	47.44	24.52
CC-1J	1.00	100.28	4.49	91.05	501.43	4.29	41.54	43.64
CC-1K	1.20	100.69	2.48	93.53	505.71	5.43	335.35	4982.29
CC-1L	1.40	99.94	4.65	98.19	502.64	5.72	102.72	248.79
CC-1M	1.60	100.83	1.05	99.23	505.52	16.52	15.93	17.72
CC-1N	1.80	80.35	0.62	99.86	418.96	2.70	194.57	6189.70
CC-1O	2.00	93.80	0.14	100.00	423.31	125.18	3.45	9.94
Step	Laser Power	% 40Ar	% Mol 39Ar	Cum. %	Age (Ma)	± 2s	K/Ca	± 2s
CC-2A	0.10	122.17	0.05	0.05	800.22	587.70	0.97	2.57
CC-2B	0.20	91.47	3.06	3.11	456.09	2.36	156.96	1265.57
CC-2C	0.30	100.15	17.11	20.22	494.47	1.35	412.48	1587.55
CC-2D	0.40	98.94	18.33	38.55	493.28	1.16	259.12	656.91
CC-2E	0.50	100.25	11.27	49.82	499.90	2.95	89.60	101.19
CC-2F	0.60	100.39	16.26	66.08	500.00	2.18	249.04	433.33
CC-2G	0.70	100.45	11.63	77.71	501.53	1.39	177.31	433.52
CC-2H	0.80	100.24	9.42	87.13	497.87	2.73	2398.39	112792.28
CC-2I	0.90	101.39	3.88	91.02	509.93	9.65	221.98	2319.80
CC-2J	1.00	100.27	4.17	95.18	502.84	5.76	41.99	72.92
CC-2K	1.20	100.37	1.73	96.91	500.95	7.76	100.56	684.00
CC-2L	1.40	102.78	2.47	99.39	525.78	10.84	35.28	61.52
CC-2M	1.60	109.05	0.38	99.77	579.10	55.26	7.76	27.37
CC-2N	1.80	111.90	0.18	99.95	692.49	100.59	15.95	135.63
CC-2O	2.00	198.35	0.04	99.99	1432.21	780.12	3.37	58.46
CC-2P	2.20	167.43	0.01	100.00	2301.07	3049.55	0.16	0.46

Table 13. Sulfur stable isotopes analyses.

Sample	$d^{34}S‰$
CC-MOLY-01	-2.50
CC-MOLY-02	-1.99
CC-MOLY-03	-1.86
SALG-MOLY-01	3.29
SALG-PY-01	3.46
BF-MOLY-01	4.17
BF-MOLY-02	4.27
BF-MOLY-03	4.24

CAPÍTULO IV

1. DICUSSÕES E CONCLUSÕES

O Capítulo I, de natureza introdutória, buscou contextualizar o leitor com relação à área e ao tema de estudo. Com o arcabouço teórico definido, os capítulos II e III, em formato de artigo, apresentaram os dados gerados, bem como suas respectivas interpretações. Deste modo, o presente Capítulo irá integrar as principais descobertas e ideias apontadas previamente.

O presente estudo teve como foco rochas melanocráticas previamente interpretadas como rochas máficas/ultramáficas (Moeri & Kloechner, 1979a,b); hornblenda-, clinopiroxênio- e/ou biotita-skarns; e gnaisses calcissilicáticos (Cavalcante et al., 2016). Com base nas informações coletadas em campo, reforçadas pelas análises realizadas sob microscópio petrográfico e em laboratório, esta tese de doutorado propõe uma nova interpretação acerca destas rochas, atribuindo a elas uma gênese hidrotermal.

Tanto na mina de Bonfim, com sua ocorrência *near-mine* Morro do Careca, quanto nas demais ocorrências estudadas, como Salgadinho, Alívio, Recanto, Caçador, Espinheiro, Galo, Cafuca, Pedro Tomás, Isidoro e Riachão, foram observadas basicamente três associações minerais, identificadas como Diopsídio-Anfibólio-Feldspato (DAF), Anfibólio-Feldspato (AF) e "Rica em Biotita" ou "Biotititos" (BR). Estas três associações de minerais representam halos e estágios do processo de alteração hidrotermal.

Na fase de alta temperatura, é formado o DAF, que se destaca pela presença de diopsídio, feldspatos ricos em Ca e Ba (cátions divalentes) e pela grande quantidade de minerais portadores de elementos terras-raras (ETR), tais como titanita, epidoto-allanita e apatita. Também destaca-se a formação de minerais de bário, como barita e hialofana. O estágio de baixa temperatura é representado pelas associações AF e BR. Aquela é caracterizada pelo consumo de diopsídio e pela presença de feldspatos ricos em Na e K (cátions monovalentes), enquanto esta é composta por rochas intensamente foliadas compostas majoritariamente por biotita. Scheelita e sulfetos são mais abundantes nas fases de baixa temperatura.

As associações minerais DAF e AF estão relacionadas a processos de alteração hidrotermal de natureza cálcica, com metassomatismo em Ca, Mg, Fe, Ba, Na, ETR, Mo e W. A associação BR, por sua vez, representa um halo potássico, apresentando metassomatismo em Na, K, Si, Mo e W. Tais verificações são apontadas por análises tanto de geoquímica de rocha total quanto por microssonda eletrônica.

Há relações espaciais, texturais e metalogenéticas entre as rochas abordadas neste estudo com os *skarns* de scheelita da Província Mineral Seridó. Sugere-se, portanto, que elas representam as zonas de raiz dos depósitos de *skarn* da região, formadas a partir do fluxo concentrado de fluido hidrotermal ao longo de zonas de cisalhamento subverticais. À época do Ciclo Brasiliano, havia condições ideais para a formação de *skarns* de tungstênio, notadamente o espessamento crustal devido à colisão de blocos; o magmatismo extensivo e duradouro; e a formação de estruturas de grande escala, como reflexo do Lineamento Transbrasiliano.

Os plutons de natureza félsica da Faixa Seridó formaram-se, em sua maioria, a partir da reciclagem crustal de um terreno que já possuía teores anômalos de W-Mo, entre outros elementos. Processos de fusão parcial desta crosta, que levaram à formação dos magmas, representam um processo inicial de reconcentração e enriquecimento em metais nas câmaras magmáticas. Em concordância com os dados de isótopos estáveis de enxofre obtidos neste estudo, estas rochas magmáticas provavelmente são a principal fonte de metais para a mineralização.

A ascensão dos magmas ao longo da crosta marca uma segunda etapa de diferenciação e reconcentração, até que o fluido hidrotermal rico em metais fosse exsolvido. Posteriormente, a solução

metassomática migrou para zonas de cisalhamento ativas, onde o fluxo canalizado levou à alteração hidrotermal das rochas encaixantes, tanto em níveis intermediários (i.e., nas zonas de raiz) quanto nos sítios de deposição final, formando os *skarns* clássicos da região.

Como principal controle para a deposição do minério, destacam-se as reações com as rochas encaixantes: nos *skarns*, a alteração ocorre principalmente em rochas carbonáticas, que, por serem mais reativas, fazem com que o minério precipite de maneira mais eficiente, geralmente como *ore shoots* ao longo de charneiras de dobras; ao passo que, nas zonas de raiz, há alteração de granitoides, que são menos reativos e podem ser a causa do minério ocorrer disseminado nas rochas.

Ambas as tipologias (i.e., zonas de raiz e *W-skarns*) de depósitos/ocorrências são cogenéticas, sendo parte do mesmo sistema regional mineralizado em W-Mo, em que cada tipo de alteração é formado sob diferentes condições de pressão, temperatura, composição, pH, REDOX, razão fluido/rocha e composição da encaixante. Há, ainda, dois fatores determinantes para a formação destas diferentes modalidades de depósito/ocorrência de tungstênio: A disponibilidade e a mobilidade de elementos químicos.

As relações temporais entre as rochas das zonas de raiz e os *W-skarns* também são evidenciadas por análises U-Pb e $^{40}Ar/^{39}Ar$. Os dados desta pesquisa, juntamente com os da literatura, ressaltam a importância da Orogenia Brasiliana para as mineralizações na área de estudo, mostrando a contemporaneidade entre as zonas de raiz, os *W-skarns*, o plutonismo regional extensivo e a formação de diques pegmatíticos, tendo, ainda, depósitos auríferos sendo formados em suas fases mais tardias. Define-se, portanto, uma época metalogenética na transição do Neoproterozoico para o Cambriano na Província Mineral Seridó.

Datações U-Pb em grãos de zircão herdados revelam que as alterações hidrotermais de natureza Ca-Ba e K ocorreram em diferentes tipos de rochas do embasamento, apesar de todas corresponderem a granitoides. Foram registradas idades Paleoarquenas e Neoarqueanas, que podem ter relação com o Maciço São José do Campestre, bem como Riacianas, correspondentes ao Complexo Caicó.

Nas rochas representativas das zonas de raiz, são formados os mesmos tipos de alteração hidrotermal, independente da rocha encaixante. Análises de geoquímica de rocha total e química mineral, bem como observações ao microscópio petrográfico, entretanto, apontam para peculiaridades inerentes a cada depósito ou ocorrência estudada. Como exemplo destacam-se o depósito de Bonfim e a ocorrência *near-mine* de Morro do Careca, que, por estarem localizados ao longo de um embasamento Paleoarqueano, apresentam valores bastante anômalos de ETR.

Outro ponto relevante está na clara associação entre rochas pegmatíticas e a mineralização nas zonas de raiz. Baseado em suas relações de corte e associação espacial, pegmatitos podem ter fornecido voláteis ou W±Mo±Ba para a mineralização. Além disso, o granito pegmatoide localizado na pedreira Mineragram pode representar uma fase transicional entre as suítes magmáticas da área de estudo e as rochas da Província Pegmatítica Borborema. É possível que este granito pegmatoide e rochas similares tenham sido as rochas-fonte não só para os pegmatitos da região, mas também de tungstênio e outros metais associados.

De maneira similar ao que ocorre no *Tintina Gold Belt*, sugere-se um zoneamento regional entre os depósitos de *skarn* e os *gold-only*, tipicamente hospedados em veios de quartzo. Ambos os tipos de depósitos têm uma provável origem – ou, pelo menos, uma forte influência – magmática para os fluidos, bem como associação espacial com intrusões. Além disso, dados geocronológicos apontam para um caráter mais tardio para os depósitos auríferos da região em comparação aos *skarns*. Esta configuração

espaço-temporal sugere uma interpretação de integração desses depósitos a um sistema do tipo *Intrusion-Related*.

Nestes sistemas, há tipicamente o desenvolvimento de *W-skarns* anidros a temperaturas mais altas, com a posterior formação de depósitos auríferos associados a Bi e Te. Nos *skarns* mineralizados da mina de Bonfim, é notável a mineralização de scheelita e molibdenita, que segue a estruturação NS-N20°E regional, sendo cortada por vênulas auríferas discordantes.

Halos de alteração hidrotermal de natureza cálcica, sódica, ou sódico-cálcica são recorrentes em depósitos magmático-hidrotermais, tais como Pórfiro, IOCG, *Intrusion-Related* e *skarns*, podendo estar associados às suas zonas de raiz. O mesmo processo ocorre com halos potássicos, frequentemente onde a mineralização atinge teores mais elevados. Apesar das peculiaridades inerentes a cada uma dessas modalidades de depósito, seus halos de alteração costumam apresentar semelhanças mineralógicas e texturais entre si. Portanto, os depósitos magmático-hidrotermais citados podem ser correlacionados com base na formação e evolução de seus halos de alteração, que podem ter como um de seus principais controles as taxas de difusão/mobilidade de elementos na solução hidrotermal.

A presente tese abordou, sob uma perspectiva integrada entre geologia regional e econômica, rochas oriundas de processos de alteração hidrotermal profunda, que representam a raiz do sistema da Província Mineral Seridó. Correlacionando diferentes classes de depósitos magmático-hidrotermais, haverá uma mudança de paradigmas, em que serão estabelecidos novos critérios prospectivos, que poderão estender-se para além da Faixa Seridó. Com as respostas para algumas perguntas neste trabalho, abrem-se novos questionamentos, que serão os responsáveis por darem continuidade ao giro das engrenagens que movem a Geologia.

2. REFERÊNCIAS BIBLIOGRÁFICAS

ALLÈGRE, C.J. 2008. Isotope Geology. Cambridge University Press, New York, United States, 534 p.

ALMEIDA, F.F.M., HASUI, Y., BRITO NEVES, B.B., FUCK, R.A. 1981. Brazilian structural provinces: an introduction. Earth Science Reviews, 17, 1-29.

AMARAL, W.S., SANTOS, T.J.S., WERNICK, E., NOGUEIRA NETO, J.A.N., DANTAS, E.L., MATTEINI, M. 2012. High-pressure granulites from Cariré, Borborema Province, NE Brazil: Tectonic setting, metamorphic conditions and U–Pb, Lu–Hf and Sm–Nd geochronology. Gondwana Research, 22, 892-909.

ANGELIM, L.A.A., VASCONCELOS, A.M, GOMES, J.R.C., WANDERLEY, A.A., FORGIARINI, L.L., MEDEIROS, M.F. 2004. Folha SB-24-Jaguaribe. In: SCHOBBENHAUS, C., GONÇALVES, J.H., SANTOS, J.O.S., ABRAM, M.B., LEÃO NETO, R., MATOS, G.M.M., VIDOTTI, R.M., RAMOS, M.A.B., JESUS, J.D.A. Carta Geológica do Brasil ao Milionésimo, Sistema de Informações Geográficas. Programa Geologia do Brasil, CPRM, Brasília.

ANGELIM, L.A.A., MEDEIROS, V.C., NESI, J.R. 2006. Programa Geologia do Brasil – PGB. Projeto Geologia e Recursos Minerais do Estado do Rio Grande do Norte. Mapa Geológico do Estado do Rio Grande do Norte. Escala. 1:500.000. Recife: CPRM/FAPERN.

ARAUJO, C.E.G., WEINBERG, R.F., CORDANI, U.G. 2014. Extruding the Borborema Province (NE-Brazil): a two-stage Neoproterozoic collision process. Terra Nova, 26, 157–168.

ARAUJO, C.E.G., CORDANI, U.G., AGBOSSOUMOUNDE, Y., CABY, R., BASEI, M.A.S., WEINBERG, R.F., SATO, K. 2016. Tightening-up NE Brazil and NW Africa connections: New U–Pb/Lu–Hf zircon data of a complete plate tectonic cycle in the Dahomey belt of the West Gondwana Orogen in Togo and Benin. Precambrian Research, 276, 24-42.

ARAÚJO, M.N.C., VASCONCELOS, P.M., SILVA, F.C.A., JARDIM DE SÁ, E., HOLCOMBE, R.J. 2002. Geometry and structural control of Au vein mineralizations in the Seridó Belt, northeastern Brazil. Journal of South American Earth Sciences, 15, 337-348.

ARAÚJO, M.N.C., VASCONCELOS, P.M., SILVA, F.C.A., JARDIM DE SÁ, E.F., SÁ, J.M. 2005. $^{40}Ar/^{39}Ar$ geochronology of gold mineralization in Brasiliano strike-slip shear zones in the Borborema province, NE Brazil. Journal of South American Earth Sciences, 19, 445-460.

ARCHANJO, C.J., BOUCHEZ, J.L. 1991. Le Seridó, une chaîne transpressive dextre au Protérozoïque supérieur du nord-est du Brésil. Bulletin de la Société Géologique de France, 162, 637-647.

ARCHANJO, C.J., OLIVIER, P., BOUCHEZ, J.L. 1992. Plutons granitiques du Seridó (NE du Brésil): écoulement magmatique parallèle à la chaîne révélé par leur anisotropie magnétique. Bulletin de la Société Géologique de France, 163, 509-520.

ARCHANJO, C.J., TRINDADE, R.I.F., BOUCHEZ, J.L., ERNESTO, M. 2002. Granite fabrics and regional-scale strain partitioning in the Seridó belt (Borborema Province, NE Brazil). Tectonics, 21, 3-14.

ARCHANJO, C.J. VIEGAS, L.G.F., HOLLANDA, M.H.B.M., SOUZA, L.C., LIU, D. 2013. Timing of the HT/LP transpression in the Neoproterozoic Seridó Belt (Borborema Province, Brazil): Constraints from U-Pb (SHRIMP) geochronology and implications for the connections between NE Brazil and West Africa. Gondwana Research, 23, 701-714.

AUDÉTAT, A., GÜNTHER, D., HEINRICH, C.A. 2000. Causes for Large-Scale Metal Zonation around Mineralized Plutons: Fluid Inclusion LA-ICP-MS Evidence from the Mole Granite, Australia. Economic Geology, 95, 1563-1581.

BARATI, M., GHOLIPOOR, M. 2014. Study of REE behaviors, fluid inclusions, and O, S stable Isotopes in Zafar-abad iron skarn deposit, NW Divandarreh, Kordestan province. Journal of Economic Geology, 6, 5-6.

BAUMGARTNER, R., ROMER, R.L., MORITZ, R., SALLET, R., CHIARADIA, M. 2006. Columbite-tantalite-bearing granitic pegmatites from the Seridó Belt, Northeastern Brazil: Genetic constraints from U-Pb dating and Pb isotopes. The Canadian Mineralogist, 44, 69-86.

BEURLEN, H., DA SILVA, M.R.R., CASTRO, C., 2001. Fluid inclusion microthermometry in Be-Ta-(Li-Sn)-bearing pegmatites from the Borborema Province, northeast Brazil. Chemical Geology, 173, 107-123.

BEURLEN, H., SILVA, M.R.R., THOMAS, R., SOARES, D.R., OLIVIER, P. 2008. Nb–Ta–(Ti–Sn) oxide mineral chemistry as tracer of rare element granitic pegmatite fractionation in the Borborema Province, Northeastern Brazil. Mineralium Deposita, 43, 207-228.

BEURLEN, H., BARRETO, S., MARTIN, R., MELGAREJO, J., SILVA, M.R.R., SOUZA NETO, J.A. 2009. The Borborema Pegmatite Province, NE-Brazil Revisited. Estudos Geológicos, 19, 62-66.

BEURLEN, H., RHEDE, D., SILVA, M.R.R., THOMAS, R., GUIMARÃES, I.P. 2009. Petrography, Geochemistry and Chemical Electron Microprobe U-Pb-Th Dating of Pegmatitic Granites in Borborema Province, North-Eastern Brazil: a Possible Source of the Rare Element Granitic Pegmatites. Terræ, 6, 59-71.

BEURLEN, H., THOMAS, R., SILVA, M.R.R., MÜLLER, A., RHEDE, D., SOARES, D.R. 2014. Perspectives for Li- and Ta-Mineralization in the Borborema Pegmatite Province, NE-Brazil: A review. Journal of South American Earth Sciences, 56, 110-127.

BOOMERI, M., ISHIYAMA, D., MIZUTA, T., MATSUBAYA, O., LENTZ, D.R. 2010. Carbon and Oxygen Isotopic Systematics in Calcite and Dolomite from the Sangan Iron Skarn Deposit, Northeastern Iran. Journal of Sciences, Islamic Republic of Iran, 21, 213-224.

BOWEN, N.L. 1928. The Evolution of Igneous Rocks. Princeton University Press. Princeton, NJ.

BOWMAN, J.R., COVERT, J.J., CLARK, A.H., MATHIESON, G.A. 1985. The CanTung E-zone scheelite skarn ore body, Tungsten, Northwest Territories: oxygen, hydrogen, and carbon isotope studies. Economic Geology, 80, 1872-1895.

BRITO NEVES, B.B., SANTOS, E.J., VAN SCHMUS, W.R. 2000. Tectonic History of the Borborema Province, Northeastern Brazil. In: CORDANI, U.G., MILANI, E.J., THOMAZ FILHO, A., CAMPOS, D.A. Tectonic Evolution of South America. 855 p.

BRITO NEVES, B.B., PASSARELLI, C.R., BASEI, M.A.S., SANTOS, E.J. 2003. Idades U-Pb em Zircão de Alguns Granitos Clássicos da Província Borborema. Geologia Série Científica USP, 3, 25-38.

BRITO NEVES, B.B., FUCK, R.A. 2014. The basement of the South American platform: Half Laurentian (N-NW) + half Gondwanan (E-SE) domains. Precambrian Research, 244, 75-86.

BRITO NEVES, B.B., FUCK, R.A., PIMENTEL, M.M. 2014. The Brasiliano collage in South America: a review. Brazilian Journal of Geology, 44, 493-518.

BROWN, P.E., BOWMAN, J.R., KELLY, W.C. 1985. Petrologic and stable isotope constraints on the source and evolution of skarn-forming fluids at Pine Creek, California. Economic Geology, 80, 72-95.

CAMACHO, A., MCDOUGALL, I., ARMSTRONG, R., BRAUN, J. 2001. Evidence for shear heating, Musgrave Block, central Australia. Journal of Structural Geology, 23, 1007-1013.

CANDELA, P.A., PICCOLI, P.M. 2005. Magmatic Processes in the Development of Porphyry-Type Ore Systems. In: HEDENQUIST, J.W., THOMPSON, J.F.H., GOLDFARB, R.J., RICHARDS, J.P. (eds). Economic Geology 100th Anniversary Volume, 25–37.

CANIL, D., GRONDAHL, C., LACOURSE, T., PISIAK, L.K. 2016. Trace elements in magnetite from porphyry Cu-Mo-Au deposits in British Columbia, Canada. Ore Geology Reviews, 72, 1116-1128.

CAO, Y., ZHENG, Z., DU, Y., GAO, F., QIN, X., YANG, H., LU, Y., DU, Y. 2017. Ore geology and fluid inclusions of the Hucunnan deposit, Tongling, Eastern China: Implications for the separation of copper and molybdenum in skarn deposits. Ore Geology Reviews, 925-939.

CARTEN, R.B. 1986. Sodium-Calcium Metasomatism, Chemical, Temporal, and Spatial Relationships at the Yerington, Nevada, Porphyry Copper Deposit. Economic Geology, 81, 1495-1519.

CAVALCANTE, R., CUNHA, A.L.C., OLIVEIRA, R.G., MEDEIROS, V.C., DANTAS, A.R., COSTA, A.P., LINS, C.A.C., LARIZZATTI, J.H. 2016. Metalogenia das Províncias Minerais do Brasil: Área Seridó-Leste, Extremo Nordeste da Província Borborema (RN-PB). CPRM, Série Províncias Minerais do Brasil, 8, 105 p.

CAVALCANTI NETO, M.T.O. 2008. A faixa cuprífera do Rio Grande do Norte e Paraíba e as relações de contato entre as formações Equador e Seridó. Holos, 3, 105-118.

CHAGAS, C.F. 2017. Caracterização do Metamorfismo de Contato Provocado pelo Plutão Ediacariano Totoró, NE do Brasil. Masters Dissertation (Unpublished), Universidade Federal do Rio Grande do Norte, 80 p.

CHANG, Z., MEINERT, L. 2004. Vermicular Textures of Quartz Phenocrysts, Endoskarn, and Implications for Late Stage Evolution of Granitic Magma. Chemical Geology, 210, 149-171.

CORDANI, U.G., PIMENTEL, M.M., ARAÚJO, C.E., FUCK, R.A. 2013. The significance of the Transbrasiliano-Kandi tectonic corridor for the amalgamation of West Gondwana. Brazilian Journal of Geology, 43, 583-597.

CORREA, R.T., VIDOTTI, R.M., OKSUM, E. 2016. Curie surface of Borborema Province, Brazil. Tectonophysics, 679, 73-87.

CORRIVEAU, L., MONTREUIL, J.F., POTTER, E.G. 2016. Alteration Facies Linkages Among Iron Oxide Copper-Gold, Iron Oxide-Apatite, and Affiliated Deposits in the Great Bear Magmatic Zone, Northwest Territories, Canada. Economic Geology, 111, 2045-2072.

CORSINI, M., FIGUEIREDO, L.L., CABY, R., FÉRAUD, G., RUFFET, G., VAUCHEZ, A. 1998. Thermal history of the Pan-African/Brasiliano Borborema Province of northeast Brazil deduced from 40Ar/39Ar analysis. Tectonophysics, 285, 103-117.

COSTA, A.P., DANTAS, A.R. 2014. Carta geológica Lajes Folha SB.24-X-D-VI, Estado do Rio Grande do Norte. Programa Geologia do Brasil – PGB. Escala 1:100.000. Recife: CPRM – Serviço Geológico do Brasil.

COUTINHO, M.G.N. 1994. The Geology of Shear-Zone Hosted Gold Deposits in Northeast Brazil. PhD Thesis (Unpublished), University of London, 391 p.

CUNHA DE SOUZA, L. 1987. Geologia e petroquímica de uma área ao norte de Equador (RN). Masters Dissertation (Unpublished), Universidade Federal de Pernambuco, 319 p.

CURTO, J.B., VIDOTTI, R.M., FUCK, R.A., BLAKELY, R.J., ALVARENGA, C.J.S., DANTAS, E.L., 2014. The tectonic evolution of the Transbrasiliano Lineament in northern Paraná Basin, Brazil, as inferred from aeromagnetic data. Journal of Geophysical Research: Solid Earth, 119, 1–19.

DANTAS, E.L. 1996. U-pb and Sm-Nd Geochronology of Archean and Paleoproterozoic Terrains of the Caldas Brandão Massif, NE Brazil. PhD Thesis (Unpublished), Universidade Estadual Paulista, Campus Rio Claro, 206 p.

DANTAS, E.L., HACKSPACHER, P.C., MAGINI, C., LEGRAND, J.M. 2002. Sistema Sm-Nd em Rocha-Total Aberto Versus Fechado: Comportamento Isotópico em Zonas de Alta Deformação. Geologia USP Série Científica, 2, 109-129.

DANTAS, E.L., SILVA, A.M., ALMEIDA, T., MORAES, R.A.V. 2003. Old geophysical data applied to modern geological mapping problems: A case study in the Seridó Belt, NE Brazil. Revista Brasileira de Geociências, 33, 65-72.

DANTAS, E.L., VAN SCHMUS, W.R., HACKSPACHER, P.C., FETTER, A.H., BRITO NEVES, B.B., CORDANI, U., NUTMAN, A.P., WILLIAMS, I.S. 2004. The 3.4-3.5 Ga São José do Campestre Massif, NE Brazil: remnants of the oldest crust in South America. Precambrian Research, 130, 113-137.

DANTAS, E.L., SOUZA, Z.S., WERNICK, E., HACKSPACHER, P.C., MARTIN, H., XIAODONG, D., LI, J.W. 2013. Crustal growth in the 3.4–2.7 Ga São José de Campestre Massif, Borborema Province, NE Brazil. Precambrian Research, 227, 120-156.

DARE, S.A.S., BARNES, S.J., BEAUDOIN, G., MÉRIC, J., BOUNTROY, E., POTVIN-DOUCET, C. 2014. Trace elements in magnetite as petrogenetic indicators. Mineralium Deposita, 49, 785-796.

DEER, W.A., HOWIE, R.A., ZUSSMAN, J. 2013. An Introduction to the Rock Forming Minerals. 3rd ed. Mineralogical Society. 510 p.

DICK, L.A., HODGSON, C.J. 1982. The MacTung W-Cu(Zn) contact metasomatic and related deposits of the northeastern Canadian Cordillera. Economic Geology, 77, 845-867.

DILL, H.G., HANSEN, B.T., WEBER, B. 2013. U/Pb age and origin of supergene uranophane-beta from the Borborema Pegmatite Mineral Province, Brazil. Journal of South American Earth Sciences, 45, 160-165.

DING, T., VALKIERS, S., KIPPHARDT, H., DE BRIÈVE, P., TAYLOR, P.D.P., GONFIANTINI, R., KROUSE, R. 2001. Calibrated sulfur isotope abundance ratios of three IAEA sulfur isotope reference materials and V-CDT with a reassessment of the atomic weight of sulfur. Geochimica et Cosmochimica Acta, 65, 2433–2437.

DING, T., MA, D., LU, J., ZHANG, R. 2018. Garnet and scheelite as indicators of multi-stage tungsten mineralization in the Huangshaping deposit, southern Hunan province, China. Ore Geology Reviews, 94, 193-211.

EBERT, H. 1970. The Precambrian geology of the "Borborema" Belt (States of Paraíba and Rio Grande do Norte; northeastern Brazil) and the origin of its mineral provinces. Geologische Rundschau, 59, 1292-1326.

ERCIT, T.S. 2002. The Mess That Is “Allanite”. The Canadian Mineralogist, 40, 1411-1419.

EUGSTER, H.P. 1985. Granites and hydrothermal ore deposits: a geochemical framework. Mineralogical Maganize, 49, 7-23.

FERREIRA, V.P., SIAL, A.N., JARDIM DE SÁ, E.F. 1998. Geochemical and isotopic signatures of Proterozoic granitoids in terranes of the Borborema structural province, northeastern Brazil. Journal of South American Earth Sciences, 11, 439-455.

FONTEILLES, M., SOLER, P., DEMANGE, M., DERRÉ, C., KRIER-SCHELLEN, A.N., VERKAEREN, J., GUY, B., ZAHM, A. 1989. The Scheelite Skarn Deposit of Salau (Ariege, French Pyrenees). Economic Geology, 84, 1172-1209.

GANGULY, J., TIRONE, M. 2009. Closure Temperature, Cooling Age and High Temperature Thermochronology. In: GUPTA, A.K., DASGUPTA, S. (eds). Physics and Chemistry of the Earth’s Interior, Springer, New York, 89-99.

GARCIA, V.B.P. 2018. A Raiz do Sistema IOCG de Carajás: alterações hidrotermais e mineralização niquelífera neoarqueana no depósito GT-34. Masters Dissertation (Unpublished), Universidade de Brasília, 88 p.

GIERÉ, R., SORENSEN, S.S. 2004. Allanite and Other REE-Rich Epidote-Group Minerals. Reviews in Mineralogy & Geochemistry, 56, 431-493.

GIOIA, S.M.C.L., PIMENTEL, M.M. 2000. The Sm-Nd Isotopic Method in the Geochronology Laboratory of the University of Brasília. Anais da Academia Brasileira de Ciências, 72, 219-245.

GOLDFARB, R.J., HART, C.J.R., MILLER, M., MILLER, L., LANG FARMER, G., GROVES, D.I. 2000. The Tintina Gold Belt – A Global Perspective. In: TUCKER, T.L., SMITH, M.T. (eds.). The Tintina Gold Belt: Concepts, Exploration and Discoveries. British Columbia and Yukon Chamber of Mines Special Volume 2, 5-34.

GOLDFARB, R.J., BAKER, T., DUBÉ, B., GROVES, D.I., HART, C.R.J., GOSSELIN, P. 2005. Distribution, Character, and Genesis of Gold Deposits in Metamorphic Terranes. In: HEDENQUIST, J.W., THOMPSON, J.F.H., GOLDFARB, R.J., RICHARDS, J.P. (eds). Economic Geology 100th Anniversary Volume, 407–450.

GROVES, D.I., BIERLEIN, F.P., MEINERT, L.D., HITZMAN, M.W. 2010. Iron oxide copper-gold (IOCG) deposits through Earth history: Implications for origin, lithospheric setting, and distinction from other epigenetic iron oxide deposits. Economic Geology, 105, 641–654.

HACKSPACHER, P.C., DANTAS, E.L., BRITO NEVES, B.B., LEGRAND, J.M. 1997. Northwestern Overthrusting and Related Lateral Escape During the Brasiliano Orogeny North of the Patos Lineament, Borborema Province, Northeast Brazil. International Geology Review 39 609-620.

HARLOV, D, TROPPER, P., SEIFERT, W., NIJLAND, T., FÖRSTER, H.J. 2006. Formation of Al-rich titanite (CaTiSiO4O-CaAlSiO4OH) reaction rims on ilmenite in metamorphic rocks as a function of fH2O and fO2. Lithos, 88, 72-84.

HART, C.J.R. 2007. Reduced intrusion-related gold systems. In: Goodfellow, W.D. (ed). Mineral deposits of Canada: A Synthesis of Major Deposit Types, District Metallogeny, the Evolution of Geological Provinces, and Exploration Methods. Geological Association of Canada, Mineral Deposits Division, Special Publication 5, 95-112.

HAWTHORNE, F.C., OBERTI, R., HARLOW, G.E., MARESCH, W.V., MARTIN, R.F., SCHUMACHER, J.C., WELCH, M.D. 2012. IMA Report: Nomenclature of the amphibole supergroup. American Mineralogist, 97, 2031-2048.

HOEFS, J. 2009. Stable Isotope Geochemistry. Springer, Berlin, Germany. 293 p.

HOLLANDA, M.H.B.M., ARCHANJO, C.J., SOUZA, L.C., DUNYI, L. ARMSTRONG, R. 2011. Long-lived Paleoproterozoic granitic magmatism in the Seridó-Jaguaribe domain, Borborema Province-NE Brazil. Journal of South American Earth Sciences, 32, 287-300.

HOLLANDA, M.H.B.N. 2012. Geocronologia de eventos magmáticos e mineralizações associadas no Precambriano da Faixa Seridó, Província Borborema. Thesis (Unpublished), Universidade de São Paulo, 94 p.

HOLLANDA, M.H.B.M., SOUZA NETO, J.A., ARCHANJO, C.J., STEIN, H., SARTORATO, A.C. 2012. Relação temporal entre mineralizações de W-Mo e magmatismo granítico neoproterozoico-cambriano na Faixa Seridó. In: Annals of the 46th Brazilian Congress of Geology.

HOLLANDA, M.H.B.M., ARCHANJO, C.J., BAUTISTA, J.R., SOUZA, L.C. 2015. Detrital zircon ages and Nd isotope compositions of the Seridó and Lavras da Mangabeira basins (Borborema Province, NE Brazil): Evidence for exhumation and recycling associated with a major shift in sedimentary provenance. Precambrian Research, 258, 186-207.

HOLLANDA, M.H.B.M., SOUZA NETO, J.A., ARCHANJO, C.J., STEIN, H., MAIA, A.C.S. 2017. Age of the granitic magmatism and the W-Mo mineralization in skarns of the Seridó belt (NE Brazil) based on zircon U-Pb (SHRIMP) and molybdenite Re-Os dating. Journal of South American Earth Sciences, 79, 1-11.

HRONSKY, J.M.A., GROVES, D.I., LOUCKS, R.R., BEGG, G.C. 2012. A unified model for gold mineralisation in accretionary orogens and implications for regional-scale exploration targeting methods. Miner. Depos. 47, 339–358.

ISMAIL, R., CIOBANU, C.L., COOK, N.J., TEALE, G.S., GILES, D., MUMM, A.S., WADE, B. 2014. Rare earths and other trace elements in minerals from skarn assemblages, Hillside iron oxide–copper–gold deposit, Yorke Peninsula, South Australia. Lithos, 184–187, 456–477.

JARDIM DE SÁ, E.F., LEGRAND, J.M., MCREATH, I. 1981. "Estratigrafia" de rochas granitóides na região do Seridó (RN-PB) com base em critérios estruturais. Revista Brasileira de Geociências, 11, 50-57.

JARDIM DE SÁ, E.F., MACEDO, M.H.F., LEGRAND, J.M., MCREATH, I., GALINDO, A.C., SÁ, J.M. 1987. Proterozoic granitoids in a polycyclic setting: the Seridó region, NE Brazil. In: Proceeding International Symposium Granites Association Mineralization, 1st, Expanded Abstract, 1, 102-110.

JARDIM DE SÁ, E.F. 1994. A Faixa Seridó (Província Borborema, NE do Brasil) e o seu significado geodinâmico na Cadeia Brasiliana/Pan-Africana. Brasilia. 804 p. PhD Thesis (Unpublished), Geosciences Institute of the University of Brasília.

JARDIM DE SÁ, E.F., FUCK, R.A., MACEDO, M.H.F., PEUCAT, J.J., KAWASHITA, K., SOUZA, Z.S., BERTRAND, J.M. 1995. Pre-Brasiliano orogenic evolution in the Seridó Belt, NE Brazil: Conflicting geochronological and structural data. Revista Brasileira de Geociências, 25, 307-314.

KOPPERS, A.A.P. 2002. ArArCALC - software for Ar-40/Ar-39 age calculations. Computers and Geosciences, 28, 605-619.

LANG, J.R., BAKER, T. 2001. Intrusion-Related gold systems: the present level of understanding. Mineralium Deposita, 36, 477-489.LAYNE, G.D., LONGSTAFFE, F.J., SPOONER, E.T.C. 1991. The JC tin skarn deposit, southern Yukon Territory: II. A carbon, oxygen, hydrogen, and sulfur stable isotope study. Economic Geology, 86, 48-65.

LAYNE, G.D., LONGSTAFFE, F.J., SPOONER, E.T.C. 1991. The JC tin skarn deposit, southern Yukon Territory: II. A carbon, oxygen, hydrogen, and sulfur stable isotope study. Economic Geology, 86, 48-65.

LEAKE, B.E., WOOLEY, A.R., ARPS. C.E.S., BIRCH, W.D., GILBERT, M.C., GRICE, J.D., HAWTHORNE, F.C., KATO, A., KISCH, H.J., KRIVOVICHEV, V.G., LINTHOUT, K., LAIRD, J., MANDARINO, J., MARESCH, W.V., NICKEL, E.H., ROCK, N.M.S., SCHUMACHER, J.C., SMITH, D.C., STEPHENSON, N.C.N., UNGARETTI, L., WHITTAKER, E.J.W., YOUZHI, G. 1997. Nomenclature of Amphiboles: Report of the Subcommittee on Amphiboles of the International Mineralogical Association Commission on New Minerals and Mineral Names. The Canadian Mineralogist, 35, 219-246.

LECUMBERRI-SANCHEZ, P., VIEIRA, R., HEINRICH, C.A., PINTO, F., WÄLLE, M. 2017. Fluid-rock interaction is decisive for the formation of tungsten deposits. Geology, 45, 579-582.

LENTZ, D.R. 1998. Mineralized Intrusion-Related Skarn Systems. Mineralogical Association of Canada Short Course Series, 26, 666 p.

LOCOCK, A.J. 2014. An excel spreadsheet to classify chemical analyses of amphiboles following the IMA 2012 recommendations. Computers and Geosciences, 62, 1-11.

LU, Y.J., KERRICH, R., MCCUAIG, T.C., LI, Z.X., HART, C.J.R., CAWOOD, P.A., HOU, Z.Q., BAGAS, L., CLIFF, J., BELOUSOVA, E.A., TANG, S.H. 2013. Geochemical, Sr-Nd-Pb, and Zircon Hf-O Isotopic Compositions of Eocene-Oligocene Shoshonitic and Potassic Adakite-like Felsic Intrusions in Western Yunnan, SW China: Petrogenesis and Tectonic Implications. Journal of Petrology, 54, 1309-1348.

LUDWIG, K.R. 2008. User's Manual for Isoplot 3.70. Berkeley Geochronology Center Special Publication, 4, 76 p.

MANNING, D.A.C., HENDERSON, P. 1984. The behavior of tungsten in granitic melt-vapor systems. Contributions to Mineralogy and Petrology, 86, 286--293.

MARK, G., FOSTER, D.R.W. 2000. Magmatic–hydrothermal albite–actinolite–apatite-rich rocks from the Cloncurry district, NW Queensland, Australia. Lithos, 51, 223-245.

MATHIESON, G.A., CLARK, A.H. 1984. The Cantung E Zone Scheelite Skarn Orebody, Tungsten, Northwest Territories: A Revised Genetic Model. Economic Geology, 79, 883-901.

MCSWIGGEN, P.L., MOREY, G.B., CLELAND, J.M. 1994. Occurrence and genetic implications of hyalophane in manganese-rich iron-formation, Cuyuna Iron Range, Minnesota, USA. Mineralogical Magazine, 58, 387-399.

MEDEIROS, V.C., NASCIMENTO, M.A.L., GALINDO, A.C., DANTAS, E.L. 2012. Augen gnaisses riacianos no Domínio Rio Piranhas-Seridó – Província Borborema, Nordeste do Brasil. Geologia USP, Série Científica, 12, 3-14.

MEINERT, L.D. 1992. Skarns and Skarn Deposits. Geoscience Canada, 19, 145-162.

MEINERT, L.D., DIPPLE, G.M., NICOLESCU, S. 2005. World Skarn Deposits. In: HEDENQUIST, J.W., THOMPSON, J.F.H., GOLDFARB, R.J., RICHARDS, J.P. (eds). Economic Geology 100th Anniversary Volume, 299–336.

MOERI, E.N., KLOECHNER, P.J.S. 1979. Mineralizações scheelitíferas na região de Santa Luzia, Paraíba. Atas do IX Simpósio de Geologia do Nordeste, Natal, 383-393.

MOERI, E.N., KLOECHNER, P.J.S. 1979. Os anfibolitos como guia de prospecção de scheelita. Atas do IX Simpósio de Geologia do Nordeste, Natal, 168-179.

MORIMOTO, N., FABRIES, J., FERGUSON, A.K., GINZBURG, I.V., ROSS, M., SEIFERT, F.A., ZUSSMAN, J., AOKI, K., GOTTARDI, G. 1988. Nomenclature of pyroxenes. American Mineralogist, 73, 1123-1133.

NACHIT, H., IBHI, A., ABIA, E.H., OHOUD, M.B. 2005. Discrimination between primary magmatic biotites, reequilibrated biotites and neoformed biotites. Comptes Rendus Geoscience, 337, 1415-1420.

NADOLL, P., ANGERER, T., MAUK, J.L., FRENCH, D.,WALSHE, J. 2014. The chemistry of hydrothermal magnetite: a review. Ore Geology Reviews, 61, 1–32.

NADOLL, P., MAUK, J.L., LEVEILLE, R.A., KOENIG, A.E. 2015. Geochemistry of magnetite from porphyry Cu and skarn deposits in the southwestern United States. Mineralium Deposita, 50, 493–515.

NASCIMENTO, M.A.L., GALINDO, A.C., MEDEIROS, V.C. 2015. Ediacaran to Cambrian magmatic suites in the Rio Grande do Norte domain, extreme Northeastern Borborema Province (NE of Brazil): Current knowledge. Journal of South American Earth Sciences, 58, 281-299.

NEVES, S.P. 2003. Proterozoic history of the Borborema province (NE Brazil): Correlations with neighboring cratons and Pan-African belts and implications for the evolution of western Gondwana. Tectonics, 22, 1031.

NEVES, S.P., BRUGUIER, O., BOSCH, D., SILVA, J.M.R., MARIANO, G. 2008. U–Pb ages of plutonic and metaplutonic rocks in southern Borborema Province (NE Brazil): Timing of Brasiliano deformation and magmatism. Journal of South American Earth Sciences, 25, 285-297.

NEVES, S.P. 2015. Constraints from zircon geochronology on the tectonic evolution of the Borborema Province (NE Brazil): Widespread intracontinental Neoproterozoic reworking of a Paleoproterozoic accretionary orogeny. Journal of South American Earth Sciences, 58, 150–164.

NEVES, S.P., BRUGUIER, O., SILVA, J.M.R., MARIANO, G., SILVA FILHO, A.F., TEIXEIRA, C.M.L. 2015. From extension to shortening: Dating the onset of the Brasiliano Orogeny in eastern Borborema Province (NE Brazil). Journal of South American Earth Sciences, 58, 238-256.

NEWBERRY, R.J. 1982. Tungsten-bearing skarns of the Sierra Nevada. I. The Pine Creek Mine, California. Economic Geology, 77, 823-844.

NEWBERRY, R.J., SWANSON, S.E. 1986. Scheelite skarn granitoids: An evaluation of the roles of magmatic sources and process. Ore Geology Reviews, 1, 57-81.

NEWBERRY, R.J. 1987. Use of intrusive and calc-silicate compositional data to distinguish contrasting skarn types in the Darwin polymetallic skarn district, California, USA. Mineralium Deposita, 22, 207-215.

OLIVEIRA, F.V. 2015. Chronus: Um novo suplemento para a redução de dados U-Pb obtidos por LA-ICPMS. Masters Dissertation (Unpublished), Universidade de Brasília, 107 p.

PARKER, R.L. 1967. Composition of the Earth's Crust. In: FLEISCHER, M. Data of Geochemistry, Sixth Edition. Geological Survey Professional Paper 440-D, 1-19.

PETRIK, I., BROSKA, I., LIPKA, J., SIMAN, P. 1995. Granitoid Allanite-(Ce): Substitution Relations, REDOX Conditions and REE Distributions (On An Example Of I-Type Granitoids, Western Carpathians, Slovakia). Geologica Carpathica, 46, 79-94.

PIRAJNO, F. 1992. Porphyry Systems and Skarns. In: Pirajno, F. (ed). Hydrothermal Mineral Deposits - Principles and fundamental concepts for the Exploration Geologist. Springer, 325-374.

PIRAJNO, F. 2009. Skarn Systems. In: PIRAJNO, F. (ed). Hydrothermal Processes and Mineral Systems, Springer, 535-580.

POKROVSKI, G.S., BORISOVA, A.Y., BYCHKOV, A.Y. 2013. Speciation and Transport of Metals and Metalloids in Geological Vapors. Reviews in Mineralogy & Geochemistry, 76, 165-218.

POLLARD, P.J. 2001. Sodic(-calcic) alteration in Fe-oxide-Cu-Au districts: an origin via unmixing of magmatic H2O-CO2-NaCl ± CaCl2-KCl fluids. Mineralium Deposita, 36, 93-100.

RASMUSSEN, K.L., LENTZ, D.R., FALCK, H. PATTISON, D.R.M. 2011. Felsic magmatic phases and the role of late-stage aplitic dykes in the formation of the world-class Cantung Tungsten skarn deposit, Northwest Territories, Canada. Ore Geology Reviews, 41, 75–111.

RASMUSSEN, K.L., MORTENSEN, J.K. 2013. Magmatic petrogenesis and the evolution of (F:Cl:OH) fluid composition in barren and tungsten skarn-associated plutons using apatite and biotite compositions: Case studies from the northern Canadian Cordillera. Ore Geology Reviews, 50, 118-142.

REID, A.J., SWAIN, G., MASON, D., MAAS, R. 2011. Nature and timing of Cu–Au–Zn–Pb mineralisation at Punt Hill, eastern Gawler Craton. MESA Journal, 60, 7-17.

RICHARDS, J.P., MUMIN, A.H. 2013. Magmatic-hydrothermal processes within an evolving Earth: Iron oxide-copper-gold and porphyry Cu ± Mo ± Au deposits. Geology, 41, 767–770.

ROBB, L. 2005. Introduction to ore forming processes. Blackwell Science, Malden, 373 p.

ROLLINSON, H.R. 1993. Using Geochemical Data: Evaluation, Presentation, Interpretation. Longman/Wiley. New York.

RUIZ, F.V., DELLA GIUSTINA, M.E.S., OLIVEIRA, C.G., DANTAS, E.L., HOLLANDA, M.H.B. 2018. The 3.5 Ga São Tomé layered mafic-ultramafic intrusion, NE Brazil: Insights into a Paleoarchean Fe-Ti-V oxide mineralization and its reworking during West Gondwana assembly. Precambrian Research, In Press.

RUNYON, S.E., STEELE-MACINNIS, M., SEEDORFF, E., LECUMBERRI-SANCHEZ, P., MAZDAB, F.K. 2017. Coarse muscovite veins and alteration deep in the Yerington batholith, Nevada: insights into fluid exsolution in the roots of porphyry copper systems. Mineralium Deposita, 52, 463-470.

SALIM, J. 1979. Geologia e Controle de Mineralizações Scheelitíferas da Região da Serra do Feiticeiro e Bonfim - RN. Masters Dissertation (Unpublished), Universidade de Brasília.

SALIM, J. 1993. Géologie, pétrologie et géochimie des skarns à scheelite de la Mine Brejuí, Currais Novos, région du Seridó, NE du Brésil. DrSc thesis, Université Catholique de Louvain, Belgium.

SALLET, R., PRICE, J.D., BABINSKI, M., MORITZ, R., SOUZA, Z.S., CHIARADIA, M. 2015. Experimental anatexis, fluorine geochemistry and lead-isotopeconstraints on granite petrogenesis in the Seridó Belt, Borborema Province, northeastern Brazil. Chemical Geology, 400, 122-148.

SANTOS, E.J., MEDEIROS, V.C. 1999. Constraints from granitic plutonism on Proterozoic crustal growth of the Transverse Zone, Borborema Province, NE Brazil. Revista Brasileira de Geociências, 29, 73-84.

SANTOS, E.J., VAN SCHMUS, W.R., KOZUCH, M., BRITO NEVES, B.B. 2010. The Cariris Velhos tectonic event in Northeat Brazil. Journal of South American Earth Sciences, 29, 61-76.

SANTOS, E.J., SOUZA NETO, J.A., SILVA, M.R.R., BEURLEN, H., CAVALCANTI, J.A.D., SILVA, M.G., DIAS, V.M., COSTA, A.F., SANTOS, L.C.M.L., SANTOS, R.B. 2014. Metalogênese das porções norte e central da Província Borborema. In: SILVA, M.G., NETO, M.B.R., JOST, H., KUYUMJIAN, R.M. (Eds.), Metalogênese das Províncias Tectônicas Brasileiras. Serviço Geológico do Brasil – CPRM, Belo Horizonte, 343–388.

SANTOS, R.V., OLIVEIRA, C.G., PARENTE, C.V., GARCIA, M.G.M., DANTAS, E.L. 2013. Hydrothermal alteration related to a deep mantle source controlled by a Cambrian intracontinental strike-slip fault: Evidence for the Meruoca felsic intrusion associated with the Transbraziliano Lineament, Northeastern Brazil. Journal of South American Earth Sciences, 43, 33-41.

SANTOS, T.J.S., FETTER, A.H., HACKSPACHER, P.C., VAN SCHMUS, W.R., NOGUEIRA NETO, J.A. 2008. Neoproterozoic tectonic and magmatic episodes in the NW sector of Borborema Province, NE Brazil, during assembly of Western Gondwana. Journal of South American Earth Sciences, 25, 271-284.

SCHOBBENHAUS, C., CAMPOS, D.A., DERZE, G.R., ASMUS, H.E., 1984. Geologia do Brasil: Departamento Nacional da Produção Mineral, Brasília. 501 p.

SEEDORFF, E., DILLES, J.H., PROFFETT JR., J.H., EINAUDI, M.T., ZURCHER, L., STAVAST, W.J.A., JOHNSON, D.A., BARTON, M.D. 2005. Porphyry Deposits: Characteristics and Origin of Hypogene Features. In: HEDENQUIST, J.W., THOMPSON, J.F.H., GOLDFARB, R.J., RICHARDS, J.P. (eds). Economic Geology 100th Anniversary Volume, 251–298.

SEEDORFF, E., BARTON, M.D., STAVAST, W.J.A., MAHER, D.J. 2008. Root Zones of Porphyry Systems: Extending the Porphyry Model to Depth. Economic Geology, 103, 939-956.

SEYMOUR, K.S., TOMBROS, S., MASTRAKAS, N., ZOUZIAS, D., SPRY, P.G., DÉNÈS, G., KRANIDIOTIS, P. 2009. Scheelite skarn mineralization associated with the Tinos pluton, Cyclades. Neues Jahrbuch für Mineralogie - Abhandlungen, 186, 37-50.

SHARMA, R., SRIVASTAVA, P.K. 2014. Hydrothermal Fluids of Magmatic Origin. In: KUMAR, S., SINGH, R.N. (eds). Modelling of Magmatic and Allied Processes, 181-208.

SIAL, A.N. 1986. Granite-types in Northeast Brazil: Current knowledge. Revista Brasileira de Geociências, 16, 54-72.

SILLITOE, R.H. 2010. Porphyry Copper Systems. Economic Geology, 105, 3-41.

SILVA, W.L. 2000. Mineralizações Auríferas em Veios de Quartzo na Faixa Seridó, NE do Brasil: Exemplos de Depósitos de Ouro de Fácies Anfibolito em Faixa Móvel Proterozoica. Rio Claro. 301 p. PhD Thesis (Unpublished), Universidade Estadual Paulista (UNESP).

SMIRNOV, V.I. 1976. Skarn deposits. In: Geology of Mineral Deposits. MIR Publications, Moscow, p. 156-188.

SOLOVIEV, S.G. 2011. Geology, Mineralization, and Fluid Inclusion Characteristics of the Kensu W-Mo Skarn and Mo-W-Cu-Au Alkalic Porphyry Deposit, Tien Shan, Kyrgyzstan. Economic Geology, 106, 193-222.

SOLOVIEV, S.G. 2014. Geology, mineralization, and fluid inclusion characteristics of the Kumbel oxidized W–Cu–Mo skarn and Au–W stockwork deposit in Kyrgyzstan, Tien Shan. Mineralium Deposita, 50, 187-220.

SOUZA NETO, J.A., LEGRAND, J.M., VOLFINGER, M., PASCAL, M.L., SONNET, P. 2008. W–Au skarns in the Neo-Proterozoic Seridó Mobile Belt, Borborema Province in northeastern Brazil: an overview with emphasis on the Bonfim deposit. Mineralium Deposita, 43, 185–205.

SOUZA NETO, J.A., VOLFINGER, M., PASCAL, M.L., LEGRAND, J.M., SONNET, P. 2012. The occurrence of gold-rich pyrite in the Itajubatiba Skarn Deposit, Borborema Province, Northeastern Brazil: A discovery by PIXE analyses. Geociências, 31, 553-566.

SOUZA, Z.S., MARTIN, H., PEUCAT, J., JARDIM DE SÁ, E.F., MACEDO, M.H.F. 2007. Calc-Alkaline Magmatism at the Archean-Proterozoic Transition: the Caicó Complex Basement (NE Brazil). Journal of Petrology, 48, 2149-2185.

SOUZA, Z.S., KALSBEEK, F., DENG, X.D., FREI, R., KOKFELT, T.F., DANTAS, E.L., LI, J.W., PIMENTEL, M.M., GALINDO, A.C. 2016. Generation of continental crust in the northern part of the Borborema Province, northeastern Brazil, from Archean to Neoproterozoic. Journal of South American Earth Sciences, 68, 68-96.

STEPANOV, A.V., BEKENOVA, G.K., LEVIN, V.L., HAWTHORNE, F.C. 2012. Natrotitanite, ideally (Na0.5Y0.5)Ti(SiO4)O, a new mineral from the Verkhnee Espe deposit, Akjailyautas mountains, Eastern Kazakhstan district, Kazakhstan: description and crystal structure. Mineralogical Magazine, 76, 37-44.

SUN, S.S., MCDONOUGH, W.F. 1989. Chemical and isotopic systematics of oceanic basalts: implications for mantle composition and processes. In: Saunders, A.D., Norry, M.J. (Eds.), Magmatism in the Ocean Basins. Special Publication Volume, Geological Society of London, 42, 313–345.

SUZUKI, K., MASUDA, A. 1996. Re-Os dating of molybdenites from ore deposits in Japan: Implication for the closure temperature of the Re-Os system for molybdenite and the cooling history of molybdenum ore deposits. Geochimica and Cosmochimica Acta, 60, 3151-3159.

TINDLE, A.G., WEBB, P.C. 1990. Estimation of lithium contents in trioctahedral micas using microprobe data: application to micas from granitic rocks. European Journal of Mineralogy, 2, 595-610.

TISCHENDORF, G., RIEDER, M., FöRSTER, H.J., GOTTESMANN, B., GUIDOTTI, C.V. 2004. A new graphical presentation and subdivision of potassium micas. Mineralogical Magazine, 68, 649-667.

TOMBROS, S.F., SEYMOUR, K.S., WILLIAMS-JONES, A.E., ZHAI, D., LIU, J. 2015. Origin of a barite-sulfide ore deposit in the Mykonos intrusion, cyclades: Trace element, isotopic, fluid inclusion and raman spectroscopy evidence. Ore Geology Reviews, 67, 139–157.

TÖRNEBOHM, A.E. 1875. Geognostisk beskrifning ofver Persbergets Grufvefält. Sveriges Geologiska Undersökning: Stockholm, P.A. Norstedt and Sons, 21 p.

TRINDADE, I., R. 2000. Estudo Geoquímico e Geocronológico Rb-Sr e Sm-Nd em Zonas de Cisalhamento Mineralizadas em Ouro e Suas Relações Com as Rochas Encaixantes e Geocronológico Sm-Nd em Mineralização de Scheelita na Faixa Seridó. Masters Dissertation (Unpublished), Universidade Federal do Rio Grande do Norte, 125 p.

VAN SCHMUS, W.R., BRITO NEVES, B.B., WILLIAMS, I.S., HACKSPACHER, P.C., FETTER, A.H., DANTAS, E.L., BABINSKI, M. 2003. The Seridó Group of NE Brazil, a late Neoproterozoic pre- to syn-collisional basin in West Gondwana: insights from SHRIMP U–Pb detrital zircon ages and Sm–Nd crustal residence (TDM) ages. Precambrian Research, 127, 287–327.

VAN SCHMUS, W.R., OLIVEIRA, E.P., SILVA FILHO, A.F., TOTEU, S.F., PENAYE, J., GUIMARÃES, I.P. 2008. Proterozoic links between the Borborema Province, NE Brazil, and the Central African Fold Belt. In: PANKHURST, R.J., TROUW, R.A.J., BRITO NEVES, B.B., DE WIT, M.J. (eds). West Gondwana: Pre-Cenozoic Correlations Across the South Atlantic Region, 69-99.

VAN SCHMUS, W.R., KOZUCH, M., BRITO NEVES, B.B. 2011. Precambrian history of the Zona Transversal of the Borborema Province, NE Brazil: Insights from Sm-Nd and U-Pb geochronology. Journal of South American Earth Sciences, 31, 227-252.

VASCONCELOS, P.M., ONOE, A.R., KAWASHITA, K., SOARES, A.J., TEIXEIRA, W. 2002. 40Ar/39Ar Geochronology at the Instituto de Geociências, USP: Instrumentation, Analytical Procedures, and Calibration. Annals of the Brazilian Academy of Sciences, 74, 297–342.

WHITNEY, D.L., EVANS, B.W. 2010. Abbreviations for names of rock-forming minerals. American Mineralogist, 95, 185–187.

WILLIAMS, P.J., BARTON, M.D., JOHNSON, D.A. FONTBOTÉ, L., HALLER, A., MARK, G., OLIVER, N.H.S., MARSCHIK, R. 2005. Iron Oxide Copper-Gold Deposits: Geology, Space-Time Distribution, and Possible Modes of Origin. In: HEDENQUIST, J.W., THOMPSON, J.F.H., GOLDFARB, R.J., RICHARDS, J.P. (eds). Economic Geology 100th Anniversary Volume, 371–405.

WINTER, J.D. 2010. Principles of Igneous and Metamorphic Petrology. Pearson Prentice Hall. New York. 703 p.

WOOD, D.A., JORON, J.L., TREUIL, M., NORRY, M., TARNEY, J. 1979. Elemental and Sr Isotope Variations in Basic Lavas From Iceland and the Surrounding Ocean Floor. Contributions to Mineralogy and Petrology, 70, 319-339.

WOOD, S.A., SAMSON, I.M. 2000. The hydrothermal geochemistry of tungsten in granitoid environments: I. Relative solubilities of ferberite and scheelite as a function of T, P, pH and m(NaCl). Economic Geology, 95, 143-182.

XIA, R., WANG, C., QING, M., DENG, J., CARRANZA, E.J.M., LI, W., GUO, X., GE, L., YU, W. 2015. Molybdenite Re–Os, zircon U–Pb dating and Hf isotopic analysis of the Shuangqing Fe–Pb–Zn–Cu skarn deposit, East Kunlun Mountains, Qinghai Province, China. Ore Geology Reviews, 66, 114-131.

YANG, M., FU, J. REN, A. 2015. Recognition of Yanshanian magmatic-hydrothermal gold and polymetallic gold mineralization in the Laowan gold metallogenic belt, Tongbai Mountains: New evidence from structural controls, geochronology and geochemistry. Ore Geology Reviews, 69, 58-72.

ZAJACZ, Z., HALTER, W.E., PETTKE, T., GUILLONG, M. 2008. Determination of fluid/melt partition coefficients by LA-ICPMS analysis of co-existing fluid and silicate melt inclusions: Controls on element partitioning. Geochimica et Chosmochimica Acta, 72, 2169-2197.

ZHENG, Y., FU, Q., HOU, Z., YANG, Z., HUANGA, K., WU, C., SUN, Q. 2015. Metallogeny of the northeastern Gangdese Pb–Zn–Ag–Fe–Mo–W polymetallic belt in the Lhasa terrane, southern Tibet. Ore Geology Reviews, 70, 510–532.

ZHENG, Y., CAI, X., DING, Z., CAWOOD, P.A., YUE, S. 2017. Geology, geochronology and isotopic geochemistry of the Xiaoliugou W-Mo ore field in the Qilian Orogen, NW China: Case study of a skarn system formed during continental collision. Ore Geology Reviews, 81, 575-586.